VILNIUS UNIVERSITY
CENTER FOR PHYSICAL SCIENCES AND TECHNOLOGY

SANDRA TAMOŠAITYTĖ

LINEAR AND NON-LINEAR VIBRATIONAL MICROSCOPY-BASED CHEMICAL IMAGING OF PATHOLOGIC CENTRAL NERVOUS SYSTEM TISSUE

Doctoral dissertation

Physical Sciences, Physics (02P)

Vilnius 2018

The dissertation has been prepared during the years 2013 – 2018 at Institute of Chemical Physics, Vilnius University and dept. of Clinical Sensing and Monitoring, Anesthesiology and Intensive Care Medicine, Faculty of Medicine, Technical University Dresden.

Supervisor – prof. dr. Valdas Šablinskas (Vilnius University, physical sciences, physics - 02P).

Advisor – prof. dr. Gerald Steiner (Technical University Dresden, physical sciences, physics - 02P).

VILNIAUS UNIVERSITETAS
FIZINIŲ IR TECHNOLOGIJOS MOKSLŲ CENTRAS

SANDRA TAMOŠAITYTĖ

PATOLOGINIŲ NERVŲ SISTEMOS AUDINIŲ CHEMINIS VAIZDINIMAS NAUDOJANT TIESINĘ IR NETIESINĘ VIRPESINĘ MIKROSKOPIJĄ

Daktaro disertacija

Fiziniai mokslai, Fizika (02P)

Vilnius, 2018

Disertacija rengta 2013 – 2018 metais Vilniaus universiteto cheminės fizikos institute ir Drezdeno technikos universiteto medicinos fakulteto anesteziologijos ir intensyviosios terapijos medicinos „Clinical sensing and monitoring“ padalinyje.

Mokslinis vadovas – prof. dr. Valdas Šablinskas (Vilniaus universitetas, fiziniai mokslai, fizika - 02P).

Mokslinis konsultantas – prof. dr. Gerald Steiner (Drezdeno technikos universitetas, fiziniai mokslai, fizika - 02P).

INDEX

Abbreviations

5-ALA – 5-aminolevulinic acid

ANOVA – analysis of variance

BP – band pass

CARS – coherent anti-Stokes Raman Scattering

CCD – charge-coupled device

CNS – central nervous system

CoA – corpora amylacea

CP-CARS – circularly polarized coherent anti-Stokes Raman scattering

CSPG – chondroitin sulphate proteoglycan

DNA – deoxyribonucleic acid

EAE – experimental autoimmune encephalomyelitis

Epi-CARS (E-CARS) – backward-propagating coherent anti-Stokes Raman scattering

F-CARS – forward-propagating coherent anti-Stokes Raman scattering

FFPP – formalin-fixed paraffin-preserved

FIR – far infrared

FPA – focal plane array

FTIR – fourier transform infrared

FWM – four-wave mixing

GBM – Glioblastoma Multiforme

HCA – hierarchical cluster analyses

H&E – hematoxylin and eosin

IR – infrared

LDA – linear discriminant analysis

MCT – mercury-cadmium-telluride

MIR – middle infrared

MISS – minimally invasive spine surgery

MNLO – multimodal non-linear optical

MOPA – master oscillator power amplifier

MRI – magnetic resonance imaging

MS – multiple sclerosis

NA – numerical aperture

NAD(P)H – reduced nicotinamide adenine (phosphate) dinucleotide

NIR – near infrared

PCA – principal component analysis

PMT – photomultiplier tubes

RGB – red-green-blue

RNA – ribonucleic acid

ROI – region of interest

RP-CARS – rotating-polarization coherent anti-Stokes Raman scattering

SAM – saturable absorber mirror

SCI – spinal cord injury

SEM – standard error of the mean

SHG – second harmonic generation

SIMCA – soft independent modeling of class analogy

SR-CARS – symmetry-resolved coherent anti-Stokes Raman scattering

SRS – stimulated Raman scattering

THG – third harmonic generation

TPEF – two-photon excited fluorescence

UV – ultraviolet

VCA – vertex component analysis

STRUCTURE OF THE THESIS

The main parts of this doctoral thesis are introduction, three chapters and list of references. Introduction is presenting the overall background and motivation of this work. Here, the main goal and four tasks are formulated as well as statements of the thesis and novelty and relevance of the results are highlighted. The list of author's publications and conference abstracts as well as participation in schools for young scientists and research funding during the doctoral research period are included. At the end of introduction, the author's contributions are presented.

In the first chapter, the vibrational spectroscopy-based imaging techniques applied in this work are reviewed based on the related literature. Here, the main focus are the theoretical aspects of underlying physical phenomena and the general description of experimental systems. Moreover, the most thesis-relevant studies describing the application of Fourier Transform Infrared and Raman microspectroscopy as well as coherent anti-Stokes Raman scattering (CARS) imaging to analyze central nervous system tissues and its pathologies, in particular the ones related with lipid alterations, are reviewed.

The second chapter is covering the materials and methods applied throughout this research. In particular, the exact experimental systems are described and the biological tissue staining protocols are explained. The reader of this thesis can refer to this chapter as the experimental basis while reading the third chapter, where only experimental-specific details are provided.

The third chapter is covering the experimental results of this work. Depending on specific problem addressed it is subdivided in three subchapters. In the first subchapter, the study regarding the applicability of deparaffinized tissue sections for CARS imaging is presented. The second subchapter is about CARS imaging of brain tumors. The last, third, subchapter is covering different means

of vibrational spectroscopic-based imaging for monitoring spinal cord injury and its treatment. In this subchapter, spinal cord injury-induced inflammation is also addressed in more detail. Each subchapter have similar structure covering: (i) problem-specific research background and motivation and/or biomedical aspects. Here, the literature review focused on particular study is also present. (ii) Specific details regarding sample preparation and experiments, (iii) results and discussion and (iv) conclusions.

At the end of the thesis, the list of the bibliographic references is given. Finally, this thesis is concluded by giving the acknowledgements.

INTRODUCTION

Studies of biological tissues and biomolecules, which are essential for both structure and growth of living systems, is of a key importance in biomedical and bioanalytical applications. Various methods are widely used in this field of studies, including optical microscopy and spectroscopy [1]. Conventional optical microscopy techniques, such as bright field [2] and differential interference contrast microscopy [3], are capable to provide morphological information of a biological tissue, but do not carry specific chemical information. Current immunohistochemical visualization techniques, which are based on labeling the molecules with special dyes, provide crucial visual and chemical information [4]. However, binding the molecules with special dies is an invasive method. What is more, the sample preprocessing is usually long and complicated, the success of evaluation is greatly based on the experience of the pathologist and the provided chemical information is not complete [5].

Due to the growing need of clinical applications and of improvements in disease diagnosis, the importance to establish sensitive, chemically selective and label-free imaging techniques that are based on fundamental properties of biomolecules and thus are non-invasive is of a great demand.

Vibrational spectroscopy imaging, which is based on intrinsic molecular vibrations, is capable to provide chemical information without exogenous labeling of biomolecules in a form of vibrational spectra [6]. However, the main limiting factors of infrared (IR) spectroscopic imaging are (i) low spatial resolution due to considerably long wavelength of IR radiation and (ii) strong water absorption in biological samples [7,8]. Raman microscopy does not suffer from the mentioned problems. On the other hand, when applied for biological samples, the spontaneous Raman scattering (or inelastic scattering) imaging also faces several limitations. Firstly, the cross sections of spontaneous Raman

scattering are roughly only one out of 10^3 to 10^6 scattered photons to be scattered inelastically [9]. Thus, the acquisition of Raman spectra requires high laser powers and integration times up to a few seconds per spectrum. Also, the background autofluorescence signal of the sample often obstructs the sample specific vibrational spectral information [10].

Detailed morphochemical information can be attained by Coherent Anti-Stokes Raman Scattering (CARS) microscopy, which is a non-linear variant of spontaneous Raman scattering imaging. The method is based on the non-linear interaction between molecules and pulsed laser radiation. During the event, information can be gained from chemically selective signals, probing particular Raman scattering mode. Therefore, endogenous morphochemical contrast of the tissue specimen can be achieved without any additional labeling. When compared with spontaneous Raman scattering microscopy, the full vibrational spectral data is not acquired and the chemical profile of the sample is incomplete. This disadvantage is compensated by the fact that CARS signal is by nature coherent and intensive, which makes the data acquisition considerably faster [11]. By simultaneous generation and acquisition of CARS, second harmonic generation (SHG) and two-photon excited fluorescence (TPEF) signals on a scanning laser microscope, a highly chemically informative multimodal image can be recorded by single imaging experiment [12].

Revived by innovation, these modern imaging techniques rapidly grow scientific interest for variety of potential applications and further development. Nevertheless, possible sample preparation methods, which would allow to successfully apply vibrational spectroscopy-based imaging for tissue morphochemical investigations are still unclear or unproven and, therefore, require additional studies. For example, formalin-fixed paraffin-preserved (FFPP) brain tissue samples could be an important source of extensive retrospective studies. However, the applicability and potential of CARS imaging

of particular samples was not yet addressed. Furthermore, the diagnostic capabilities of vibrational spectroscopic imaging and CARS microscopy are especially promising to investigate nervous tissue of central nervous system (CNS) and, especially, lipid content altering diseases of CNS [13], such as spinal cord injury or brain tumors. Despite this fact, linear vibrational spectroscopic imaging and CARS microscopy still requires more extensive studies in the field of neuroimaging. Also, the potential of these particular means of imaging to be applied in a complementary fashion is not yet extensively exploited.

High death rate due to the both primary and secondary brain tumors is mainly related to the remaining tumor tissue and cells in the healthy brain tissue after surgical resection. Thus, the precise identification of tumor borders is on a high demand. It is challenging, because tumor cells are often infiltrating in the surrounding normal brain tissue [14]. Currently, Magnetic Resonance Imaging (MRI) is mainly used for imaging of the brain tumors. However, the imaging resolution of this modality is not enough for identification of single cell or subcellular structures [15].

The early and accurate diagnosis of brain tumors is another important issue to be addressed. The “gold standard”, which is implemented in clinical practice nowadays, is histochemistry of the biopsies. Label-free imaging modality with subcellular lateral resolution, which overcomes the aforementioned problems of immunohistochemical stainings, is CARS microscopy.

Evans et al. was the first to successfully implement CARS imaging for characterization of tumor in mouse brain tissue [16]. While CARS and multiphoton microscopy was used to image surgically removed lung carcinoma metastasis from human brain by Meyer et al. [17], it has not yet been demonstrated for a significant number of different metastases. Also, studies of CARS imaging potential for human brain tumors is still lacking.

Spinal cord, which is responsible for transmitting the sensory and motor information between the brain and body, is a part of CNS. Together with other cellular structures, the two major types of cells, namely neurons and glial cells, reside in the spinal cord [18]. The degeneration of these cells (damage of axons, loss of neurons and glia, demyelination of spared axons) in and around the lesion site is the consequence of the spinal cord injury (SCI). After the acute phase of SCI, secondary processes, such as vascular changes, biomolecular alterations, apoptosis, excitotoxicity, oxygen free radical formation, lipid peroxidation, proceed [19]. After-traumatic spinal cord has a limited capacity to regenerate; however, without introduction of any additional treatment, the spontaneous full functional recovery is not possible in mammalians. Due to the complexity of the pathophysiology of SCI, the stimulation of nervous tissue regeneration is challenging. While the number of potential ways to promote axon regeneration and treat SCI is increasing, the most of suggested treatment strategies still require comprehensive investigation to understand the underlying pathophysiological and biomolecular mechanisms [20].

Imaging of damaged spinal cord is essential for better understanding the processes occurring during the spinal cord degeneration/regeneration. Visualizing the specific biochemical changes, which follow after the introduction of the treatment therapies for SCI, could explain the mechanisms that underline the recovery. The specific treatment strategy could be also evaluated qualitatively and quantitatively [21].

CARS microscopy was used for SCI imaging, but never with introduced treatment, by different authors, for example by Shi et al. [22]. SCI imaging by means of both CARS and vibrational microspectroscopy was successfully implemented by Galli et al. in research group of Technical University of Dresden [23]. The approach to combine non-linear microscopy and vibrational

microspectroscopy for gaining morphochemically specific information of SCI, when treatment strategies are introduced, is thus very promising.

Goals and tasks of the thesis

The fundamental goal of this thesis was to combine experimental vibrational spectroscopy-based imaging techniques and spectral data analysis approaches to (i) evaluate these imaging modalities as a tool for diagnostic neuropathology and monitoring of SCI treatment strategies and to (ii) gain new insights in biochemical status of diseased nervous tissue. Therefore, this work covers the following tasks:

1. Analyze the effects of formalin-fixed paraffin-preserved brain tissue sections deparaffinization in order to evaluate compatibility of formalin-fixed paraffin-preserved brain tissue samples for multimodal CARS imaging and to decide for the most suitable brain tissue sample preservation approach for CARS microscopic imaging.
2. Validate applicability of CARS microscopy as a tool for precise delineation and assessment of primary and secondary brain tumors and confirm the results with the help of Raman microspectroscopy.
3. Apply and evaluate infrared and Raman microspectroscopy as well as multimodal CARS microscopy for assessing the effects of and monitoring novel soft alginate hydrogel implants for spinal cord injury treatment.
4. Apply Raman microspectroscopy in a combination with CARS and TPEF microscopy to retrieve the biochemical information about the inflammation-related alterations of lipids triggered by spinal cord injury.

Statements of the thesis

1. Despite the loss of lipids and artifacts induced by residual paraffin, sections of deparaffinized brain tissue provide morphochemical

information, when imaged by Raman microspectroscopy and CARS microscopy. However, the study of brain tissue pathologies is limited, when deparaffinized sections are used, and sample cryoprotection is a better choice for more biochemically comprehensive results.

2. The average reduction of CARS signal intensity in brain tumors was decreased by 30% – 40% with respect to normal gray matter, depending on type of tumor. Therefore, CARS signal intensity ratio between tumor and normal gray matter can be used as a robust parameter to identify tumor borders, infiltrations and small tumor islands.
3. According to semi-quantitative infrared spectral data analysis, in the chronic state of spinal cord injury, implants of soft alginate hydrogel result in significantly higher lipid content in contralateral white matter and significantly reduced fibrotic scarring.
4. Spectral information provided by FTIR and Raman microspectroscopy techniques enables to detect alginate hydrogel implant and monitor its chemical stability in spinal cord injury.
5. Mapping the intensity of carbonyl Raman band at 1743 cm^{-1} allows to localize inflammatory regions of spinal cord injury, while chemometrical analysis of Raman spectral data reveals these regions to be enriched with saturated fatty acids.

Novelty and relevance of the results

- Vibrational spectroscopic imaging and multimodal CARS microscopy have a great potential to be applied as separate methods as well as in a complementary manner to morphochemically visualize various CNS tissue pathologies with the future diagnostic, monitoring of treatment and even intraoperative prospects in clinical application.
- As detailed and comparative approach was still lacking to evaluate CARS imaging potential for brain tumor delineation and characterization,

extended set of primary and secondary tumors grown in mouse model as well as human tumors were investigated in this work.

- The decrease of CARS signal intensity in brain tumors was for the first time evaluated in detail and correlated with tissue structures and cellularity: it might result not only from higher occurrence of lipid-poor structures within the tissue, but also be related with a general biochemical signature of tumorous tissue.
- Novel unfunctionalized soft alginate hydrogel implant was applied as a treatment strategy to SCI in rat model. Combined approach to apply FTIR, Raman and multimodal CARS imaging is excellent for comprehensive biochemical assessment of SCI treatment strategies.
- Until now only SCI-induced demyelination and scarring were already studied elsewhere by Raman spectroscopy. Inflammation was so far neglected in spectroscopic studies of SCI and was successfully addressed in this work.

Publications included in the thesis

1. **S. Tamosaityte**, R. Galli, O. Uckermann, K. H. Sitoci-Ficici, M. Koch, R. Later, G. Schackert, E. Koch, G. Steiner, M. Kirsch. Inflammation-related alterations of lipids after spinal cord injury revealed by Raman spectroscopy. *J. Biomed. Opt*. (2016).
2. R. Galli, **S.Tamosaityte**, M.Koch, K.H.Sitoci-Ficici, R.Later, O.Uckermann, R.Beiermeister, M.Gelinsky, G.Schackert, M.Kirsch, E.Koch, and G.Steiner. Raman-based imaging uncovers the effects of alginate hydrogel implants in spinal cord injury. *Proc. SPIE*. 9536 (2015).
3. **S. Tamosaityte**, R. Galli, O. Uckermann, K. H. Sitoci-Ficici, R. Later, R. Beiermeister, F. Doberenz, M. Gelinsky, E. Leipnitz, G. Schackert, E. Koch, V. Sablinskas, G. Steiner, M. Kirsch. Biochemical Monitoring of Spinal

Cord Injury by FT-IR Spectroscopy—Effects of Therapeutic Alginate Implant in Rat Models. *PLoS ONE* 11(2): e0150237 (2015).

4. O. Uckermann, R. Galli, **S. Tamosaityte**, E. Leipnitz, K. D. Geiger, G. Schackert, E. Koch, G. Steiner, M. Kirsch. Label-Free Delineation of Brain Tumors by Coherent Anti-Stokes Raman Scattering Microscopy in an Orthotopic Mouse Model and Human Glioblastoma, *PLoS ONE*, 9(9), 1-9 (2014).

Publications not included in the thesis

1. M. Pucetaite, **S. Tamosaityte**, R. Galli, V. Sablinskas, G. Steiner. Microstructure of urinary stones as studied by means of multimodal nonlinear optical imaging. *J. Raman Spectrosc.* (2016).
2. M. Pucetaite, M. Velicka, **S. Tamosaityte**, V. Sablinskas, Application of SERS spectroscopy for detection of trace components in urinary deposits. *Proc. SPIE.* 8957 (2014).
3. M. Pucetaite, **S. Tamosaityte**, A. Engdahl, J. Ceponkus, V. Sablinskas, P. Uvdal. Microspectroscopic infrared specular reflection chemical imaging of multi-component urinary stones: MIR vs. FIR. *Cent. Eur. J. Chem.* 12(1), 44-52 (2014).

Conference abstracts

1. **S. Tamosaityte**, R. Galli, O. Uckermann, E. Leipnitz, G. Steiner, M. Kirsch. Multiphoton imaging of deparaffinized brain tissue sections, 68th Annual Meeting of the German Society of Neurosurgery (DGNC), 2017 May, Magdeburg, Germany.
2. **S. Tamosaityte**, R. Galli, O. Uckermann, K. H. Sitoci-Ficici, M. Koch, R. Later, G. Schackert , E. Koch, G. Steiner, M. Kirsch, Raman spectroscopy uncovers inflammation changes of lipids initiated by spinal cord injury,

10th CRTD Summer Conference on Regenerative Medicine 2016 June, Dresden, Germany.

3. **S. Tamosaityte**, R. Galli, O. Uckermann, K. H. Sitoci-Ficici, E. Koch, G. Steiner, M. Kirsch, Raman spectroscopy reveals inflammation-related changes of lipids following spinal cord injury, 67th Annual Meeting of the German Society of Neurosurgery (DGNC), 2016 June, Dresden, Germany.
4. **S. Tamosaityte**, R. Galli, O. Uckermann, K. H. Sitoci-Ficici, E. Koch, M. Gelinsky, M. Kirsch, G. Steiner, Alginate implants for regeneration of spinal cord injury – biochemical monitoring by FT-IR imaging, 10th European Biophysics Congress (EBSA 2015), 2015 liepos 18-22, Drezdenas, Vokietija.
5. R. Galli, **S. Tamosaityte**, M. Koch, K. H. Sitoci-Ficici, R. Later, O. Uckermann, R. Beiermeister, M. Gelinsky, G. Schackert, M. Kirsch, E. Koch, G. Steiner, Raman-based imaging uncovers the effects of alginate hydrogel implants in spinal cord injury, European Conferences on Biomedical Optics (ECBO 2015), 2015 birželio 21-25, Miunchenas, Vokietija.
6. **S. Tamosaityte**, R. Galli, O. Uckermann, K. Hakan Sitoci-Ficici, E. Koch, M. Gelinsky, M. Kirsch, G. Steiner, Label-free infrared spectroscopy imaging helps to assess the morphochemistry of experimental alginate-implanted spinal cord injury, 8th CRTD Summer Conference on Regenerative Medicine 2014 June, Dresden, Germany.
7. **S. Tamosaityte**, R. Galli, O. Uckermann, K. Hakan Sitoci-Ficici, E. Koch, M. Gelinsky, M. Kirsch, G. Steiner, Morphochemical effects of alginate implants for treatment of experimental spinal cord injury, 65th Annual Meeting of the German Society of Neurosurgery (DGNC), 2014 May, Dresden, Germany.

8. **S. Tamosaityte**, V. Sablinskas, FT – Raman spectroscopy for assessment of chemical composition of urinary sediments, Developments in Optics and Communications, 10th International Young Scientist conference, Riga, Latvia 2014 April 9 – 12.

Participation in schools and workshop for young scientists

1. Satellite Workshop „Spectroscopies in Biology“. Organized by European Biophysical Societies' Association (EBSA), Radeberg, Germany, 2015 July 15 – 18.
2. Summer school „Biophotonics '15“. Organized by Department of Physics, Lund University, Sweden and Department of Photonics Engineering, Technical University of Denmark, Denmark. Island of Ven, Sweden, 2015 June 6-13. Presented poster “S. Tamosaityte, Vibrational spectroscopy based imaging techniques provide biochemical information of effects of alginate hydrogel implants in spinal cord injury model” received best poster award.
3. Laserlab III Training School for Potential Users “Laser Applications in Spectroscopy, Industry and Medicine”. Organized by Institute of Solid State Physics, Riga, Latvia, 2014 April 9 – 12.
4. Fall school „Science with advanced coherent light sources“. Organized by DESY (Deutsches Elektronen-Synchrotron National Research Center), Hamburg, Germany, 2013 October 7-11.

Funding

Major part of the research in this work was supported by the German Federal Ministry of Education and Research (MediCARS project, A.Z. 13N10777).

Author's contributions

The major part of the experimental design, experimental work and data analysis, altogether leading to this work, was done by the author, whereas

without a close collaboration with several people this research would have been not possible or complete.

Dr. rer. nat. Ortrud Uckermann and Dipl. Biol. Elke Leipnitz implemented brain tumor animal experiments. Human tissue biopsies were provided by Prof. Matthias Kirsch and Dr. med. K. Daniel Martin. Surgery of rat spinal cords and implantation of hydrogel implants were performed by Dr. med. Kerim Hakan Sitoci-Ficici. The alginate hydrogels and their characterization were done by the students Rudolf Beiermeister and Falko Doberenz of Prof. Michael Gelinsky research group. Tissue sample preparation, histological and immunohistochemical stainings and quantification of histopathological parameters of brain tumors were done by Dipl. Biol. Leipnitz and Juliane Hartmann. Partial contribution of the author in sample preparation was to deparaffinize tissue sections according to different protocols in the study of the effects of tissue deparaffinization on multimodal CARS images.

Dr. Roberta Galli shared her expertise on a great extent on experimental design, spectral data analysis and multimodal CARS images interpretation. Dr. Uckermann provided biological knowledge for data analysis and interpretation.

Dr. Uckermann and Dr. Galli wrote the publication “Label-Free Delineation of Brain Tumors by Coherent Anti-Stokes Raman Scattering Microscopy in an Orthotopic Mouse Model and Human Glioblastoma”. The publications “Biochemical Monitoring of Spinal Cord Injury by FTIR Spectroscopy—Effects of Therapeutic Alginate Implant in Rat Models” and “Inflammation-related alterations of lipids after spinal cord injury revealed by Raman spectroscopy” were written by the author together with Dr. Galli and Dr. Uckermann. Undergraduate student Maria Bonsack partly performed experiments and data analysis regarding the study of the effects of tissue deparaffinization on multimodal CARS images.

CHAPTER 1 VIBRATIONAL SPECTROSCOPY-BASED CHEMICAL IMAGING: PRINCIPLES AND APPLICATIONS FOR CNS TISSUES ANALYSIS

1.1. Linear vibrational spectroscopic imaging techniques

1.1.1 Infrared Spectroscopy

Infrared spectroscopy is a vibrational spectroscopic technique based on interaction between infrared radiation and materials. IR radiation covers the spectral range of electromagnetic waves between microwaves and red end of visible light, i.e. approximately between 1 and 100 micrometers of the wavelength. Generally, infrared spectrum is grouped into three regions: near-infrared (NIR), mid-infrared (MIR) and far-infrared (FIR), covering the wavenumber range in 14285-4000 cm^{-1}, 4000-400 cm^{-1} and 400-100 cm^{-1}, respectively. Depending on atomic bonds in particular molecular system it contains, the sample can absorb IR radiation at some of IR frequencies and transmit at the others. IR radiation can also be reflected [24].

The absorption of IR radiation induce the change of vibrational energy state of molecular system, i.e. specific molecular vibrations are being triggered [25]. Typically, the transmitted IR radiation, carrying information about the transmission at specific frequencies, is obtained by a detector. By comparing the spectra of incident and transmitted IR radiation, the absorbed frequencies specific to particular molecular vibrations can be identified. Therefore, IR spectroscopy is especially favorable to obtain information about presence or absence of certain functional groups [26].

The absorption of IR radiation is only possible at the resonant frequencies: the energy of absorbed radiation must be equal to the energy of vibrational

transition. Not all the frequencies of molecular vibrations are “IR active”, i.e. the molecule can absorb IR radiation at only those frequencies at which molecular vibrations are associated with changes of dipole moment. The intensity of IR absorption is related with the magnitude of dipole moment associated with molecular bond [25]. While strongly polar bonds such as carbonyl groups cause strong IR absorption, weakly polar and symmetric bonds are causing weak or no IR radiation absorption [27]. The transmission (T) of IR radiation in infrared spectroscopy is described by Beer–Lambert law [28]:

$$T(\tilde{\nu}) = \frac{I(\tilde{\nu})}{I_0(\tilde{\nu})} = \exp(-a(\tilde{\nu})b), \quad (1)$$

where $I(\tilde{\nu})$ is the intensity of transmitted radiation, $I_0(\tilde{\nu})$ is the intensity of incident radiation, $a(\tilde{\nu})$ is a linear absorption coefficient, b is thickness of the sample and $\tilde{\nu}$ is the wavenumber. Optical density, which describes the absorption, is expressed as follows [29]:

$$A = \log_{10}\left(\frac{1}{T}\right) = -\log_{10}\left(\frac{I}{I_0}\right). \quad (2)$$

Here T is the transmission.

As in the experiments of this thesis mid-infrared (MIR) spectroscopic imaging was applied, the infrared (IR) spectral region will be referred to MIR spectral region throughout the following text of this thesis.

1.1.2 FTIR Microspectroscopy

The combination of IR spectrometer and a microscope enables IR microspectroscopy technique. Imaging, based on IR microspectroscopy allows to obtain sample’s morphochemistry: not only to obtain sample’s morphology, but, most importantly, to couple it with the sample’s chemical information. The chemically-rich information is linked to each spatial position of a sample, therefore a single data set consists both of spectral and spatial information [30].

Even though that the earlier IR microspectroscopy instruments were based on dispersive spectrometers, where the signal intensity was detected at each

wavenumber separately, modern IR microspectroscopy instruments are usually equipped with Fourier transform infrared spectrometers [31]. Opposite to relatively slow dispersive spectrometers, FTIR spectrometers allow simultaneous acquisition of complete frequency range of incident polychromatic IR radiation in one measurement. As the name of the technique suggests, mathematical processing of the measured spectral data is related with application of Fourier transform [32].

The main component of FTIR spectrometer is an optical element with interferometer, for example Michelson interferometer. Briefly, the main parts of Michelson interferometer are a fixed mirror, a movable mirror and a beam splitter. IR radiation, emitted from the source, is divided by a beam splitter. One part of the radiation is directed to the fixed mirror and, after reflection from it, is reflected again by beam splitter towards the detector. The other half of initial radiation is directed towards movable mirror, where the beam is reflected back to the beam splitter, which further reflects it to the detector. The movable mirror allows to create variable optical path difference between the two splitted beams. As these two beams recombine by constructively or destructively interfering depending on their optical path difference, the inteferogram, i.e. the signal intensity relative to the position of movable mirror, is measured. Interferogram is converted to the spectrum by applying Fourier transform [33].

Principal layout of an IR microscope operating in transmission mode is shown in Figure 1. The polychromatic IR radiation is collected from interferometer, delivered and focused to selected position of the sample. The transmitted radiation is collected and delivered to detector. The spectroscopic dataset for vibrational spectroscopic imaging is collected either by raster-scanning the IR radiation beam incident on the sample or by using wide-field illumination and focal plane array (FPA) or linear array detectors. The conventional IR sources include global, synchrotron and quantum-cascade lasers [6].

The main difference between infrared and standard visible light microscopes are the optical components. While in typical visible light microscopes glass optical components are used for directing and delivering the light, IR

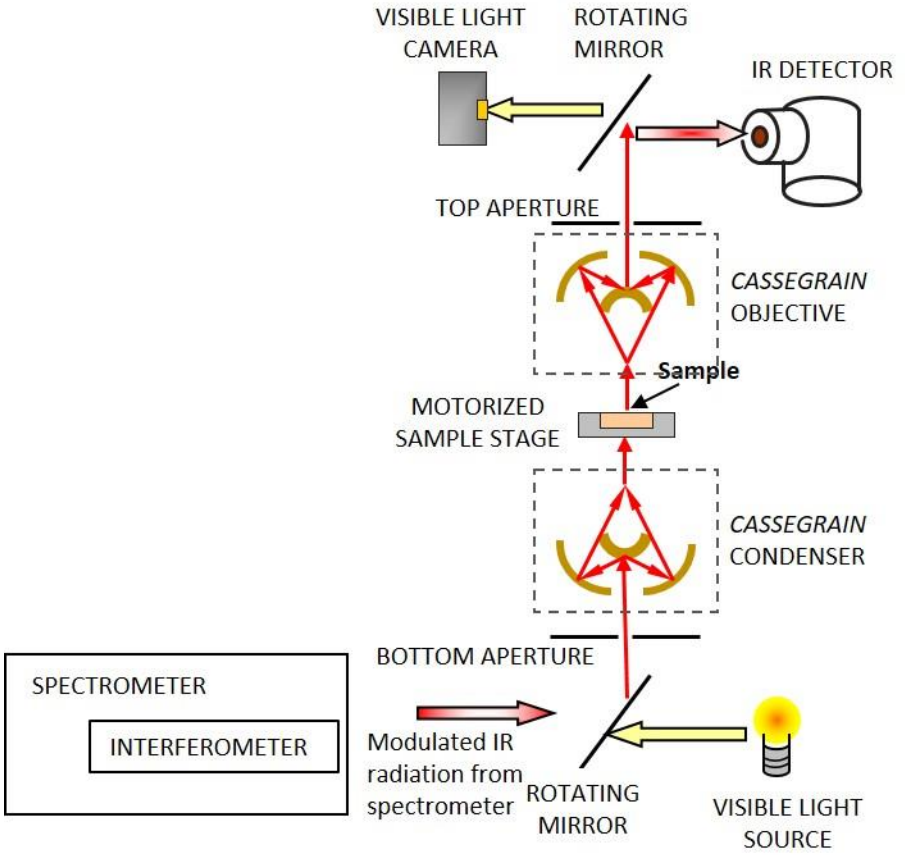

Figure 1. Principal optical diagram of an infrared microscope in transmission mode. The optical components, which are focusing modulated IR radiation from the spectrometer and visible light from visible light source to *Cassegrain* condenser, as well as those, which from *Cassegrain* objective deliver the transmitted IR radiation to IR detector and visible light to visible light camera, are not shown.

microscopes require more complicated *Cassegrain* optics. Glass is not suitable to be used in IR spectroscopy, as it absorbs electromagnetic radiation in mid-infrared spectral region, which wavelengths are above 5 μm. The reflecting mirrors, used in *Cassegrain* optics allows to deliver broader spectrum of frequencies without substantial absorption [34].

FTIR microspectroscopy is a relatively simple technique that is well suitable for tissue analysis: FTIR microspectroscopy is reproducible, non-destructive, do not require extensive means of sample preparation. Furthermore, relatively small

amounts (micrograms to nanograms) of the sample are usually enough to obtain decent chemical information. These superior features and advancements in modern infrared microspectroscopy instrumentation enabled it to emerge as one of the major tools for biomedical research [8].

1.1.3 Infrared microspectroscopy of central nervous system tissues

Infrared absorption of central nervous system tissues

Biological tissues, including CNS tissue, are of complex nature: various different proteins, nucleic acids, lipids and carbohydrates are incorporated in their structure with varying concentrations. Therefore, the spectral bands of infrared absorption spectrum of a biological tissue are due to vibrational modes from

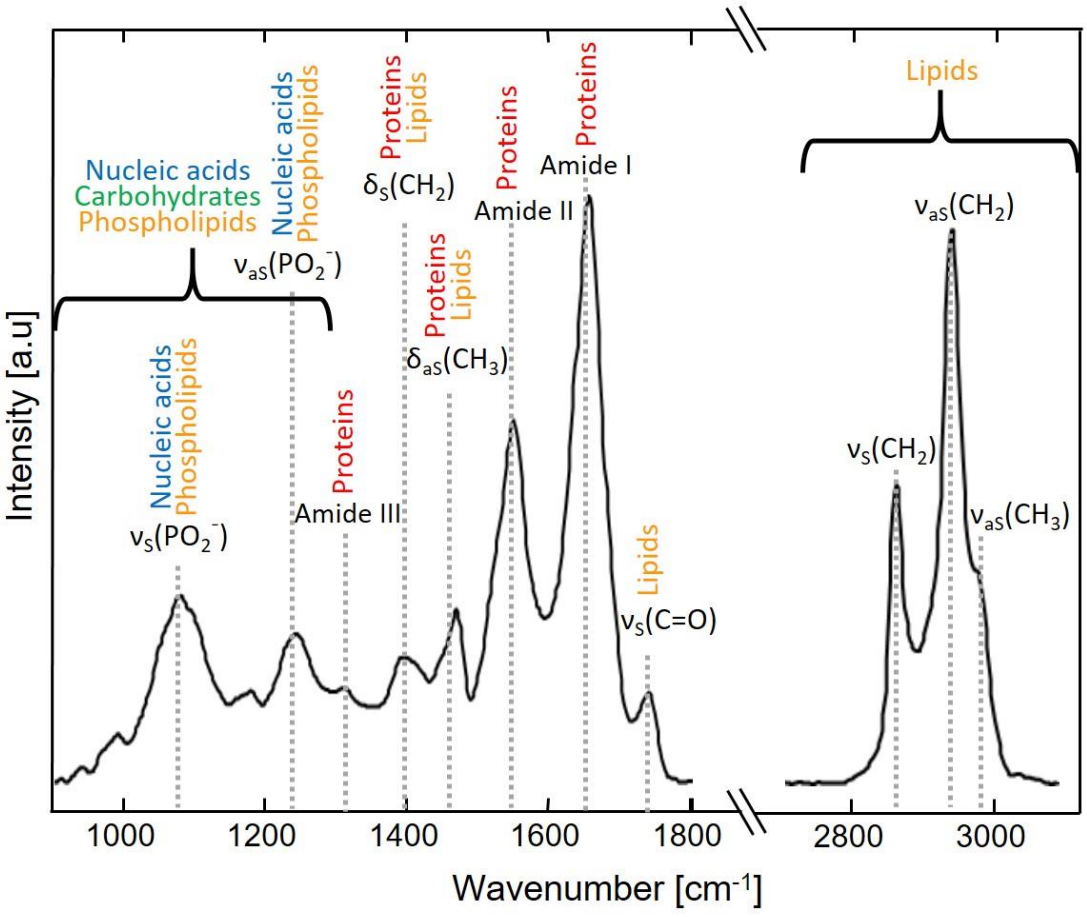

Figure 2. Infrared absorption spectrum of lipid-rich biological tissue with most prominent vibrational modes and them representative tissue components. Particular spectrum was acquired for the reference by author of this thesis from 16 µm thick cryosection of white matter of a mouse brain.

all the molecules and are strongly overlapping (Fig. 2). The correlation of distinct tissue biomolecules with separate absorption bands is thus complicated and the precise attribution of particular band to particular biomolecule cannot be straightforward. Practically, the absorption bands are rather attributed to those biomolecules, which have the most of the particular characteristic functional groups.

In mid-infrared spectral region, the frequency range of infrared absorption in around 900 – 3500 cm^{-1} carries most vibrational information about the CNS tissue components.

The spectral region between 900 cm^{-1} and 1500 cm^{-1} is so called fingerprint region [6]. The vibrational modes below 1300 cm^{-1} are mainly associated with carbohydrates, nucleic acids (DNA and RNA) and phospholipids. Carbohydrates-associated vibrational modes, such as C—O stretching coupled with C—O bending from glucose and glycogen lead to absorption at ~1025 cm^{-1}, ~1045 cm^{-1} and ~1150 cm^{-1} [35]. Symmetric and asymmetric stretching of PO_2^- in phosphodiester groups yield characteristic absorption at 1080 cm^{-1} and 1235 cm^{-1}, respectively [35]. CNS tissues are phospholipid-rich, therefore phospholipids are substantially contributing to PO_2^- stretching vibrations at 1235 cm^{-1} [36]. Relatively weak spectral contributions in 1200 – 1350 cm^{-1} spectral region are due to N—H in-plane bending and C—N stretching vibrations of proteins (amide III vibrations). The IR spectral bands at ~1400 cm^{-1} and at ~1460 cm^{-1} are attributed to, of C—H bond`s symmetric and asymmetric bending vibrations, respectively, in methyl (CH_3) and methylene (CH_2) functional groups in both proteins and lipids [37].

Another important spectral region between 1500 cm^{-1} and 1700 cm^{-1} include amide I and amide II bands, which are usually the most prominent in the infrared spectra of most biological tissues and are dominated by C=O and C— N

stretching vibrations of amide groups [6]. Amide II spectral bands are located at ~1548 cm^{-1} and arise due to C—N stretching with contributions from N—H bending in proteins [35]. Amide I band is due to C=O stretching with contributions from N—H bending in proteins [35]. The amide I band is particularly suitable to address changes in protein secondary structure. These changes are identified by the position of the band maximum and its shoulders: α-helical structures at ~1655 cm^{-1}, β-pleated sheet structures at 1623 – 1637 cm^{1}, anti-parallel pleated sheets and β-turns at 1675 – 1695 cm^{-1} [38].

The higher-wavenumber region (2800 – 3500 cm^{-1}) is associated with stretching vibrations of methyl, methylene and methine (=C—H) functional groups, commonly found in fatty acids. In CNS lipid-rich tissue samples, the spectral band at 1725 – 1745 cm^{-1} attributed to the ester carbonyl vibrations and minor bands of C=C stretch and (C=C)H stretch at 1650 cm^{-1} and 3010 cm^{-1}, respectively, indicate high content of unsaturated lipids [36,39].

FTIR vibrational spectral imaging applications in central nervous system research: assessing brain tumors and myelin

Many studies were assessing FTIR spectroscopy as a tool to diagnose and grade brain tumors. For example, in the study carried out by Krafft et al., IR spectroscopic chemical imaging was applied to compare spectral signatures of normal brain, astrocytic gliomas and human glioblastoma cell lines. A parameter based on characteristic vibrational bands for calculating lipid to protein ratio was introduced for statistical analysis of 71 samples. As this parameter correlated with the grade of gliomas, it was applied to classify brain tissue sections imaged by IR microspectroscopy [40]. In the study performed by Steiner et al., it was demonstrated that cancerous human brain tissue (astrocytoma, glioblastoma) can be distinguished from control tissue due to differences in respective IR spectra. Also, the IR spectra were shown to provide

sufficient biochemical information to assess the malignancy grade of the tissue. A combination of genetic optimal region selection routine linear discriminant analysis revealed that the nature and relative amounts of brain lipids appear to be altered in cancerous compared to control tissue [41]. Additionally, to this iterative two-step algorithm, series of classification models were built by using a k-fold cross validation scheme. To provide an aggregated prediction classification, predictions from the various models were combined and classification success was improved [42]. Amharref et al. investigated molecular changes associated with the development of brain glioma in C6 rat glioma model. Multivariate statistical analysis and imaging was applied and, as a result, all normal brain structures were discriminated from tumor. Moreover, the structure attributed to infiltrative events, such as peritumoral oedema observed during tumor development, could be identified all around the tumor [43]. Bambery et al. also showed in rat C6 glioma model that the tumor tissue has a characteristic chemical signature of IR spectra in comparison with tumor-free brain tissue. The physical-chemical differences between cancerous and tumor-free brain tissue were determined by image and spectral comparison and were characterized by changes in total protein absorbance, phosphodiester absorbance and physical dispersive artefacts [44]. Further, Krafft et al. extended the IR microspectroscopic studies of human glioma tumors extended to primary tumors of brain metastases. The SIMCA (soft independent modeling of class analogy) model was applied to distinguish normal brain tissue from brain metastases and to identify the brain tumors of metastases. All specimens were ranked to the correct tissue class [45]. Ali et al. undertook a study to determine, whether human meningiomas could be identified by using IR microspectroscopy. In this study, hierarchical cluster analysis (HCA) using Ward's algorithm was applied to analyze spectral datasets and allowed to discern tumor and its specific spectral pattern [46]. Multivariate statistical analysis in the study carried out by Beljebbar et al. enabled to

distinguish between normal, tumoral, peri-tumoral, and necrotic tissue structures in rat C6 glioma model from IR spectral imaging data. For that, a model consisting spectra acquired from normal and glioma brain constituents such as lipids, DNA, and protein was used as a linear combination for fitting measured spectra of brain tissues [47]. Based on comparative evaluation of FTIR imaging, histopathology, and MRI in malignant gliomas of six patients, a diagnostic classification system was described for the first time by Sobottka et al. The grading based on IR spectroscopic data agreed with histopathology and MRI findings for almost all specimens [48]. Tumor vasculature as a measure by IR imaging to differentiate between normal and tumor tissue in mice and human was also addressed by Wehbe et al. [49].

By applying infrared spectroscopic methods, the myelin degradation was mainly assessed in the studies of multiple sclerosis (MS). The early work of Choo et al., which was published in 1993, investigated chronic MS plaques dissected from autopsy material and reported the reduction of lipid-related IR absorption bands, which is in agreement with the loss of the lipids during the demyelination. MS plaques and control white matter could be readily distinguished based entirely on lipid representative absorption bands. However, these differences were not as evident when compared with grey matter [50]. LeVine et al. demonstrated that in addition to a prominent decrease of overall lipid content associated with the demyelination, an increase of carbonyl-to-CH_2 ratio was detected in lesions, indicating oxidation [29].

Recently, experimental autoimmune encephalomyelitis (EAE), which is an animal model for multiple sclerosis, is most often used to study MS. Heraud et al. reported that reduction of lipid ester carbonyl spectral band (1735 cm^{-1}) and an increase of nucleic acids representative spectral band (965 cm^{-1}) were found as prominent spectral markers representing lesions found in the brain cerebellum and spinal cords. PCA on FTIR spectra in 900 – 1800 cm^{-1} spectral

region allowed differentiation between different tissue layers of the brain cerebellum and the lesion [51]. From IR spectral data of several studies, it was suggested that the lesions in Nogo-A vaccinated mice contained myelin proteins with different protein secondary structure [51–53].

1.1.4 Raman spectroscopy

Raman spectroscopy belongs to linear vibrational spectroscopy. The physical background of Raman spectroscopy is inelastic scattering, i.e. Raman scattering, of electromagnetic radiation as it interacts with the media. In this phenomenon, the photons of incident light are absorbed and re-emitted during the characteristic times of $\tau \approx 10^{-14}$ s [54]. The difference between the frequencies of incident and scattered photons provide information about vibrational, rotational and other low-frequency vibrational processes related with excitation of the molecule. Raman spectroscopy is suitable for qualitative and quantitative analysis of solid, liquid and gaseous materials [55].

The essence of Raman scattering process can be at easiest explained by classical electromagnetic field description [56]. The dipole moment is induced as the incident monochromatic electromagnetic field interacts with the material and is characterized by following equation:

$$\mathbf{P} = \alpha \mathbf{E}. \tag{3}$$

Here, α is molecular polarizability, which is material-specific property depending on molecular structure and characteristics of chemical bonds. $\mathbf{E}$ is the strength of incident electric field and is time-dependent, as the following equation describes:

$$\mathrm{E} = E_0 \cdot \cos(\omega_0 t), \tag{4}$$

where ω_0 and E_0 is the frequency and amplitude of incident electric radiation, respectively. The time-dependent induced dipole moment acts as a source for generation of secondary radiation:

$$P = \alpha E_0 \cos(\omega_0 t). \quad (5)$$

The nuclear coordinates q, along which the molecule oscillates, are called normal modes. As the electron cloud perturbation with electric field depends on the relative molecule`s atoms nuclear coordinates, polarizability is a function of nuclear coordinates. For the small deviations from the equilibrium nuclear coordinates (q = 0), this dependence can be expanded into a Taylor´s series:

$$\alpha = \alpha(q) = \alpha_0 + \left(\frac{\partial \alpha}{\partial q}\right)_{q=0} \cdot q + \cdots . \quad (6)$$

Here, α_0 is the polarizability at the equilibrium nuclear position. Due to interaction with incident electromagnetic field, the nuclear coordinate q oscillate with a characteristic frequency of normal mode ω_m around q = 0 and is expressed in the following equation:

$$q = q_0 \cdot \cos(\omega_m t). \quad (7)$$

Inserting Eq. (6) and Eq. (7) into Eq. (5) gives the following expression for the induced dipole moment:

$$P(t) = \alpha E_0 \cos(\omega_0 t) = \alpha_0 \cdot E_0 \cdot \cos(\omega_0 t) + \frac{1}{2}\left(\frac{\partial \alpha}{\partial q}\right)_{q=0} \cdot q_0 \cdot E_0 \cdot$$

$$\cos[(\omega_0 - \omega_m)t] + \frac{1}{2}\left(\frac{\partial \alpha}{\partial q}\right)_{q=0} \cdot q_0 \cdot E_0 \cdot \cos[(\omega_0 + \omega_m)t], \quad (8)$$

Eq. (8) indicates that the induced dipole moment can oscillate at three different frequencies, namely ω_0, $\omega_0 - \omega_m$ and $\omega_0 + \omega_m$, and as a result generate at three distinct frequencies scattered light [57]:

1. The first term in Eq. (8) oscillates at ω_0, i.e. at the same frequency like the incident radiation. After the excitation, the molecule relaxes back to the initial vibrational level. This constitutes the elastic light scattering and is called Rayleigh scattering, which is present for any molecule.
2. The scattering radiation at $\omega_0 - \omega_m$ frequency is energetically red- shifted compared with the incident radiation. It constitutes inelastic light scattering and is called Stokes scattering. In this case, part of the incident photon energy is transferred to excite molecular vibrations at frequency ω_q.
3. The third term in Eq. (8) corresponds to oscillations with the characteristic frequency $\omega_0 + \omega_m$: the inelastically scattered radiation, which is called anti-Stokes scattering, is energetically blue-shifted with respect to incident radiation. In this case, the molecule, which already exists in excited vibrational state, relaxes to the ground vibrational energy level by releasing the excess energy to produce the photon at $\omega_0 + \omega_m$ frequency.

Different molecular polarizability between vibrational energy states is prerequisite for a Raman transition between these states to be allowed. In other words, molecular vibrations, for which $\left(\frac{\partial \alpha}{\partial q}\right)_{q=0} \neq 0$, i.e. the derivative of the polarizability with respect to the normal coordinate associated to the vibration is non-zero, are necessary for inelastic scattering of light [58].

Another way to explain Raman scattering is based on energy levels diagrams (Fig. 3). According to this model, a molecule can absorb a photon and subsequently undergo a transition to virtual energy state. The energy of virtual energy level is higher than of the vibrational energy level, however do not have to be equal to the energy of excited electronic energy level of the molecule. Therefore, as the virtual energy level can be present at any energy, Raman and

Rayleigh scattering can occur independently from the frequency of incident electromagnetic radiation. The lifetime of virtual energy level compared with the real energy levels is very shot, i.e. ~10^{-14} s [54]. When a part of the incident electromagnetic radiation energy is transferred to induce molecular vibrations, the relaxation from the virtual energy level will result in generation of a lower energy photon – the Stokes photon. As can be seen in Fig. 3, the energy difference between incident and scattered photons is equal to that required to induce particular molecular vibration. In the case of anti-Stokes scattering, the molecule is already in an excited vibrational state and absorb incident photon to experience transition to virtual energy level. Molecule disposes its vibrational energy by relaxation to ground vibrational level via radiation of a photon of higher energy than the incident photon – the anti-Stokes photon is generated. Under thermal equilibrium conditions, the population of molecules is higher in ground vibrational energy state than in excited vibrational state, therefore the spontaneous Raman Stokes scattering is more intense than anti-Stokes. It should be noted that the cross-sections of inelastic scattering are small compared to those of elastic scattering. Therefore, the intensity of Rayleigh scattering is several hundred times stronger than the intensity of spontaneous Raman scattering [55].

The output of Raman spectroscopy are the Raman spectra, which represent the scattered radiation intensity versus characteristic vibrational frequencies of the molecule [59]. In Raman spectra, these frequencies are related to so called Raman shift as follows:

$$\Delta\nu = \frac{1}{\lambda_0} - \frac{1}{\lambda_1}, \tag{9}$$

where λ_0 and λ_1 are the wavelengths of incident and scattered radiations, respectively.

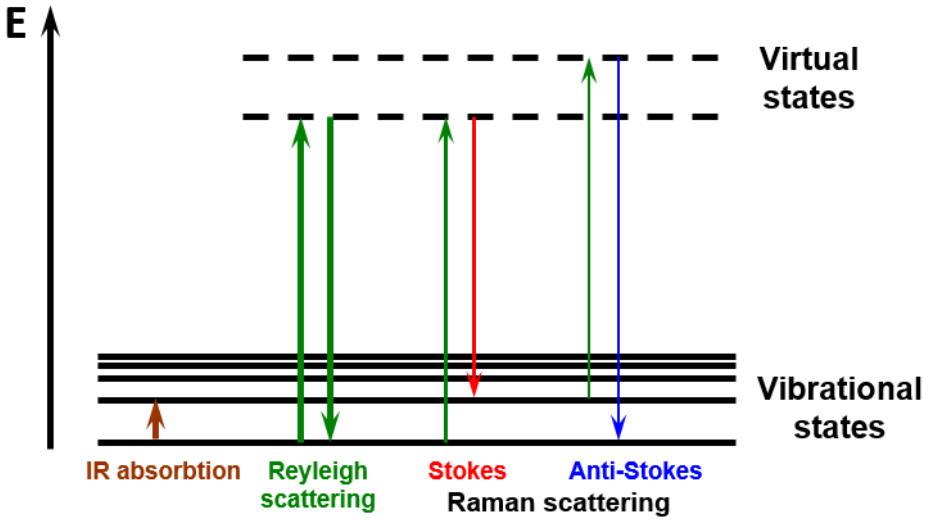

Figure 3. Energy diagrams, showing the energy transitions occurring in infrared absorption, Reyleigh and Raman scattering events. The thicknesses of the arrows representing transitions involved in scattering processes illustrate (but are not proportional to) the probabilities of different spontaneous scattering phenomena to occur.

1.1.5 Raman microspectroscopy

Raman chemical imaging (mapping) provides chemical information coupled with spatial information of the sample. In typical Raman microspectroscopy experiment, the sample is excited with one laser wavelength. All Raman-active molecular vibrations of the specimen are excited simultaneously. Typically, the laser radiation is used to excite the sample, as: (i) monochromatic laser radiation allows to register relatively small Raman shifts; (ii) intense and collimated laser beam in most cases favors appropriate lateral resolution and signal-to-noise ratio [55].

The incorporation of Raman spectroscopy tool to a microscopy system amongst other present two main advantages. Firstly, a better lateral resolution can be achieved (to the Abbe‘s diffraction limit). Furthermore, the tight focusing of the radiation by microscope objective provides the higher density of excitation

photons and, therefore, more intense scattering at the sample´s unit surface area [60].

In typical Raman microspectroscopy imaging experiment, the spectra are collected by point-wise scanning the sample surface and the full spectroscopic information is acquired in every pixel. As a result, molecular information-rich spectral dataset is acquired. The sample scanning by laser beam is achieved by using the mirrors or/and piezoelectrically driven sample stages. A microscope objective focuses a laser beam on the sample. The common approach to collect the Raman scattering signal is to employ the same objective. The lateral resolution, laser beam diameter and signal detection sensitivity are dependent on microscope objective numerical aperture (NA) [60]. As elastic scattering is dominating over the inelastic Raman scattering (elastic scattering is 10^3 – 10^6 times stronger [57]), it is important to use special filters (Rayleigh filters) to cut off the signal of elastic scattering [55].

Raman microspectroscopy has proved to be a powerful method for investigating and assessing chemical content of various materials. This wide range of applications include, among others, studies of pharmaceuticals [61], plant and algae [62,63], in fields of nanotechnology [64–66], food quality and safety [67,68] and, of course, a broad variety of applications in biology and biomedicine [69–72]. In particular, the latter applications range from single cell [73,74] and tissue [75,76] imaging to medical diagnostics [77,78].

1.1.6 Raman microspectroscopy of central nervous system tissues

Raman scattering of central nervous system tissues

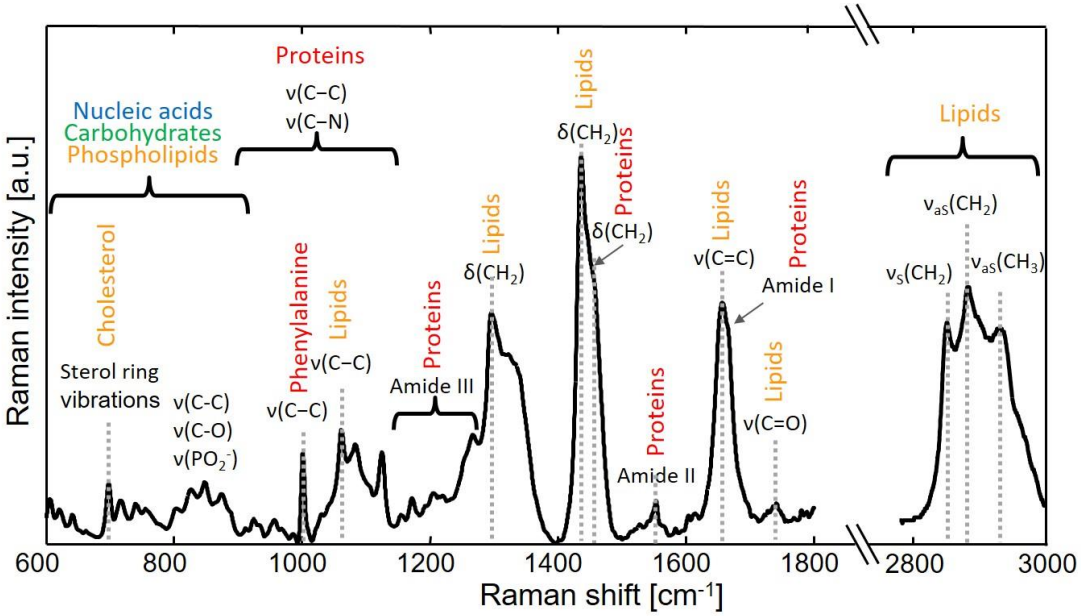

Figure 4. Typical Raman spectrum of lipid-rich CNS tissue with most prominent vibrational modes and them representative tissue components. Particular spectrum was acquired for the reference by author of this thesis from 16 µm thick cryosection of white matter of a mouse brain.

Once again, as in the case of IR absorption spectra of CNS tissue samples, Raman spectrum provides a fingerprint of the sample's biochemical composition. Raman spectra of CNS tissue are characterized by a number of spectral bands. The bands in the spectra are the result of the complex overlap of different vibrational modes (Fig. 4). They indicate the presence and quantity of a certain molecular group and can be assigned to the main tissue components.

Relevant Raman spectral bands of CNS tissue samples are in the Raman-shift range between 600 and 3500 cm^{-1}. The cholesterol specific spectral bands are at 608 cm^{-1} and 702 cm^{-1} and are due to sterol ring vibrations. A characteristic spectral band at 719 cm^{-1} is attributed to symmetric stretching vibration of choline group $N^{+}(CH_3)_3$ in phospholipids such as phosphatidylcholine and sphingomyelin [79]. Lipids and their chemical structure can be further

evaluated by analyzing the Raman bands at 1300 cm^{-1} (CH_2 twisting), 1440 cm^{-1} (CH_2 bending), 1656 cm^{-1} (C=C) and 1754 cm^{-1} (C=O) [80].

Spectral range 770 – 830 cm^{-1} is dominated by the O—P—O stretching vibrations arising from backbone of nucleic acid [81]. This spectral region is especially favorable for assessment of nucleic acid content in the CNS tissue. In the spectral region of 900 – 1150 cm^{-1}, the C—C and C—N bond vibrations characteristic to proteins are responsible for intense Raman bands. Especially evident is the characteristic spectral band of phenylalanine at 1004 cm^{-1}. Vibrations associated with lipids, namely C—C band vibrations, are giving characteristic band at 1070 – 1080 cm^{-1} [80].

In the spectral region 1100 – 1375 cm^{-1}, the amide III Raman band due to C—N stretching and N—H bending vibrations is observed. The amide II band is observed in the region between 1480 and 1580 cm^{-1} and is due to a coupling of C—N stretching and N—H in-plane bending vibrations [80]. However, the amide II band in Raman spectra is often overwhelmed by the contributions of C—H bending vibrations in lipids. CH_2 bending vibrations in proteins are also giving intense spectral band at 1450 cm^{-1}. Finally, the amide I band of proteins is observed at 1656 cm^{-1} due to C=C stretching vibrations.

The spectral region 2800 – 3500 cm^{-1} is dominated by spectral contributions from symmetric and asymmetric C—H stretching vibrations of methyl (CH_3) and methylene (CH_2) functional groups [80]. Important to highlight that in lipid-rich CNS tissue samples, the Raman spectral band at 2850 cm^{-1} is mainly due to vibrations of CH_2 functional groups of fatty acids [82].

Raman vibrational spectral imaging applications in central nervous system research: assessing brain tumors and injury of the spine

The early attempts to apply Raman spectroscopy for assessment of brain tissue were limited to Raman spectra analysis based on differences of concentration

of individual molecules. By attempting to analyze the water content, Tashibu was for the first time applying Raman spectroscopy for brain tissue in 1990. He was able to detect relative differences in water concentration due to changes of intensity of O—H stretching vibrational mode at 3390 cm^{-1} [83]. In 1994, Mizuno et al. was for the first time reporting Raman spectroscopy application for the brain tumor research. Gliomas of grades II and III, neurinoma and neurocytoma of choroid plexus were compared with normal brain tissue by using near-infrared Fourier transform Raman spectroscopy. However, it was concluded that Raman spectra of brain tumors were essentially the same as to that of grey matter [84].

With the prominent improvements of Raman microspectroscopy, the later studies were already able to extract key biochemical information from Raman imaging spectral data and, therefore, were focusing on gaining more detailed insights in tumor structure and distribution for diagnostic as well as intraoperative applications. For example in the study carried out by Koljenović et al., Raman microspectroscopic imaging was utilized on unfixed cryosections of glioblastoma, obtained from 20 patients to differentiate viable from necrotic tumor. For that, cluster and linear discriminant analysis were performed [85]. Kalkanis et al. used Raman spectroscopy to analyze gray matter, viable GBM and necrosis in frozen brain tissue sections. Grey matter contained higher lipid content as specified by spectral bands at 1061 and 1081 cm^{-1}, whereas necrosis could be characterized by increased protein and nucleic acid content, as obtained from analyzing the Raman bands at 1003, 1206, 1239, 1255–1266 and 1552 cm^{-1}. GBM was in between of these two extremes. Discriminant function analysis allowed to differentiate these brain tissue types with 97.8% accuracy in samples without freeze artifacts and with 77.5% accuracy of samples with freeze artifacts [86]. Kast et al. reported similar study, where, in addition to the identification of regions of normal brain, necrosis and solid GBM, also diffusely infiltrating GBM was also taken into account. Spectral maps produced by

calculating intensities/intensity ratios of characteristic spectral bands at 1003, 1313, 1431, 1585, and 1659 cm^{-1} enabled to visualize normal, necrotic, and GBM histologies, grey matter and white matter boundaries, areas of infiltrating glioma and hemorrhage [87]. Raman microspectroscopic imaging experiments by Amharref et al. of C6 tumor model in rats showed spectroscopic data based discrimination between healthy and tumoral brain tissue and yielded spectroscopic markers associated with the proliferative and invasive properties of glioblastoma *ex vivo* [88]. In 2005, Krafft et al. for the first time reported application of Raman spectroscopic imaging to study native specimens from normal brain tissue and frequent intracranial tumors, such as astrocytoma, glioblastoma multiforme and meningioma, and demonstrated measurable spectroscopic and morphological differences between different tissue types [89]. In other work of the same author, Raman chemical images were collected from six regions of two GBM tissue sections. Vertex component analysis (VCA), which is a factor method and for which no data preprocessing was required, was applied for data processing. Among other molecular differences, increased nucleic acid bends in the spectra of high-grade glioma, were reported. The results of Raman imaging were correlating with morphological features from hematoxylin and eosin (H&E) staining [90].

The aforementioned studies were all using Raman spectroscopy to investigate *ex vivo* human or animal model brain tumors. Nevertheless, due to growing need of *in vivo* clinical applications, the development of fiberoptic Raman spectroscopy probes for intraoperative use earned substantial attention. The first Raman fiberoptic probes were used to acquire Raman spectra in gastrointestinal, bladder, and cervical cancer surgery [91–93]. Already in 2010, Beljebbar et al. reported the use of a portable Raman spectrometer coupled to a microprobe to acquire Raman spectra from C6 rat GBM model *ex vivo* and *in vivo* with a signal integration time of 5 s. The quality of obtained Raman spectra was high, so that the normal tissue from tumor could be differentiated with

100% accuracy. Also early and mature tumor tissues could be delineated [94]. In the same year, Kirsch et al. for the first time reported the application of *in vivo* Raman spectral imaging of the brain surface in a mouse model. Raman system coupled to a fiber-optic probe was used for detection of cerebral brain metastases. The generated Raman images allowed to localize cortical and subcortical tumor cell aggregates with accuracy of roughly 250 µm [95]. Recently, a handheld Raman probe was developed and used in a clinical trial by Jermyn, Desroches and collegues. Using this probe intraoperatively in adult neurosurgical patients (n = 17), researchers were able to differentiate normal brain from solid tumor and normal brain invaded by tumor cells with a sensitivity of 93% and a specificity of 91%. Also, the previously undetectable diffusely invasive brain cancer cells were detected at cellular resolution by particular Raman probe in patients with grade II to IV gliomas [96]. Also, by analyzing Raman spectra *in vivo* measured in 10 patients, necrosis was distinguished from vital tissue (including tumor and normal brain tissue) with an accuracy of 87%, a sensitivity of 84% and a specificity of 89% in the study performed by the same researchers [97]. Whereas aforementioned results were based on the fingerprint Raman spectroscopy, the most recent publication of this research group demonstrates intraoperative use of integrated Raman probe engineered into a commercial biopsy system and based on high wavenumber Raman spectroscopy. The applicability of this system applied in biopsy collection was for the first time presented in a small-scale animal study. It was demonstrated that the novel optical needle can measure Raman spectra from deep brain and collect tissue samples at the same location. By using the Raman probe *in vivo* human validation study was performed in 19 adult patients undergoing open cranium surgery for grade II–IV gliomas with minimal disruption to the surgical workflow. It was demonstrated that a high wavenumber Raman spectroscopy probe can detect

dense human tumor with >60% cancer cells in situ during the surgery with 80% sensitivity and 90% specificity [98].

There are only few studies reporting the use of Raman spectroscopy to investigate spinal cord. Couple of them report the use of Raman spectroscopy for the purpose of minimally invasive spine surgery (MISS). In the study performed by Chen et al., a fiberoptic Raman sensing system was used *ex vivo* on swine backbone samples in order to identify spinal cord and spinal nerves from surrounding tissues. Principal component analysis (PCA) classification model using linear discriminant analysis (LDA) on 750 raw Raman spectra obtained in spine bone, fat, muscle and spinal cord gave an overall accuracy of 93.1% in discriminating between different spine structures [99]. In other study carried out by Anderson et al., the ability of real-time spectral guidance using a fiber optic probe-in-needle device to distinguish each of the spine tissues in the path of neuraxial needles was tested. The comparison of the extent of biochemical information provided by Raman, diffuse reflectance, and fluorescence spectroscopies revealed that in contrast to diffuse reflectance and fluorescence, Raman spectroscopy enabled to distinguish all tissue types. The tissue-unique spectral signatures were also observed in Raman spectra collected in real-time during needle insertion through intact paravertebral and neuraxial porcine tissue [100].

To the knowledge of the author of this thesis, up to now there were only two publications related with application of Raman spectroscopy to address the biochemical changes induced by spinal cord injury, both in rat model. In the study performed by Saxena et al., Raman spectral data acquired in spinal cords with induced lateral hemisection and a moderate contusion were investigated and compared with healthy tissue of spinal cord: the injured spinal cords were clearly distinguished from healthy spinal cords in both models of SCI due to significant differences in corresponding spectral data. Also, it was shown that

these differences and their time course post-injury correlated with demyelination and chondroitin sulfate proteoglycans as well as glycosaminogylcan upregulation [101]. In the work of Galli et al., the ability of IR, Raman and multimodal CARS microscopy to detect biomolecular changes between normal and altered regions in a rat model of spinal cord hemisection was assessed. The spectra acquired by the use of IR and Raman microspectroscopy methods enabled to distinguish the lesion, the surrounding scar, and unharmed normal tissue and allowed to probe the extent of nervous tissue degeneration. CARS, SGH and TPEF imaging yielded information about the lipid content distribution, scar formation and inflammation, respectively [23].

1.2 Non-linear vibrational imaging

1.2.1 Coherent anti-Stokes Raman scattering

CARS microscopy is a technique based on the, as the name suggests, coherent anti-Stokes Raman scattering phenomenon. In particular, CARS is a four-wave mixing process and is a coherent and a non-linear variant of Raman scattering process [54]. In experimental implementation, the radiation of two frequencies is usually used for sample excitation: the so called pump field at frequency ω_p and a Stokes field at frequency ω_s.

A diagram, illustrating the energy transitions in CARS process, is shown in Fig. 5 (A). In a ground energy level existing molecule absorbs the pump photon of frequency ω_p and is excited to a virtual energy level. A molecular system localized in the excitation volume of ω_p field is thus experiencing population inversion in this virtual level. The Stokes field tuned at ω_s is then inducing the transition of the molecules from virtual level to rotational-vibrational level. Therefore, all molecules of the system are coherently oscillating in this real energy level at frequency $\omega_m = \omega_p - \omega_s$. These molecules being resonant

oscillators are probed by so called probe photons ω_p' to undergo the transition to a higher virtual level. When ω_p' = ω_p, the CARS process is called degenerate CARS. From the virtual level the molecule is relaxing back to the ground energy level by emission of anti-Stokes photon of frequency ω_{aS}, so that in the degenerate case [102]:

$$\omega_{aS} = 2\omega_p - \omega_S \tag{10}$$

In molecular system this corresponds to radiation of coherent anti-Stokes field at frequency ω_{aS} – coherent anti-Stokes Raman scattering signal.

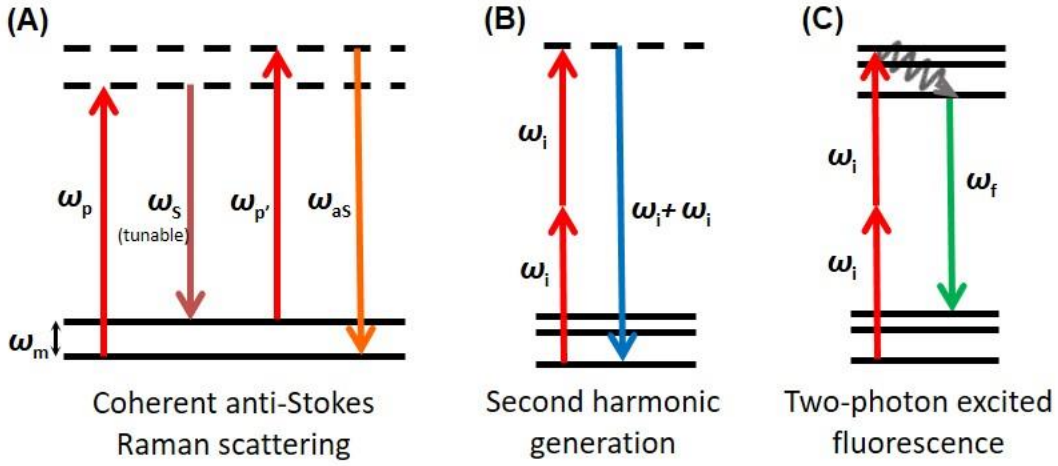

Figure 5. Energy diagrams of selected non-linear optical processes: (A): coherent anti-Stokes Raman scattering; (B): Second harmonic generation; (C): Two-photon excited fluorescence.

The pump and Stokes electric fields with amplitudes $\mathbf{E_p}$ and $\mathbf{E_S}$ and corresponding wave vectors $\mathbf{k_p}$ and $\mathbf{k_S}$, respectively, are inducing the third order non-linear polarization, which is the source for the CARS signal. Classically, the third order non-linear polarization $\mathbf{P}^{(3)}$ induced in CARS process can be expressed based on a driven, damped harmonic oscillator model to give a following equation [57]:

$$\mathbf{P}^{(3)} = \varepsilon_0 \chi^{(3)} \mathbf{E}_p^2 \cdot \mathbf{E}_S e^{i[(2\omega_p - \omega_S)t - (2\mathbf{k}_p - \mathbf{k}_S)z]} = \varepsilon_0 \chi^{(3)} \mathbf{E}_p^2 \cdot \mathbf{E}_S^*, \tag{11}$$

Where ε_0 is the electric permittivity of vacuum, $\chi^{(3)}$ is the third-order non-linear susceptibility of the material and is expressed:

$$\chi^{(3)} = \frac{N}{2m}\left[\left(\frac{\partial\alpha}{\partial q}\right)_{q=0}\right]^2 \frac{1}{\omega_{\mathrm{m}}^2-(\omega_{\mathrm{p}}-\omega_{\mathrm{S}})^2+i\gamma(\omega_{\mathrm{p}}-\omega_{\mathrm{S}})} \quad (12)$$

The N in Eq. (12) corresponds to the number of oscillators per volume element, γ is the damping constant, which reflects the natural bandwidth of Raman active transition and m indicates the reduced mass of the nuclear oscillator. The coherent excitation is only possible for Raman active vibrational modes, as $\chi^{(3)} = 0$, when $(\partial\alpha/\partial q)_{q=0} = 0$. As the Eq. (11) indicates, the induced third order non-linear polarization $\mathbf{P}^{(3)}$ oscillating at the CARS frequency $\omega_{\mathrm{aS}} = 2\omega_{\mathrm{p}} - \omega_{\mathrm{s}}$ is the driving polarization for the CARS signal. Moreover, the CARS radiation is propagating in the phase-matched direction $\mathbf{k}_{\mathrm{aS}}=2\mathbf{k}_{\mathrm{p}} - \mathbf{k}_{\mathrm{S}}$ [57]. The Eq. (12) also shows that the amplitude of coherent oscillations is the strongest, when the difference between ω_{m} and $\omega_{\mathrm{p}} - \omega_{\mathrm{s}}$ is smallest.

By evaluating the interaction between plane pump and Stokes waves and calculating the wave equation, the intensity of CARS signal can be expressed as follows [57]:

$$I_{aS} \propto \left|\chi^{(3)}\right|^2 I_{\mathrm{p}}^2 I_{\mathrm{S}} \mathrm{sinc}^2\left(\frac{\Delta\mathbf{k}l}{2}\right) \quad (13)$$

Where l is the interaction length between the exciting radiation and sample, I_{p} and I_{S} are the intensities of pump and Stokes beams, respectively, and $\Delta\mathbf{k}=\mathbf{k}_{\mathrm{aS}}-(2\mathbf{k}_{\mathrm{p}}-\mathbf{k}_{\mathrm{S}})$ is the phase mismatch [103]. The *sinc* function and CARS

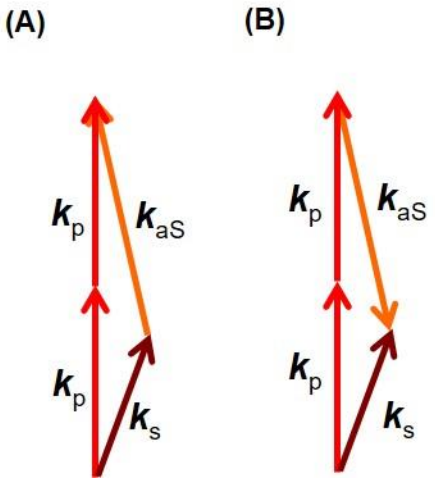

Figure 6. Phase matching conditions for CARS signal generation in the case of: (A) forward-generated CARS (or F-CARS) and (B) backward-generated (or E-CARS) CARS.

signal intensity are maximal, when $\Delta\mathrm{k}l$ = 0, i.e. when phase match condition is fulfilled. Phase-matching is schematically shown in Fig. 6 for forward (A) and backward (epi) (B) generated CARS. While $\chi^{(3)}$ depends linearly on the number of vibrational oscillators, the intensity of CARS signal is proportional to square number of oscillators, as in Eq. (13) the CARS signal intensity $I_{\mathrm{aS}}\sim\left|\chi^{(3)}\right|^2$. Moreover, as $I_{\mathrm{aS}}\sim I_{\mathrm{p}}{}^2 I_{\mathrm{s}}$, CARS signal is very intensively generated only in the small sample volume at the focus of laser radiation.

CARS signal is combined of resonant and non-resonant contributions [10]. The non-resonant signal is generated, as the pump and Stokes fields induce polarization at anti-Stokes frequency as a result of electronic response of the material. The non-resonant contribution is present regardless of whether the frequencies of pump and Stokes fields are tuned to address Raman active vibrational mode or not. Therefore, the non-resonant signal does not provide resonant molecular vibrations attributable information and create non-resonant background, which is to be avoided for high contrast CARS

images. On the other hand, when the Raman active vibrational frequency is addressed, the anti-Stokes signal is enhanced. Thus, the third-order non-linear susceptibility $\chi^{(3)}$ in CARS process is a combination of resonant term $\chi_{\mathrm{R}}^{(3)}$ and non-resonant term $\chi_{\mathrm{NR}}^{(3)}$ [104]:

$$\chi^{(3)} = \chi_{\mathrm{NR}}^{(3)} + \frac{\chi_{\mathrm{R}}^{(3)}}{\Delta - i\Gamma}, \tag{14}$$

where $\Delta = \omega_{\mathrm{p}} - \omega_{\mathrm{s}} - \omega_{\mathrm{m}}$ is the detuning and ω_{m} is the central frequency of homogeneously broadened Raman band with bandwidth Γ.

The intensity of anti-Stokes signal is thus expressed as follows [104]:

$$I_{\mathrm{aS}}(\Delta) \propto \left|\chi_{\mathrm{NR}}^{(3)}\right|^2 + \left|\chi_{\mathrm{R}}^{(3)}(\Delta)\right|^2 + 2\chi_{\mathrm{NR}}^{(3)}\mathrm{Re}\chi_{\mathrm{R}}^{(3)}(\Delta), \tag{15}$$

where $Re\ \chi_R^{(3)}$ is the real part of the resonant contribution of $\chi^{(3)}$. The first term of Eq. (15) does not depend on the Raman shift and characterize the non-resonant background contribution on the overall signal intensity. In fact, this non-resonant part of the susceptibility may result to dispersive and complex CARS band shapes through interference with the resonant field and contributes to constant background signal to the measured CARS signal [60]. While the second term of Eq. (15) gives the contributions only due to resonant signal and is dominant in the case of high concentrations of resonant oscillators, the combination between the resonant and non-resonant contributions make up the third term with the real part of the vibrational response. The shape of the third term is dispersive and the addition of all three terms causes the CARS spectral band to red-shift, while a negative pitch, which, when addressed, gives a negative contrast, appears at the blue end of the CARS spectral band. The asymmetric shapes of CARS spectral bands make the direct quantitative interpretation of CARS spectrum complicated, as the adjacent spectral bands may influence the one another's intensity [104].

1.2.2 Single-band coherent anti-Stokes Raman scattering microscopy

Single-band coherent anti-Stokes Raman scattering microscopy, in the following text referred to CARS microscopy, is based on collecting CARS signal intensities of a single Raman band by utilizing laser scanning microscopy. The most prominent advantages of CARS microscopy arise from the capability to record morphochemical images of an unstained sample, as the image contrast is due to vibrational fingerprint of the sample itself. The main advantages of CARS imaging are the following:

1. The intensity of CARS signal is several orders of magnitude (~10^6) stronger than that of spontaneous Raman scattering [102]. Because of that, even at moderate excitation powers the vibrational imaging at video-rate is possible.
2. The intensity of CARS signal is non-linearly dependent on the excitation intensity, therefore the coherent scattering is excited in small focus volume of the specimen only (<1 μm^3). As a result of intrinsic confocality, the submicrometer imaging resolution can be achieved [102]. Moreover, the non-linear nature of CARS process allows 3D sectioning, as the focal plane of the excitation can be adjusted.
3. The wavelength of anti-Stokes signal is smaller than the wavelengths of pump and Stokes radiations. The wavelength of CARS signal is thus spectrally well separated from one-photon fluorescence signal and can be easily detected in the presence of otherwise overwhelming one-photon fluorescence.
4. The energy of NIR excitation radiation is sufficient to generate CARS signal due to non-linear CARS nature. This results in: (i) decrease of sample heating, as there is no prominent radiation absorption by water; (ii) decrease of two-photon non-resonant signal generation possibility;

(iii) allows imaging from relatively deep tissue sections (up to 0.4 mm imaging depths) [104].

5. The sample photodamage and photobleaching are minimized as CARS process is devoid from molecular system transitions between electronic energy levels [10]. Furthermore, photodamage and photobleaching are minimaly affecting specimen regions, which are not located in excitation focal volume [103].

In common CARS microscopy experiments, the sample is scanned by the beams of two lasers, which frequencies are tuned to address the specific Raman active vibrational mode. The generated CARS signal is pixel-wise registered from the excited volumes of the sample. As already explained, the intensity of CARS signal is proportional to the square number of the vibrational oscillators in the volume of excitation. The CARS image is created as the CARS signal intensities are registered and attributed to the corresponding positions of the sample.

In general, the chemical contrast of the CARS image is dependent from:

1) Raman scattering cross-section of the vibrational mode, which is addressed for the chemical imaging;
2) How well this spectral band is spectrally separated from adjacent spectral contributions;
3) The concentration of molecular oscillators featuring this mode and the changes of this concentration over the sample [57];

The important requirement for the design of CARS microscopy experiments, is that the phase matching condition, i.e. $\mathbf{k}_{aS} = 2 \cdot \mathbf{k}_{p} - \mathbf{k}_{S}$, must be fulfilled [10]. The wave vector mismatch is induced by the spectral dispersion of the refractive index of the sample. The application of non-collinear phase matching geometries in microscopy of dispersive media is limited by their complexity. However, Zumbusch and colleagues were first to show the possibility of CARS

microscopy with collinear optical geometry under the tight focusing conditions [105]. In such experimental set-up, the use of microscope objective with a large numerical aperture (NA ≈ 1) is used for k-vectors of pump, Stokes and signal beams to co-propagate. As the excitation volume is small and the wave vectors are propagating in a cone geometry with a large angle, the wave vector mismatch is compensated, i.e. the $\mathbf{k}_{\mathrm{s}}$ fulfills the phase matching for every vector $\mathbf{k}_{\mathrm{p}}$ present in the focus so that $\Delta\mathbf{k}l << \pi$ [10].

The CARS signal can be generated in both forward (F-CARS) and backward (epi-CARS) directions. As the interaction length l with laser radiations is short and the phase mismatch is small for thin slabs of oscillators [see Eq. (13)], the CARS signal is generated rather equally in F- and epi-directions. As the sample thickness increases, the constructive interference of the induced dipole radiation is present in the forward direction, where $\Delta\mathbf{k}$ is small, while destructive interference occurs in the backward direction, where $\Delta\mathbf{k}$ becomes large. Therefore, the epi-CARS signal is generated only in the cases of very small objects, where the l is small enough for the *sinc* function in Eq. (13) to reach the maximum. The one may expect that the CARS radiation for bulk objects would be generated in the forward direction only. However, this is not the case, as epi-CARS radiation can be resulted by following mechanisms: (i) the objects with small dimensions (of the order $\lambda_{\mathrm{p}}/_{3}$) generate epi-CARS as the destructive interference is incomplete in backward direction; (ii) the discontinuities or edges are behaving as small objects to break destructive interference and thus the epi-CARS arise; (iii) the sample contains numerous local index of refraction changes, therefore initially forward propagating photons are multiple times linearly scattered and redirected to the backward direction[104]. The latter mechanism was found to mainly contribute to epi-CARS signal from tissues [103].

The appropriate choice of laser parameters for CARS microscopy plays an important role. The non-resonant CARS signal is way more likely to be generated, when the wavelength of the pump laser is near the peak of a two-photon resonance. The excitation wavelengths in NIR spectral region minimize these two-photon interactions. Furthermore, the use of NIR laser sources reduce multiphoton absorption induced photodamage. Another advantage of using NIR excitation is the reduced scattering of the laser beams inside the specimen. While the scattering of the excitation radiation in the specimen results in loss of laser intensity and increase the focal spot size, the reduced scattering of pump and Stokes beams allows to increase the sample penetration depth and collect CARS images from deeper layers of even turbid media [103].

CARS is a non-linear process, therefore, the efficient signal generation requires high field strengths, which can be achieved by the use of pulsed lasers. The typical bandwidth of Raman spectral bands are 5 – 10 cm^{-1} [57]. However, for example, the spectral bandwidth of ~100 fs laser pulse in NIR spectral region is ~ 150 cm^{-1}. If the femtosecond laser pulses are used for the excitation, the spectral width of laser pulse is likely to significantly exceed the Raman band and therefore cause strong contributions of non-resonant background signal [10]. The optimal compromise between spectral bandwidth and pulse peak power in CARS microscopy is to use the picosecond pulses of which the spectral bandwidth is similar to that of typical Raman spectral bands [106].

1.2.3 CARS imaging applications in central nervous system research: assessing myelin and brain tissue

Since the revival of CARS microscopy by Zumbuch and collegues [105], this technique experienced prominent advances over past two decades and proved as a powerful tool for various biochemical and biomedical investigations. For example, CARS microscopy was successfully applied to investigate such

biological samples as skin [103], cells [107], kidney tissue [108], lung tissue [109], atherosclerotic plaques [110,111]. Furthermore, CARS imaging of kidney stones, which are mineral-like structures, was also shown by Pucetaite et al. [112].

Nevertheless, perhaps the most common application of CARS microscopy is to visualize distribution of lipids in biological tissue by addressing CH_2 stretching vibrational mode at 2845 – 2850 cm^{-1} [113]. As the lipid content is highly varying in CNS tissue, either between different nervous tissue structures or as a result of nervous tissue diseases, CARS microscopy is capable to provide morphochemically specific information to study CNS tissue. Therefore, in the case of CNS disease or/and damage, it holds potential to give valuable diagnostic insights or to help to evaluate the performance of therapeutic approaches.

Being lipid-rich brain component, usually myelin is the main focus in CARS imaging of nervous tissue. Several research groups were performing studies based on nervous tissue CARS imaging. Wang et al. was imaging spinal cord white matter strips isolated from guinea pigs to image myelin under physiological conditions by both forward- and epi-CARS. The ordering degree and the spectral profile of myelin lipids as well as myelin thickness and axon diameter were measured. Detailed structures of the node of Ranvier and Schmidt-Lanterman incisures could be also resolved in CARS images [114]. In 2007, Huff and Cheng for the first time reported *in vivo* CARS imaging of mouse sciatic nerve tissue. Epi-detected CARS of myelinated axons and SHG imaging of the surrounding collagen fibres were demonstrated [115]. More accurate CARS measurements of myelin were performed on fixed and live rat spinal cord tissue by Belanger et al. It was shown, how circularly polarized laser beams can be used to avoid the CARS signal intensity dependence on excitation polarization and, therefore, the contrast dependence on the orientation of the

myelin membrane [116]. Further, Bioud et al. showed that based on the measurements of the second and fourth orders of symmetries of the macroscopic-scale angular distribution of bond dipoles, which are accessible by polarization-resolved four-wave mixing and CARS microscopy, determination of the high order of symmetry permits high level of detail in the angular disorder behavior at the molecular scale on myelin in tissues [117].

CARS imaging to study demyelination was for the first time published in 2007 by Fu et al. It was shown that the reduction of CARS intensity and loss of excitation polarization dependence allow to characterize lysophosphatidylcholine-induced myelin degradation [118]. In the study performed by Ouyang et al., immunofluorescence imaging and CARS microscopy were used to assess tissue deformation, the integrity of the axoglial junction and the role of potassium channels in conduction pathophysiology in compression spinal cord trauma induced in adult guinea pig spinal cord [119]. In a pilot study, Shi et al. used CARS imaging to measure the intra- and extra-axonal space in uninjured, compression-injured and injured/nanoscale block copolymer micelle treated white matter ventral white strips isolated from adult guinea pigs. The effectiveness of particular polymeric micelles in repair of injured spinal cord was shown [120]. Rotating-Polarization CARS (RP-CARS) imaging based on the readout of intrinsic molecular architecture rather than on the image analysis was used by de Vito et al. to assess the myelin health condition in mouse sciatic nerves and proved to be well suited to visualize even the smallest alterations in myelin sheaths [121]. In a pilot study investigating the gene-activated fat grafts for the repair of spinal cord injury, CARS microscopy was used by Betz et al. for imaging of rat hemisection injured spinal cord sections with and without fat implant as well as to monitor the fat graft, which was characterized by intense CARS signal [122]. The novel approach of symmetry-resolved CARS (SR-CARS) imaging on *ex vivo* mouse spinal cord transverse sections was shown by Cleff et al. SR-CARS revealed local

heterogeneities and to reveal the full molecular lipid organization in a single image acquisition [123]. By applying circularly polarized (CP-CARS) technique together with Stokes parameters in the Poincare sphere Bae et al. reported the quantitative assessment of the birefringent effect of myelin sheaths on spinal cord contusive injury induced in rat spinal cord. The phase retardance of injured spinal cord tissue was significantly increased as compared to normal tissue. This study suggests that the degree of tissue phase retardance obtained by CP-CARS imaging could serve as a unique diagnostic parameter associated with nervous tissue injury [124]. The ability of CARS microscopy to retrieve morphochemical information on demyelination after SCI in rat spinal cord hemisection was assessed by Galli et al. The lesion characterized by loss of myelin and preserved myelinated axons were visualized in CARS images. Simultaneously acquired SHG and TPEF signals provided additional information about scarring and inflammation [23].

Multiple sclerosis was also addressed using CARS microscopy by studying EAE models. In spinal cord of mouse, Fu et al. investigated progressive demyelination with retraction of paranodal myelin at the onset of the disease and at the borders of acute demyelinating lesions. Also, the partial paranodal myelin restoration during disease remission was also visualized [125]. Imitola et al. applied multimodal CARS microscopy to image EAE-induced mice forebrain and spinal cord: demyelination and neurodegeneration were monitored over time in brain slices. Local areas of pronounced loss of CARS signal indicative of demyelination and loss of the reflectance signal from axons were found in the brain corpus callosum and spinal cord of EAE animals. Even in myelinated areas of EAE tissue, the intensity of CARS signal was significantly reduced, indicating lower content of myelin lipids. The critical role of activated microglia in chronic inflammatory neurodegeneration was confirmed by identifying activated microglia by green fluorescence signal [126]. The demyelination and neurodegeneration were assessed again in more detail in

the study carried out by Gasecka et al. In particular study, polarized CARS was used to probe lipid orientational organization at the molecular level within the myelin sheath of mice spinal cord. Molecular order of lipids in myelin was studied and quantified. It was found to be significantly reduced throughout the progression of EAE even in myelin regions that appeared morphologically unaffected [127].

Huff et al. implemented real-time CARS imaging on myelin in fresh spinal cord white matter strips isolated from guinea pigs to observe the response of myelin to electrical stimulation. CARS imaging provided direct evidence of myelin retraction at the nodes of Ranvier during high-frequency electrical stimulation [128]. *In vivo* multimodal CARS imaging was implemented by Shi et al. for longitudinal visualization of de- and remyelination at a single axon level to sequentially monitor spinal cord of rats over a 3 week period [22]. Turcotte et al. developed a system combining a live zebrafish spinal cord model together with CARS microscopy and polarization-resolved measurements allowing *in vivo* studies of developmental myelination and screening of promyelination drugs [129].

CARS imaging was also shown to be a powerful tool to investigate brain tissue. In 2007 Evans et al. published a proof-of-principle study reporting CARS microscopy to image fresh unfixed *ex vivo* mouse brain: normal gray and white matter structures were identified as well as glioma tumor and its margin could be distinguished from normal brain tissue [16]. One year later, section of whole brain was CARS-mapped clearly showing distinct brain tissue structures based on varying lipid content. Myelinated axons and other cells could be visualized by multimodal CARS and TPEF imaging. Moreover, *in vivo* CARS imaging of brain on an upright CARS microscope was demonstrated for the first time [130]. Imaging of fresh mouse brain was also demonstrated by multiplex CARS microscopy by Pohling et al. In contrast to previous CARS studies of brain tissue,

different brain structures were visualized simultaneously and separated from each other in false-color maps [131].

The first application of CARS microscopy to study brain tumors to show proof-of-principle was reported by Evans et al. in 2007. By *ex vivo* experiments on fresh unfixed brain tissue in mice tumor model the glioma was distinguished from normal brain tissue and the tumor margin was clearly identified. These results established the feasibility of CARS imaging for label-free brain tissue diagnosis [16]. In the study carried out by Meyer et al., unstained samples from the brain of a domestic pig have been investigated by a multimodal imaging combining CARS, SHG and TPEF to examine the morphology of brain tissue sections. Furthermore, the application of CARS imaging to investigate human brain metastasis of a lung carcinoma sections was demonstrated. This study demonstrated that multimodal non-linear CARS microscopy can provide similar morphological information as does conventional H&E staining in neuropathology [17]. Afterwards, the same research group applied image processing techniques in order to detect cell nuclei in CARS images of brain metastasis of squamous cell carcinoma [132]. Recently, Galli et al. exploited TPEF imaging of green fluorescent protein-labelled experimental glioblastoma in the mouse model (*n=7*) on fresh brain slices and *in vivo* as well as of 5-aminolevulinic acid-induced protoporphyrin IX in fresh unfixed biopsies of human glioblastoma (*n = 10*) to directly verify neoplastic nature of cells imaged by CARS microscopy and to prove the interpretation of CARS images, which is based on CARS signal intensity variations, of solid and infiltrative tumors [133].

Some studies regarding the use of CARS microscopy to study other types of tumors than the brain tumors were also reported. For example, CARS microscopy was employed to study lung cancer cells in excess lipid environments [134], circulating cancer cells of metastatic prostate cancer patients [135], to identify breast cancer [136] as well as lung cancer [137,138]

from non-neoplastic surrounding tissues and to differentiate the subtypes of breast and lung tumors. Galli et al. reported on multimodal microscopy combing CARS, SGH and TPEF for imaging of renal tumors. Multimodal CARS images enabled to discern between normal kidney tissue, tumor and necrosis [108].

1.3 Multimodal Non-linear Optical Microscopy: Coupling CARS with TPEF and SHG

1.3.1 Multimodal Non-linear Optical Microscopy

Non-linear optical processes are those, in which, upon interaction of electromagnetic radiation with material, the induced dielectric polarization $\mathbf{P}$ responds non-linearly to the electric field $\mathbf{E}$ of the incident radiation. The polarization for material can be defined by [139]:

$$\mathbf{P} = \chi^{(1)} \otimes \mathbf{E} + \chi^{(2)} \otimes \mathbf{E} \otimes \mathbf{E} + \chi^{(3)} \otimes \mathbf{E} \otimes \mathbf{E} \otimes \mathbf{E} + \cdots \quad (16)$$

Where $\mathbf{P}$ is the polarization vector, which induced by the electric field of the incident radiation, $\mathbf{E}$ is electric field vector of the incident electromagnetic radiation, $\chi^{(i)}$ is the i^{th} non-linear susceptibility tensor of the material and $\otimes$ represents a combined tensor product and integral over frequencies. Depending on its order, $\chi^{(i)}$ is related with various resultant optical effects: (i) first order susceptibility $\chi^{(1)}$ is related with absorption and reflection; (ii) second order susceptibility $\chi^{(2)}$ is related with second harmonic generation, sum and difference frequency generation, (iii) third order susceptibility $\chi^{(3)}$ is related with multiphoton absorption, third harmonic generation, coherent anti-Stokes scattering.

In NLO phenomena, opposite than in the case of linear optical processes, the energies of absorbed photons are smaller than those of generated photons. In particular, in the case of biological tissue samples, the excitation radiation is

typically in NIR spectral region. The penetration depth of, for example, UV and visible light into optically turbid sample, such as tissue, is limited by absorption and scattering. Therefore, the imaging is strongly limited to outermost layers of the specimen. The energies of NIR photons are relatively smaller (wavelengths between ~800 nm and ~2500 nm), therefore, NIR radiation is less diffusively scattered and absorbed and, as a result, can penetrate deeper into the sample [140].

While the out-of-focus excitation is present in the sample in the case of linear optical phenomena, it is minimized in the NLO microscopy, as the induction of NLO processes requires high photon flux density [~10^{20} – 10^{30} photons/(cm^2·s)] [141] and the NLO signal generation is confined to small in-focus sample volume [142]. It is theoretically calculated that the lateral NLO signal intensity profile for $z = 0$, i.e. at the surface of sample, exhibits FWHM = $0{,}4\lambda$, whereas longitudinal NLO signal intensity profile for $x = y = 0$, exhibits FWHM = $1{,}0\lambda$, where FWHM is full width at half maximum and λ is the wavelength of excitation radiation [142]. By controlling sample excitation focal plane over the sample volume, it is possible to acquire three-dimensional NLO microscopy images. What is more, the generation of the signal from the "out-of-focus" molecules, which decreases the spatial resolution as well as increases photodamage and photobleaching, is minimized. Compared with sample excitation by visible or UV light, photodamage and photobleaching are also less likely to be present as the sample is irradiated with lower energy NIR photons. The above explained properties of NLO microscopy make it especially suitable for both *ex vivo* and *in vivo* imaging of biological samples [143].

Multimodal non-linear optical (MNLO) microscope is an imaging tool, in which distinct non-linear optical imaging modalities are coupled to allow simultaneous generation and acquisition of different non-linearly generated signals. Depending on the number of excitation beams used for generation of

non-linear signals, the MNLO microscopies are categorized into one-beam and two-beam modalities. One-beam modalities are multiphoton fluorescence, second harmonic generation, and third harmonic generation (THG) microscopies, whereas two-beam modalities include CARS, four-wave mixing (FWM), stimulated Raman scattering (SRS), pump-probe microscopies. The combination of one-beam and two-beam induced signal generation in one microscopic system is also widely used [112].

One such combined approach, which is particularly used in this work, is the simultaneous generation and acquisition of CARS, TPEF and SHG signals. When MNLO microscopy is achieved through a CARS microscopy platform, two laser beams are needed for generation of CARS, whereas TPEF and SHG signals are generated by one, namely, pump laser beam. As each of MNLO imaging mode is susceptible to specific molecular species or structures [144], it provides multiple morphochemical information at one imaging experiment and is especially suitable to image morphochemically complex samples as well as to assess the relationships between the sample structures [145].

1.3.2 Two-photon excited fluorescence

Two-photon excited fluorescence is a non-linear optic process occurring when two photons, which possess enough total energy to induce the transition of the fluorophore to an excited electronic energy state [Fig. 5 (C)], are interacting with this fluorophore in a very short time duration (~10^{-18} s) [146]. In particular, one photon is exciting the fluorophore to a virtual energy state. The same fluorophore is subsequently experiencing a transition to an excited electronic energy state by absorption of the second photon. Excited fluorophore is experiencing a transition back to the ground electronic energy state by radiating a photon, which energy is higher than the energy of one incident photon of excitation. In other words, TPEF process requires lower energy photons than in the case of respective one photon excited fluorescence

process, in which only one photon has to possess enough energy to induce fluorophore transition to an excited electronic energy state. In general, for two-photon excitation to be induced, the wavelengths of the excitation photons have to meet the following condition [147]:

$$\frac{1}{\lambda_{1\mathrm{P}}} \cong \left(\frac{1}{\lambda_1} + \frac{1}{\lambda_2}\right), \tag{17}$$

where $\lambda_{1\mathrm{P}}$, λ_1 and λ_2 are the wavelengths of the one photon, which energy is required to induce the transition of a fluorophore to an excited energy state, as well as of the first and the second photons that are present in TPEF process, respectively. The practical experimental choice is $\lambda_1 = \lambda_2$ and, therefore, $\lambda_1 \approx 2\lambda_{1\mathrm{P}}$. The average intensity of TPEF process depends on square of excitation radiation intensity, photon absorption cross-section and to the quantum yield.

1.3.3 Second harmonic generation

Second harmonic generation is a second order non-linear coherent optical process that occurs, when two photons are interacting with the material and are re-emitted as one photon, which energy is exactly double than that of the incident photon [148]. The energy level diagram of SHG process is shown in Fig. 5 (B). For SHG phenomena to happen, the electric field, which interacts with material, must induce second order dipole moment [149]:

$$\mathbf{P}^{(2)}(2\omega_i) = \varepsilon_0 \chi^{(2)} \mathbf{E}^2(\omega_i), \tag{18}$$

where $\chi^{(2)}$ is the second order non-linear optical susceptibility, ω_i is the frequency of the incident radiation. Second order non-linear optical susceptibility characterizes the non-linear second order response of the material, as it interacts with the incident radiation, i.e. materials likelihood to prompt SHG.

Molecular hyperpolarizability β is related to the second order non-linear optical susceptibility. This relation can be expressed as follows [139]:

$$\chi^{(2)} = \mathrm{N}\langle\beta\rangle, \tag{19}$$

where N is a number of elemental dipole emitters. As brackets denote an orientational average, $\chi^{(2)}$ is only non-zero in non-centrosymmetric materials, i.e. in materials that are lacking center of symmetry. Furthermore, intense second harmonic signal is only generated, when material is characterized by strong hyperpolarizability [150].

SHG intensity in non-centrosymmetric materials is also dependent on laser pulse energy p and duration τ [139]:

$$I_{\mathrm{SHG}} \propto p^{(2)}\tau\left(\chi^{(2)}\right)^2. \tag{20}$$

Ideally, the phase matching condition $\mathbf{\Delta k} = \mathbf{k}_{2\omega} - 2\mathbf{k}_{\omega} = 0$, where $\mathbf{k}_{2\omega}$ is $\mathbf{k}_{\omega}$ are wave vectors of SHG and excitation photons, respectively, have to be met for SHG process to take place. As phase mismatch is zero in this case, SHG is 100% forward directed. Under real experimental conditions, the phase matching condition is never fully met and SHG radiation is propagating in both forward and backward directions [148].

CHAPTER 2 MATERIALS AND METHODS

2.1 Linear vibrational spectroscopic imaging systems

2.1.1 FTIR microspectrometer

FTIR spectroscopic data was collected by a FTIR spectrometer Tensor 27 equipped with infrared microscope Hyperion 3000 (both from Bruker Optic GmbH, Ettlingen, Germany).

The interferometric element in Tensor 27 is a Michelson interferometer containing three main optical components: a moving mirror, a fixed mirror and a beam splitter. The beam splitter is an optical device, partially reflecting and partially transmitting the incident radiation. It is made of flat KBr substrate onto which a thin film of germanium is deposited. The broadband infrared irradiation generated by Globar light source made of SiC is collimated and directed towards the interferometer, where an interference pattern is generated. Such modulated IR beam leaves the interferometer and is directed to the microscope.

The objective of the microscope Hyperion is an 15×/0.4 NA infrared objective. The microscope is also equipped with a visible light source, which illuminates the sample, and a camera, which enables sample observation. The sampling area of the specimen can be adjusted by knife edge aperture, consisting of two pairs of blades. The dimension of the variable aperture can reach the minimal sampling area of about 10 × 10 μm^2. The IR beam is focused on the sample by a condenser and collected by the infrared objective. This beam is delivered to and detected by a 64x64 mercury-cadmium-telluride (MCT) focal plane array detector.

The signal reaching the detector is registered at precise intervals during the mirror scan of the interferometer. This sampling rate is controlled by an internal reference. Briefly, it is a helium-neon laser generating a monochromatic beam, which is modulated and focused on a separate detector. As the intensity of the sinusoidal interferogram of the laser beam crosses the zero value, the signal of interferogram is registered. Therefore, the optical path difference, the wavenumber and the signal are of discrete values and the discrete inverse Fourier transform is used to calculate the spectrum.

The movable mirror of the interferometer travels a limited distance from $-x$ to $+x$. As a consequence, interferogram do not extend from $-\infty$ to $+\infty$ and in practice is truncated. As such truncated interferogram is Fourier transformed, the resultant spectrum contains side peaks. The suppression of these side lobes is attained by mathematical apodization, i.e. by multiplying the inferferogram with appropriate weighting function. In FTIR spectroscopy experiments of this work, a three-term Blackmann-Harris apodisation function was used.

The general procedure of FTIR spectrum acquisition is the following. Firstly, a background spectrum, which is a response curve of the spectrometer, is collected by registering and Fourier transforming an interferogram without the sample. The background spectrum takes into account the operational performance of the system components (especially the source, interferometer and detector) in a combined way. Moreover, the spectral contributions of a sample substrate as well as of any ambient water vapor, carbon dioxide and other atmospheric chemical components, which are present in the optical bench at the moment of experiment, are included into the background spectrum. In this way, the background spectrum allows to minimize the two irregular groups of spectral lines at about 1600 cm^{-1} and 3600 cm^{-1} arising from absorption by water vapor and a spectral doublet at around 2360 cm^{-1} from absorption by carbon dioxide. A spectrum from the sample is afterwards

collected. The sample spectrum contains spectral contributions from both the sample and the background. To minimize the sample-unrelated contributions of the background in the sample-spectrum, it is ratioed on the background spectrum and final transmittance spectrum of the sample is produced. Finally, the transmittance spectrum is converted to absorbance spectrum in logarithmic scale.

2.1.2 Raman microspectrometer

Raman spectra were recorded with a holographic Raman spectrograph RamanRxn1 (Kaiser Optical Systems Inc., Ann Arbor, MI) equipped with a microscope DM2500 P (Leica Microsystems GmbH, Wetzlar, Germany).

Samples were excited with a GaAlAs diode laser (Invictus 785, Kaiser Optical Systems Inc., Ann Arbor) to produce spontaneous Raman scattered radiation. This laser emits at 785 nm and has maximum nominal power of 400 mW. Instead of conventional end-reflectors (e.g. dielectric coatings at the end of semiconductor), an external resonator with externally mounted gratings is used, which increases the stability of the emission wavelength and the power of the laser. In this way, the laser emission fluctuation arising from thermal expansions of the semiconductor device during the operation are minimized. The safety class of the laser source is 3B, however, the microscope is enclosed with interlock and, therefore, the system operates in class 1. The microscope enclosure also serves as shield against ambient light during the measurement.

The laser beam is propagated with 100 µm multimode optical fiber to the coupled epi-fluorescence microscope to excite the sample. The main components of this microscope are a motorized x-y micrometer stage, a halogen lamp, a camera and an objective. The microscope objective focuses laser beam of excitation onto the specimen and collects the back-scattered radiation. Two objectives, namely, 10×/0.12 NA and 50×/0.75 NA, are available. When beam is focused with 50×/0.75 microscope objective, the resultant laser focal spot on the sample is about 20 µm.

Intense Raman signal of the silica of the optical fibers generates the background signal. To remove this additional contribution, a filtered fiber optic probe head is used. The laser radiation emerging from the delivery fiber is collimated and

directed to a holographic transmission grating. It diffracts the laser radiation to a spatial filter, where the laser wavelengths are transmitted and the background generated by excitation fiber is rejected. The collected Raman scattering radiation and the reflected laser radiation are both delivered to notch filters. The purpose of these filters is to reject the reflected laser light, which would otherwise further contribute to a background signal in the collection fiber.

The collected light is coupled and delivered to the spectrograph by a multimode optical fiber with core diameter of 62.5 µm. In the spectrograph, the input signal is collimated and passed through a pre-filter stage, where the notch filter attenuates the laser radiation. Here, a holographic element is used, namely, a thin film with volume fringes parallel to surface, which operates as a wavelength selective mirror.

The pre-filtered signal is delivered and focused on the 50 µm wide entrance slit of the spectrograph. The slit serves as a spatial filter and enables to minimize the transmission of the stray light into the dispersion stage of the spectrograph. A holographic Raman spectrograph RamanRxn1 is equipped with a thin film HoloPlex®, which can obtain a large spectral bandwidth. A tilt of 45° is used in order to avoid diffraction of radiation in orders other than the 0 and +1, so that all the diffraction orders, which are higher than +1, are evanescent. The HoloPlex® takes advantage of a multiplex technology, which allows to cover a broader wavelength region than it would be possible with a single grating, while preserving the spectral resolution. The fringes of the grating are tilted and the gratings are slightly rotated so that one grating is deflecting the radiation upward, while the other is deflecting downwards. The diffracted radiation is focused onto array CCD detector, which registers the actual spectrum. Here, each track of the radiation with low wavenumbers or high wavenumbers impinges on a discrete space on the CCD array detector. In this way, the

radiation covering the spectral range above and below approximately 2000 cm^{-1}, is creating a streak on the upper and the lower part of the detector, respectively. Therefore, the frequency coverage of the grating system is increased, covering 100 – 3450 cm^{-1}, while the dispersion is preserved and the average spectral resolution is 4 cm^{-1}.

Operation of the spectrograph at very low f/number is enabled by axial transmissive design. The spectrograph has a focal length of 85 mm and operates at f/1.8. As it is coupled with multimodal optical fibers, which f/numbers are generally close to f/2, nearly 100% efficiency in light collection can be reached.

The Raman spectral microscope (or microspectrometer) is controlled by the software “Holograms”. The available acquisition modes are (i) collection of the spectrum from single point, (ii) acquisition of a line spectral map or (iii) two-dimensional spectral map. The software Holograms automatically performs a calibration by joining of the low and high wavenumber tracks for each spectrum. Cosmic ray correction from the spectra is also automatically calculated.

2.2 Multimodal CARS microscope

CARS system, which is capable to operate in multimodal fashion, i.e. which allows simultaneous generation and acquisition of CARS, SHG and TPEF signal, was assembled in house by Dr. R. Galli. Multimodal CARS system contains three main parts: (i) the laser sources, (ii) the relay optics for correct superposition of laser radiation in time and space as well as for delivery of the laser beams and (iii) the scanning microscope.

The laser sources are two picosecond Erbium fiber lasers. The “pump” beam is generated by a laser Femto Fiber pro NIR (Toptica Photonics AG, Munich, Germany) emitting at 780 nm with pulse length of 1.2 ps. The source of the “Stokes” beam is laser Femto Fiber pro TNIR (also from Toptica Photonics AG), which is tunable in the range 850 – 1100 nm and has the pulse length of 0.8 ps. The pulse repetition rate of the sources is 40 MHz and provides sufficient energy of the pulse for efficient generation of non-linear processes. As the safety class of both lasers is 3B, the emitted radiation possess a potential to damage eyes and skin. Therefore, the use of the lasers during the experiments complied with the European safety specification IEC 60825.

A laser unit, which is common for both NIR and TNIR laser sources, emit the fundamental laser beam at 1560 nm. Here, active laser medium is a core-pumped Erbium-doped fiber. A laser diode at wavelength close to 980 nm acts as a pump source, while passive mode-locking is based upon saturable absorber mirrors (SAM). Optical isolator protects SAM mode-locked ring oscillator against the back reflections. The oscillator is running in the solitonic regime. The amplification of the soliton pulses to very high peak power is achieved in a following core-pumped fiber amplifier. This master oscillator power amplifier (MOPA) platform is all based on polarization-maintaining fibers. The smooth spectral shape is preserved by a motorized silicon prism

compressor. In time domain it provides ultrashort and nearly pedestal-free pulse shapes.

The „pump" beam at 780 nm is generated in the NIR source, where the original emission at 1560 nm is duplicated with a second harmonic crystal placed after the silicon prisms. The tunable "Stokes" beam originates from TNIR source, where a highly non-linear fiber positioned after the MOPA generates the supercontinuum. The supercontinuum is frequency doubled by a manually tunable SHG crystal to provide the final output emission in the range of 830 – 1100 nm. Both laser sources emit linearly polarized electromagnetic radiation with electric field oscillating in the horizontal plane. "Pump" and "Stokes" pulses are emitted in synchronic fashion.

The tunability range between 850 nm and 1100 nm of the "Stokes" emission enables to address Raman bands approximately in the spectral region from 1000 to 3100 cm^{-1}. The corresponding CARS signal covers the range 610 – 730 nm. Throughout this work, the symmetric C—H stretching vibrational mode at 2850 cm^{-1} in Raman spectrum was addressed. With the emission of "pump" laser at 780 nm, it requires tuning the "Stokes" laser source to 1005 nm and generates CARS signal at 647 nm, as schematically represented in Fig. 7.

The laser scanning microscope is an upright Axio Examiner Z.1 equipped with a scanning module LSM 7 MP (all from Carl Zeiss AG, Jena, Germany). It is controlled by software ZEN 2010, which allows to control laser scanner, filtering and detection.

The microscope allows to collect the non-linear signals by four independent photomultiplier tubes (PMT), whereas the detector filters can be adapted to particular experimental use. The system can, therefore, be used as a multimodal non-linear microscope, where the non-linear signals are acquired simultaneously. The “pump” laser of the particular system efficiently generates TPEF and second harmonic signals. In this work, the CARS, TPEF and SHG signals are simultaneously generated and collected. CARS and SHG signals are collected in transmission configurations, while TPEF is collected in reflection configuration.

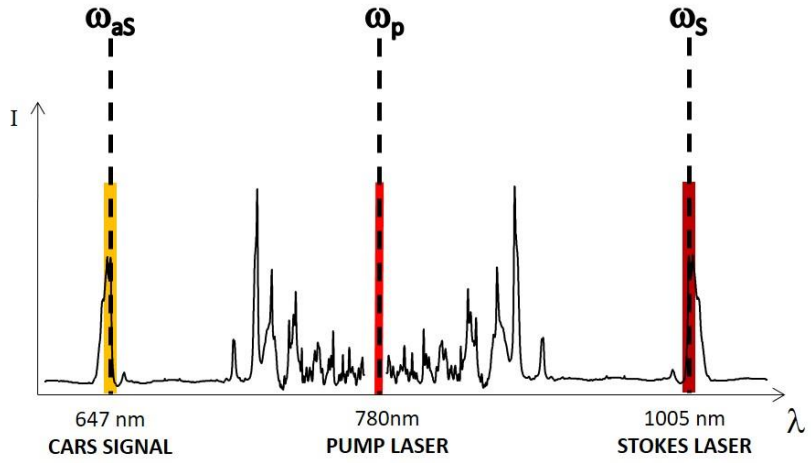

Figure 7. Diagram illustrating the spectral distribution of the pump and Stokes emission and CARS signal when CH_2 symmetric stretching vibration in Raman spectrum is addressed.

The optical path of the laser beams in the microscope is the following: firstly, the laser beams arrive into LSM 7 MP, which is equipped with two scanning mirrors. The laser beams are then propagating through the microscope, where a dichroic mirror reflects them towards the lens turret. Here, in order to fill the objective pupil of the microscope, the beams are expanded. There are four positions in the lens turret, which adapts the diameter of the beam according to the aperture of particular objective and which is typically controlled by the system itself. The beams proceed into the objective and is focused onto/into

the sample. The available objectives are: (i) Plan-Apochromat, 5×/0.18 NA (only for white light microscopy), (ii) Plan-Apochromat, 10×/0.45 NA, (iii) Plan-Apochromat, 20×/0.8 NA, (iv) Plan-Apochromat 20×/1 NA, water immersion and (v) C-Apochromat, 32×/0.85 NA, water immersion.

In transmission geometry of the signal collection, a condenser with variable NA (from 0.3 to 1.2) allows optimal collection with all objectives. The collected light is afterwards side-reflected to two PMTs by a dichroic mirror with edge at 760 nm. The residual excitation wavelengths are firstly filtered by reflecting with a low-pass filter. Subsequently, specified spectral windows are provided for radiation to enter the PMTs by a series of filters. For that, a filter cube is positioned in front of the entrance of each PMT. A dichroic mirror and a band pass (BP) filter is mounted in each filter cube. The longer wavelengths are transmitted by the first filter cube. After being filtered by a BP filter, these wavelengths enter the PMT. The shorter wavelengths, which are reflected by a dichroic mirror in the first filter cube, proceed to the second filter cube. It is placed in front of second PMT and also mounts a mirror and a BP filter. Therefore, the two signals with different spectral range can be collected simultaneously. The spectral window for the first detector is always at a longer wavelength. The signal in reflection geometry is collected by a microscope objective. The signal proceeds back to a dichroic mirror with edge at 760 nm, where it is side-reflected and travels to the system of mirrors, filters and detectors of the same structure as in the case of detection in transmission. The combination of detection in transmission and in reflection allows simultaneous acquisition of four non-linear signals and, therefore, enables multimodal

imaging. The spectral windows allowed to address with multimodal microscope by available filters (Table 1) are schematically shown in Fig. 8.

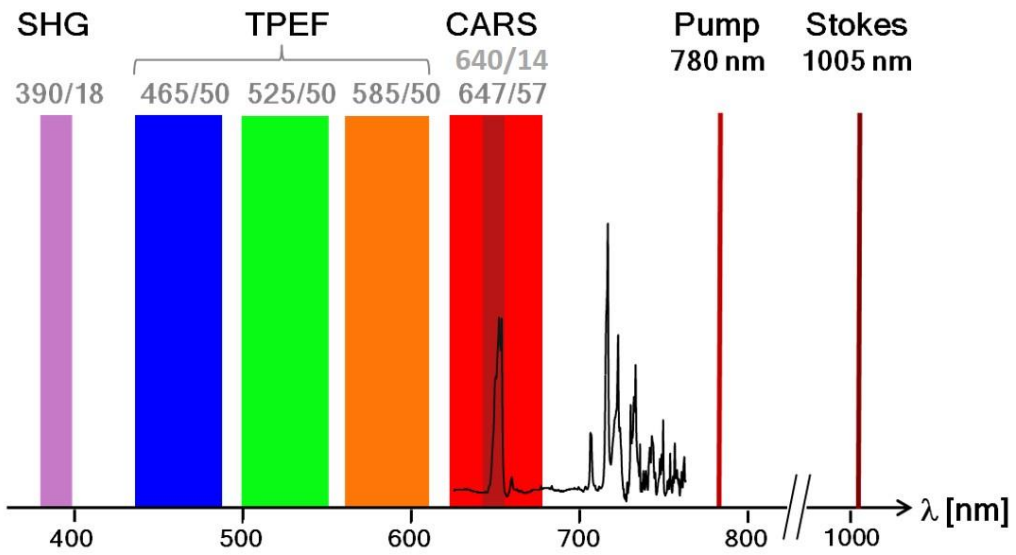

Figure 8. Schematic representation of the spectral regions available to detect by multimodal CARS microscope and relative spectral positions of excitation beams. The numbers in grey: central frequency of the bandpass filter/bandwidth. SHG, TPEF and CARS signals are detected simultaneously by three distinct detectors. For acquisition of TPEF and CARS signals one of three and one of two options of the filter is, respectively, available.

The microscope is additionally equipped with halogen light source and a color camera enabling bright field image acquisition. A mercury lamp also installed in microscope can be used for excitation of blue, green and red fluorescence. The camera images of these signals can be acquired with the correct setting of an excitation-detection filter turret inside the microscope.

The relay optics aligned between the lasers and the microscope are responsible for conforming, overlaying and steering the laser beams inside the microscope. While the fundamental pulses emitted at 1560 nm are synchronized, the pulses of the “Stokes” source are delayed with respect of the ones emitted by “pump” source. The correct overlap of laser pulses in time is obtained by using a delay line, which is composed of two 45^{o} dielectric laser mirrors that fold the “pump” pulse back. The overlap in time is achieved by a dichroic beam splitter

(short-pass dichroic mirror with edge at 810 nm from Thorlabs), which acts as a beam combiner. This mirror transmitting the “pump” beam and reflecting the “Stokes” beam is mounted in front of “Stokes” laser.

The scanning module of the microscope accepts laser beams with diameter of 1.2 mm, which is also a nominal diameter of emitted laser beams. As the beam diverge after traveling the optical path through all optical elements, the beam diameter at the entrance of the scanning module becomes approximately 3.5 mm. The 1:1 Keplerian beam expander re-collimating two laser beams is therefore positioned after the dichroic beam combiner.

Table 1. Specifications of band pass filters available for the CARS microscope system to detect various non-linear signals.

Nonlinear signal	**Band-pass filter**	
	Center wavelength (nm)	Bandwidth
CARS (addressing Raman band at 2850 cm^{-1})	647	57
CARS (addressing Raman band at 2850 cm^{-1})	640	14
TPEF (red)	585	50
TPEF (green)	525	50
TPEF (blue)	465	50
SHG	390	18

Several broad-band dielectric laser mirrors with R>99% for S and P polarizations in the range of 750 – 1100 nm are used to guide the laser beams. One periscope with the height of 120 mm is positioned between the “pump” source and the delay line. Another periscope with the height of 530 mm is positioned before the scanning module and steers the overlaid laser beams inside it. A mechanical shutter provided by Zeiss is placed before this second periscope. It stops the laser beams whenever the scanning is inactive. The whole multimodal imaging system is schematically shown in Fig. 9.

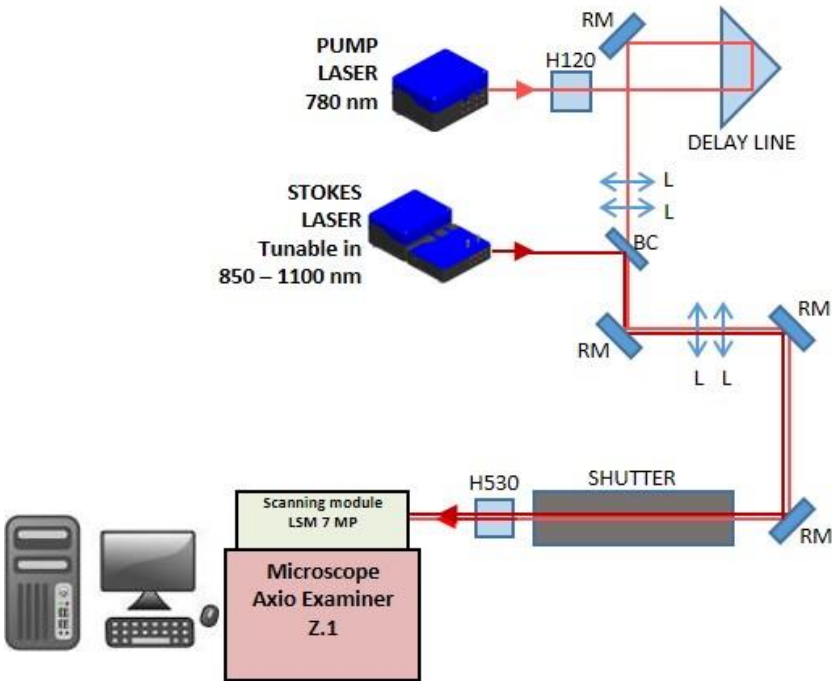

Figure 9. Principal optical diagram of multimodal CARS microscopy system used in this work. RM: reflecting mirror, BC: beam combiner, L: lens, H120: 120 mm high periscope, H530: 530 mm high periscope.

2.3 Stainings

2.3.1 H&E staining

H&E stain is the gold standard in histopathology. Hematoxylin binds to nucleic acids and stains them blue. Eosin binds to acidophilic substances such as proteins and stains them pink.

To perform H&E staining, sections were washed in distilled water and incubated in Meyer's hematoxylin/hemalum for 3 min. After washing in distilled water, sections were briefly destained in HCl-ethanol and washed using tap water for 5 min. After 3 min. of staining in eosin (1% (w/v) eosin G in 80% ethanol), the sections were dehydrated with rising ethanol concentrations, cleared in xylene and coverslipped using DePeX mounting medium (SERVA Electrophoresis GmbH, Heidelberg, Germany).

2.3.2 Alcian blue staining

To provide a reference for spectroscopic imaging of alginate hydrogel implants in spinal cord tissue, sections were stained with alcian blue, which is specific for polysaccharides. Alcian blue solution (pH = 2) was placed on sections and the staining success was observed under the microscope. Then, the sections were washed with running tap water for 3 min. and stained with nuclear fast red for 10 min. After 10 min. of washing with running tap water, the sections were dehydrated with rising ethanol concentrations, cleared in xylene and coverslipped using DePeX mounting medium.

2.3.3 Immunohistochemical stainings

Immunohistochemical stainings were used to get references about tumor position, extension and structure. Anti-Ki67 staining was used to mark nuclei of proliferating cells. Ki67 is a protein, which expression is strictly related with cell proliferation. Anti-CD31 staining was used to show the endothelial cells and highlights blood vessels and capillaries.

For immunochistochemistry, the sections were blocked with 0.1% bovine serum albumine and 3% normal goat serum in 0.3% TritonX for 1 h and probed with the primary antibody for 1 h. After washing with PBS, the sections were incubated with the secondary antibody followed by colorimetric detection of the antibody signal. In detail, anti-CD31 (1:500, provided by Prof. Breier, Pathology, University Hospital Dresden, Germany) was detected using Vectastain Elite ABC Kit Rat IgG (Vector Laboratories Inc., Burlingame, CA, USA) followed by AEC-kit (Vector laboratories). The sections were counterstained with eosin and coverslipped with aquatex (Merk, Darmstadt, Germany). Anti-Ki67 (1:500, Leica Biosystems GmbH, Nußloch, Germany) was used with prior heat antigen retrieval in citrate buffer and in combination with histofine simple stain MAX Po (Nichirei Biosciences Inc., Tokyo, Japan) followed by histogreen (LINARIS Biologische Produkte GmbH, Dossenheim, Germany)

detection, counterstaining with nuclear fast red, and mounting with DePeX (SERVA Electrophoresis GmbH, Heidelberg, Germany).

2.4 Ethics Statement

Rats' and mice experiments were performed in accordance with the guidelines of the Dresden University of Technology, based on institutional and national laws that are in full agreement with the European Union directive on animal experimentation. They were approved by the animal welfare committee of Saxony, Germany (Regierungspräsidium Dresden, AZ: 24-9168.11-1/2011-39 for mice experiments and AZ 24–9168.11-1/2013-37 for rats' experiments). All surgery was performed under anesthesia with an intraperitoneal injection of xylazine / ketamine (10 mg / kg xylazine; 90 mg / kg ketamine), and all efforts were made to minimize animal suffering.

Mice were sacrificed by cervical dislocation. For rats, in the first two postoperative days, analgesia was achieved with carprofen (5 mg / kg) once a day subcutaneously. Rarely, buprenorphine (0.05 mg / kg) was needed for an appropriate analgesia. The bladder was expressed by gentle massage twice daily during the first two weeks after surgery until the spontaneous urination or reflex bladder emerged.

Human brain tumor tissue was obtained during routine tumor surgery. The patients gave written consent and the study was approved by the ethics committee at University Hospital Carl Gustav Carus, Technische Universität Dresden, Germany (EK 323122008).

CHAPTER 3 EXPERIMENTAL RESULTS

3.1 Effects of tissue sections deparaffinization for multimodal CARS images

3.1.1 Research background and motivation

The compatibility with standard pathological procedures is important for uncomplicated and successful translation of vibrational spectroscopy and multimodal CARS microscopy into histopathological praxis. Moreover, CARS microscopy based on addressing the lipid-specific spectral band at 2850 cm^{-1} is most established and common to investigate nervous tissue. As lipid content is highly variable in nervous tissue structures, addressing this spectral band is the best choice and became standard for acquisition of brain tissue images with fine chemical contrast [13,57,103,151]. Detuning CARS microscope to address other spectral bands can be complicated or requires expensive tunable laser sources. Therefore, it is desirable that nervous tissue preparation protocol would be optimal or at least preserve eligible biomolecular moieties for imaging with conventional CARS microcopy, i.e. addressing spectral band at 2850 cm^{-1}.

Raman spectroscopy and multimodal CARS imaging have been often applied to study frozen, i.e. cryo-protected, and fresh tissue samples. It was already shown that the spectral pattern of fresh and frozen tissues do not differ significantly [152,153]. However, the amount of available frozen and fresh tissue samples is usually rather limited, therefore narrowing the scope of studies to relatively small number of samples. On the other hand, the most common and routinely used in clinical praxis approach to preserve tissue for a long term is the embedding of the tissue specimens in paraffin wax [154]. Briefly, the tissue is dehydrated, cleared in some organic solvent and immersed

in molten paraffin wax, which is allowed to solidify to eventually embed and preserve the tissue. The storage of such specimens is uncomplicated compared with frozen samples, which require storage in freezers under minus temperatures.

The most extensively used preservation in paraffin protocol involves fixation the tissue with the formalin prior the embedding and is therefore called formalin-fixation paraffin-preservation. Despite the fact that retrieval and assessment of antigens and nucleic acids are successfully preformed in the case of FFPP tissues stored for long periods [155,156], the alterations of biochemical composition are nevertheless present to some extent in such samples [157].

However, the knowledge about the influence of tissue sample preprocessing on spectroscopic data and especially CARS images is still limited. Galli et al. investigated the effects of tissue fixation on CARS images of cryosectioned brain [158]. Fixation with formalin of placenta specimens was also addressed in the study performed by Faolain et al. and revealed that the changes of the Raman spectral characteristics are induced [159]. Several other studies focused to study the effects of tissue preprocessing for vibrational spectroscopy of brain [160] and other organs [159,161].

The main disadvantage of deparaffinization arises due to the need to use dewaxing agents: as the molecular structure of paraffin wax is similar to the native tissue lipids, the dewaxing agents such as xylene also leach out these lipids [160]. While lipids are one of the main components of nervous tissue, the rest of chemical content must be sufficient for vibrational spectroscopy studies.

Although, the effects of FFPP tissue samples' deparaffinization for vibrational spectroscopy, namely, biochemical changes that occur in the archived FFPP tissues, and the effectiveness of the most commonly used dewaxing agents, were addressed elsewhere [160,162,163], the consequences of FFPP and

deparaffinization on CARS image quality were not described so far. Once these effects are known, one can decide if the information extracted from CARS images is sufficient for retrospective and diagnostic studies as well as to select the most appropriate methods of tissue preprocessing for particular CARS imaging experimental tasks.

Here, the feasibility for multimodal non-linear and, in particular, CARS imaging of FFPP brain tissue sections preprocessed by different methods of deparaffinization, namely by using xylene or xylene substitutes, were analyzed and compared with cryo-protected sections. The effects of deparaffinization with the xylene as paraffin solvent on multimodal CARS images were addressed in more detail and confirmed by Raman spectroscopy.

3.1.2 Sample preparation and experimental details

The mouse brain or human brain tissue removed during brain tumor surgery were formalin-fixed and paraffin-preserved. They were immediately fixed with formalin and then preserved in paraffin blocks by using standard automatized process. For embedding in paraffin the tissue samples were placed in an embedding cassette, dehydrated by immersion in increasing alcohol concentration solutions and xylene and subsequently infiltrated by paraffin at 60°C. The solidified tissue blocks of mouse brain and 8 human brain tumors tissues (3 primary tumors and 5 metastases) were sectioned at 4 µm at room temperature on Leica SM 2000 R microtome and mounted onto SuperFrost® Plus microscope glass slides or CaF_2 slides for multimodal multiphoton microscopy or Raman micro-spectroscopy, respectively.

To deparaffinize the FFPP tissue sections the following protocol was applied: the paraffin was removed by immersing the slides with the samples three times (each time for 5 min.) into xylene/xylene substitute. Afterwards, to remove xylene/xylene substitute, the slides were immersed in a series of baths

consecutively consisting of three baths of 100% ethanol, one bath of 96% ethanol, one bath of 80% ethanol. Finally, the ethanol was washed away by 5 min. bath in distilled water. All paraffin solvents tested in this study are summarized in Table 2.

Table 2. Paraffin solvents used for depraffinizing FFPP brain tissue sections.

Paraffin solvent	Manufacturer
Xylene	Merck KGaA, Darmstadt, Germany
Neo-Clear®	Merck KGaA, Darmstadt, Germany
Citrosol	PanReac AppliChem GmbH, Darmstadt, Germany
Histo-Clear	National Diagnostics, Atlanta, Georgia, USA
HistoChoice®	Merck KGaA, Darmstadt, Germany
Shandon™ Xylene Substitute	Thermo Fisher Scientific, Waltham, Massachusetts, USA

In multimodal CARS microscopy, a Plan-Apochromat 20×/1 NA water immersion objective was used to focus the excitation light. The CARS signal was collected in forward direction and filtered by a band-pass filter centered on 640 nm with a bandwidth of 14 nm. For SHG, also collected in forward direction, a bandpass filter centered at 390 nm with bandwidth of 18 nm was used; for TPEF the bandpass range of the filter was 500 – 550 nm. Tiling procedure was applied for the images larger than the microscope objective field of view.

ImageJ software was used for analysis of multimodal images. Intensities of CARS and TPEF were calculated by measuring the mean gray values of ten 20 µm x 20 µm regions of interest. Values were normalized to selected tissue areas. Graphs were calculated by using GraphPad Prism 5 (GraphPad Software Inc., USA). Deparaffinized sections and cryosections were compared by two-tailed t-test with 95% confidence interval. Images were processed with the Photoshop software (Adobe Systems Software Ireland Ltd.).

Raman spectral maps, covering different structures of the mouse brain were collected with the step size of 20 µm. The dimensions of these maps were from 20×18 up to 115×89 points of excitation. For each position of sample excitation ten spectra were recorded with 0.5 s integration time. The spectra were collected in the 150 – 3250 cm^{-1} spectral region with a spectral resolution of 4 cm^{-1}. Point Raman spectra form different regions of cryosections, paraffine-embedded sections and deparaffinized sections were also acquired. For that, an integration time of 1 s and two accumulations were used at each point.

The datasets of Raman maps or Raman spectral data of single point measurements were imported in MATLAB (MathWorks Inc., Natick, Massachusetts). The spectra were reduced to the region 450 to 1850 cm^{-1} for spectral map data and to region 450 to 3000 cm^{-1} for single point spectra. For each spectrum, a variable baseline was calculated (function “msbackadj” of the MATLAB Bioinformatics Toolbox) and normalization was obtained by standardizing the area under the spectra (function “msnorm” of the MATLAB Bioinformatics Toolbox).

3.1.3 Results and discussion

Effects of deparaffinization: mouse brain samples

Complete removal of paraffin from FFPP tissue samples is usually desirable in vibrational spectroscopy experiments, as the paraffin spectral bands are dominant and particularly strongly interfere with the spectroscopic signature of the tissue.

Figure 10 shows the CARS images comparing cryosection and deparaffinzed section of the cerebellum of the mouse brain. For analysis of the images, axons of the cerebellum medulla were selected structures: due to high CARS intensity they are easy to recognize in the multimodal image of cryosections and therefore are superior for assessment of morphochemical contrast. The

morphochemical contrast in cryosection [Fig. 10 (B)] is mainly due to different lipid content: white matter can be readily recognized as it is rich in myelin and thus in lipids (generates intense CARS signal, indicated by #) compared with lipid poor grey matter (appears darker in CARS image, indicated by *). In contrast, in the case of FFPP deparaffinized section, the tissue morphochemical contrast available from CARS signal [Fig. 10 (E)] was based on different protein content, as lipids were removed during deparaffinization. The deparaffinized samples showed reduced CARS signal intensities (p-value<0.0001). All used solvents showed relative values of about 1 indicating that there is no contrast between axons and surrounding cell bodies [Fig. 10 (G)]. The white matter of cerebellum medulla showed an increase in TPEF intensity after deparaffinization [compare Figure 10 (C) and (F)]. This change was significant (p-value<0.0001). The different solvents likewise led to about 1.5-fold higher fluorescence intensities [Fig. 10 (H)].

Due to low CARS contrast some tissue structures, like the white matter in the medulla of mouse cerebellum, could not be distinguished from surrounding cell layers. As a result, studies of nervous tissue pathologies like multiple sclerosis or tumors might be limited in deparaffinized sections.

On the other hand, a trend of TPEF signal intensities increase was observed in deparaffinized samples. The contrast of tissue structures is improved and thereby contributes to the definition of tissue morphological architecture. This is in agreement with prior findings of Wilson et al., who attributed the

autofluorescence of deparaffinized sections to a byproduct of formalin fixation [164].

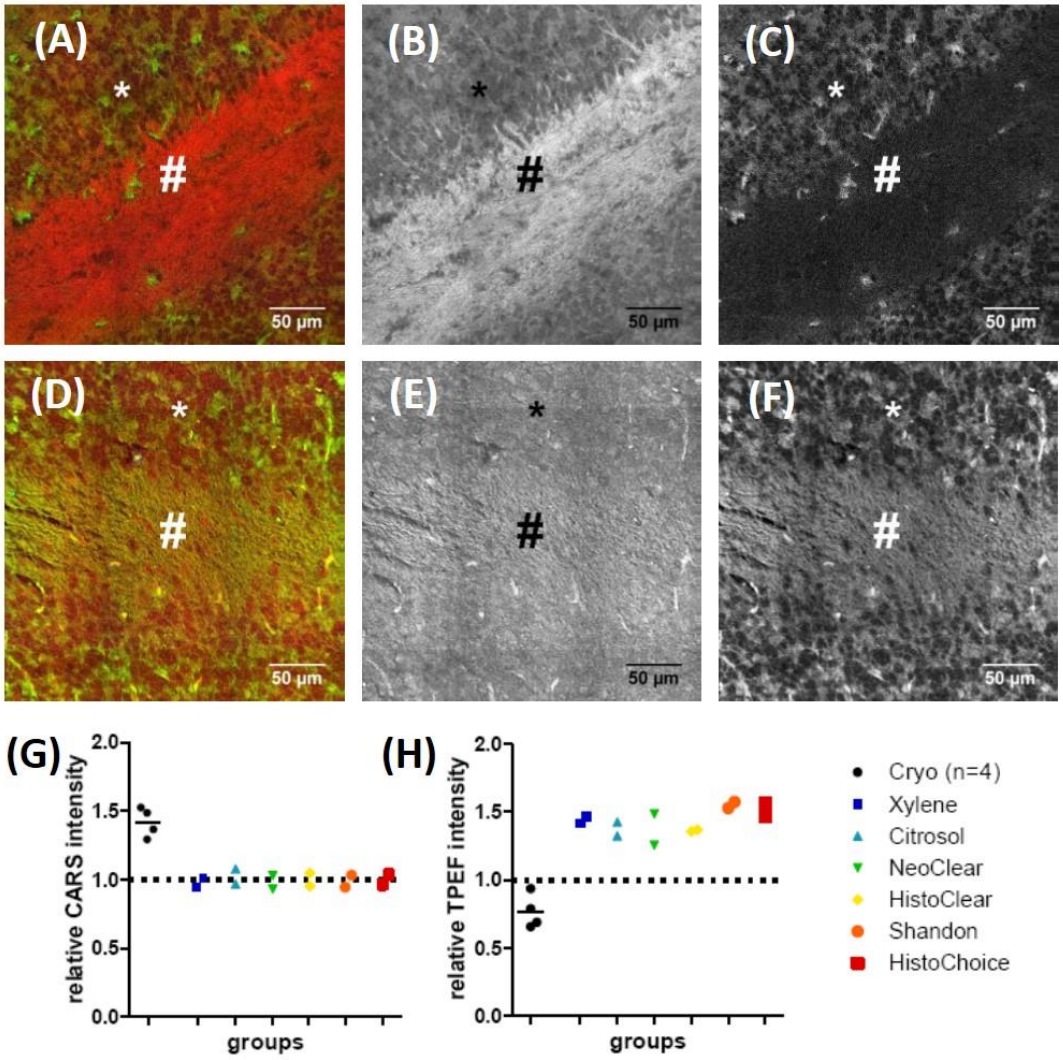

Figure 10. CARS and TPEF signal intensity changes at the white matter in medulla of mouse cerebellum. Cryosections (A-C) and deparaffinized sections (D-F) of the white matter are shown as multimodal (A, D) and grayscale images of CARS (B, E) and TPEF (C, F) signals. The mean CARS (G) and TPEF (H) signal intensities are displayed for the axons (#) normalized to granulated cells (*).

Better insights in the biochemical changes, which appear due to the deparaffinization of FFPP samples, can be gained by using Raman spectroscopy. The reference spectrum of paraffin is shown in Figure 11 and the Raman spectral bands` assignments are summarized in table 3 [165].

In the fingerprint region 800 – 1800 cm^{-1} it is characterized by most intense Raman spectral bands at 1062 cm^{-1}, 1132 cm^{-1}, 1295 cm^{-1}, 1418 cm^{-1}, 1440 cm^{-1}

and 1460 cm^{-1}, corresponding to C—C symmetric stretch, C—C asymmetric stretch, CH_2 twisting deformation, CH_3 in-plane scissoring deformation, CH_2 asymmetric deformation and CH_2 in-plane scissoring deformation, respectively. In the region 2700 – 3000 cm^{-1} the most prominent spectral bands are at 2847 and 2881 cm^{-1} assigned to symmetric and asymmetric CH_2 stretching, respectively. Two shoulders at 2932 and 2958 cm^{-1} are due to symmetric and asymmetric CH_3 stretching, respectively. A weak band at 2722 cm^{-1} is assigned stretching vibrations of the CH_3—CH_2.

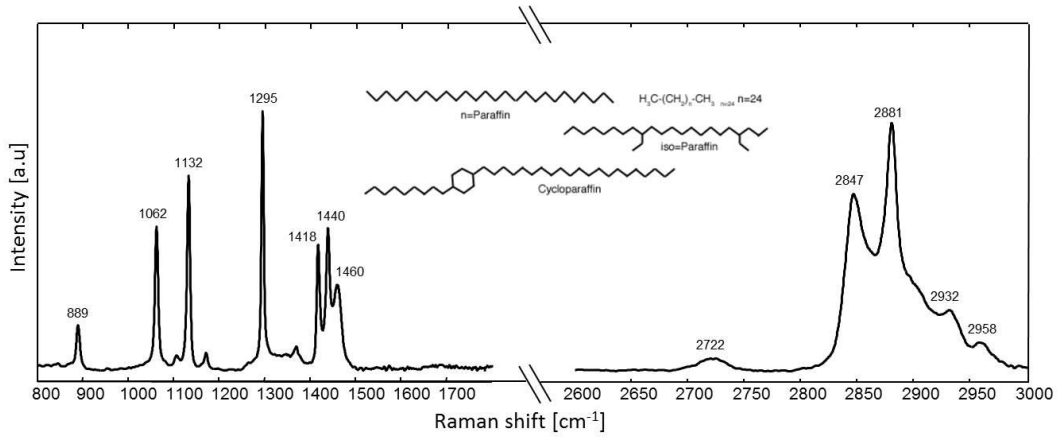

Figure 11. Chemical structure and Raman spectrum of paraffin.

To compare the spectral contributions and thus the provided chemical information between the undeparaffinized FFPP sample, deparaffinized FFPP sample and cryo-protected sample, point Raman spectral measurements were done in all corresponding tissue sections. Fig. 12 shows the representative spectra, which were all acquired in white matter of the mouse brain. Before tissue section deparaffinization, the spectral bands of paraffin were predominant in the spectrum (ν[C-C], δ[CH_2], δ[CH_3] vibrations, indicated by * in Fig. 12). As spectral contributions of tissue were not observed in this spectrum, this indicates the importance of tissue deparaffinization for vibrational spectroscopy-based studies. As expected, the Raman spectrum of the deparaffinized sample shows the substantial decrease of the spectral bands at 1130 cm^{-1}, 1300 cm^{-1}, 1440 cm^{-1}, 1668 cm^{-1} all attributed to lipids (compare with spectrum of cryosection, arrows indicate reduced lipid-related spectral bands). This indicates the removal of the tissue lipids during the deparaffinization.

Table 3. Raman spectral bands and their assignments to specific group vibrations of paraffin.

Raman band (cm^{-1})	Group vibration
889	$\rho(CH_2)$
1062	$\nu_s(C—C)$
1132	$\nu_{as}(C—C)$
1172	$\nu(C—C)$
1295	$\delta_{twist}(CH_2)$
1418	$\delta_s(CH_3)$
1440	$\delta_a(CH_2)$ bend
1460	$\delta_s(CH_2)$
2722	$\nu(CH_3—CH_2)$
2847	$\nu_s(CH_2)$
2881	$\nu_{as}(CH_2)$
2932	$\nu_s(CH_3)$
2958	$\nu_{as}(CH_3)$

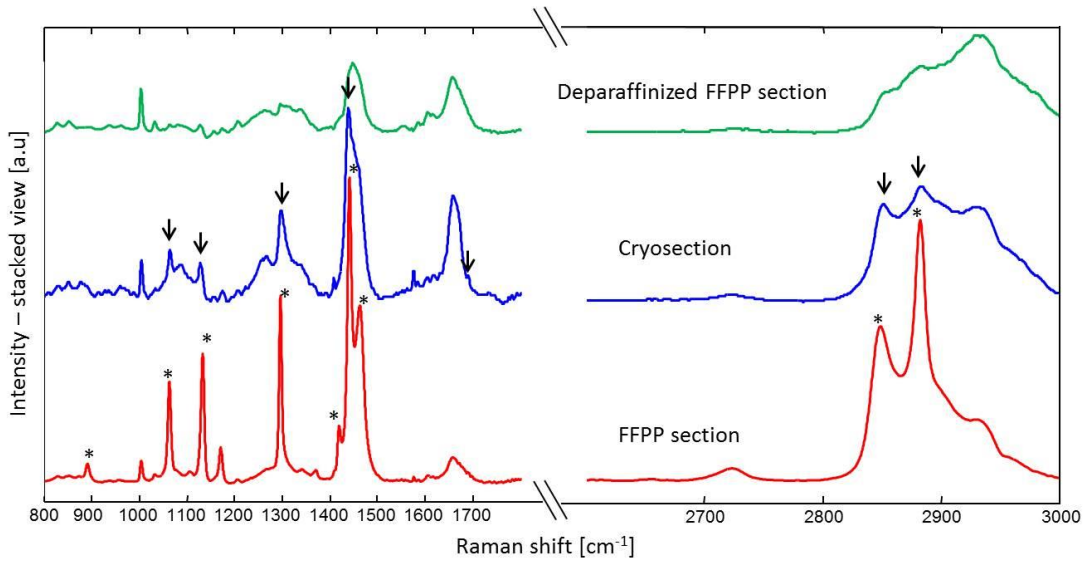

Figure 12. Effects of brain tissue section deparaffinization on Raman spectra. The red spectrum is acquired form the section prior deparaffinization. Green spectrum is from the same section after deparaffinization. Blue spectrum is acquired from cryosection for comparison. Asterisks (*) mark most prominent spectral contributions of paraffin. Arrows indicate lipid-related spectral bands, which are not observed in FFPP section after deparaffinization.

The treatment of the biological specimen before the spectroscopic and microscopic measurements should be so that afterwards acquired biochemical or morphochemical information would be sufficient and reliable. Ideally, all the unnecessary contributions and artifacts should be eliminated, while preserving as much as possible the native state of the biological sample. However, in the case of FFPP samples, there is still no protocol, which would lead to complete removal of paraffin wax.

In the case of CARS imaging, the deparaffinization conserved the general tissue morphology. However, CARS images of dewaxed tissue samples also contained some unusual artifacts, showing the intense signal in 633-647 nm spectral region, where CARS signal is acquired (defined by central frequency and band-pass of the filter positioned before detector for CARS signal, further referred to as “red” signal). Typically, these artifacts were observed as some single droplets distributed randomly within tissue or accumulations of droplets in cells, in outer regions of cortex and in blood capillaries (Figure 13).

Accumulations of droplets were especially pronounced in pyramidal cells as illustrated by arrows in Fig. 13 (A). Interestingly, this was not imperative for all cells of any type and appeared randomly. For example, the cell laying in between two droplets-laden cells in Fig. 13 (A) is completely droplets-free (indicated by asterisk). Fig. 13 (B) shows single droplets within tissue and accumulation of droplets in capillary. The cell nuclei can be readily observed as darker regions, whereas single droplets showing intense "red" signal reside in the tissue randomly (arrows). The droplets in capillary are on the other hand strictly bound within it (asterisk). Opposite as in the case when lipid rich structures are generating intense CARS signal in cryosections of nervous tissue, the biological origin of these "red" signal intense structures in deparaffinized sections is not evident. In fact, morphologically they could not be related to any particular biological structure: as aforementioned, they generally appeared droplet-like and likely tended to fill tissue structural components, but not to be directly related with any biochemical marker. The physical nature of the "red" signal is therefore doubtful and could be either intense fluorescence or CARS signal at 2850 cm^{-1}.

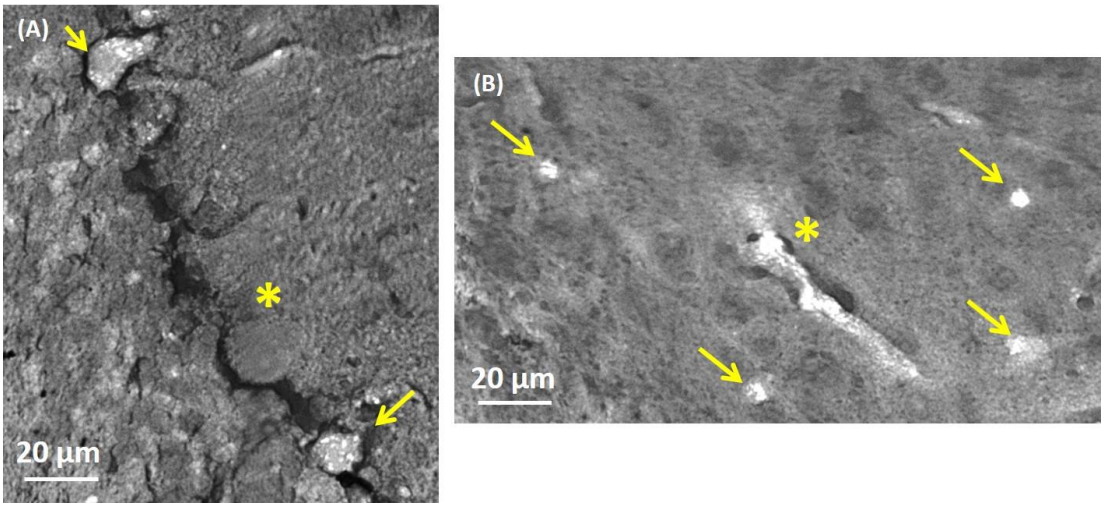

Figure 13. CARS images in grayscale of artifacts characterized by intense signal in 633 – 647 nm spectral region in mouse cerebellum (A) and cortex (B). Arrows in (A) indicate accumulations of droplets in pyramidal cells, while asterisk (*) indicate droplets-free cell in between. Arrows and asterisk (*) in (B) indicate single droplets and accumulation of droplets in capillary, respectively.

To understand the physical nature of this intense “red” signal, the “Stokes” laser was switched off so that only the “pump” laser excited the sample. If the extraordinary structures were only due to the fluorescence signal in 633-647 nm spectral region, they should appear similar as in the case when the “Stokes” laser is “on”. If they are due to CARS signal, their intensity should noticeably decrease. Such experiment is illustrated in Fig. 14, where Fig. 14 (A-C) and Fig. 14 (D) were acquired in the same region of mouse brain cerebellum with the “Stokes” laser on and off, respectively, corresponding to CARS together with fluorescence and only fluorescence signals.

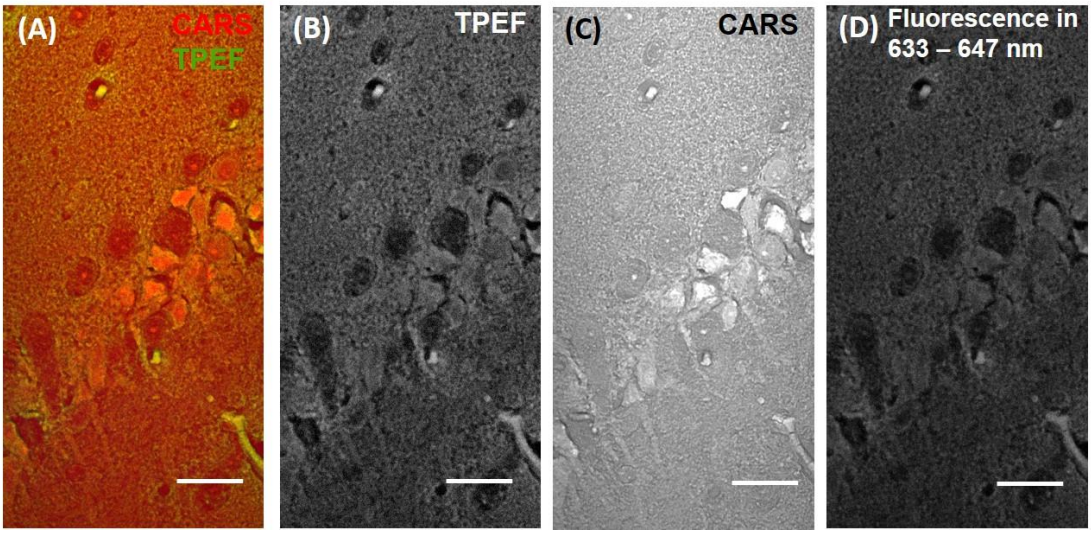

Figure 14. Imaging same region of deparafifinized mouse brain section with (A-C) and without “Stokes” excitation (D). (A): merged multimodal image of CARS (red) and TPEF (green) signals. (B): TPEF intensity image in grayscale. (C): CARS intensity image in grayscale. (D): Intensity image of signal in 633 – 647 nm when only “pump” excitation is present. Scale bar: 20 µm.

The TPEF signal [Fig. 14 (B)] provides contrast of tissue structures and is similar to fluorescence in 633 – 647 nm [compare with Fig. 14 (D)]. The image with the “Stokes” laser on, i.e. CARS image, can be generally characterized by higher intensities, than only fluorescence in 633 – 647 nm signal [compare Fig. 14 (C) and (D)], because varying protein content generates additional CARS morphochemical contrast. For example, bright little spots in the center of nuclei corresponds to CARS signal from nucleoli. Various structures generating

most intense signal can however be only observed in CARS image, confirming that they are strongly CARS active. These structures were not observed in similar cryo-protected samples. They can occur either as a result of some particular paraffinization- or deparaffinization-induced tissue changes producing chemical components with strong Raman spectral contributions at 2850 cm^{-1} or as residuals of paraffin, which by itself has an intense spectral band at 2847 cm^{-1} (symmetric CH_2 stretching, see Figs. 11 and 15).

To understand the chemical nature of these CARS intense structures, Raman spectroscopy enabling to profile the entire chemical composition was applied. Point Raman spectra were acquired in several different CARS active artifacts in mouse brain. Figure 15 depicts one of the examples, where the Raman spectra were acquired from pyramidal cell laden with CARS active droplets after dewaxing the section and from pyramidal cell in cryosection. The spectral bands corresponding to paraffin are intense and therefore clear to observe in the spectrum of deparaffinized FFPP section (indicated by *). These spectral contributions are not present in the spectrum of cryosection. This allows to conclude that the CARS at 2850 cm^{-1} active structures can be attributed to residuals of paraffin wax, which was not completely removed during the deparaffinization. In fact, both CARS images and Raman spectra acquired from with different xylene substitutes deparaffinized sections showed that none of the xylene substitutes is capable to completely clear away the residues of paraffin wax. Qualitative assessment of CARS images and Raman spectra allowed to conclude that the paraffin clearance with xylene leave fewest residuals of paraffin in the sample. However, there is no evident answer, why

and under which mechanisms the paraffin molecules tend to keep immobilized in pyramidal cells or other specific brain structures.

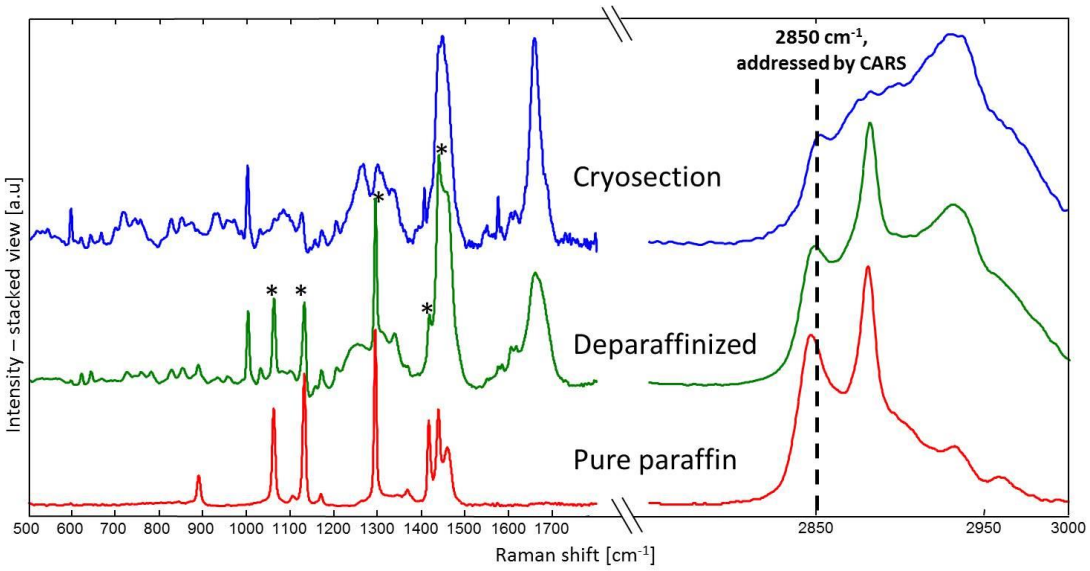

Figure 15. Raman spectral contributions of CARS active artifacts in deparaffinized mouse brain tissue section. Raman spectrum (green) of pyramidal cell laden with CARS active droplets in deparaffinized section is compared with Raman spectrum (blue) of pyramidal cell in cryosection. Raman spectrum (red) of paraffin is shown for direct reference of its spectral bands. Spectral bands corresponding to paraffin are marked by asterisks (*) in spectrum of deparaffinized section.

It is important to notice that xylene was used in dewaxing procedure. Xylene, which was used in this study, is composed of three isomers of dimethylbenzene, namely, ortho-xylene, meta-xylene and para-xylene with approximate molar concentrations of 1:1:1. Ineffective removal of xylene could also result to some parasitic spectral contributions and/or could cause artifacts or signal alterations in multimodal CARS imaging. However, the latter can be excluded, as none of three isomers of xylene has Raman active vibrations at and around 2850 cm^{-1}. Also, Raman spectra of deparaffinized tissue either with paraffin spectral contributions or without do not show spectral fingerprint of any of Xylene isomers [166].

It was already shown in some studies that the current paraffin removal strategies are not completely effective [159,163,167]. The paraffin

contributions are always present, even when different dewaxing agents are used or by using different durations of immersion in dewaxing agents [162]. To further understand if deparaffinized FFPP sections can nevertheless be used for label-free imaging of nervous tissue by multiphoton microscopy, it is important to realize to what extent the artefacts of paraffin have effect on overall tissue biochemistry. Therefore, Raman mapping capable to reveal fine biochemical differences was performed over larger regions of deparaffinized sections.

After the dewaxing of sections, large Raman maps (several square millimeters in size) were obtained and compared with CARS multimodal images on same sections. The CARS multimodal image in Fig. 16(A) shows different regions of brain cerebellum tissue, based on different content of proteins. Intense CARS signal, which definitely cannot be attributed to high lipid content, is observed in pyramidal cells. Raman spectral data can provide further biochemical details, if this CARS signal can somehow be related to higher protein content or to paraffin artifacts. The representative Raman spectral classification map in pseudo-color in Fig.16 (B) was obtained by applying cluster analysis. Seven clusters were needed to sufficiently show different features of the particular brain region for comparison with CARS multimodal image. They are shown in Fig. 16 (C) and depict different regions of the brain tissue mainly based on varying concentrations of proteins. All the centroid spectra contains protein spectral bands: phenylalanine at 1003 cm^{-1}, Amide III band (30% C–N stretching, 30% N–H bending) of proteins at around 1270 cm^{-1}, CH_2 bending mode of proteins at 1450 cm^{-1} and amide I band (70–85% C=O stretching; 10–20% C–N stretching) of proteins at 1656 cm^{-1}. Bands at 1062, 1128 and 1296 cm^{-1} are attributed to vibrations of aliphatic side chains [88]. The centroid spectra 1-3 possess more background noise due to the tissue border or trimming, which results because of sample preprocessing during the deparaffinization. The centroid spectra 4-6 correspond to slightly different areas of cerebellum (compare with classification image in Fig. 16 (B). The

centroid spectrum 7 clearly possesses the spectral contributions of the paraffin wax when compared with the reference paraffin spectrum given above in Fig.16 (C). The spectral contributions of paraffin at 1063, 1133, 1296 cm^{-1} do closely overlap with aliphatic side chains vibrations, what could diminish the ability to directly associate the centroid spectrum 7 with paraffin artifacts. However, the relative intensities of above mentioned spectral bands with other protein spectral bands are too strong when compared with other centroid

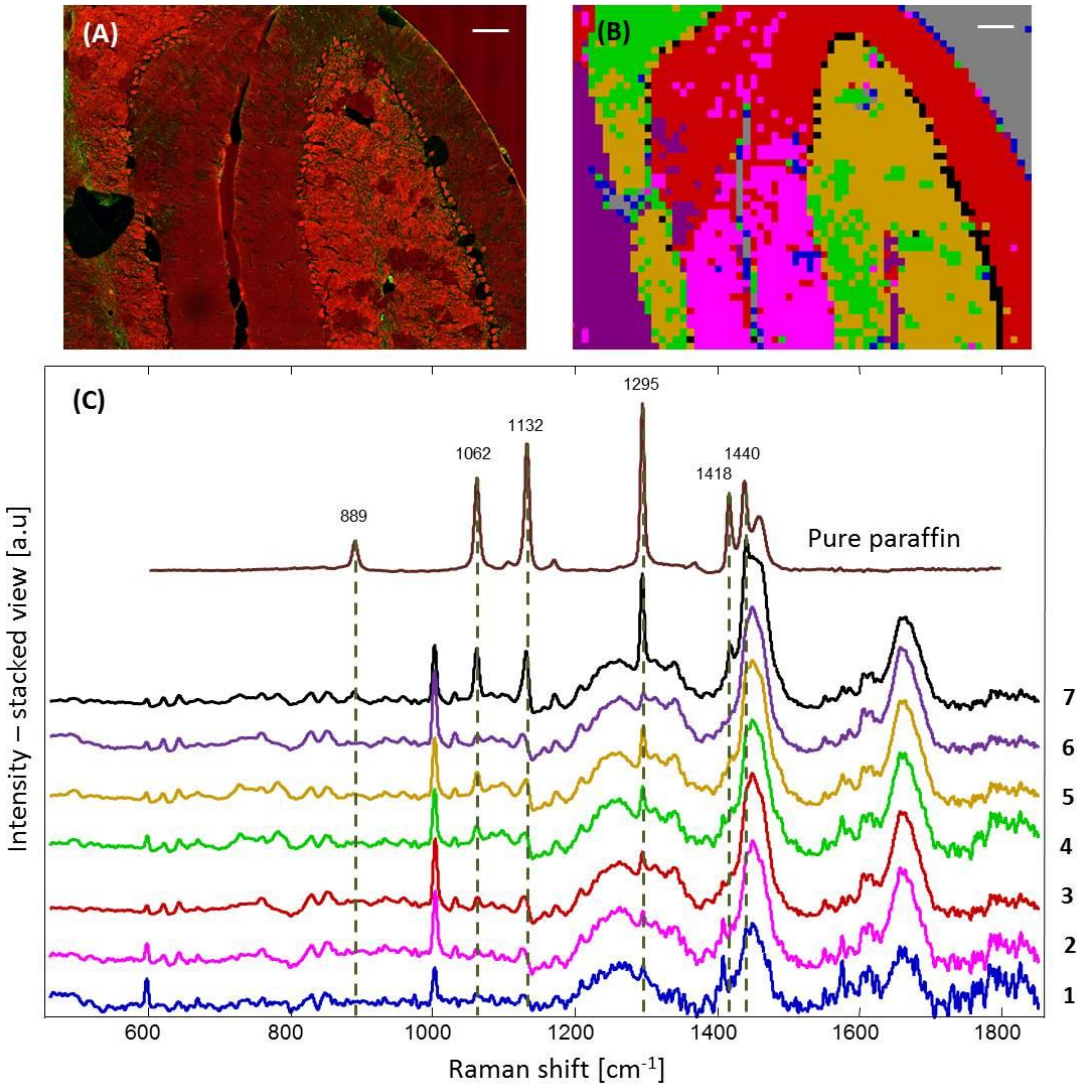

Figure 16. Merged CARS (red) and TPEF (green) image (A), Raman spectral map produced by clustering analysis (B) and corresponding centroid Raman spectra (C) acquired from mouse brain cerebellum. TPEF and CARS image and Raman spectral data were acquired from the same deparaffinized section. Cluster colors were attributed randomly. Raman spectrum of paraffin (brown) in (C) is given for direct reference of spectral bands. Scale bar: 100 µm.

spectra. For example, the band intensity of phenylalanine is ~3,5 – 4,5 times higher than 1062 cm^{-1} band in centroid spectra 1-6, compared with the similar intensities of these bands in centroid spectrum 7. Even more, the paraffin spectral bands at 890, 1419, 1441 cm^{-1}, are unambiguously present in spectrum 7. The corresponding pixels of Raman spectral map in Fig. 16 (B) can be readily attributed to CARS intense pyramidal cells in Fig. 16 (A).

The main brain tissue structures can be discerned in multimodal CARS image. Raman microspectrocopy confirmed that despite the substantial loss of lipids, other tissue chemical content and, in particular, proteins are preserved. Cleared by xylene, paraffin do not leave gross amounts of residues and few deposits do not hinder a morphology-based evaluation of such samples. However, the artifacts of paraffin residues should be taken into consideration and eventually confirmed by Raman spectroscopy in the case of doubts to confidently leave them out from interpretation of multimodal images.

Effects of deparaffinization: human brain samples

FFPP human brain tissues are valuable resources for retrospective studies of various nervous tissue diseases. The re-evaluation of older cases to gain new insights to nervous tissue pathologies by novel or improved and therefore more precise and/or efficient diagnostic methods is of importance.

However, the dewaxing of FFPP sections is a crucial step to make nervous tissue morphology apparent in microscopic images. As shown and discussed previously in the investigations of mouse brain, while awareness of the existence of paraffin artifacts still allow to take advantage of multimodal imaging, the main drawback of deparaffinization of the nervous tissue samples for vibrational spectroscopic studies is the removal of the tissue lipids. Therefore, it is important to understand if multimodal images acquired from

the dewaxed sections of human brain tissue can nevertheless provide diagnostically valuable morphochemical information.

Several different FFPP human brain tumor biopsies obtained during routine tumor surgery were investigated with multimodal non-linear microscopy. Figure 17 shows CARS image acquired from human GBM tumor. Similar to the findings obtained in mouse brain, several paraffin artifacts generating intense CARS signal can be observed (some are highlighted by asterisks in Fig. 17). Tissue morphology is visualized due to spatially definite protein distribution based on differences in protein content. For example, areas with bright spots in the center represent cell nuclei and nucleoli, respectively, as exemplarily shown by arrows in Fig.17. In fact, the nucleus, which shows major changes in neoplastic cells, plays a major role in assessment of tumor malignancy [168]. Label-free CARS images from FFPP samples that had undergone conventional deparaffinization have the potential in tumor assessment based on morphological characteristics of nuclei.

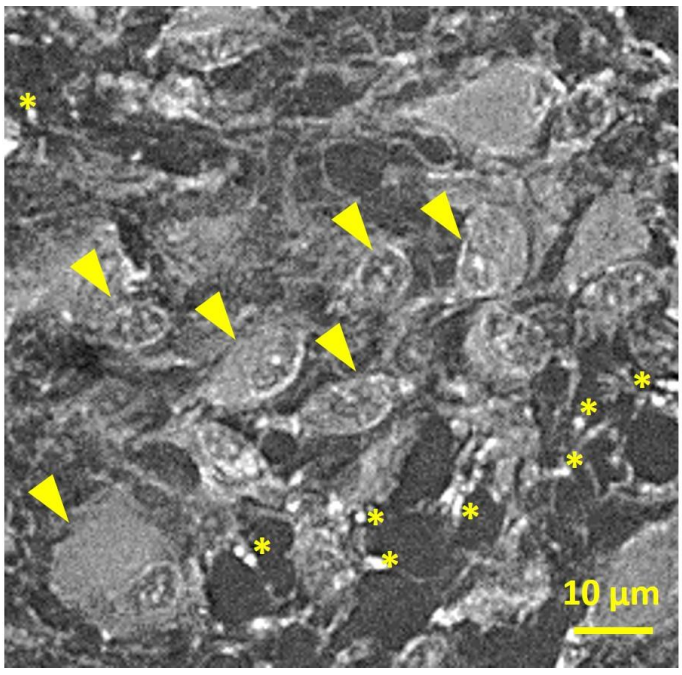

Figure 17. CARS image in grayscale acquired from deparaffinized section of human GBM tumor. Several residuals of paraffin are exemplarily indicated by asterisks (*). Arrowheads indicate cell bodies with nuclei and nucleoli.

Additionally to the potential to image the content of proteins by CARS, simultaneous collection of CARS, TPEF and SHG signals opens possibilities to obtain supplementary information about the tumor structure and the surrounding tissue features.

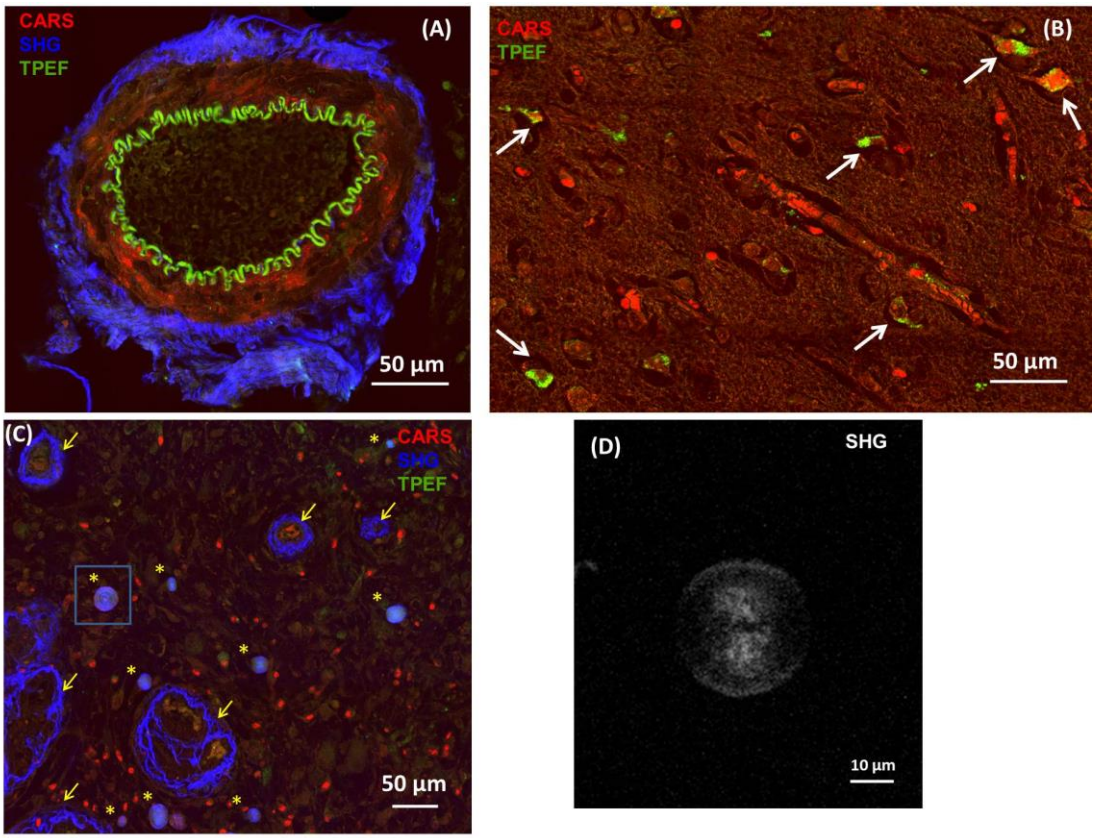

Figure 18. Multimodal images of deparaffinized sections illustrating various structures in human brain tumors. (A): large blood vessel in GBM tumor. (B): Region of human oligodendroglioma tumor, where some cells are well delineated due to TPEF signal (arrows). (C): Collagen of blood vessels indicated by arrows and corpora amylacea indicated by asterisks (*) generate intense SHG signal in human GBM tumor. (D): Zoom-in of the box in (C) showing SHG signal in grayscale from corpora amylacea in more detail. Pseudo-color images in (A) and (C) show merge of CARS (red), TPEF (green) and SHG (blue) signals. Pseudo-color image in (B) shows merge of CARS (red) and TPEF (green) signals.

Figure 18 (A) shows the architecture of a large blood vessel in human GBM tumor. SHG highlights the outermost layer (adventitia) of a blood vessel in the middle of the tumor. This layer is connective tissue rich in collagen as confirmed by SHG signal. The middle layer (tunica media) is primarily protein-rich smooth

muscle exhibiting more intense CARS signal. Distribution of elastin in the inner layer of the blood vessel can be observed due to emission of endogenous two-photon fluorescence. As the autofluorescence signal arises from some cells bodies [arrows in Fig. 18 (B)] these cells appear easier to identify. Indicated by arrows in Fig. 18 (C), the blood vessels can be again readily recognized due to intense SHG signal. Furthermore, SGH-active round structures were observed in human GBM tumor and identified as corpora amylacea (CoA) due to characteristic pattern of SGH signal generation [Fig. 18 (D)], which was recently reported by Galli et al. [169].

Finally, the ability of multimodal CARS microscopy to identify brain tumor borders in the FFPP and subsequently deparaffinized samples was assessed. Fig. 19 shows deparaffinized sample of breast metastasis: It illustrates the morphology and the biochemical information about tissue components. Tumor tissue and surrounding brain parenchyma can be readily distinguished due morphological differences provided by multiphoton signals [Fig. 19 (A)]. It is confirmed by H&E staining shown in Fig. 19 (B). The tumor is mainly characterized by lower TPEF signal intensity. The paraffin artifacts are not prominent and do not obstruct overall image quality.

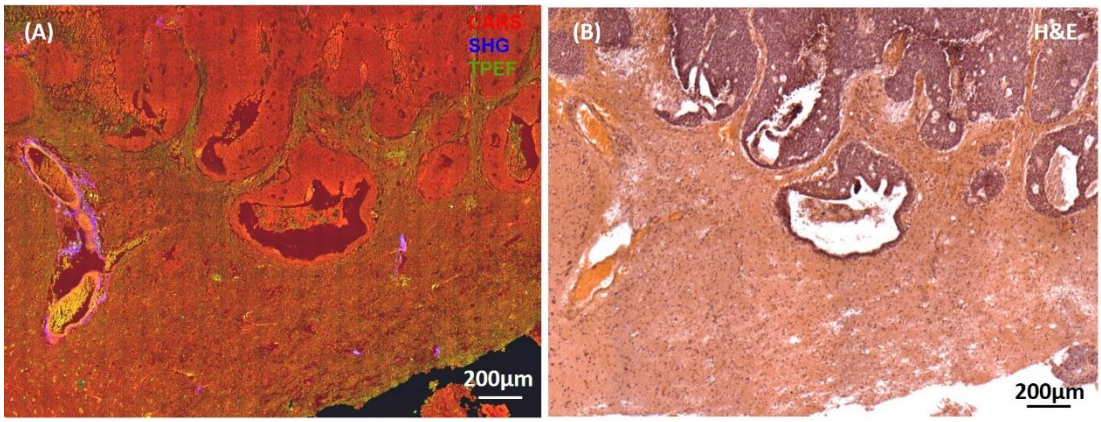

Figure 19. Multimodal non-linear imaging of human breast metastasis brain tumor with defined borders. (A): Multimodal image in pseudo-colors (CARS – red, SHG – blue, TPEF – green). Combination of the non-linear signals allows to delineate tumor (upper part of the image) from normal tissue (lower part of the image) and to track its borders. (B) H&E staining of consecutive section for the reference.

3.1.4 Conclusions

1. Lipids are removed from the tissue during its deparaffinization. The morphochemical contrast in CARS images of deparaffinized sections is, therefore, provided by varying content of proteins.
2. Compared with cryosections, TPEF signal intensity values and morphological contrast in TPEF images of deparaffinized brain tissue sections are increased. This contributes for better definition of various brain tissue structures.
3. Paraffin is not completely removed from FFPP tissue sections during conventional deparaffinization process. Paraffin artifacts have to be taken in account when interpreting CARS images of deparaffinized brain tissue samples.
4. In deparaffinized samples, multimodal CARS/TPEF/SHG microscopy is suitable to image various structures of mouse and human brain tissue and to distinguish brain tumor borders.
5. However, the morphochemical information provided by variations of lipid content is no longer available. The resultant lack of lipid-related CARS contrast brings substantial limitations to studies of CNS tissue pathologies, which are related with lipid content alterations. In this case, cryoprotected or fresh tissue specimens are best choice for conventional CARS imaging based on addressing the Raman band at 2850 cm^{-1} of CH_2 vibrations.

3.2 CARS microscopy of brain tumors

3.2.1 Research background and motivation

The primary malignant brain tumor annual worldwide age-standardized incidence is approximately 3.7 (males) and 2.6 (females) cases per 100,000 persons. The annual global age-standardized mortality from primary malignant brain tumors is approximately 2.8 (males) and 2.0 (females) per 100,000

persons. The mortality from these tumors was constantly increasing over the past years. The average 5-year survival rate of malignant brain tumors are around 30% and varies significantly depending on type of the tumor. For example, while lower grade gliomas such as pilocytic astrocytoma, oligodendroglioma, and ependymoma have 5-year survival rates of over 70%, the 5-year survival rate of glioblastoma multiforme (GBM) is only 3.3%. The 5-year survival rates of astrocytoma, anaplastic astrocytoma, malignant glioma, and lymphoma are less than 40% [170].

Gliomas are the type of brain tumors, which form due to abnormal reproduction and growth of glial cells. In general, gliomas are divided into four grades depending on their morphological features. The grade IV glioma, GBM, is not only the most aggressive of human gliomas, but, unfortunately, also the most common. As the name “Multiforme” suggests, GBM tumors are of complex character. The cells of GBM are rapidly dividing (proliferation), the blood vessels are growing (vascularization) inside the malignant tissue and there are areas of dead tissue (necrotic areas) and hemorrhage. Individual tumor cells show invasive behavior and, therefore, spread diffusely over long distances into various regions of the brain [171].

The standard care for treatment of GBM generally consists of MRI to define the position and borders of the tumor followed by surgical resection of as much malignant tissue as safe. The chemotherapy and radiotherapy are subsequently applied. However, this standard treatment strategy results in poor outcome, as is clear from high rate of mortality. One of the main reasons for this poor outcome is the incomplete resection of malignant cells from the brain tissue. The tumor infiltrate beyond the imaging sensitivity of MRI, which is not enough to visualize fine structural differences [172]. To enhance the precision of tumor resection, the 5-aminolevulinic acid (5-ALA)-induced fluorescence is widely accepted for intraoperative GBM tumor visualization. 5-ALA is administered

orally and metabolizes to fluorescent compounds. This approach helps to better recognize the regions of tumor cells infiltration during surgical intervention, however, for the precise intraoperative tumor diagnosis, the tissue has to be removed, processed, stained and evaluated by a trained neuropathologist [173]. The final diagnosis is obtained by performing multiple immunohistochemical stainings on tissue sections only days after the surgery.

Therefore, it is important to develop novel means of label-free *in situ* brain tumors pathologic assessment and precise methods for intraoperative identification of tumor borders up to single cell.

3.2.2 Sample preparation and experimental details

Animal experiments

Experiments were performed on 16 immune deficient female nude mice NMRI nu/nu (Experimental Center, University Hospital Dresden, Germany). Animals were kept under pathogen-free conditions in a 12h:12 h light-dark cycle and received food and water ad libitum. Brain tumors were induced by stereotactic implantation of human tumor cell lines into the brain parenchyma as described elsewhere [174]. Eight animals were implanted with GBM cells (U87MG), four animals with melanoma (A375) cells, and four animals with breast cancer cells (MCF-7). Within three weeks, the tumor-bearing brains were removed, embedded in tissue freezing medium (Leica, Nussloch, Germany), and frozen on dry ice.

Human brain tissue

Human brain tumor tissue was obtained during routine tumor surgery. The patients gave written consent and the study was approved by the ethics committee at University Hospital Carl Gustav Carus, Technische Universität Dresden, Germany (EK 323122008). Human brain tumor samples

(glioblastoma, n= 6) were snap frozen in liquid nitrogen and stored at –80°C. For sample preparation, tissue was embedded in tissue freezing medium.

Quantification of proliferation and vascularization

The microvessel density was determined at 200-fold magnification in three representative fields of view [175]. Additionally, the morphology of microvessels was evaluated. The thickness of the structures and the pattern of the vessels were analyzed and transformed to a scoring system: 0 = very fine, regular; 1 = fine, regular; 2 = coarse, regular; 3 =coarse, irregular [175].

To evaluate the proliferation index within the tumors, the proportion of Ki67 positive nuclei was determined in three fields of view within the neoplastic tissue at 400-fold magnification. All cells displaying a positive signal in more than 50% of their nuclei were included. In normal brain parenchyma, no Ki67-positive cells were detected.

The cross-sectional area of nuclei was measured using images acquired at 200-fold magnification in three (104 X 104) mm^2 large fields-of-view using Fiji software [176]. The quantification was done in a blinded fashion.

CARS imaging

In the present study, the excitation beams were focused with a C-Apochromat 32X/0.85NA objective. An individual field-of-view image was acquired within 300 ms. Acquisition of large areas was performed with a tiling procedure; z-stacks were acquired in order to compensate for the lack of planarity of samples and followed by maximum intensity projections to obtain the final images. Acquisition times for the CARS overview images ranged from ~5 min. [Fig. 22 (A)] to ~30 min. [Fig. 20 (A)].

CARS signal quantification

The intensity values of the CARS signal in the images were evaluated using the Fiji software. Regions of interest (ROIs) of the tissue (gray matter and tumor) were manually chosen and the average pixel intensity in the ROIs was calculated.

Raman microspectroscopy

Spectral line maps with a step size of 17 mm were collected by sequentially exciting 50 to 70 sample points spanning over regions of tumor and normal tissue. For each position, two spectra were recorded with an accumulation time of 2 s and averaged.

The intensity of the symmetric stretching of C—H bond in CH_2 groups was calculated as integral of the area under the spectrum in the range (2850±15) cm^{-1}. This range approximates the bandwidth of the Stokes laser used in CARS microscopy.

Statistics

All data is expressed as mean ± standard deviation. Statistical analyses to analyze brain tumors (paired t-test or one-way ANOVA followed by Tukey Multiple Comparison test) were performed using Graph Pad Prism 6.0 (Graph Pad Software Inc., La Jolla, CA, USA).

3.2.3 Results and discussion

CARS imaging for localization of primary and secondary brain tumors

The unstained cryosection imaged by CARS microscopy shows a section of whole horizontal mouse brain containing a GBM in the hippocampus [Fig. 20 (A)]. The CARS signal intensity is represented in grayscale, namely, pixels of higher CARS intensity are brighter, whereas pixels of lower CARS

intensities are darker. As the C—H molecular vibrations are addressed in these experiments of brain tissue, the higher CARS intensities represent mainly higher lipid content. In this way, tracts of white matter, which is rich in lipids, can be readily distinguished from gray matter regions, where lipid content is low.

The growing tumors distort normal structure and chemical composition of the brain tissue. It is known that in the fresh tissue human GBM and astrocytic tumors are characterized by less total lipids compared to both normal white and gray matter [177]. Other studies involving vibrational spectroscopy were already comprehensively addressing this feature in primary [47,89,178,179] and secondary [180] brain tumors. This lower lipid content in brain tumors creates the chemical contrast in CARS images, i.e. low lipid content corresponds to the regions with the lowest CARS signal intensity (Fig. 20 (A), arrow).

The same tumor at higher magnification is shown in Fig. 20 (B). It can be readily recognized that the CARS signal intensity contrast is also present at smaller scales allowing straightforward discrimination of an interface between the tumor and the delineating white matter. Lower intensities of CARS signal compared with normal nervous tissue were also characteristic for brain metastases of breast cancer [Fig. 20 (C)] and of melanoma [Fig. 20 (D)]. The borders of the tumors displayed by CARS imaging are well in agreement with corresponding H&E staining [Fig. 20 (E-H)]. Lower CARS intensity allowed to precisely distinguish tumors and their borders from the surrounding normal nervous tissue in all 16 tumors that were analyzed in this study. Importantly, the hippocampal layers which are rich in nucleus and therefore are intensively stained by hematoxylin, did not display reduced CARS signal intensity [arrowheads in Fig. 20 (B/F) and 20 (D/H)].

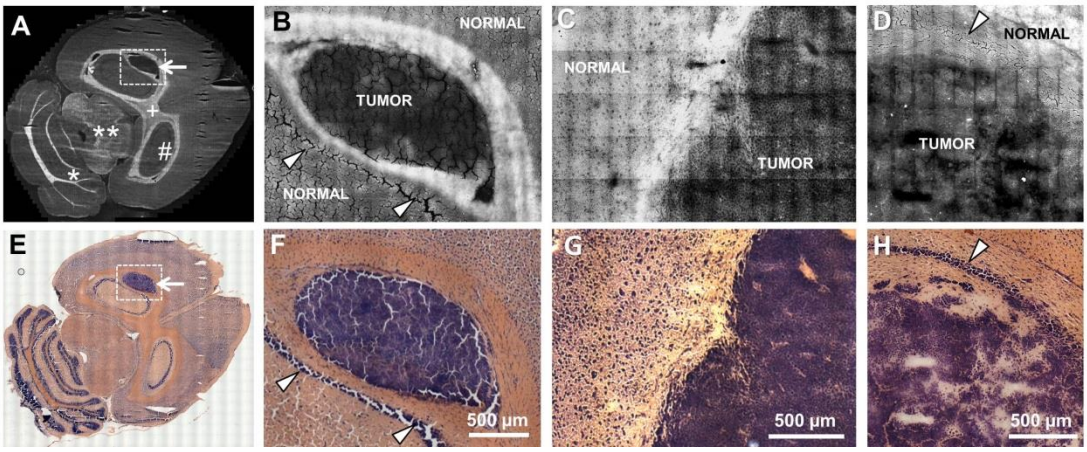

Figure 20. Imaging of experimental human glioblastoma and brain metastases in a mouse model. A: CARS image of a whole mouse brain section with an experimental human U87MG glioblastoma; tracts of white matter are generating more intense CARS signal, while the tumor (arrow) generate lower CARS intensity than the normal brain tissue. # hippocampus, + corpus callosum, **mesencephalon, *cerebellum. B: Magnified CARS image of the area indicated in A; the difference in the CARS signal intensity between the neoplastic tissue and the surrounding white matter creates morphochemical contrast, which enables discerning the tumor border. C: CARS image of a breast cancer metastasis (induced by MCF-7 cells) in a mouse brain. D: CARS image of a metastasis of melanoma (induced by A375 cells) in the hippocampal region of a mouse brain. E–F: H&E staining of consecutive sections corresponding to A–D. Nuclei rich layers in gray matter of the hippocampus are indicated by arrowheads.

Tumor structures at cellular resolution

The system configuration of CARS microscope applied in this work is characterized by lateral resolution of 0.6 µm. This lateral resolution enables imaging at cellular resolution and, therefore, imaging of small tumor infiltrates [Fig. 21 (A)]. The inset in Fig. 21 (A) and Fig. 21 (B) shows that even separate cells can be perfectly detected: the nuclei of single cells are present as dark structures localized in the tumor [arrows in inset in Fig. 21 (A) and Fig. 21 (B)]. The non-nuclear parts, such as cytoplasmic or extracellular regions are also appearing darker than the surrounding gray matter. The decreased CARS signal intensity allows direct qualitative identification of the interface between tumor islands and healthy regions of the tissue in CARS images. The anti-Ki67 immunohistochemical staining of the same tissue section was done for reference. The identification of tumor cells was based on cell proliferation activity and/or cell morphology (also from H&E staining), as not all tumor cells were Ki-67 positive. Indeed, the position and dimensions of micrometastases revealed by CARS imaging precisely matched the histological findings [Fig. 21 (C) and (D)].

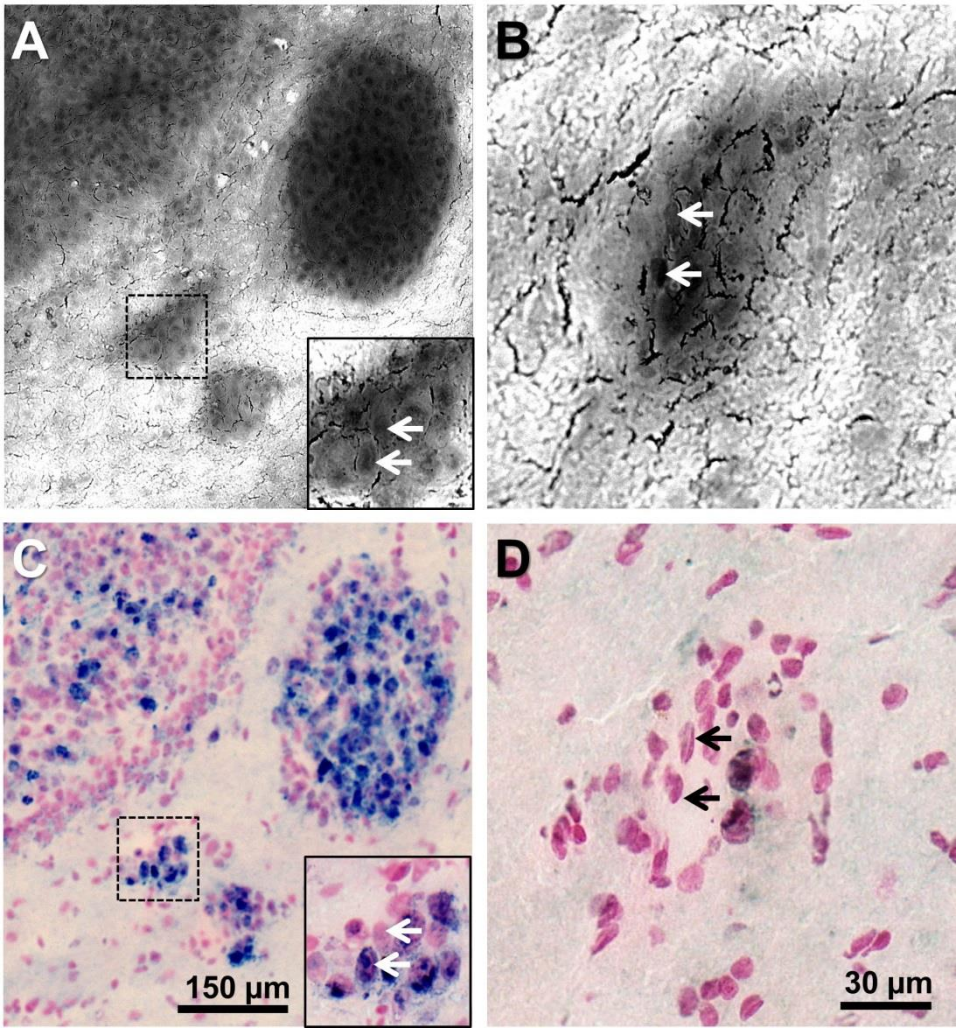

Figure 21. Imaging of the infiltrating tumor margin. A: CARS image of a human U87MG glioblastoma in a mouse brain. B: CARS image of a separate small glioblastoma island in a mouse brain. C/D: Anti-Ki67 immunohistochemical staining corresponding to A/B. In both examples, the very same section was used for CARS imaging and for staining.

Fig. 22 (A) shows CARS image of the brain region, where the normal gray matter is surrounded by an infiltrating tumor, which is followed by a solid tumor. Corresponding H&E reference staining [Fig. 22 (C)] confirms these different states of brain tissue. The CARS signal intensity gradually increases from solid tumor over the infiltration zone to normal gray matter, as confirmed by CARS intensity plot in Fig. 22 (B). In this plot, the CARS intensity values are plotted along the area indicated in Fig. 22 (A) and reveal an evident change: average CARS intensity values of normal gray matter, infiltrative zone and solid tumor are 126, 85 and 60, respectively.

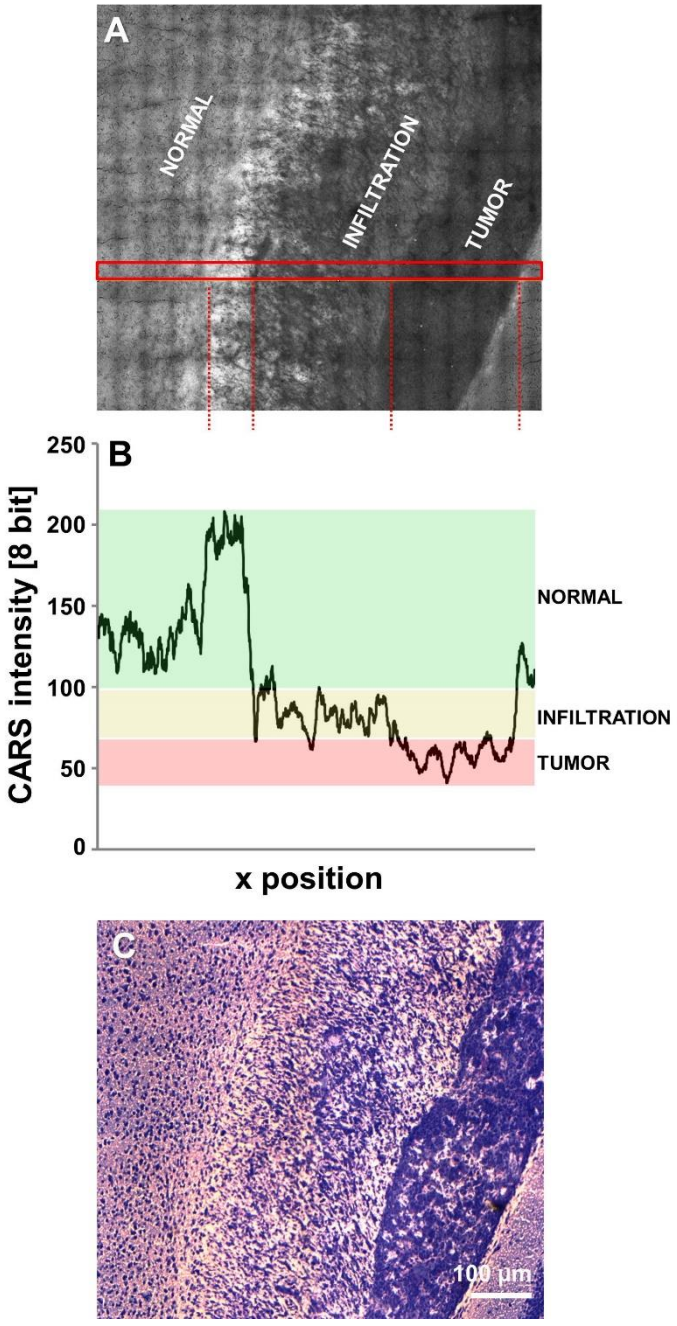

Figure 22. Quantification of the CARS signal intensity of infiltrative tumor areas. A: Unprocessed CARS image of a human U87MG glioblastoma in a mouse brain, displaying a solid tumor and a large infiltrative region. B: CARS signal intensity along the area indicated in A. The CARS signal intensity range indicative of normal tissue is underlined in green, the intensity range indicative of infiltrative areas in yellow and the intensity range indicative of tumor in red. C: H&E staining corresponding to A.

The objective location of infiltrative zone is therefore possible: even though that CARS intensity values from infiltrating tumor are higher than those from solid tumor, they are still lower compared with the surrounding gray matter.

Quantitative evaluation of CARS signal intensity decrease

The decrease of CARS signal intensity, which was previously discussed qualitatively, was quantified as the ratio I_{tumor}/I_{grey}, where I_{tumor} and I_{grey} are average pixel intensity of tumor and gray matter, respectively. Only photomultiplier gain was adjusted to optimize the dynamic range of each image, whereas all other parameters of CARS imaging system (laser parameters and microscope objective) were kept the same for acquisition of all images. However, the ratio I_{tumor}/I_{grey} is independent from photomultiplier gain. Therefore, this ratio can be considered as a suitable parameter to quantitatively characterize the tumor-related reduction of CARS signal intensity among different samples.

As demonstrated in Fig. 23 (A), in all samples that were investigated, CARS signal intensity values were found to be lower within the tumor than within the grey matter ($P<0.001$). Fig. 23 (B) reveals that the reduction of CARS signal intensity is more prominent in GBM compared with the both types of metastases. On average, the CARS signal intensity with respect to normal gray matter was reduced to 61%, 71% and 68% in GBM, brain metastases of melanoma and brain metastases of breast cancer, respectively.

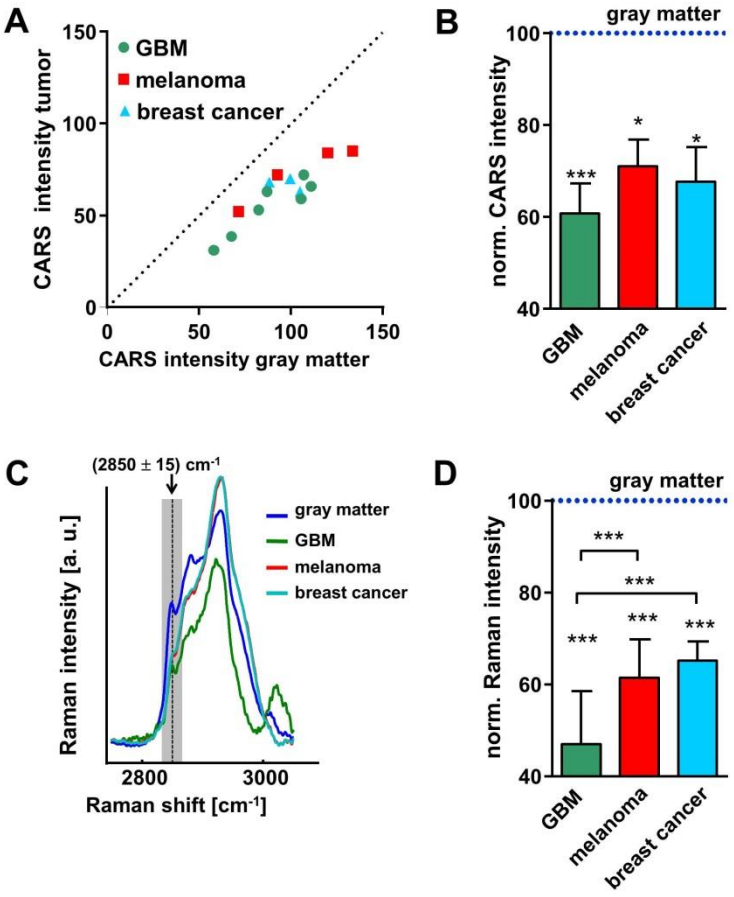

Figure 23. Quantification of the CARS signal intensity and lipid related Raman band intensity. A: Dot plot showing the CARS signal intensity in normal gray matter vs. the intensity of the CARS signal in the neoplastic tissue for each sample. B: CARS signal intensities of tumors normalized to the respective intensities in gray matter. C: Average Raman spectra of normal gray matter, glioblastoma, melanoma, and breast cancer metastases. D: Intensity of the Raman band generated by symmetric stretching of the C-H bonds in CH_2 groups at 2850 cm^{-1}, calculated as integral in the range (2850±15) cm^{-1}. Values were normalized to values of gray matter. B/D: Bars represent mean ±SD, GBM: n = 8; melanoma metastases: n = 4; breast cancer metastases: n = 4; * significant difference vs. gray matter: P<0.05; *** significant difference vs. gray matter or as indicated: P<0.001.

However, the non-resonant CARS signal contribution does not allow to directly relate the CARS signal intensity to concentration of lipids within the tissue. Also the ratio I_{tumor}/I_{grey} cannot be applied as a proper measure for lipid content differences. On the other hand, Raman spectroscopy can be applied for quantitative assessment of lipid content and its differences within the tissue [40,179,181]. Raman spectroscopy was, therefore, used to explain lipid distribution to the observed CARS signal intensity changes.

Multiple Raman spectra were registered from all tumors and of gray matter in the same samples. The average Raman spectra in CARS signal-relevant spectral region between 2800 and 3000 cm^{-1} (range of C—H stretching vibrations) of each different type of tumor and of gray matter are shown in Fig. 23 (C): the spectral profiles are different from one another. The intensity of Raman spectral band at 2850 cm^{-1} was calculated to confirm the findings of CARS signal intensity differences. The intensities of Raman band at 2850 cm^{-1} in tumors were normalized to those of gray matter and shown in Fig. 23 (D) for different tumor entities. The intensity of this Raman band in the case of GBM is significantly lower than of both types of metastases ($P<0.001$) and compared with gray matter was reduced to 47%, 61% and 65% in GBM, melanoma metastases and breast cancer metastases, respectively.

Even though that one cannot directly compare CARS signal intensity and Raman band at 2850 cm^{-1} intensity values [13], the results, which were acquired by both these methods, are in the good agreement. This suggests the potential of CARS microscopy as a reasonable alternative method to provide information about tumors based on CARS signal intensity values changes even at the presence of non-resonant background signal and morphological sample artifacts.

Tumor growth in the brain tissue induce complex processes of lipid alterations. The decrease or even increase of various lipids and the scope of this change greatly depend on the type and proportion of brain lipids, such as gangliosides and phospholipids [41]. For example, when compared with non-malignant brain tissue, it was shown that in human glioma the content of docosahexaenoic acid and phospholipids were significantly decreased. On the other hand, the fraction among total lipids of linoleic acid was increased [182]. The information about changes in proportions of different lipid species cannot be obtained by CARS imagining based on addressing single Raman band.

Simultaneous assessment of different lipid species and/or other biochemical tissue compounds by addressing multiple Raman spectral bands through CARS-based imaging could be realized by means of multiplex CARS [131] or high spectral resolution CARS [183]. As the spectral profiles of GBM and metastases in the spectral region of C—H stretching vibrations differ from each other [Fig. 23 (C)], it might be expected that the discrimination between primary and secondary tumors may be possible by addressing other Raman bands than 2850 cm^{-1}. For example, the Raman band at 2930 cm^{-1} is more intense in the spectra of metastasis than in the one of GBM and could enable the distinction between them.

The potential of CARS imaging to characterize tumors by decreased intensity of CARS signal was already exemplarily reported [16,17,132]. In this thesis, the scope of the research was extended to different type of brain tumors. Regardless type and histopathological characteristics of brain tumor, the decrease of CARS signal intensity was demonstrated to be a solid parameter to distinguish brain tumors from surrounding healthy brain tissue.

Tissue properties influencing CARS signal intensity

It is generally considered that the reason for contrast enabling to visualize tumors versus normal brain tissue in CARS images is the degradation and displacement of normal lipid-rich brain tissue by relatively cellular-rich and therefore lipid-low tumor tissue [16]. As nuclei are of low lipid nature, they generate relatively weak CARS signal and appear darker in CARS images. Because of that, regions with higher cellularity and/or larger nuclei are supposed to show lower average CARS intensity. It is, however, had not been yet assessed in detail, whether high cellularity of tumor is directly leading to decreased CARS signal. Therefore, the total cross-sectional area covered by nuclei within the tumors was calculated by assessing the cellular density and dimensions of single nuclei. As predicted, all investigated tumors showed

significantly increased nuclear density [Fig. 24 (A)] as well as a marked increase of nuclear sizes [Fig. 24 (B)]. Compared to normal gray matter, the significant increase of total cross-sectional area covered by nuclei was calculated: while in the normal gray matter it is of 9.3%, in GBM, melanoma metastases and breast cancer metastases this cross-sectional areas are of 35.1%, 38.7% and 43.8%, respectively. Interestingly, as it is seen in Fig. 24 (C), the tumors total cross-

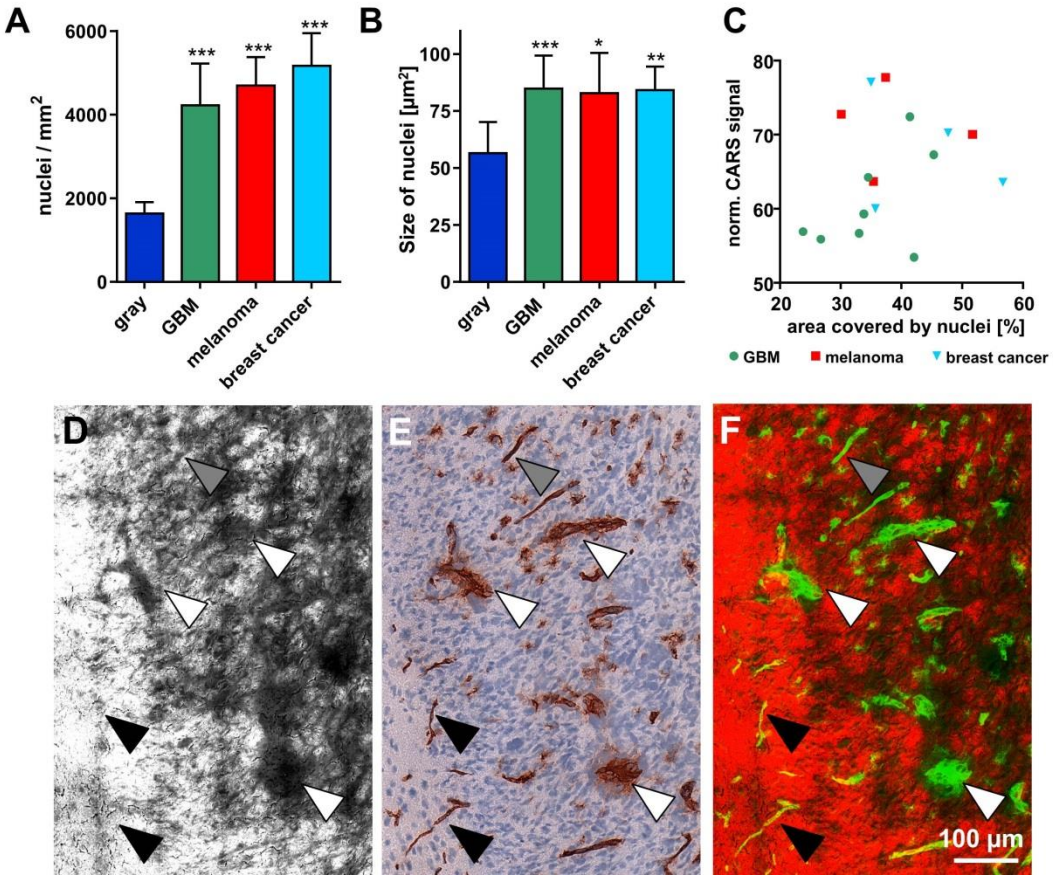

Figure 24. Influence of tumor-induced alteration of brain tissue on CARS signal intensity. A/B: Number of nuclei/mm^2 representing cellular density (A) and size of single nuclei (B) within normal gray matter and different experimental tumors in a mouse brain. Bars represent mean ± SD, GBM n = 8; melanoma metastases n = 4; breast cancer metastases n = 4; *** significant difference vs. normal gray matter: P<0.001. C: Dot plot showing the total area occupied by cell nuclei vs. the normalized CARS signal intensity of the respective tumor. D: CARS image of an experimental GBM induced in a mouse brain. E: Anti-CD31 staining of a consecutive section of the one shown in D. F: Overlay of CARS (red) and anti-CD31 (in false color: green). Coarse blood vessels (white arrowheads) and fine blood vessels (gray arrowheads) are detected in the CARS image. Very fine (normal) blood vessels do not cause any alterations of the CARS signal (black arrowheads).

sectional area covered by cell nuclei and average CARS signal intensity did not show the correlation.

The proliferative behavior of cells is different in neoplastic tissue than that in normal tissue. In tumors investigated in this work, proliferation patterns were varying. For example, in Fig. 21 (C) upper left, an uneven and discontinuous distribution of Ki67-positive and -negative nuclei is seen, while in large tumor island in the same Fig. 21 (C) almost all nuclei showed positive for Ki67. CARS image and anti-Ki67 immunohistochemical staining image of the same cryosection were compared at a cellular level. However, it was found that the CARS signal is reduced in the same manner among the whole micrometastasis [Fig. 21 (A) inset and Fig. 21 (B)]. The proliferation index was also determined for each tumor, however it did not show correlation with the CARS signal reduction (Fig. 25).

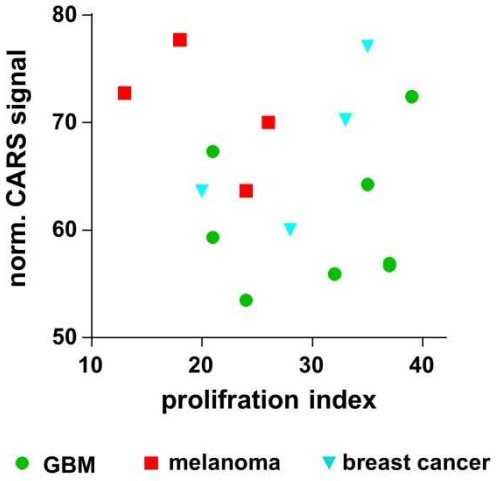

Figure 25. The decline of CARS signal intensity is not related to the tumor's proliferation rate. Dot plot showing the proliferation index of each tumor investigated vs. the normalized CARS signal intensity of the respective tumor.

Tumor growth and development is followed by tumorigenic alterations of brain microvessels: they tend to become coarse and irregular. Fig. 24 (D) and Fig. 24 (E) show and compare CARS image and corresponding anti-CD31 immunohistochemical staining, respectively, of a tumor, which infiltrates white matter. The reduced CARS signal tend to match the positions of the coarse and

highly altered blood vessels (white arrows). The fine and almost normal appearing blood vessels in the tumor (gray arrows) are as well detected due to lower CARS signal intensity, while the very fine blood vessels in normal brain tissue are not apparent in the CARS image (black arrows). CARS image and image of corresponding region, where CD31-positive blood vessels are depicted, are overlaid and shown in false colors in Fig. 24 (F) (red and green color representation for CARS and blood vessels, respectively). One may expect that those tumors, which are characterized by highly transformed and coarse blood vessel network would demonstrate a lower overall CARS signal intensity. Microvessel density and micromorphology was analyzed in all tumors. In all of them, the similar degree of microvessel network transformation towards coarse and irregular phenotype was observed. Namely, the vascular index for GBM, melanoma metastases and breast cancer metastases is found to be 2.71, 2.75 and 2.65, respectively. The microvessel density was rather similar in GBM (154.9/mm^2) and melanoma metastases (153.6/mm^2), but was lower in breast cancer metastases (87.9/mm^2). However, this did not show correlation with the degree of CARS signal decrease within corresponding tumors (Fig. 26).

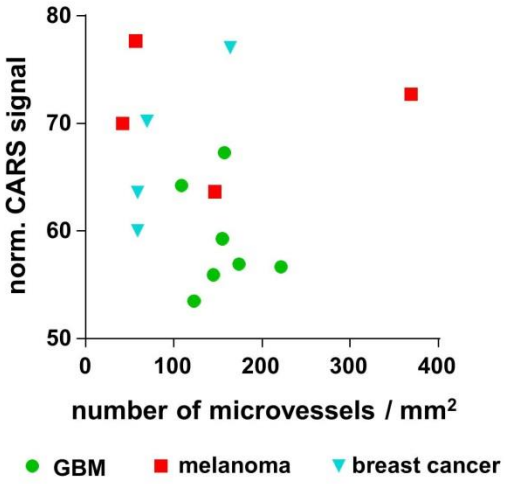

Figure 26. Dot plot showing the microvessel density of each tumor investigated vs. the normalized CARS signal intensity of the respective tumor. The decline of CARS signal intensity is not related to the tumor's microvessel density.

As discussed above, the decrease of CARS signal intensity was found to be related to tumor-induced alterations of cyto- and tissue morphology, e.g. nuclear size and density as well as blood vessel transformation. However, a correlation to the decrease of CARS signal intensity was not present with any of the related histopathological parameters alone. The quantity of lipid-rich structures in tumor is probably inherently different from that of gray matter. As a matter of fact, this presumption is supported when taking in account the following observations: (i) CARS signal intensity is always lower in tumors, while its relevant reduction is not observed in other nuclear-rich structures (as in the case of the normal hippocampus, see Fig. 20 B/F and D/H, arrowheads); (ii) the CARS signal intensity is lower in cytoplasmic regions of tumor cells than in the gray matter (see Fig. 21 A/B). Therefore, most likely not only presence of lipid-poor components, but also a common biochemical lipid-reduced characteristic of tumor tissue contribute to the reduction of CARS signal intensity. Important to mention that this conclusion is restricted to the experimental setting used in this work and in this work investigated brain tumors and needs further verification by studies of a bigger scope. Nevertheless, this observation might make sense, when taking in account the altered metabolism and signaling pathways in tumor cells [184].

CARS microscopy of human Glioblastoma Multiforme

The samples of human GBM tumors, which were obtained during routine biopsy test, were investigated by CARS microscopy. CARS images of human GBM tumors, as seen in the one example shown in Fig. 27 (A), were of similar characteristics as those of brain tumors grown in mouse model. In particular, CARS signal intensity values are lower in tumor region than in surrounding normal brain tissue. The changes of CARS signal intensity values were also sufficient for discrimination between tumor, tumor infiltration region and normal tissue [Fig. 27 (B)]. CARS intensity values within these tissue regions fall

in separated ranges, which is in agreement with the results obtained by investigation of mouse tumors (see Fig. 22). It was shown by quantification [Fig. 27 (C)] that in all investigated samples of human GBM, the tumor could be characterized by reduced of CARS signal intensity compared with surrounding almost normal brain tissue. The average CARS signal intensity in human GBMs was found to be to 72.2 ± 8.8% (n=6, P<0.005), when compared with gray matter (100%). Therefore, in all human primary brain tumors, CARS microscopy

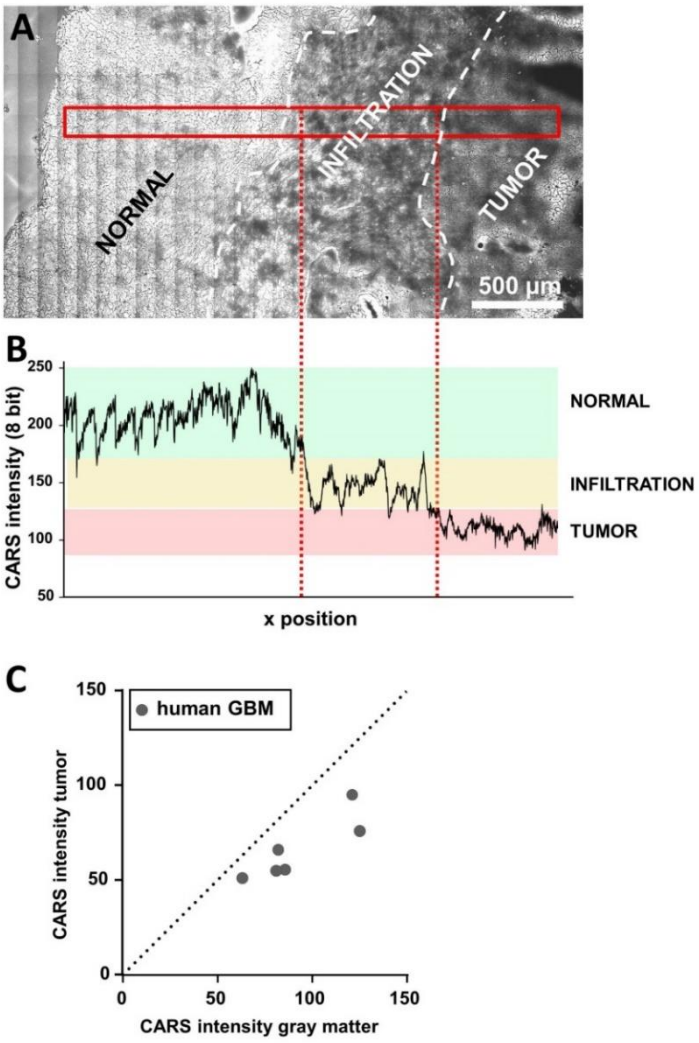

Figure 27. Quantification of the CARS signal in human GBM. A: An unprocessed CARS image of a cryosection of a human GBM specimen, which was obtained during routine surgery. The margin of a solid tumor and an infiltrative region can be readily distinguished in CARS image. B: CARS signal intensity along the area indicated in panel A. The range of CARS signal intensity of normal tissue is underlined in green, of infiltrative areas in yellow, and of tumor in red, respectively. C: Dot plot showing the CARS signal intensity in normal gray matter vs. the intensity of the CARS signal in human GBM for various GBM samples.

provided morphochemical contrast to delineate tumors and their margins in totally label-free manner.

3.2.4 Conclusions

1. Morphochemical contrast of CARS images enables to discern brain tumors from the normal parenchyma of both primary and secondary brain tumors irrespective from characteristics of these tumors.
2. Tumor margins, infiltrations and small tumor islands can be identified with cellular resolution due to lower intensity values of CARS signal in tumor than in normal brain parenchyma. The reduction of CARS signal intensity is more pronounced in glioblastoma than in metastases. The decrease of CARS intensity is related with the decrease of total lipid content in tumors as confirmed by Raman spectroscopy.
3. Significant correlation between independent tumor-induced cytological changes and the degree of CARS signal intensity reduction was not found.

3.3 Vibrational microspectroscopic imaging and multimodal CARS microscopy for biochemical monitoring of spinal cord injury treatment

3.3.1 Research background and motivation

Traumatic spinal cord injury is a complicated condition with highly devastating neurological dysfunction outcomes for the patient. The traumatic SCI leads to complex biochemical changes, which eventually cause the inhibition of CNS nervous tissue regeneration. Briefly, the initial trauma of spinal cord is associated with immediate necrotic cell death and vascular damage. The secondary damage is following with cascade of events, including inflammation, edema and ischemia, which lead to indirect additional cell death, demyelination and axonal degeneration. These secondary mechanisms result in further loss of nervous functions [185]. A fibrous meshwork of scar tissue composed of reactive astrocytes, proteoglycans and extracellular matrix is also formed during this cascade [186]. It is well known that such fibrous scar results in formation of an inhibitory barrier for axonal regrowth [187].

Inflammatory response to spinal cord trauma leads to accumulations of activated microglia and macrophages, which remove myelin debris. Namely, to remove the myelin fragments, microglia transforms into large phagocytes, while invading macrophages migrate from the blood through disrupted blood-brain barrier into the injured region of the spinal cord [188]. As myelin is of very high lipid content, in demyelinated lesions, the inflammatory cells engulf large amounts of these myelin derived lipids. These cells become lipid-enriched and develop distinctive morphology of foam cells [189]. Foam cells develop from both activated microglia and infiltrating macrophages [190].

It is well known that the main components of cytoplasmic lipid droplets, which are present in foam cells, are lipid esters surrounded by a phospholipid monolayer. However, the processes involved in lipid metabolism within activated microglia/macrophages are of complex nature. As a result, despite

that lipid metabolism was addressed in several studies, the results are still not complete and partly contradictory [191,192]. Analysis of histological staining in several studies revealed that macrophages in SCI contain myelin [193,194]. *In vitro* studies demonstrated that macrophages, which were incubated with myelin, transformed into foam cells heavily laden with intracellular droplets of myelin. Still, the neutral lipids were also present [189]. Many studies showed that the composition of lipid droplets in foam cells is strongly influenced by the types of lipids, which were engulfed by the cell. For example, depending on the culture media composition *in vitro* cultured macrophages accumulated saturated fatty acids, unsaturated fatty acids [195], triglycerides [196] and cholesteryl fatty acid esters [197]. As shown *in vitro*, microglia activation results in accumulation of lipid droplets and triglyceride biosynthesis [198].

As a result of wide range of heterogeneous events following the traumatic damage, the ability to regenerate of mammalian tissue of spinal cord is almost completely limited. However, it was already reported that also axons of the central nervous tissue can overcome the inhibitory cues [199] and can potentially regenerate if an appropriate environment is provided [200]. The design of a permissive and promoting environment, which direct and support the transverse of axons through the injury site, plays and important role in the research of the new SCI treatment therapies [20]. There were encouraging studies reporting the treatment approaches, which take advantage of using the growth and neurotropic factors [201–203] or neuroprotective and neutralizing drugs [204–206] as well as engineering approaches using biomaterials [207].

The hydrogels belong to the space-filling biomaterials with the potential to provide permissive environment for axonal regeneration. Hydrogel polymers are biocompatible, biodegradable, have tissue-like mechanical properties [208–210]. They also hold the ability to be functionalized in such a way that neuroprotective or neurotropic factors could be co-delivered at the injury region [211]. The hydrogel structure can also be engineered to adapt its

degeneration rate and porosity to match the requirements for effective axonal guidance. Such physical properties as stiffness, permeability, swelling and strength can be modulated [208–210].

One of the promising candidates to be used as a scaffold for axonal regeneration is alginate hydrogel. Alginate is a natural biopolymer, namely, linear polysaccharide, typically obtained from brown algae. It is composed of blocks of (1,4)-linked β-D-mannuronate (M) and α-L-guluronate (G) residues. The structure of these blocks can be either consecutive G residues, consecutive M residues or alternatively varying G and M residues [212]. In aqueous solutions, it forms hydrogels by physical interaction of polymer chains via ionic cross-linking by multivalent cations. It is generally considered that the blocks of only G residues are responsible to form intermolecular cross-linking. Therefore, the physical properties of alginate and from it derived hydrogels are highly dependent on its structural composition (i.e. M/G ratio), M and G sequence, G-block length, and molecular weight [213]. Soft alginate hydrogels are those with gelation of no more than 10% of gelation sites.

It was already reported that alginate hydrogel implants possess a potential to provide a supporting platform for the outgrowth of regenerating axons [214]. Since the first experiments over a decade ago, alginate hydrogels functionalized with signaling molecules and used as implantable scaffolds were found to boost the elongation of regenerating axons [214,215]. Different research groups were mainly focusing on functionalization of alginate hydrogels to form composite structures [216,217] and incorporated neurotrophic [218–221] or neuroprotective agents [222–224]. Interestingly, recently it was also demonstrated that soft alginate hydrogels formed by crosslinking with Ca^{+}, Ba^{2+} or Sr^{2+} possess the ability to act as neurotrophic and neuroprotective intrinsically, i.e. without the need of any functionalization. It was, for example, shown that unfunctionalized soft alginate hydrogels, which were produced via crosslinking with Ca^{+}, not only support neurite growth *in vitro*, but also protect

neuronal cells against oxidative stress [225]. Soft alginate hydrogels were also demonstrated to maintain their mass and volume after immersion in saline solution, which makes them interesting candidates for *in vivo* applications [226].

3.3.2 Sample preparation and experimental details

Alginate hydrogel implants

Low viscosity sodium alginate (Pronova up lvm, Novamatrix, Sandvika, Norway) was used to prepare alginate hydrogel implants. The ratio of guluronic acid to mannuronic acid building blocks of alginate was 1. To prepare a 4% alginate solution, it was stirred for 12 h in deionized water and afterwards sterile filtrated using a 0.45 µm filter. 700 µl of this solution was transferred to a petri dish (ø 6 cm) and incubated at room temperature. Then it was overlaid with 10 ml crosslinking solution which was composed of 4 mM $CaCl_2$ and 150 mM NaCl and incubated at room temperature. After 12 h, the crosslinking solution was removed and the produced samples were overlaid until utilization with 10 ml solution which contained 2 mM $CaCl_2$ and 150 mM NaCl. The rheological measurements of the particular alginate hydrogel were performed as explained

in Ref. [225]. To produce the implants for spinal cord, the hydrogel was manually cut in blocks with dimensions 2 mm × 2 mm × 1.5 mm.

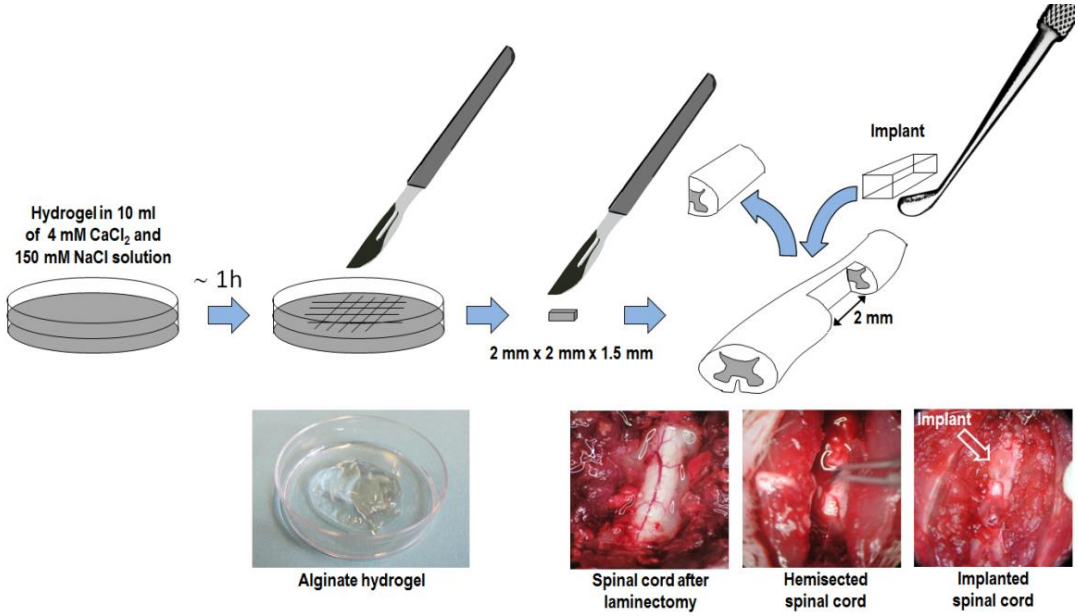

Figure 28. Workflow of implantation procedure. After cross-linking, the alginate hydrogel in a 6 cm dish is overlaid with a 10 ml of 4 mM $CaCl_2$ and 150 mM NaCl solution; within 1 h it is removed from the dish and manually cut in blocks with dimensions of 2 mm x 2 mm x 1.5 mm using a scalpel. The spinal cord is exposed by laminectomy and a 2 mm long and 1.5 mm deep hemisection is produced; the hydrogel block is inserted in the hemisection with the help of a surgical micro-spoon.

Animal experiments

28 female Wistar rats, aged 16 weeks and weighting between 200 g and 250 g, were used. The workflow of alginate hydrogel implantation procedure is shown in Figure 28. Rats were anesthetized and a hemisection at the level T9 of the thoracic vertebrae of the spinal cord was surgically induced under a surgical microscope. The left side of the spinal cord was bisected along a medial longitudinal plane for a length of 2 mm as described earlier [227]. 14 randomly selected rats received alginate hydrogel into the lesion. The blocks of alginate hydrogel were transferred to the animal using a surgical micro-spoon spatula and delivered in the hemisection. No therapies were attempted for the remaining 14 rats (control animals). The musculature and the thin superficial muscle layer were closed and animals were allowed to recover on a commercial

electric heating pad. Seven rats of the control group and seven rats with alginate implant were perfusion-fixed using 4% (w/v) paraformaldehyde in tris-buffered saline at one and six months after surgery. The spinal cords were isolated and cryoprotected in rising sucrose concentration (10% (w/v) for 24 h and 30% (w/v) for 24 h), embedded in tissue freezing medium (Leica, Nussloch, Germany) and frozen on dry ice. Finally, 16 µm thick longitudinal cryosections were prepared on CaF_2 slides or on glass slides. The cryosections were 20 mm long and the lesion was located roughly in the center. Cryosections were stored at −20°C until use.

FTIR spectroscopic data acquisition

15× Cassegrain objective (0.4 NA) imaged an area of 175 µm × 175 µm. The radiation was collected by a 64 × 64 MCT focal plane array detector. 8 × 8 binning was applied and the spectral resolution was set to 6 cm^{-1}. A background spectrum was recorded on a clean position of the CaF_2 slide. Composite images of several square millimeters depending on the sample size (max. 116 × 18 fields of view, 20.4 mm × 3.2 mm) were captured in an automatized step-wise manner by moving the sample stage. For each pixel, 8 interferograms were collected, co-added and Fourier transformed by applying Blackman–Harris apodization and zero filling factor of 0. Each spectrum was ratioed to the background spectrum and the transmission spectra were converted to absorbance values.

Reference spectra of pure materials

The reference alginate hydrogel sample was prepared by embedding, freezing and sectioning; 16 µm thick cryosections were placed on a CaF_2 slide. The reference spectrum of collagen was acquired from collagen IV from human placenta (Sigma−Aldrich, Steinheim, Germany). The reference spectrum of sucrose was acquired from sucrose solution dried on a CaF_2 slide. Reference

spectra were collected in transmission mode with a single-channel MCT detector using the same acquisition parameters as for imaging of spinal cord samples.

FTIR data processing and analysis

An atmospheric compensation was calculated to subtract contributions of residual water vapor bands from the spectra. FTIR data was then reduced to the fingerprint region (900– 1800 cm^{-1}) and baseline corrected in OPUS 7.2 (Bruker Optic GmbH, Ettlingen, Germany).

Further processing and analysis were performed using Matlab Packages (version 7, Math Works Inc. Natick, MA, USA). The integral intensity of the amide I band was calculated in the spectral range 1633–1673 cm^{-1} and used as a marker to identify the tissue. Spectra of embedding medium and of the CaF_2 slide displaying absorbance value of amide I<0.3 were excluded. The selected spectra were vector normalized.

A semi-quantification of lipid content was based on the integral intensities calculated in the following spectral ranges: 1218 – 1232 cm^{-1}, 1459 – 1473 cm^{-1} and 1728 – 1742 cm^{-1}. ROIs of 0.2 cm^2 were chosen contralateral to the lesion. Mean band intensities were normalized to the intensities calculated the same white matter tract caudal to the lesion (4.5 mm away from the hemisection center).

To assess the extension of the scar, the intensity values of the spectral band at 1242 cm^{-1} were calculated along a line crossing the scar center. Pixels with intensity values above the background of the nervous tissue were assigned to fibrous tissue and used to evaluate the thickness of the scar (Fig. 29).

Data is expressed as mean ± SEM. For comparison of control and alginate group, a two-tailed t-test was performed using Graph Pad Prism 6.0 (Graph Pad Software Inc., La Jolla, CA, USA).

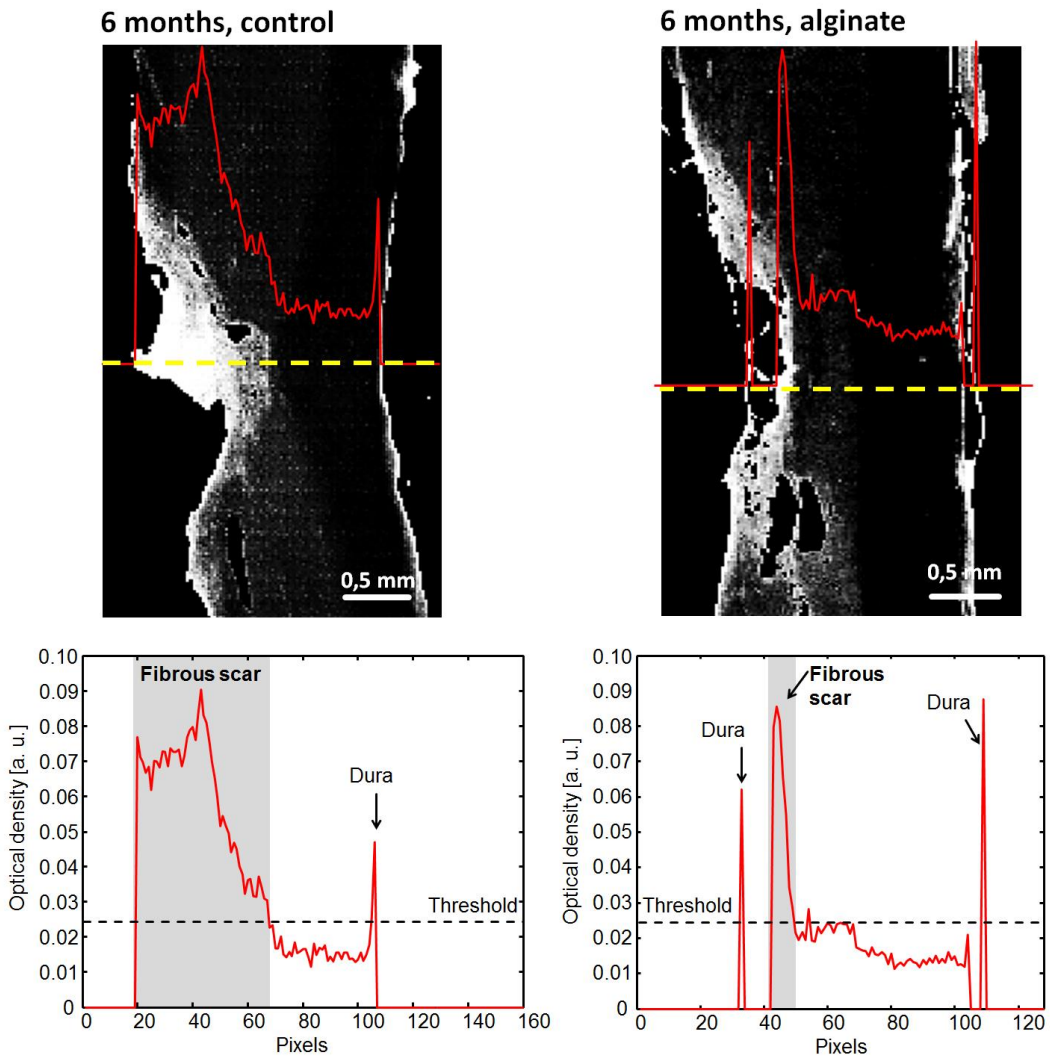

Figure 29. Assessment of scar extension. The intensities of the spectral band at 1242 cm^{-1} were used to retrieve the distribution of collagen in the cryosection (here displayed as gray scale image). The intensity profile (shown in red) was calculated along a line crossing the scar center (dotted yellow line). Pixels characterized by an intensity values above the threshold of 0.025 (corresponding to the maximum background value of the nervous tissue among all samples) were assigned to fibrous tissue and used to evaluate the thickness of the scar. The dura left at the sample borders was excluded from the calculation.

Raman spectroscopic data acquisition

The Raman scattering was collected in reflection configuration. Raman spectra were acquired in the range 150 to 3250 cm^{-1}. The spectral resolution was 4 cm^{-1}. An integration time of 750 ms and two accumulations were used for spectra acquisition. Maps were recorded with a step size of 23 µm both in x and y directions.

Raman data processing and analysis

The datasets were imported in MATLAB (MathWorks Inc., Natick, Massachusetts). The spectra were reduced to the region 450 to 1800 cm^{-1}. A variable baseline was calculated for each spectrum (function "msbackadj" of the MATLAB Bioinformatics Toolbox) and normalization was obtained by standardizing the area under the spectra (function "msnorm" of the MATLAB Bioinformatics Toolbox).

Cluster analysis (function "kmeans" of the Statistical Toolbox) and band intensities were used to obtain biochemical tissue maps. In the study concerning assessment of inflammation, Raman maps were generated by plotting the intensity of selected bands. The band intensities were calculated as the area under the curves in the following range: 1375 to 1455 cm^{-1} (for evaluation of lipids) and 1728 to 1758 cm^{-1} (for evaluation of lipid esterification). Principal component analysis was performed on a dataset formed by the spectral data of all samples. The function "pca" of the Statistics and Machine Learning Toolbox of MATLAB was used. The score values were reassembled and used to plot the intensity maps of each sample.

Multiphoton microscopy

The laser beams were focalized on the samples by a 20 ×⁄1.0 water immersion objective. Using non-descanned detection, CARS (band-pass filter 633 to

647 nm) and SHG signals were collected in transmission, while endogenous TPEF in the range 500-550 nm was acquired in reflection. CARS and TPEF images were merged using complementary colors (CARS: magenta, TPEF: green) to comply with color perception deficiencies [228].

3.3.3 Results and discussion

3.3.3.1 FTIR microspectroscopic imaging

General overview of the samples

IR imaging was performed on longitudinal cryosections of 28 rat spinal cords. For general representation of the sample structure, the IR spectroscopic maps shown in Fig. 30 (A) were obtained by calculating the integral intensity of the Amide I band at 1653 cm^{-1}. The overall distribution of proteins and, therefore, morphological structure of the spinal cord samples are represented. Different kinds of tissue can be readily recognized: tracts of white matter are indicated by a lower Amide I band intensity (light blue and green pixels) compared with grey matter characterized by a higher Amide I band intensity (yellow and red pixels). The injury regions of the spinal cord tissue can be distinguished, as the typical structure of alternating strands of gray and white matter is notably disrupted at the lesion site. As seen in Fig. 30, the lesion position is located approximately in the center of the samples. Large cysts developed anterior and/or posterior to the lesion center and cover up to approximately 2 mm [asterisks in Fig.30 (A)]. For reference, the tissue morphology in Fig. 31 is shown by H&E stained consecutive sections.

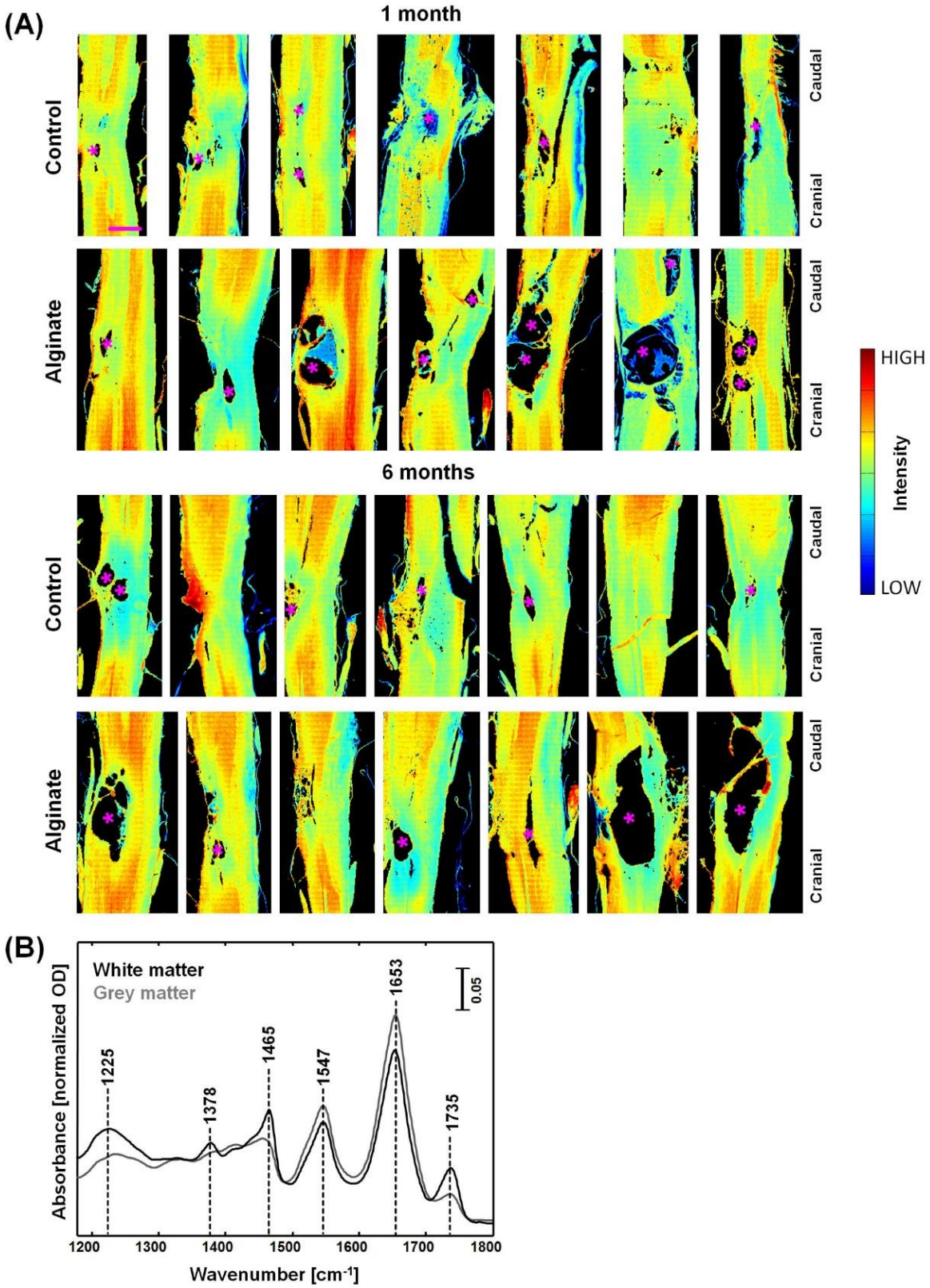

Figure 30. IR spectroscopic imaging of SCI in rat models with and without alginate hydrogel implant at one and six months post-injury. (A): Spectroscopic images of longitudinal cryosections of the investigated samples, showing the intensity of the amide I band at 1653 cm^{-1}; asterisks (*) indicate large cysts. Scale bar: 1 mm. (B): Representative IR absorption spectra of white and grey matter.

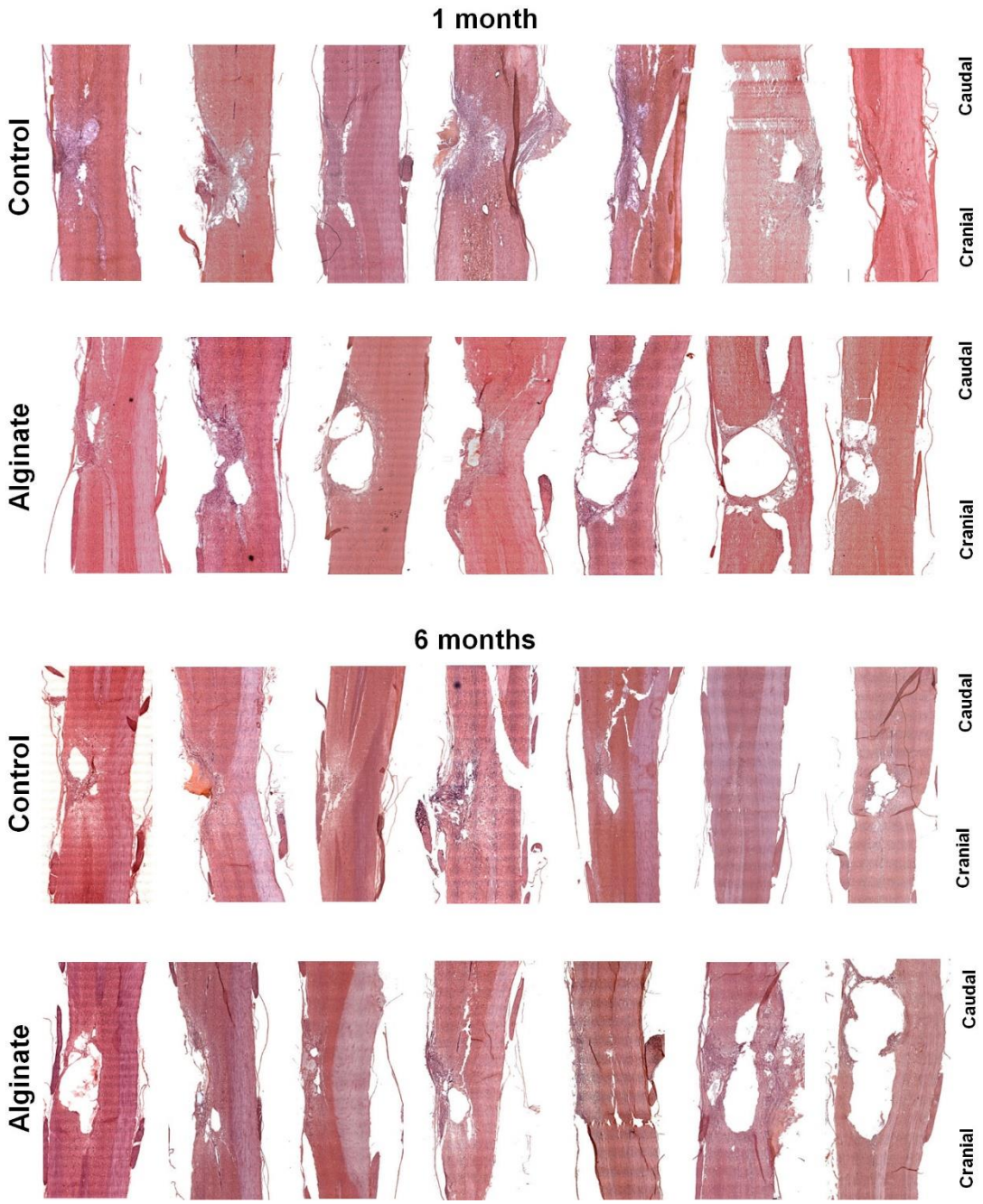

Figure 31. H&E stained sections of SCI in rat models with and without alginate hydrogel implant at one and six months after injury.

The use of sucrose during the preparation of the samples for cryoprotection was important in order to preserve structure and morphology of the tissue. However, the IR spectra in the spectral region 900 – 1180 cm^{-1} of rat spinal cord samples investigated in this study were strongly overwhelmed by spectral contributions of sucrose. Fig. 32 shows the spectrum of reference sucrose compared with those of white and gray matter of cryoprotected spinal cord tissue. The tissue biochemistry representing spectral contributions in the spectral region at 900 – 1180 cm^{-1}, where C—O stretching modes of sucrose [229] contribute predominantly to the IR absorption, cannot be retrieved. Therefore, the spectral region 900 – 1180 cm^{-1} was excluded from all analysis of IR spectral data.

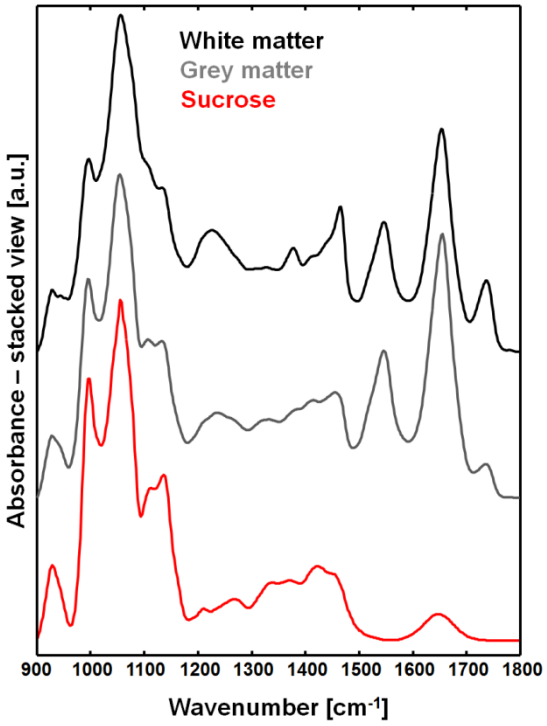

Figure 32. Representative IR spectra of white and grey matter and IR spectrum of sucrose. In the spectral region comprised between 900 and 1180 cm^{-1}, the spectral contributions of nervous tissue is overwhelmed by the contribution of sucrose.

Fig. 30 (B) shows representative IR spectra of white and grey matter in 1180 – 1800 cm^{-1} spectral region. The most prominent spectral contributions of rat spinal cord tissue are at 1653 cm^{-1} and 1547 cm^{-1}, corresponding to

Amide I and Amide II, respectively. These are the characteristic vibrational modes of proteins and polypeptides. The lipid-related spectral bands are more prominent in white matter, which is predominantly composed of myelinated axons compared with grey matter mainly composed of neuronal cell bodies with only few myelinated axons. Myelinated axons possess high content of cholesterol and phospholipids [230]. The spectral bands, which are mainly due to molecular vibrations of cholesterol and phospholipids, are at 1225, 1378, 1466, 1735 cm^{-1}, corresponding to $\nu_{as}(PO_2^-)$, $\delta[(CH_3)]$, $\delta[(CH_2)]$, $\nu_s(C=O)$ molecular vibrations, respectively [23,231].

Demyelination

The degree of axonal degeneration and, on the other hand, the axonal regeneration potential are strongly influenced by the alterations of lipid content, which follows SCI [232]. The primary decrease of total lipid content is due to the damage of neuronal membranes and lipid peroxidation, caused by ischemia [233]. The further decrease of lipids proceeds in the secondary phase of SCI, as the demyelination of the nervous tissue adjacent to the site of injury progresses further [234].

To address the influence of the soft Ca^{2+}-alginate hydrogel implant to myelin alterations in damaged spinal cord tissue, the distribution of the lipids in and around the damaged tissue was investigated by addressing the spectral bands that are attributed to lipids. For example, integral intensity maps of spectral band at 1735 cm^{-1} [$\nu_s(C=O)$] generated for all the samples are shown in Figure 33. The general distribution of lipids can be readily observed within longitudinal spinal cord tissue sections in false-color IR maps: because of different lipid content, white matter is localized by red/yellow pixels and grey matter by green pixels, whereas lesion core is severely depleted of lipids (blue pixels).

Alternating streaks of white and gray matter represent gross and typical morphology of longitudinal sections of spinal cord.

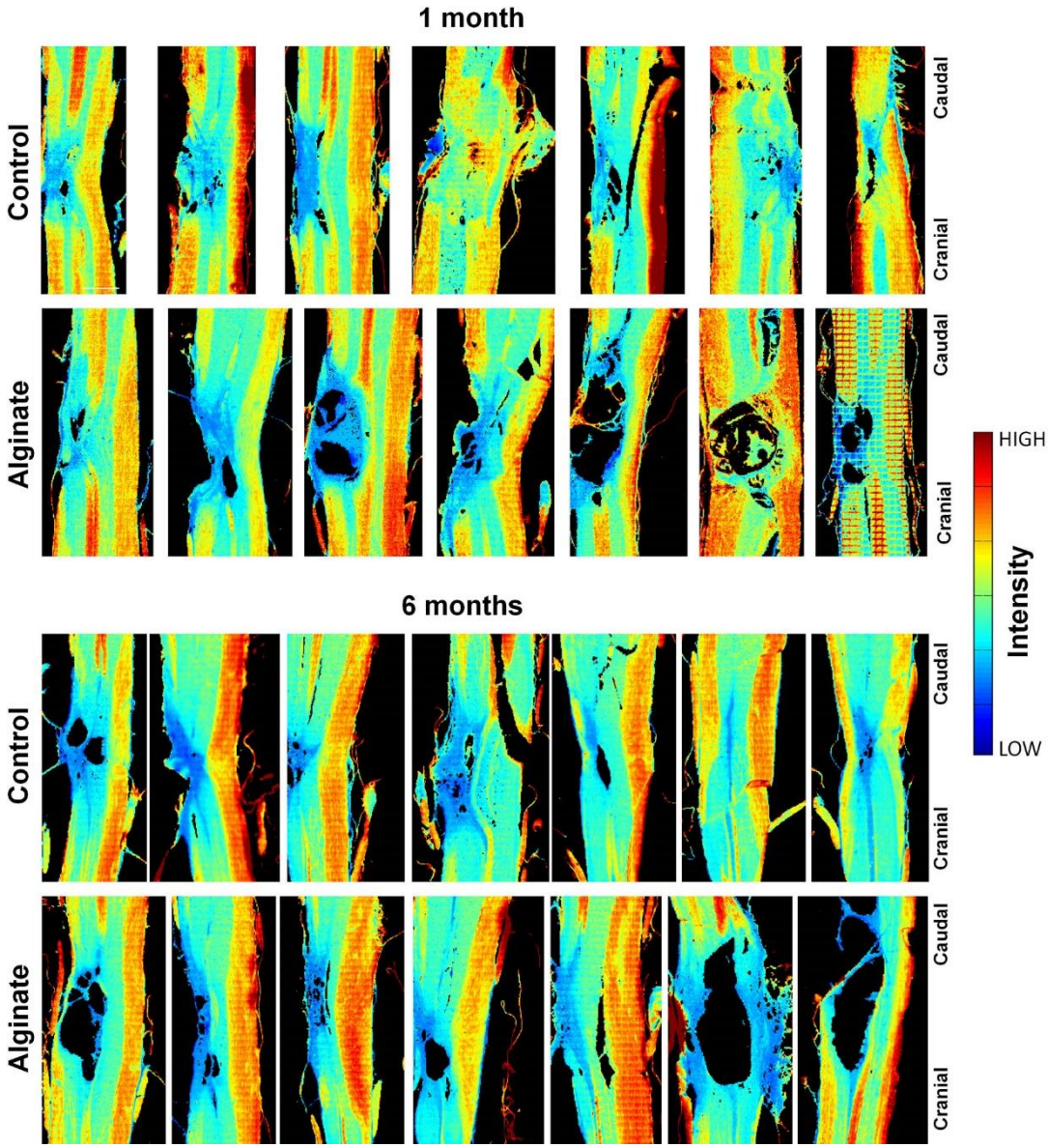

Figure 33. Analysis of the contralateral nervous tissue. IR spectroscopic images of SCI in rat models with and without alginate hydrogel implant at one and six months after injury, obtained plotting the intensity of the lipid-related band at 1735 cm^{-1}.

Importantly, the generated spectral maps enabled to observe regions with decreased lipid content in the white matter contralateral to the lesion. This reduced lipid content indicate indirect to initial mechanical damage, but injury-induced, demyelination. To better illustrate the observed demyelination,

the selected representative examples from Figure 33 are demonstrated in Figure 34 (A) for each group of samples. Here, the integral intensities of 1735 cm^{-1} spectral band in the regions indicated by black boxes, i.e. in contralateral tract of white matter just across from the injury center, were lower than the intensities of the same tract distant from the lesion (indicated by white boxes).

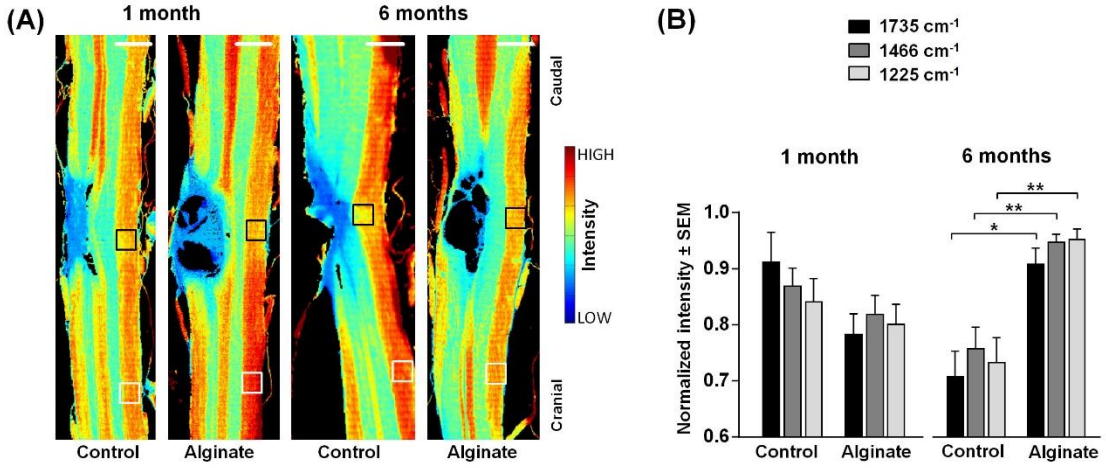

Figure 34. Analysis of the contralateral nervous tissue. (A) Spectroscopic images showing integral intensity of the band at 1735 cm^{-1} [ν_s(C = O)]. They depict the distribution of lipids in control and alginate-implanted samples at one and six months post-injury. Scale bar: 1 mm. (B) Intensities of the bands at 1735 cm^{-1}, 1466 cm^{-1} (δ[(CH_2)], also showing the distribution of lipids) and 1225 cm^{-1} ($\nu_{as}(PO_2^-)$, showing the distribution of phospholipids) in the white matter contralateral to the lesion indicated by the black boxes in panel A normalized for each samples to the intensity in the region indicated by white boxes in panel A. For each group n = 5–6. Two-tailed t-test, *: $p < 0.05$, **: $p < 0.01$.

More accurate inspection of spectroscopic images in Fig. 33 and Fig. 34 suggests the different severity of demyelination between control and alginate samples. To further evaluate the effect of alginate hydrogel implant for severity of injury-induced demyelination of the contralateral white matter tract, not only the intensity of spectral band at 1735 cm^{-1}, but also of other two lipids-representative bands, namely at 1225 cm^{-1} and 1466 cm^{-1}, in all groups of the samples were analyzed [Fig. 34 (B)]. Even though that the intensities of all lipid-related spectral bands were decreased in contralateral tract of white matter just in front of injury center compared with the intensities distant from

the lesion center in all groups of the samples, this decrease was of the different extent. No significant difference between the control and alginate groups was found in one month after injury removed spinal cord samples. However, the significantly higher intensities of above noted lipid-related spectral bands were calculated in six months post-injury samples with alginate hydrogel implants. Particularly, the two-tailed t-test, which results are shown in diagrams in Figure 34 (B), gave the values of $p = 0.019$, $p = 0.0095$ and $p = 0.0095$ for 1735 cm^{-1}, 1466 cm^{-1} and 1225 cm^{-1} IR absorption spectral bands, respectively.

It is known that in rat SCI model, the degradation of contralateral white matter, which includes demyelination and affects function, occur at the chronic stage (secondary stage) of the hemisection injury [235,236]. The above discussed findings suggest that the presence of non-functionalized Ca^{2+}-alginate hydrogel has a positive impact for the presence of myelin in contralateral white matter in chronic stage of SCI. This positive impact may be either reduced demyelination or improved axonal remyelination or a combination of both. The explanation for possible neuroprotectory function of soft non-functionalized Ca^{2+}-alginate hydrogel used in this study might be following. Extracellular ions are released after the nervous tissue damage and trigger excitotoxicity and apoptosis. In such extracellular ions rich media implanted alginate hydrogel may act as a buffer for these ions. This theory is supported by the study, which showed that alginate hydrogel incubated in cerebrospinal fluid-like media is highly sensitive to Ca^{2+} [216]. The case of increased remyelination may be related to the reduction of axonal growth inhibitory molecule chondroitin sulphate proteoglycan (CSPG). Actually, one study demonstrated that CSPGs were reduced upon presence of alginate hydrogel implant in the spinal cord contusion injury [237].

Fibrotic Scarring

The ongoing formation of scar tissue is an indication for continuing laceration of SCI. SCI scar tissue is categorized into glial scar and fibrotic scar. While the glial scar is usually related to astrogliotic region formed around the injury center, the fibrotic scar comprises a dense extracellular matrix, which main constituent is collagen IV and which creates a barrier for regenerating axons. The suppression of fibrous scar is thus profoundly addressed in therapeutic strategies for SCI treatment [186].

The IR spectral fingerprint of fibrous tissue in rat SCI compared with spectrum of healthy grey matter is shown in Fig. 35. In IR spectrum of fibrotic tissue, several bands observed in the spectral region of 1200 – 1450 cm^{-1} are attributed to collagen, when compared with reference spectrum of pure collagen. More precisely, the spectral bands at 1205, 1242, 1282 and 1338 cm^{-1} are all assigned to Amide III vibrations, the band at 1406 cm^{-1} is attributed to $\delta(CH_3)$ vibrations and the band at 1453 cm^{-1} corresponds to $\delta(CH_2)$ and $\delta(CH_3)$ vibrations [238,239]. Other spectral features in the spectrum of the fibrotic lesion that are consistent with the IR absorption of collagen are a shift of the Amide II band to 1554 cm^{-1} and a shoulder of the Amide I band at 1634 cm^{-1}. Therefore, as these contributions are very prominent in the spectrum of fibrotic lesion and the spectrum of fibrotic scar corresponds more to the spectrum of collagen as to that of nervous tissue [compare all the spectra in Fig. 35 (A)], collagen is the main component in SCI-induced scar tissue. Nevertheless, some minor contributions can be observed in the spectral region 1200 – 1500 cm^{-1} and at 1735 cm^{-1}. These minor contributions are presumably due to the IR absorption of glial scar. As other studies report, the formation of glial scar that includes reactive gliosis and upregulation of CSPGs is most likely taking place simultaneously with the formation of dense collagen meshwork [101].

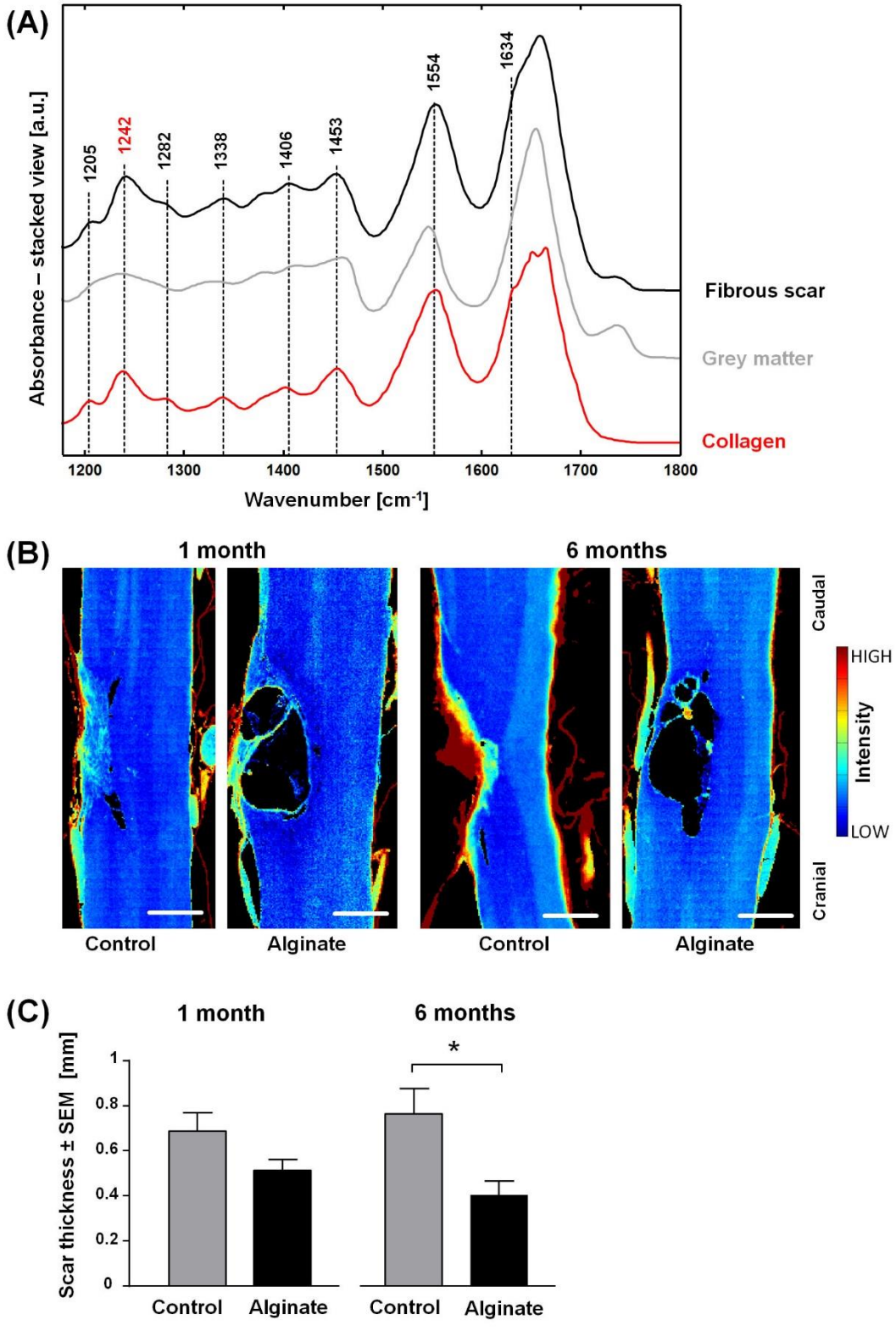

Figure 35. Analysis of the fibrotic lesion. (A): Representative IR spectra of the fibrous scar at six months post-injury, of healthy grey matter and of reference collagen. (B): Pseudo-color spectroscopic images showing the integral intensity of the band 1242 cm^{-1}. They depict the distribution of collagen in control and alginate-implanted samples at one and six months post-injury. Scale bar: 0.5 mm. (C): Fibrous scar thickness of control and alginate-implanted samples at one and six months post-injury, n = 5–7, two-tailed t-test, *: $p < 0.05$.

The spectroscopic images demonstrating the location and extension of the nervous tissue scar are shown in Fig. 36. Here, the spectral band of collagen at 1242 cm^{-1} was selected to calculate its integral intensity and to analyze the scarring and effects of alginate hydrogel implant for extent of fibrous scar that formed at the lesion site after SCI. As the CNS nervous tissue naturally barely contains collagen, the chemical contrast in IR spectral maps allows to localize the collagen in the lesion region of all samples and show varying amounts of it. It can be better observed in selected examples of each group of the samples in Fig. 35 (B) that the fibrous scar has developed in the core of the injury, as in agreement with other studies [186]. The meningeal tissue at the borders of the spinal cord also consists high content of collagen. It can be identified in all IR integral intensity maps of 1242 cm^{-1} spectral band and thus confirm the applicability of this band as the spectral marker to address collagen.

Spectral images of collagen revealed that, while the lesion region of the spinal cord tended to be extensively filled by the fibrous tissue in control samples, the samples with alginate hydrogel implants tended to contain only thin layers of collagen enclosing the cysts. For example, as can be seen in Fig. 35 (B), the six-months control sample contains thick chunk of collagen compared with almost undetectable layer and small lump of collagen in the six-month alginate-implanted sample.

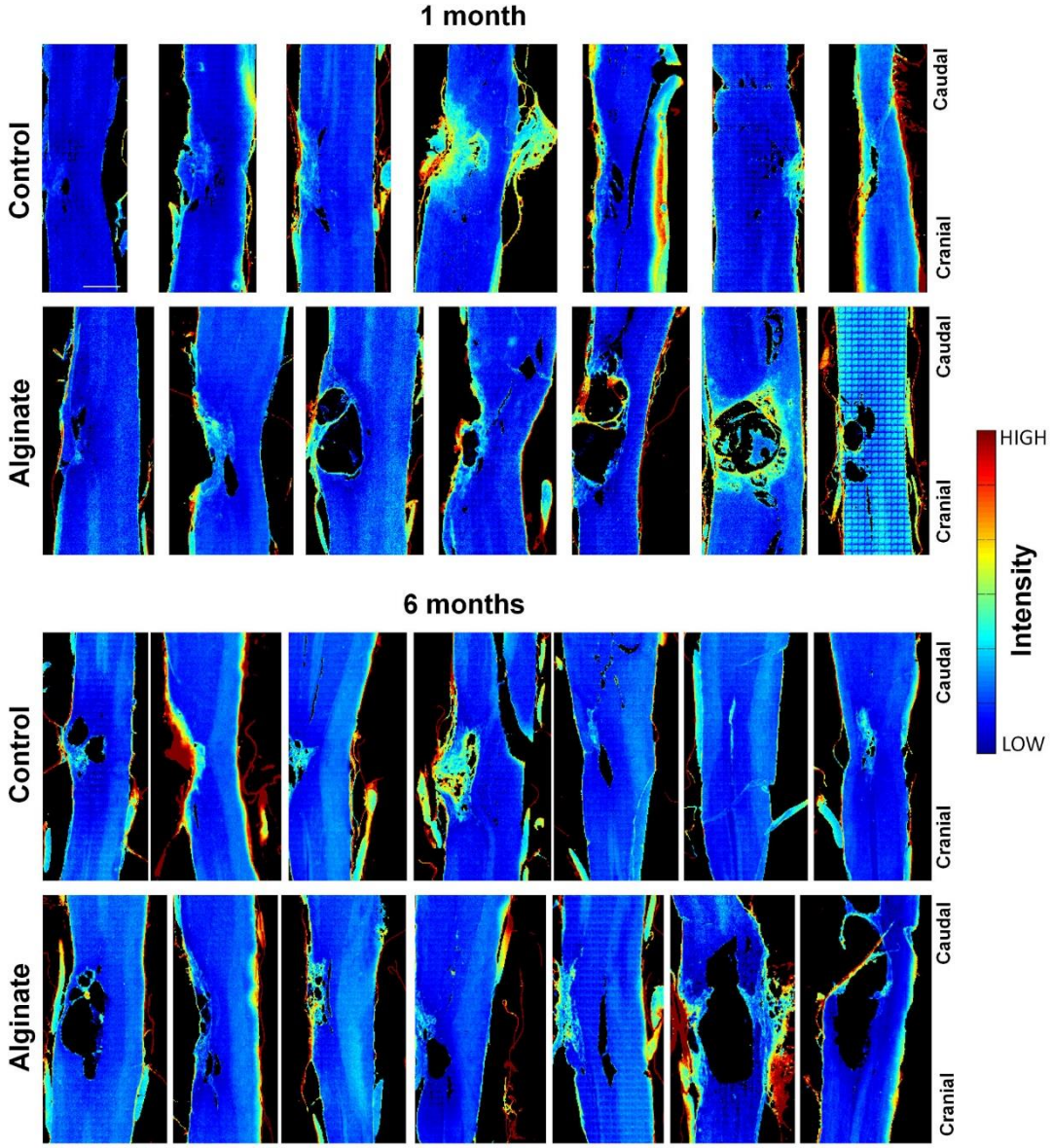

Figure 36. Analysis of the fibrotic lesion. IR spectroscopic images of SCI in rat models with and without alginate hydrogel implant at one and six months post-injury, obtained by plotting the integral intensity of the collagen-representative IR spectral band at 1242 cm^{-1}.

To quantify the differences in extent of fibrous scar formation between different experimental groups, the mean thickness of collagenous tissue was calculated. When compared with control samples, the mean thickness of collagenous tissue was significantly smaller in the samples with alginate hydrogel implant at six months after the injury (Fig. 36 (C), t-test, p=0.0153). The particular finding indicates that the alginate hydrogel suspends the development of fibrous scar in the chronic stage of SCI. In fact, this is in agreement with previous studies, which reported that the use of alginate hydrogel implants is related with the reduction of collagen meshwork surrounding the CNS traumatic lesions [215,240]. Fibroblasts are the cells responsible for synthesizing collagen. The meninges do have fibroblasts, but, under the normal conditions, there are no meningeal fibroblasts in the tissue of the spinal cord. However, the fibroblasts are invading into the spinal cord when the dura is damaged [186]. The reduced fibrotic scarring may be governed by relatively poor attachment, proliferation, spreading and viability of fibroblasts on pure alginate hydrogel [241].

Fate of the alginate hydrogel implant

The soft Ca^{+2}-alginate hydrogel, which was used as an implant in the SCI treatment experiments represented in this work, has shear storage modulus G´ = 0.195 kPa (Fig. 37) and 5% gelation of the gelation sites. These properties make up substantially to exclusivity of particular alginate hydrogel when compared with all other alginates studied so far. Also, particular characteristics were also regarded as critical to transfer the abilities of soft alginate hydrogel to support neural adhesion and substantial neurite outgrowth reported in *in vitro* experiments into rat SCI model [225]. It is important to notice that the cross-linking reaction leaves many polysaccharide sequences uninvolved. As a result, they may potentially interact with cell surface molecules [225].

It was shown that after immersion into saline solution this type of alginate hydrogel preserve its mass and volume [226,242]. However, the penetration of exogenous sodium ions of nervous tissue into the hydrogel may result in leakage of calcium ions and following dissolution of the hydrogel [243].

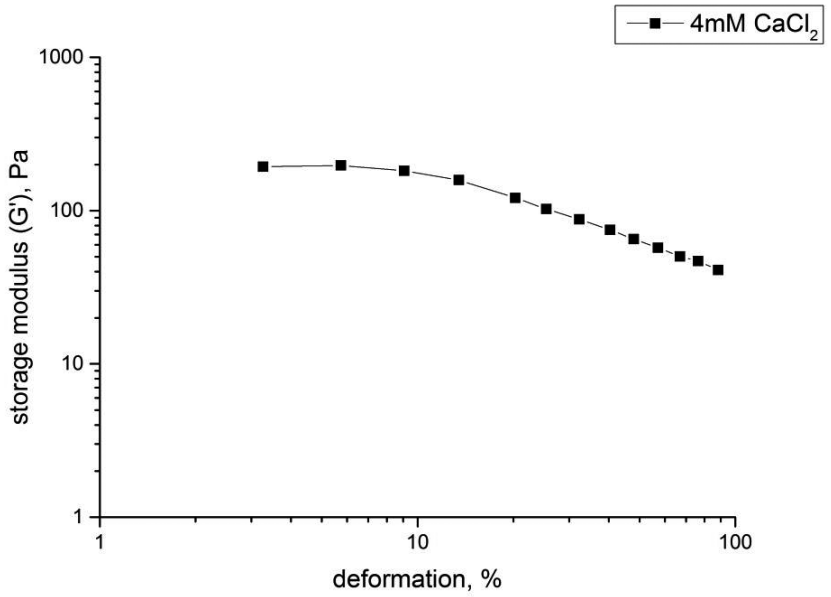

Figure 37**.** Storage modulus vs. deformation of 4% alginate crosslinked in a 4 mM $CaCl_2$ solution. The measurements were performed as explained in Ref. [225].

Therefore, the stability of soft Ca^{2+}-alginate hydrogel implants and ion exchange were examined.

The chemical structure of Ca^{2+} alginate hydrogel is represented in Fig. 38. The IR absorbance spectrum of pure alginate hydrogel obtained before its implantation is shown in black color in Fig. 39. The most prominent spectral contributions in the spectral region of 1180 – 1800 cm^{-1} are the spectral bands at 1614 cm^{-1} and 1420 cm^{-1}, which are attributed to carboxylate salt ion antisymmetric and symmetric stretching [242].

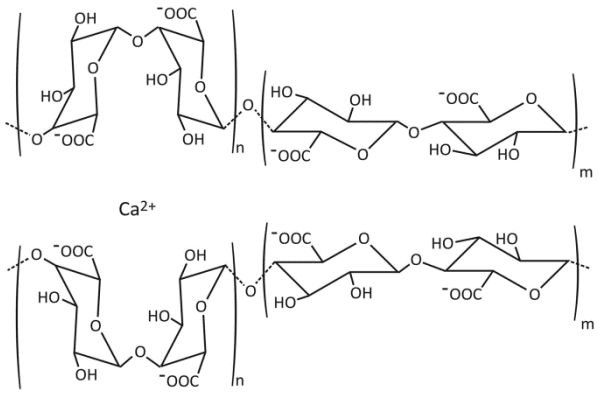

Figure 38. Chemical structure of Ca^{2+}-alginate hydrogel. Alginate is a negatively charged linear polysaccharide, composed of covalently linked D-mannuronic acid and L-guluronic acid monomers. It forms hydrogels by physical interaction of polymer chains via ionic cross-linking by multivalent cations at the sites of guluronic acid monomers sequences between different chains.

The residues of alginate hydrogel implants were identified in six cases of the seven samples and in five cases of the seven samples of spinal cords resected one month and six months after the injury, respectively. However, as the spectral contributions of alginate hydrogel were relatively weak with respect of those of sucrose, the spectra of reference sucrose was always subtracted from the spectra of implanted alginate hydrogel. Such difference spectra were used for the following analysis and are depicted in Fig. 39, where the difference spectra of alginate hydrogel in the spinal cord tissue at one month and six months after the injury are represented in red and blue colors, respectively. The minor spectral contributions in difference spectra compared with the

reference alginate hydrogel spectrum arise due the background noise, which influence is enhanced when difference spectra is calculated.

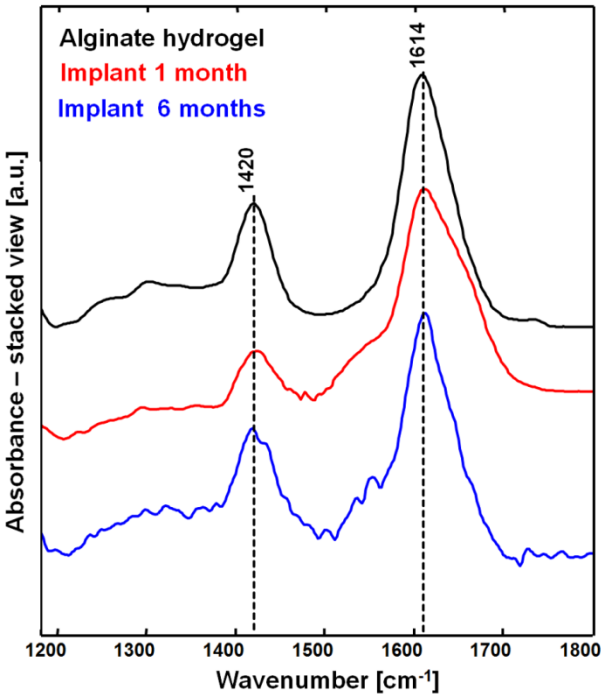

Figure 39. FTIR spectroscopy of the alginate hydrogel implants. IR spectrum of pure alginate hydrogel before its implantation (black) compared with the spectra of alginate hydrogel in spinal cord tissue at one (red) and six (blue) months post-injury.

It can be readily observed from Fig. 39 that the overall spectral fingerprints of reference and implanted alginate hydrogels are very similar, i.e. the positions of the bands at 1614 cm^{-1} and 1420 cm^{-1} are steady. The alginate structures from their chemical derivatives can be distinguished by referring to the wavenumber shifts of both 1614 cm^{-1} and 1420 cm^{-1} spectral bands. The absence of the shifts of these bands, therefore, indicate that no substantial exchange of crosslinking ions appear in the alginate hydrogel after its implantation and the implants maintain their chemical structure over the time. Moreover, the bands shoulders at approximately 1550 cm^{-1} and 1650 cm^{-1} in the spectra of alginate hydrogel implants were observed. As these shoulders are very consistent with the spectral positions corresponding to amide II and amide I molecular vibrations, the mixing of alginate hydrogel with proteins is

very likely. No spectral band shifts between the spectra were observed among the samples of one and six months alginate-implanted samples: implants retained their chemical structure over the time of implantation in SCI. Nevertheless, the changes of the mechanical properties of alginate hydrogel implants may be changing over the implantation period and thus cannot be excluded.

These results are in line with the rather slow degradation rate of calcium alginate hydrogels, as it might last several months until they lose their chemical stability under physiological conditions [244]. The digestion of alginate hydrogel by enzymes can be excluded, as there are no endogenous enzymes, degrading alginate hydrogel in spinal cord of rodents. Therefore, the degradation is most likely resulting from gradual diffusion of calcium ions, which leads to unlinking and dissolution of alginate polymer chains and loss of the hydrogel structure [243]. It is known that ions are released in elevated levels in the extracellular matrix of damaged CNS tissue [245]. This might support the enhanced diffusion rate of Ca^{2+} cross-linkers from the alginate hydrogel. The hydrogel degradation rate may thus be different among the samples depending on the intensity of extracellular ions influx in each case of the nervous tissue damage. This could potentially explain the varying amounts or complete absence of alginate hydrogel implants between the samples.

Distribution of the alginate hydrogel in the lesion

Information of the distribution of the alginate hydrogel implant in the injured spinal cord was obtained by generating the RGB spectroscopic images, i.e. simultaneously representing the location of the implant, nervous tissue and the fibrous scar. The integral intensities of the spectral bands at 1420 cm^{-1} (Fig. 39), 1653 cm^{-1} (Fig. 30, amide I band) and 1242 cm^{-1} (Fig. 35, band assigned to collagen) were calculated and mapped to indicate and visualize alginate hydrogel, nervous tissue and fibrous scar, respectively.

An RGB spectroscopic image of injured spinal cord, in which soft alginate hydrogel implant was present for six months, is exemplarily shown in Fig. 40 (A). Here, the red, green and blue pixel colors represent alginate hydrogel, nervous tissue and fibrous scar tissue, respectively. The consecutive spinal cord section was alcian blue stained and used as a reference for the alginate hydrogel distribution [Fig. 40 (B), indicated by asterisks or arrows]. In both RGB microspectroscopic and alcian blue staining microscopic images, the small cysts varying in size and occupied by alginate hydrogel are observed within the lesion (in Fig. 40 (A) and (B) indicated by arrowheads). The sample morphology shows that the small alginate residues are rather tightly surrounded by tissue suggesting that the tissue is possibly growing through the soft alginate hydrogel. Furthermore, the larger cysts containing alginate hydrogel residues but no nervous tissue ingrowth (Fig. 40, indicated by asterisks) indicate that nervous tissue could not completely transverse across the alginate-filled lesions. Such large cysts are a well-known physical restraint for regenerating axons [246]. On the other hand, the fibrous collagen scar, surrounding these cysts in spinal cords with alginate hydrogel implants, was shown to be generally thin. This is a promising positive outcome compared with voluminous fibrous collagen scars, which, in the case of untreated animals, tend to firmly fill the lesion and act as a solid physical barrier against regenerating axons. Accordingly, a worse outcome of the alginate hydrogel implants received animals cannot be predicted *per se* by the presence of large alginate hydrogel filled cysts.

Infrared spectra from different points of the sample were selected to gain better insights of tissue-alginate interactions. The selected positions are marked with numbers in Fig. 40 (A) and the corresponding spectra are reported in Fig. 40 (C). The spectrum of the implant (position 1) has alginate-specific bands at 1420 cm^{-1} and 1614 cm^{-1} and lacks amide bands.

The spectrum of position 2 displays bands at 1205, 1242, 1282, 1338, 1402 and 1453 cm^{-1} that match the specific spectral features of pure collagen, as well as the alginate specific band at 1420 cm^{-1} and shoulder at 1614 cm^{-1}. This spectral pattern suggests that the scar is penetrating the hydrogel at this position of the sample.

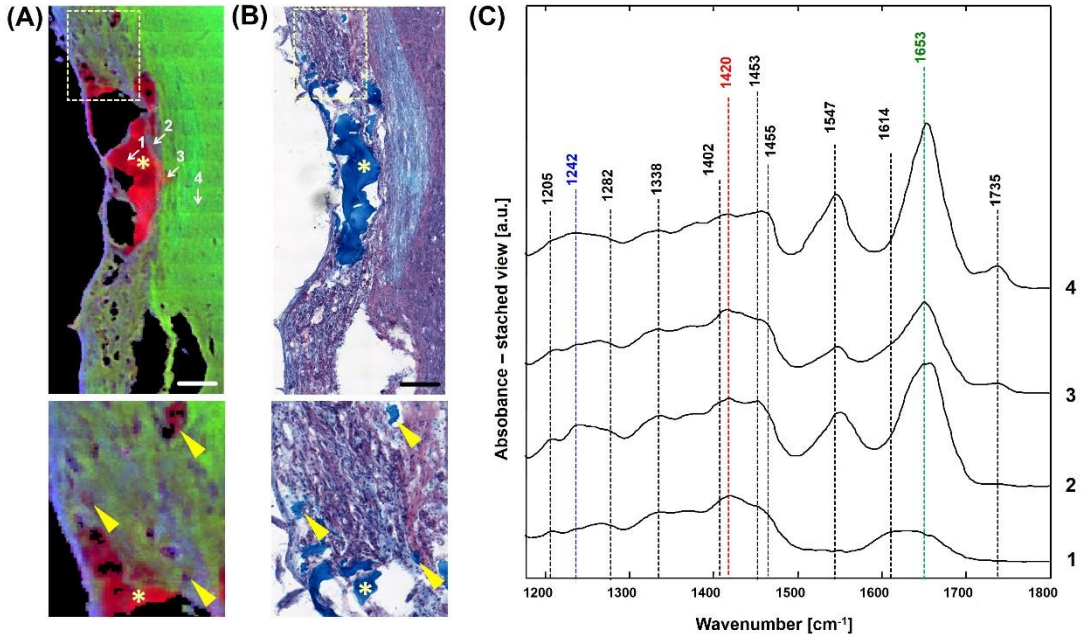

Figure 40. Distribution of alginate within the tissue six months after the injury. (A): IR spectroscopic RGB image, produced by combining the intensity of bands at 1420 cm^{-1} (representative of alginate hydrogel–red), 1653 cm^{-1} (representative of nervous tissue–green) and 1242 cm^{-1} (representative of collagen—blue). (B): Alcian blue staining of a consecutive section. Scale bar: 100 µm. The boxes in A and B indicate the area of magnification. The arrowheads in the magnifications indicate small inclusions of alginate hydrogel into the tissue that co-localize in the spectroscopic image and in the staining. The asterisks indicate residues of alginate hydrogel inside large cysts. (C): IR spectra of positions indicated in the spectroscopic image in (A), showing mixing of alginate and tissue.

The RGB-image suggested that nervous tissue was mixed with alginate, for example at position 3. Therefore, the spectrum at this position was compared with the spectrum of nervous tissue at position 4. The amide bands were clearly identified in the spectrum from position 3 as well as lipid-related spectral features at 1455 cm^{-1} and 1735 cm^{-1}. These spectral features are superimposing with the alginate bands at 1420 cm^{-1} and 1614 cm^{-1}, the latter producing a broad shoulder on amide I band at 1614 cm^{-1}). Spectra from similar

“alginate-tissue combination” sites were selected from the RGB images and showed similar superimposing spectral features. This might indicate a growth of nervous tissue through the alginate hydrogel.

Tissue damage classification

In previous sections, the biochemical outcomes of alginate implants in SCI were assessed in detail from respective spectral markers of FTIR microspectroscopy data. Moreover, by deciding for appropriate approach of spectral data classification, FTIR imaging could hold potential to be utilized for global classification of spinal cord tissue and its damage and, therefore, become as an alternative method to monitor and optimize future SCI treatment strategies.

To localize the eventual tissue damage, which results from the combination of various biochemical alterations of the tissue, unsupervised cluster analysis was applied to each sample and enabled to distinguish preserved vs. damaged tissue regions, as well as the localization of alginate implants [Fig. 41 (A)]. By comparison of cluster maps and histological staining images [Fig. 41 (B)], matching between clusters and tissue type was obtained, enabling to define: 1) fibrous scar, 2) tissue damage, 3) grey matter, 4) damaged white matter, 5) white matter and 6) alginate hydrogel. The centroid spectra [Fig. 41 (C)] of the selected clusters in all samples were extracted and averaged to provide the spectral “fingerprint” of the injury [Fig. 42 (A)]. Thanks to the big number of animals investigated, the spectral fingerprints are not affected by inter-animal variability.

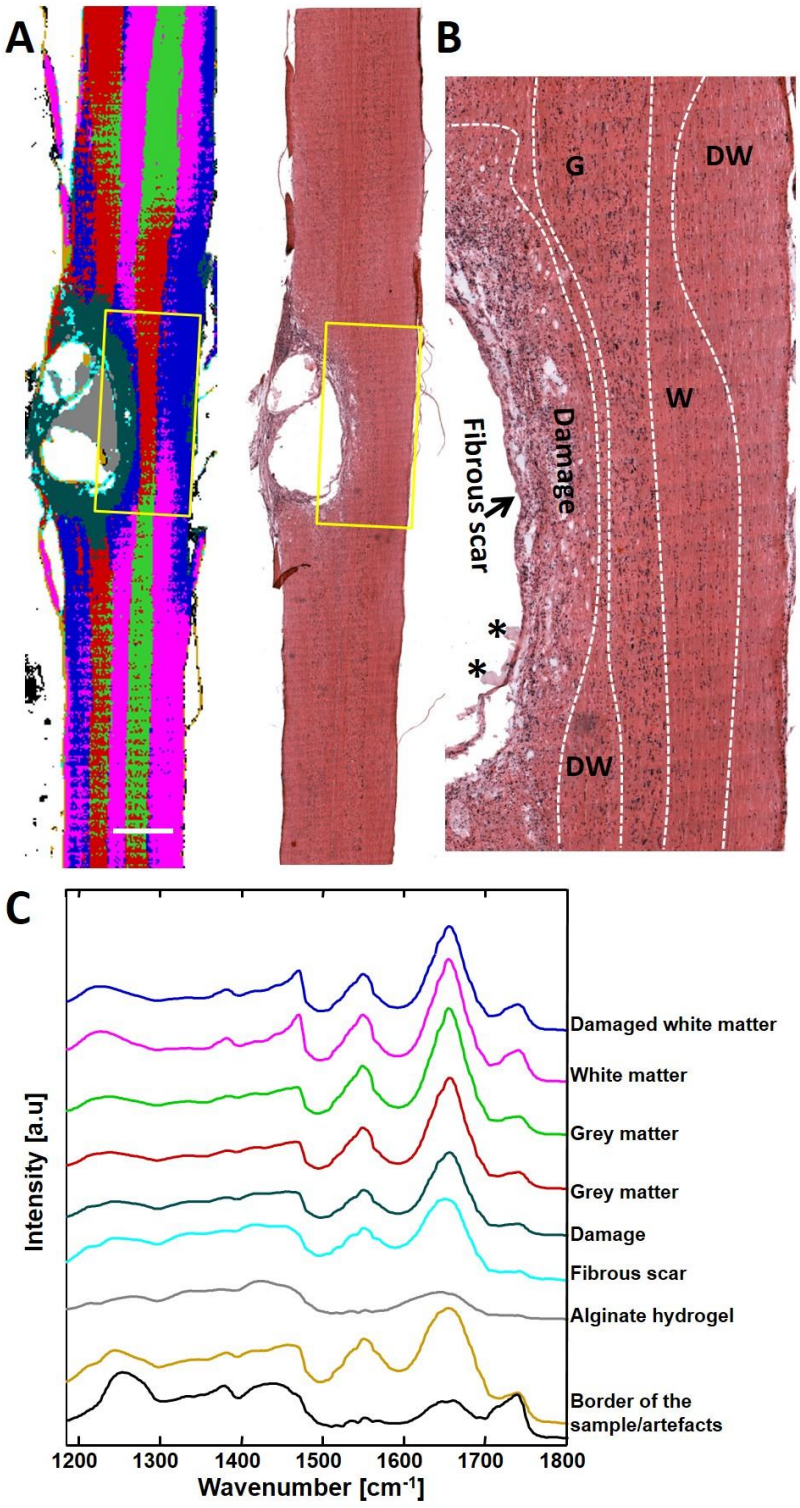

Figure 41. Example for the evaluation of clustering results on IR spectral data: (A): cluster map and H&E histological staining on the consecutive section, scale bar – 1mm; (B): area of magnification in H&E staining indicated by box in (A). G – gray matter, W – white matter, DW – regions of damaged white matter, asterisks (*) indicate residues of alginate hydrogel. (C): centroid spectra attributed to different states of spinal cord tissue. Cluster colors were attributed randomly.

The analysis of the fingerprint of normal vs. damaged tissue spectra confirms that damaged tissue is characterized by lower lipid content: the intensity of all lipid related bands is reduced. Moreover, the spectra of damaged nervous tissue show a marked decrease in amide I and amide II, which could be a consequence of nervous cell death.

While cluster analysis enabled a closer insight in the biochemical alterations triggered by injury, a direct comparison between samples was not possible with this approach. Therefore, a supervised classification was applied using the six spectra defined above [Fig. 42 (A)] as training set to identify biochemically comparable tissue regions in entire the data set comprising the spectra of all 28 samples.

Examples of class membership images are shown in Fig. 42 (B). The alginate implant (green color) was precisely localized. In all samples, white (red color) and gray (gray color) matter, damaged tissue (yellow and black) as well as the lesion core with the fibrous scar (blue) are correctly localized and are in agreement with the histological staining. For example, Figure 42 (C) [the higher magnification of regions indicated by boxes in Fig. 42 (B)] shows tracts of white and grey matter in the H&E staining correctly attributed in the FTIR image by yellow/red and gray colors, respectively. The tissue areas with microcysts were identified in the H&E image (indicated by dashed line) and were correctly

attributed as damage by the classification and are shown in black color in FTIR image.

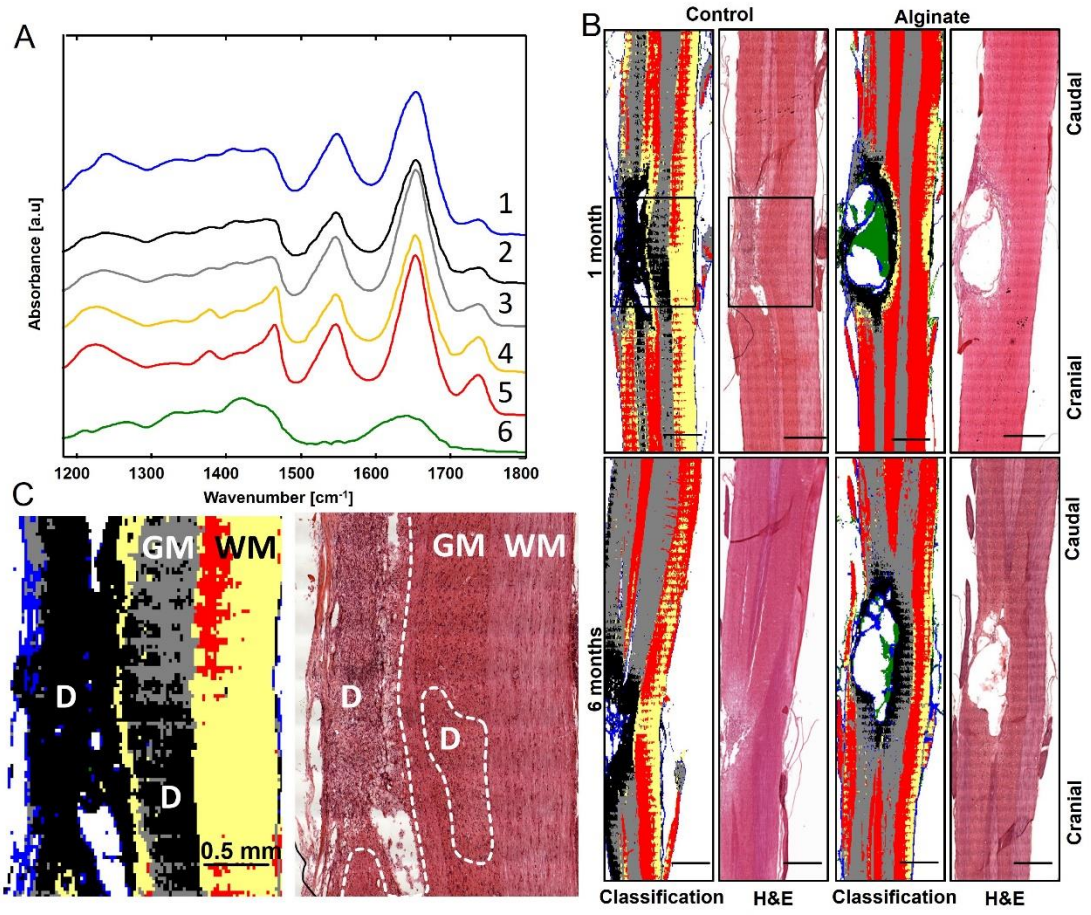

Figure 42. (A): Fingerprint IR spectra, used as training set for classification: 1 - Fibrous scar; 2 – Tissue damage; 3 - Grey matter; 4 - Damaged white matter, 5 - White matter; 6 - Alginate hydrogel. (B): Examples of images generated by nearest neighbor classification and H&E staining of consecutive sections. Scale bar – 1mm. (C): Zoom-in into FTIR image and H&E staining of the region in the box in panel (B). Damaged tissue areas are correctly detected by the classification and match histological findings. GM – grey matter, WM- white matter, D – regions of tissue damage indicated by dashed line.

Localization and extent of damage could be directly compared among all samples. The damage (black regions) is always confined around the injury center showing the collapse of the grey matter, in accordance with other studies [247,248]. The region of damaged white matter (yellow) is most commonly localized in the tissue contralateral to the lesion, extends to both anterior and posterior directions and is larger in control animals. The overall tissue architecture and morphology of alginate samples appears more

preserved, presumably thanks to less tissue shearing and compression. These findings suggest that alginate hydrogel serves also as a mechanical support to preserve the gross spinal cord morphological structure and may help to limit secondary damage of nervous tissue. The same approach of data analysis can be applied to standardized evaluation and comparison of the spectroscopic data of SCI of future experiments.

3.3.3.2 Raman microspectroscopic imaging and CARS microscopy

The image acquisition time is considerably slower in the case of Raman microspectroscopy compared with other vibrational imaging modalities used in this work. Nevertheless, large Raman maps covering several square millimeters in size were acquired on cryosections in the region of SCI to confirm the results of FTIR microspectroscopic imaging discussed in previous section and/or to provide complementary morphochemical information.

Unsupervised “k-means” cluster analysis was applied for ubiquitous representation of sample morphochemical structure and enabled to identify regions with different types of tissue. Raman cluster maps of representative examples of control group and alginate-implanted group at both one and six months post-injury are shown in Fig. 43 and Fig. 44, respectively. The centroid spectra provided information about tissue biochemistry. Analysis of centroid spectra allowed to identify alternating regions of gray and white matter as well as to localize the lesion region, which is indicated by dotted line in the figures.

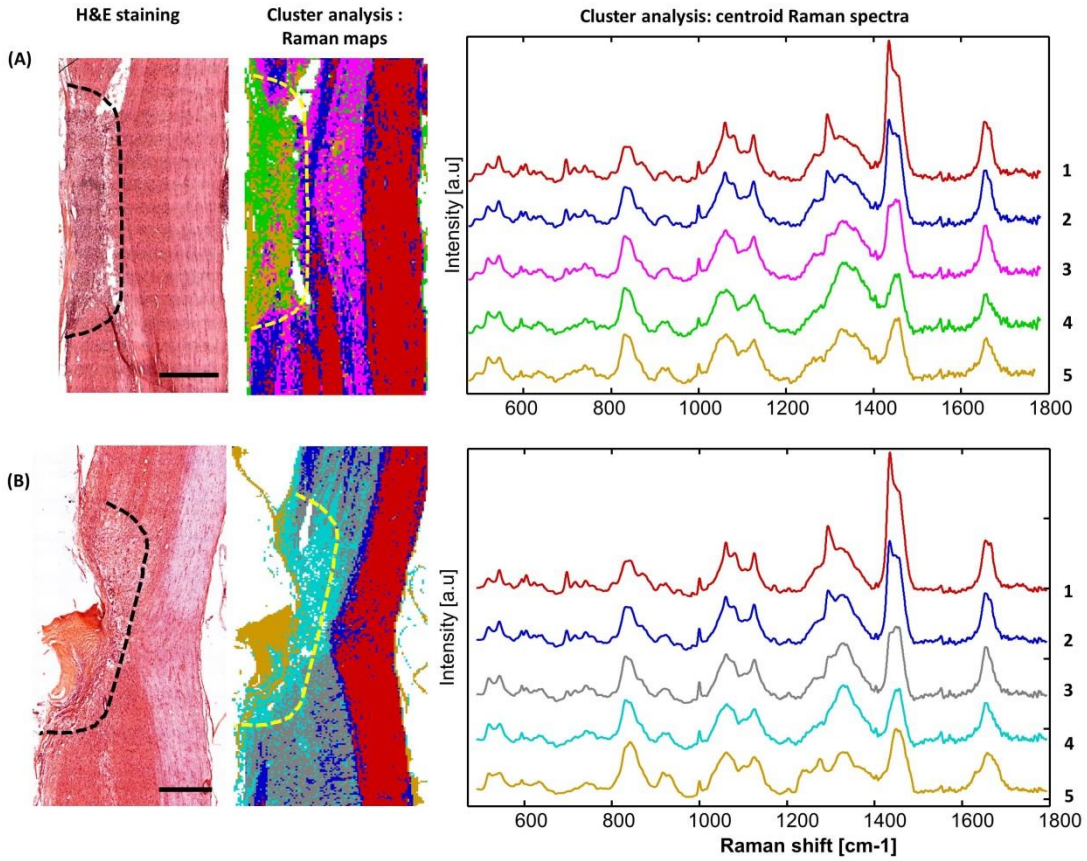

Figure 43. H&E histological staining, cluster maps and centroid spectra produced from Raman spectral data of two control samples of SCI in the rat model. (A): 1-month post injury; (B): 6-months post injury. Dotted lines bound the core of hemisection injury. Cluster 1: white matter, clusters 2 and 3: grey matter, clusters 4 and 5: lesion. Cluster colors were attributed randomly. Scale bar: 1mm.

In control specimens (Fig. 43), the cluster analysis revealed a lipid-poor region inside the injury site, which is characterized by intensity decrease of cholesterol band at 700 cm^{-1} and of CH deformation bands at 1300 and 1440 cm^{-1}. These spectral bands are all lipid-related and their intensity decrease clearly demonstrates the loss of lipids and, therefore, gives clues for demyelination and axonal degeneration. The profoundly reduced lipid content in lesion area is in agreement with the results of FTIR microspectroscopy. The clusters 4 and 5 indicate the fibrotic scar, which is well retrieved by spectral bands at 1243 and 1276 cm^{-1}. The fibrotic scar is present in the lesion area at both one and six months control samples. When centroid spectra of clusters 5 are compared, the fibrotic scar-indicative spectral bands are more intense in six-month sample

than in one-month sample and indicate higher collagen content in the chronic stage of injury. This clearly suggests that the formation of fibrous scar is extending over several weeks and reach the highest content of collagen in the chronic stage of injury.

Raman spectral maps retrieved by cluster analysis of alginate-implanted spinal cord samples are shown in Figure 44. The tracts of white and gray matter can be readily distinguished. Similar as in the case of control samples, the injury region is captured by cluster analysis and is characterized by a decrease of lipid-related band intensities. Fibrotic scar corresponding to regions with higher intensities of collagen bands in the centroid spectra (clusters 4 and 5) is present in the lesion region. The centroid spectra of clusters in the lesion center at the same time point are however characterized by lower intensities of collagen

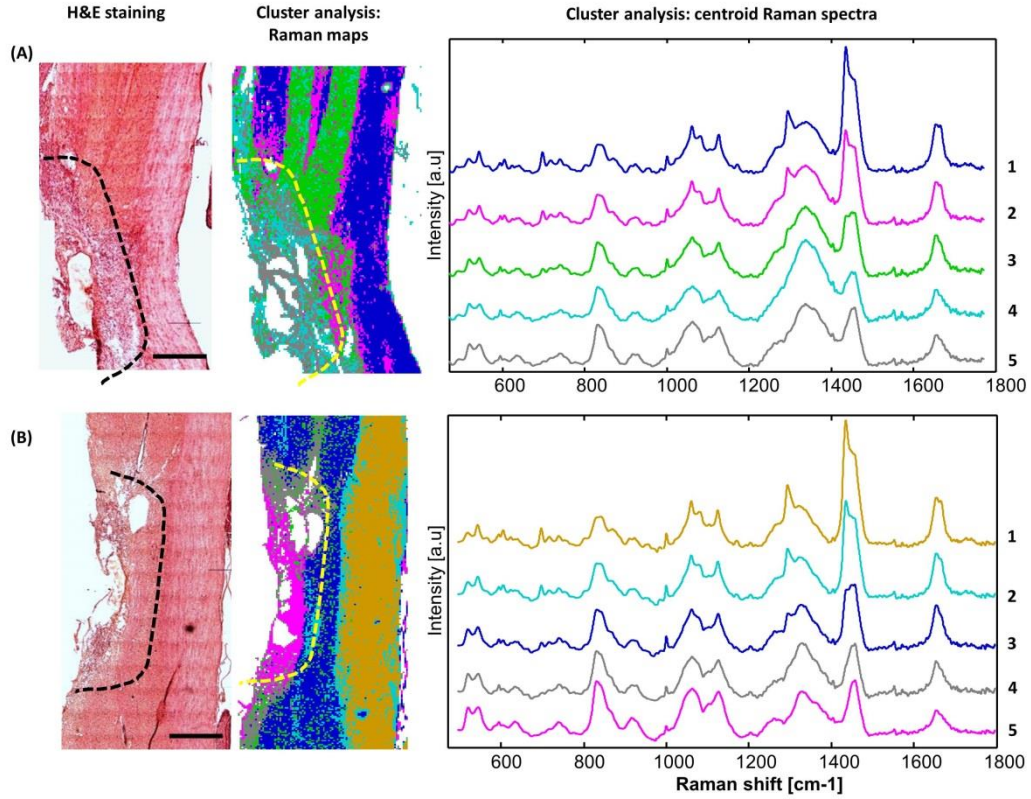

Figure 44. H&E histological staining, cluster maps and centroid spectra produced from Raman spectral data of two alginate-implanted samples of SCI in the rat model. (A): 1-month post injury; (B): 6-months post injury. Dotted lines bound the core of hemisection injury. Cluster 1: white matter, clusters 2 and 3: grey matter, clusters 4 and 5: lesion. Cluster colors were attributed randomly. Scale bar: 1mm.

spectral bands in alginate-implanted specimens than in control ones. This is especially evident by comparing clusters 5 in Figs. 43 and 44.

The potential of infrared microspectroscopy to monitor the implants was shown in previous subchapter. As an alternative linear vibrational microspectroscopy technique, Raman microspectroscopic imaging also allowed to track the alginate hydrogel implants. The Raman spectrum of native soft unfunctionalized alginate hydrogel is shown in Fig. 45. The most prominent spectral bands are at 811, 886, 955, 1090, 1307 and 1418 cm^{-1}. The spectral bands at the shorter wavelengths than 1300 cm^{-1} are due to the polymer backbone vibrations, namely, due to C—C and C—O bonds stretching vibrations as well as C—C—H and C—C—O bonds deformation vibrations. The band at 1090 cm^{-1} is attributed to glycosidic ring breathing. The spectral bands at the longer wavelengths than 1300 cm^{-1} arise mainly due to stretching vibrations of the carboxylate functional group COO^- [249].

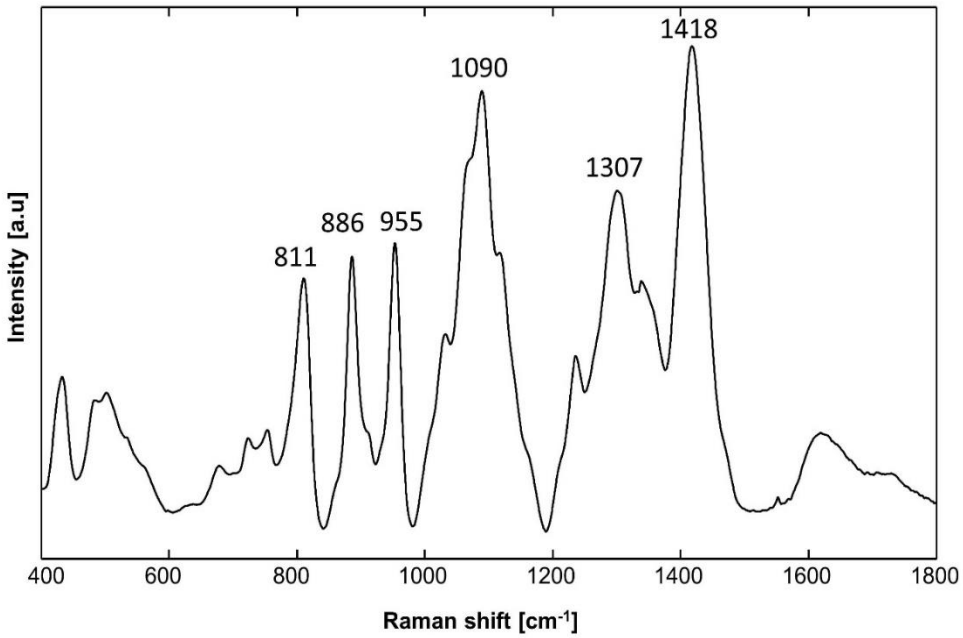

Figure 45. Raman spectrum of native (before implantation) non-functionalized soft Ca^{2+}-alginate hydrogel.

The intensity of the band at 1090 cm^{-1} in Raman spectrum of native alginate hydrogel was selected to address the presence of the implants in the SCI samples at both time points. The implant residues in the lesion were detected in the same samples as in the study by infrared microspectroscopy, therefore confirming the results of infrared spectral imaging and alcian blue staining. The spectral profile of Raman spectra acquired from the residues of implants in SCI samples were characterized by a mixture of spectral features typical of the alginate hydrogel and those of the nervous tissue. A variable degree of mixture between alginate hydrogel, proteins and lipids is evident when the spectra of distinct tissue components, centroid spectra of clusters and spectrum of native alginate hydrogel are all compared together. The shape and intensity of the band envelope at around 1100 cm^{-1} is modified in the centroid spectra of clusters 4 and 5, which are associated to the regions of the lesion core, as can be seen in Figure 44. This modification arise due to variable degree of overlap of the glycosidic ring breathing of alginate polymers with other C—C stretching vibrations of tissue components.

As already discussed, the origin of the degradation of the alginate hydrogel implant in the tissue can be exchange of calcium ions by sodium ions [250]. It is known that the substitution of cross-linking ions results in shifts of the Raman bands [249]. In particular, in the spectral region corresponding to glycosidic ring breathing mode, shifts around 10 cm^{-1} towards higher wavenumbers should be expected. The reason for these shifts is the strengthening of C–C and C–O bonds, which is the indirect consequence of the alginate polymers binding to sodium ions [249]. However, the ion exchange cannot be directly addressed by Raman spectroscopy, as the alginate spectral band was overwhelmed by the overlap with the tissue spectral profile. Therefore, detection of the discrete band shifts was elusive to address ion exchange from Raman spectroscopic data.

It was shown that by application of cluster analysis to acquired Raman spectral data, Raman microspectroscopy is a suitable vibrational spectroscopy technique to address myelin and collagen distribution in the lesion region as well as to confirm the presence of alginate hydrogel implants. Better visualization of the lipids, collagen and alginate implants was retrieved by calculating the integral intensity of selected spectral bands respectively attributable to each of these components, plotting the corresponding spectral maps and merging these maps as RGB images as shown in Figures 46 and 47. The distribution of lipids, sugars (e.g. alginate) and collagen was retrieved from the integral intensity of the bands at 1440 cm^{-1} (displayed in red in the merged image), 1090 cm^{-1} (displayed in green in the merged image) and 1243 cm^{-1} (displayed in blue in the merged image), respectively. The differences among samples were made readily visible in this representation. In comparison with surrounding region of undamaged tissue the lesion core is lipid-poor. Moreover, the fibrotic scar is collagen-rich at 6 months after the SCI and tends to be more pronounced in control samples. The residues of the alginate hydrogel implants can be clearly identified.

The arrows shown in the intensity maps of the spectral band at 1440 cm^{-1} in Figures 46 and 47 indicate the lipid-rich regions inside the lesion or immediately near the implants. However, Raman mapping with the lateral resolution that characterizes Raman microscope used in this work did not allow to recognize single axons. Therefore, the lipid-rich regions could not be verified to accommodate functional myelinated axons.

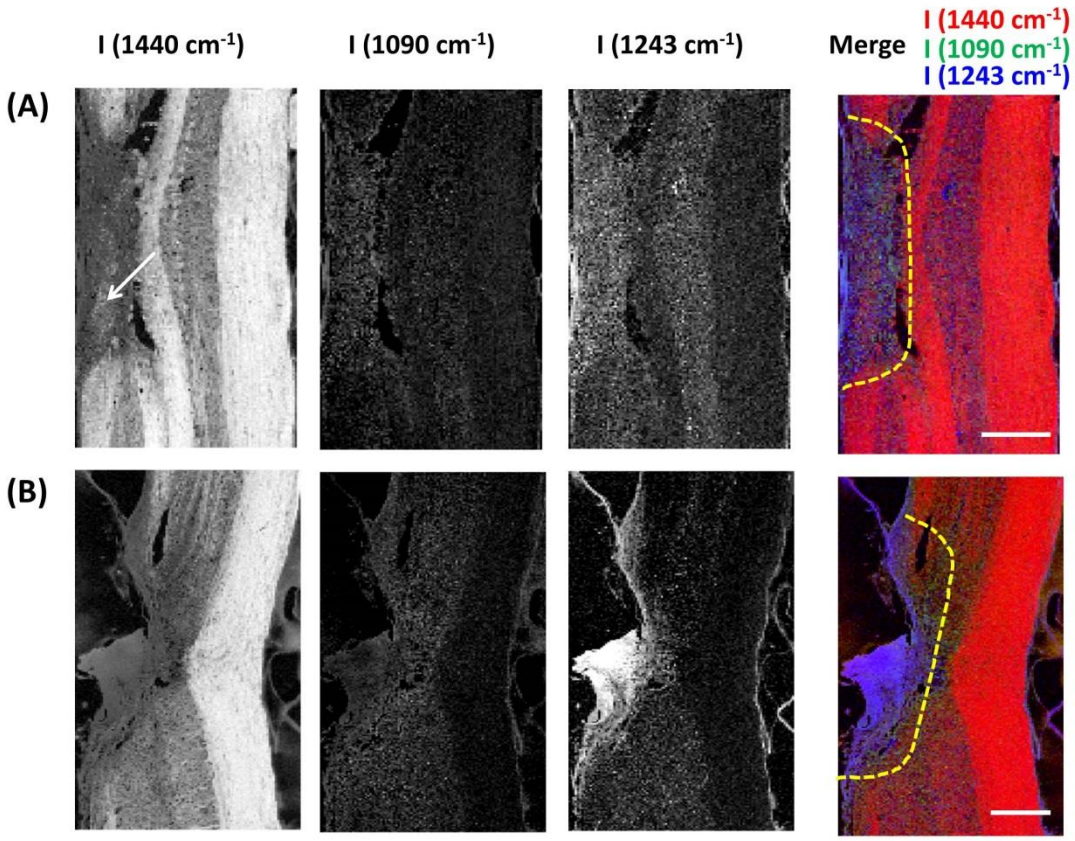

Figure 46. Control samples of SCI in the rat model: integral intensity maps of Raman bands calculated at 1440 cm^{-1} (representative of lipids), at 1090 cm^{-1} (representative of alginate), at 1243 cm^{-1} (representative of collagen), and merged RGB image. (A): 1-month after SCI; (B): 6-months after SCI. The samples are the same demonstrated in Figure 43. Dotted line on the merged RGB image bound the core of hemisection injury. The arrow in A indicates a region inside the lesion that displays high content of lipids. Bar: 1 mm.

To obtain chemical specific cellular and subcellular morphology of the tissue and, therefore, identify axons and types of the cells, multimodal CARS microscopy was applied. In particular, CARS, SHG and TPEF signals from samples of SCI were acquired simultaneously to provide morphochemical

contrast of different tissue components. CARS signal allows to visualize the distribution of lipids and thus address the demyelination. SHG signal provides the information about the distribution of fibrillary collagen to assess the extent of fibrous scar. TPEF signal in SCI tissues predominantly arises from endogenous fluorescence of nicotinamide adenine dinucleotide phosphate (NAD(P)H) [23] and adds information about number and distribution of autofluorescent cell bodies.

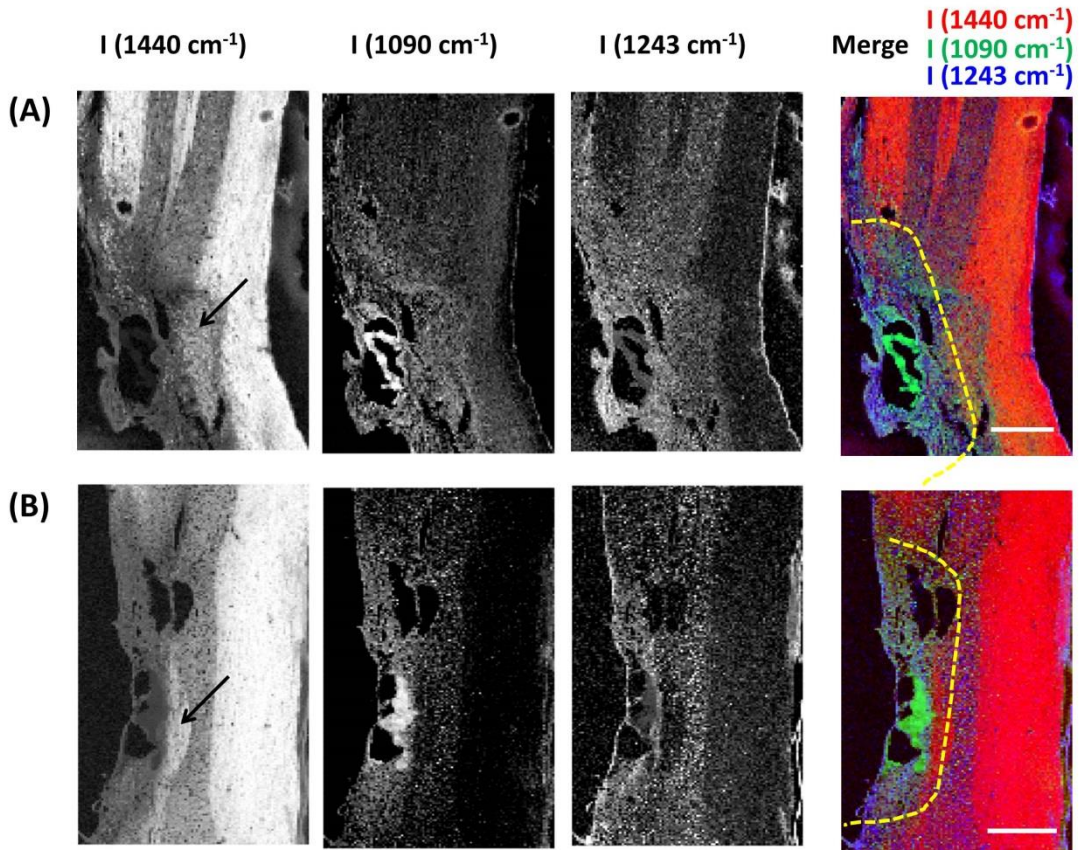

Figure 47. Alginate implanted samples of SCI in the rat model: integral intensity maps of Raman bands calculated at 1440 cm^{-1} (representative of lipids), at 1090 cm^{-1} (representative of alginate), at 1243 cm^{-1} (representative of collagen), and merged RGB image. (A): 1-month after SCI; (B): 6-months after SCI. The samples are the same demonstrated in Figure 44. Dotted line on the merged RGB image bound the core of hemisection injury. The arrows indicate regions at the border of the lesion that display a high content of lipids. Scale bar: 1 mm.

No bundles of axons or single axons were detected by CARS imaging inside and at close proximity of the SCI core in control samples. Instead, lipid droplets, which co-localized with fluorescent cells were visualized in the most of one-

month specimens. The fluorescent cells were identified as macrophages and foam cells, which function is to clear up myelin debris [249]. Fig. 48 (A) depicts the multiphoton image of the region indicated by an arrow in Fig. 46 (A) at a higher magnification and shows that the intense CARS and TPEF signals arise from foam cells. These foam cells reside in a dense meshwork of collagen detected by SHG signal. High lipid content region nearby the lesion in one-month alginate-implanted sample shown by arrow in the Raman intensity map of Fig. 47 (A) do not correspond to axonal structures, but once again to accumulations of foam cells [Fig. 48 (B)]. The presence of foam cells and related alterations of lipids in the SCI will be discussed in detail in the following subchapter 3.3.3.3.

Nevertheless, Fig. 48 (C) demonstrates that myelinated axons were detected by CARS imaging in six months alginate-implanted sample inside the lipid rich region near the injury core indicated by arrow in Fig. 47 (B). No decrease of the CARS signal was detected in the white matter in close proximity to the implant suggesting these axons to be normally myelinated. However, the massive growth of functional white matter tracts bridging through the alginate hydrogel could not be identified in any of the samples analyzed.

Alginate-implanted samples at both time points after SCI showed the presence of very thin layer of collagen fibers surrounding the cysts. Fibrotic scar tissue was not heavily filling the lesion core [Fig. 48 (C)] as in the case of control samples. These observations obtained from SHG imaging are in agreement with previously discussed results of infrared microspectroscopic imaging. Taken together SHG imaging results with the results of Raman and infrared spectroscopic imaging, this suggest that the implantation of alginate hydrogel in rat spinal cord does not induce, but even inhibit the formation of a thick capsule of fibrous scar.

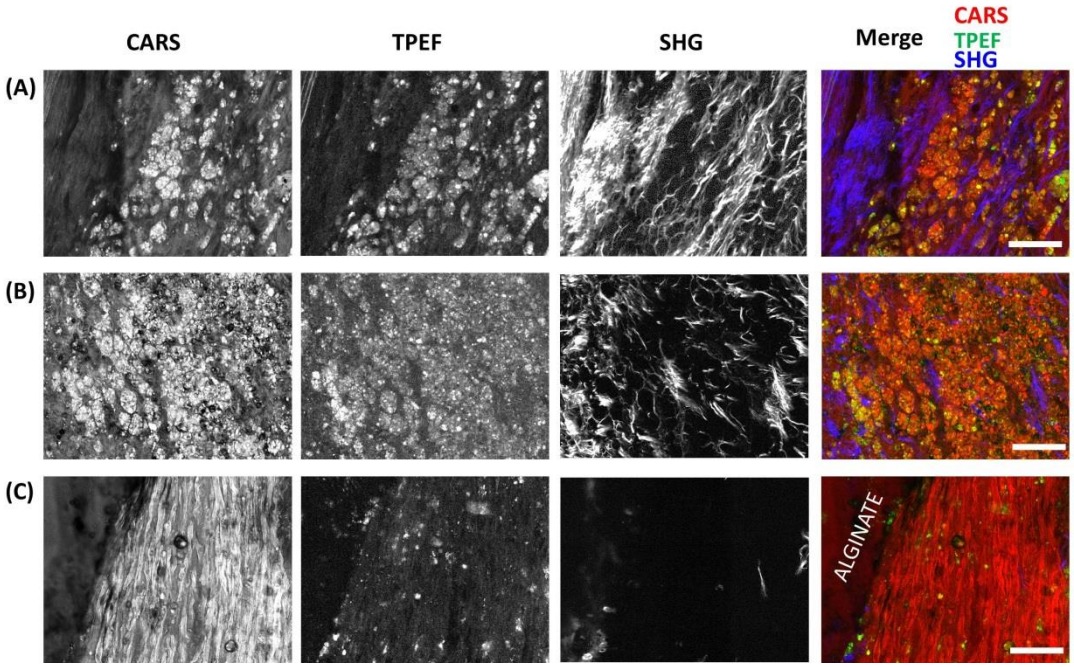

Figure 48. Multiphoton microscopy images of SCI in the rat model in columns as following: CARS, TFEF, SHG and merged image of all these signals. (A): 1-month control sample; (B): 1-month alginate-implanted sample; (C): 6-month alginate-implanted sample. The images were acquired in the regions indicated by arrows in Figures 46 and 47. Scale bar: 150 µm.

3.3 3.3 Inflammation-related alterations of lipids triggered by spinal cord injury

Distribution of lipids

According to H&E staining, five samples of SCI, where the inflammatory responses were observed, were selected for further analysis of inflammation- and myelin degradation-related tissue lipids. These samples are shown in Figs. 49 (A) – 49 (E). Here, the spinal cord lesion sites are indicated by dotted lines. Fig. 49 (A), 49 (C) and 49 (E) show the samples with outspread inflammation inside and around the lesion, whereas Fig. 49 (B) demonstrates the case of SCI with the areas of inflammation at the lesion site only. The sample in Fig. 49 (D) has less inflammatory cells, which are mainly distributed near the large cysts.

To investigate the distribution of various lipid-based structures of injured nervous tissue, Raman spectral maps were generated by plotting the integral intensity of the band at 1440 cm^{-1}. This particular band corresponds to deformational vibrations of CH_2 functional groups [80]. The dimensions of Raman maps were of several square millimeters in size and covered the lesion area and part of the surrounding preserved nervous tissue. In corresponding Figs. 49 (F) – 49 (J), it can be readily recognized that the injury is altogether characterized by lower lipid content than the surrounding undamaged tissue: intensity values of Raman scattering at 1440 cm^{-1} are lower at the lesion, therefore, allowing it to be discerned.

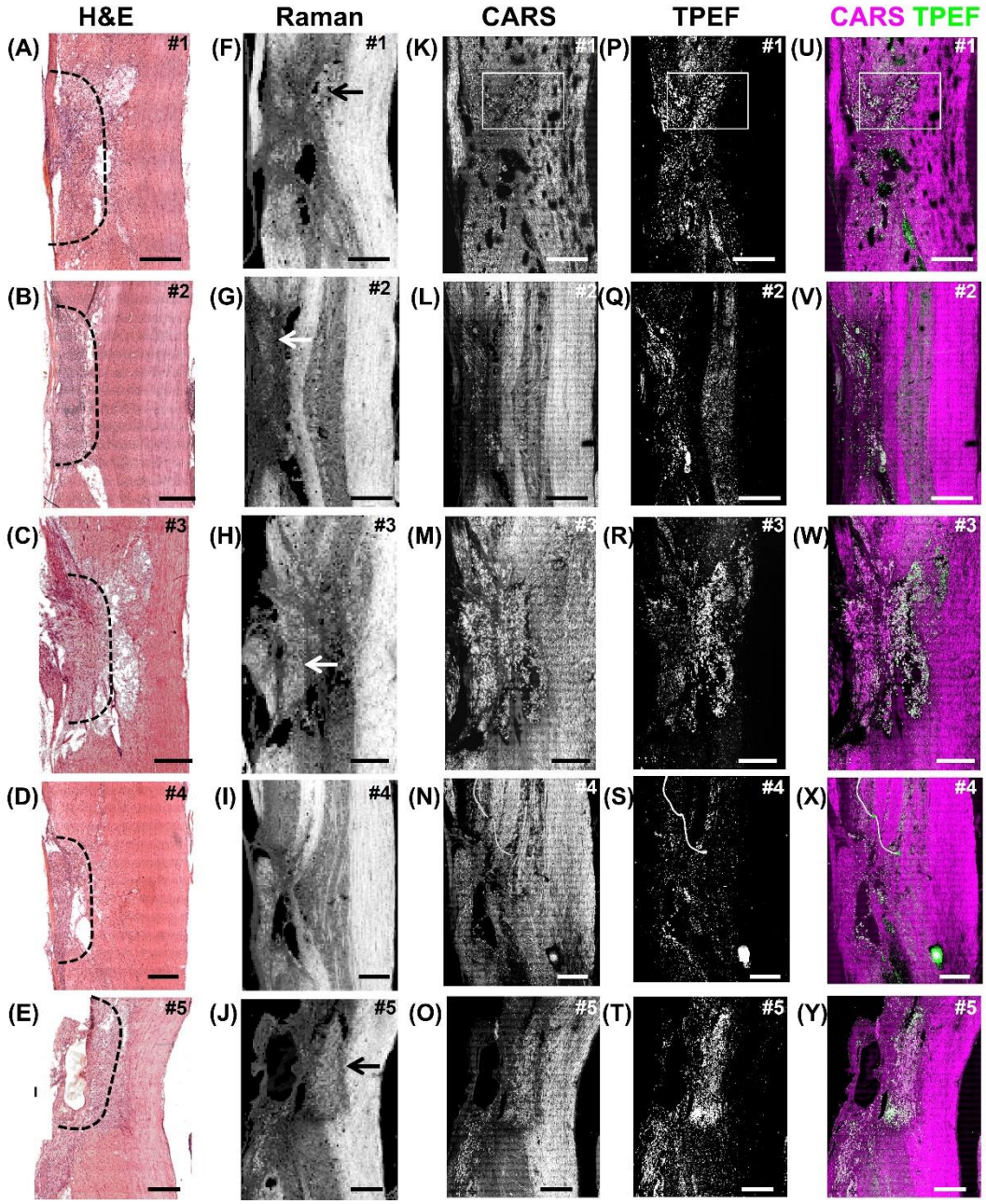

Figure 49. Cryosections of SCI samples, where the inflammatory responses were observed: (A–E) H&E staining; (F–J): Raman intensity maps of the band at 1440 cm^{-1}; (K–O): CARS images; (P–T): endogenous TPEF; (U–Y) merged CARS (magenta) and TPEF (green) images. The dotted lines in A–E indicate extent of hemisection. Arrows in (F–H) and (J) indicate lipid-rich areas in the injured region. The boxes in (K), (P), and (U) indicate the position of zoom-in images of Fig. 50. Scale bar: 0.5 mm.

As already pointed out in subchapter 3.3.3.2, the regions with considerably higher lipid content were observed inside or directly near the lesion site in four of the samples [marked by arrows in Figs. 49 (F) – 49 (H) and 49 (J)]. However, the lateral resolution of the Raman maps, which were acquired with the Raman

microspectrometer used in this work, is too low to distinguish single myelinated axons. That is why it is not possible to tell whether the particular high lipid content-related areas correspond to bundles of functional myelinated axons.

CARS microscopy providing submicrometer lateral resolution was applied for identification of the nature of lipid species observed near and inside the injury sites. The ability to combine CARS microscopy for gaining morphochemical information and Raman spectroscopy for gaining insights to chemical fingerprint of lipid species was already shown in a study of lipid droplets [251].

Images obtained by CARS microscopy show the overall distribution of lipids and, in this way, provide similar information as the Raman spectral maps generated by calculating integral intensity of a CH_2 deformation spectral band. The both particular ways of imaging the spinal cord tissue can be compared in Fig. 49 (F) – (J) showing the Raman maps and Fig. 49 (K) – (O) showing CARS microscopy images. Importantly, CARS microscopy provides submicrometric lateral resolution resulting in ability to visualize the finer morphological details of the tissue.

The region with dense lipid formation directly near the injury site of the sample #1 is shown at higher magnification in Figure 50. Fig. 50 (A) corresponds to light microscopy image of H&E staining, which shows damaged nervous tissue characterized by microcystic morphology (left side of the image), opposed to aligned and densely packed white matter in the contralateral tissue (left side of the image). CARS image in Fig. 50 (B) shows that the fragmented myelin sheets and lipid droplets are confined in the area of damaged tissue compared with contralateral white matter with highly ordered myelinated axons.

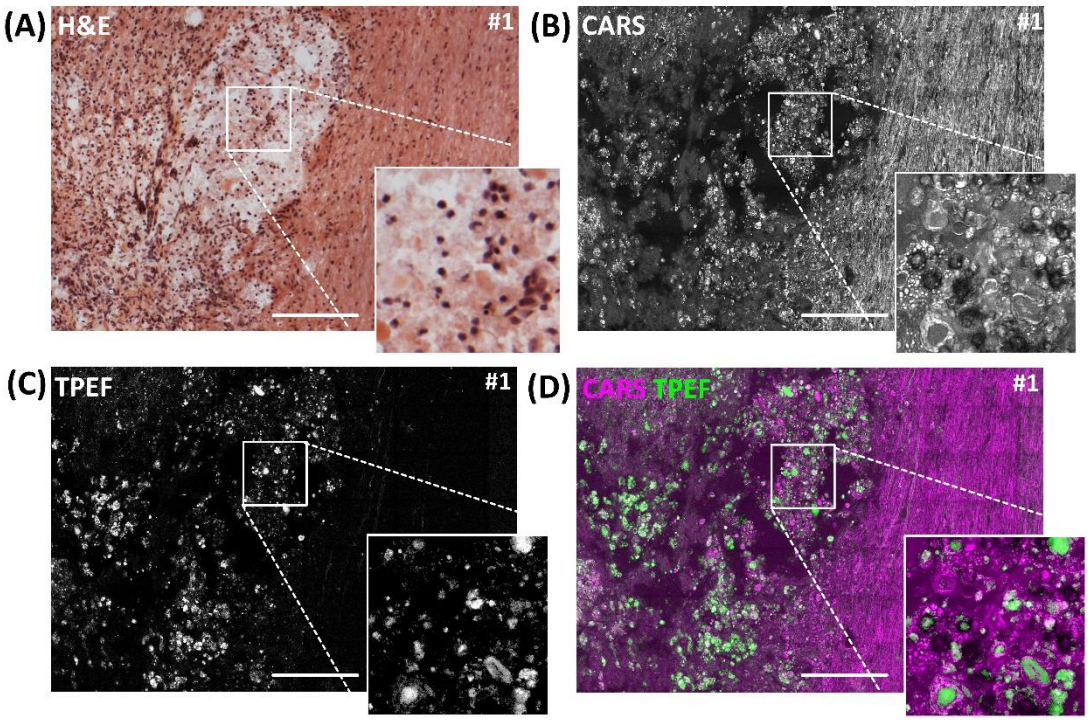

Figure 50. Higher magnification view of the SCI region with high lipid content. (A): H&E staining, (B): CARS, (C): TPEF, and (D): merged CARS/TPEF images comparing morphology of normal white matter in preserved spinal cord and foam cells in the injured rat spinal cord (sample #1). Scale bar: 200 µm.

Information about the extent of inflammation is provided by simultaneous acquisition of TPEF signal [Fig. 50 (C)], as in damaged spinal cord tissue it visualizes activated microglia/macrophages [23,252]. No TPEF active inflammatory cells appear in the healthy white matter tissue, whereas inflammation localizes in the damaged tissue region. Figure 50 (D) represents merged CARS and TPEF images, where it is seen that a clear overlap between distribution of lipid droplets and inflammatory cells exists. The co-localization of lipid droplets and activated microglia/macrophages indicate the presence of the foam cells in particular lipid dense regions distributed in the vicinity of the lesion core. Foam cells are activated microglia/macrophages, which engulf substantial amounts of myelin debris, which, in case of SCI, is deposited as a result of a white matter damage. As a result, foam cells are laden with cytoplasmic lipid droplets. The presence of foam cells was also confirmed by

H&E staining. With the addition of the submicrometer morphochemical information provided by CARS/TPEF imaging, it can be concluded that lipid dense regions indicated by arrows in the Raman spectral maps in Figs. 49 (F) – (H) and (J): (i) are inflammatory regions; (ii) incorporate disrupted myelin sheets; (iii) contain fluorescent foam cells; (iv) they are devoid of integer myelinated axons.

Particularly, CARS/TPEF microscopic imaging provided the above listed additional information. This clearly shows that the evaluation of lipid species that are present in the injury region of damaged spinal cord tissue by assessing lipid distribution with Raman spectroscopic mapping of CH_2 spectral band is not comprehensive, i.e. Raman spectral band at 1440 cm^{-1} is not a suitable spectral marker to exclusively address inflammation. It is also known that the clearance of myelin debris in CNS is slow: after the CNS injury the myelin debris and inflammatory foam cells can remain for weeks [253,254]. Therefore, the sole lipid content evaluation cannot be a reliable way of analysis to distinguish between regions of preserved tissue with myelinated axons and regions of ongoing fragmentation of myelin sheets and inflammatory activity.

Distribution of esterified lipids

Myelin is mainly composed of cholesterol, phospholipids, galactolipids and plasmalogens with a molar ratio of approximately 2:2:1:1 [188]. Myelin debris produced as a consequence of SCI is being cleared up by phagocytic cells. It is, therefore, to be expected that metabolites of cholesterol and phospholipids should mainly make up the composition of lipid droplets in macrophages. Thus, it is important to analyze spectral markers of cholesterol and phospholipids metabolites to retrieve chemical selectivity of Raman microspectroscopy for inflammation.

The cholesterol is stored in a form of cholesteryl esters in intracellular lipid droplets [255]. Free cholesterol and cholesteryl esters generate characteristic sharp Raman signal at 697 cm^{-1} attributed to sterol ring vibrations [256]. However, the direct approach to map the integral intensity of this sterol ring vibration did not enable to clearly visualize the inflammation in Raman maps. This result can be explained in following way. To maintain cellular cholesterol homeostasis, the hydrolysis of neutral cholesteryl esters, which opposes the esterification of cholesterol, is crucial [257]. The free cholesterol can be released by macrophages intracellularly to be processed on site. Otherwise, it can be transferred away from the lesion by migrating macrophages [257]. However, mammalian cells, including foam cells, do not have the ability to degrade the sterol ring. This explains why tracking the sterol ring distribution

by Raman spectroscopy cannot provide reliable information to localize degrading myelin and foam cells.

For storage in lipid droplets, lipid esterification process is critical. The phospholipids are completely hydrolyzed in foam cells. As a result, large amounts of free fatty acids are produced [258], which are afterwards esterified [259]. Cholesteryl and fatty acids esters are best represented in Raman spectra by a carbonyl group stretching vibration at 1743 cm^{-1} [260,261]. Therefore, the integral intensity of this particular band was calculated and representative Raman spectral maps are shown in Fig. 51 (A) – (E). The lipid esterification is most prominent in the injured tissue regions. By comparison with Fig. 49, it can be seen that the lipid esterification localizes together with the foam cells, which were detected with CARS/TPEF. The average Raman spectrum from 12 × 12

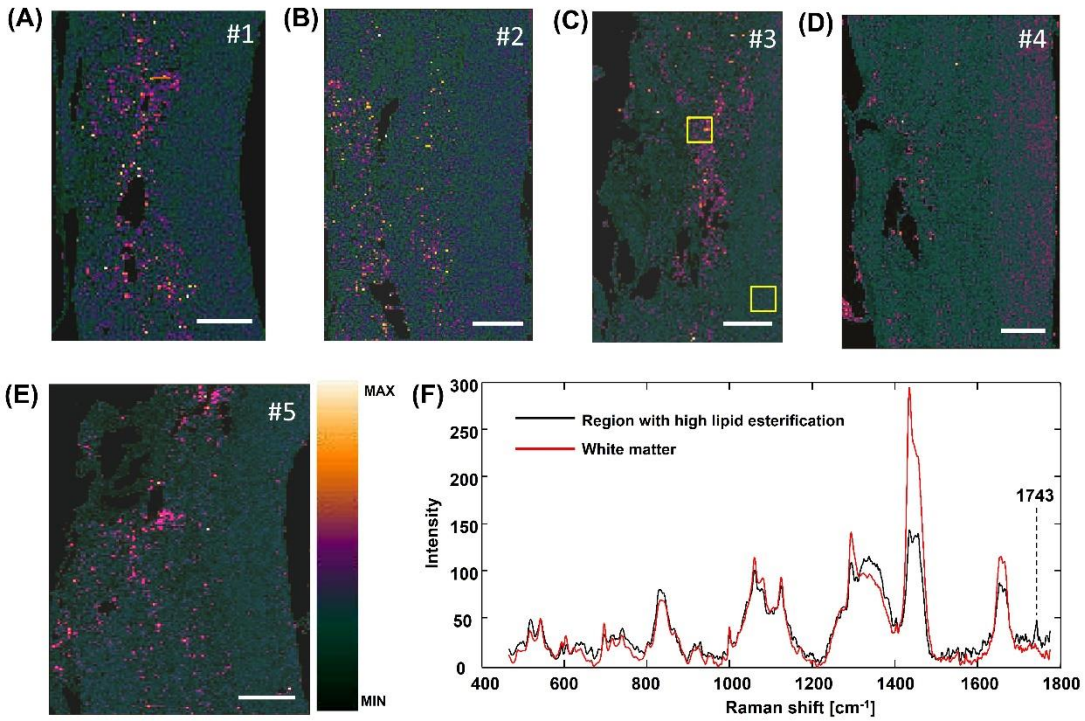

Figure 51. Raman spectral maps produced by calculating integral intensity of carbonyl vibrational band of samples #1 - #5. (A) – (E): Carbonyl stretching vibration at 1743 cm^{-1} integral intensity maps, illustrating the distribution of esterified lipids. Scale bar: 0.5 mm. (F): Raman spectra of regions with high lipid esterification (injury) and low lipid esterification (white matter); the spectra were calculated by averaging all spectra in 12 × 12 pixels large regions, as indicated by boxes in C.

pixels area, corresponding to injured tissue characterized by strong lipid esterification, was calculated and compared with average spectrum from 12 × 12 pixels area, corresponding to normal white matter. These spectra shown for comparison in Fig. 51 (F), clearly demonstrate that the carbonyl band is visible in the spectrum from the region with high lipid esterification and is absent in the spectrum from preserved white matter.

By interpreting the Raman spectral maps in Fig. 51, it should be taken into account that the lipids of CNS contain large amounts of unsaturated fatty acids and, therefore, are particularly sensitive to oxidation. Increased oxidative damage and lipid peroxidation in regard of CNS damage were reported in other studies [262]. As a consequence of oxidative damage, various reactive carbonyl compounds are generated as part of advanced lipid peroxidation end-products [263]. Taken generally, these carbonyl compounds cannot be excluded from contribution to the intensity of the Raman spectral band at 1743 cm^{-1}. However, in the case of SCI in the rat, the lipid oxidation is restricted to acute phase and complete at around 5 days after the injury [233]. As in Fig. 51 shown rat spinal cord tissue samples are collected one month after the injury, it can be stated that no significant lipid peroxidation is expected in this case.

Inflammatory regions are enriched with saturated fatty acids

Spectral Raman maps based on integral intensity of spectral band at 1743 cm^{-1} highlight the distribution of esterified lipids in the lesioned spinal cord region versus preserved nervous tissue and allow to localize inflammation. Also, the information about other types of lipids or fatty acids, which accumulate in injured and inflammatory regions of spinal cord and which are produced in process of myelin degradation in foam cells or as part of inflammatory pathways, is of importance. This particular information from Raman data can

be retrieved by using chemometrical spectral data processing methods. Particlarly, PCA was applied to Raman spectral data.

The PCA was performed on the Raman spectral data merged in one dataset of all the samples. The five principal components were needed to retrieve the information about the distribution of inflammation. The first to fourth principal components correspond to the different nervous tissue components as, for example, lipids or collagen. Raman spectral fingerprints representative for these tissue components were already discussed in subchapter 3.3.3.2.

The inflammation clearly appears to be associated with the fifth principal component (Fig. 52). By comparing the Raman maps in Figs. 52 (A) – 52 (E) with the TPEF images in Figs. 49 (P) – 49 (T), the presence of fluorescent activated microglia/macrophages is seen in the same regions with high pixel intensities (representing higher score) in Raman maps of the fifth principal component. The more detailed map of fifth component of PCA and corresponding CARS and TPEF images are shown in Figs. 52 (G) – Fig. 51 (J) and clearly indicate the co-localization of the regions representing fifth component with lipid droplets and fluorescent activated microglia/macrophages. The fraction of variance determining fifth component is relatively small, namely, 0.13%. Therefore, the concentration of related compound within the SCI is very low. The associated loading vector [Fig. 52 (F)] indicate the presence of saturated fatty acids. The bands at 1060 cm^{-1} and 1126 cm^{-1} are due to C—C stretching vibrations and the ones at 1293 and 1434 cm^{-1} are attributed to CH_2 and CH_3 deformational vibrations [261,264]. The negative spectral band at 1658 cm^{-1} corresponds to

C=C stretching vibration [261] and confirms the relation of this component with saturated type of lipids.

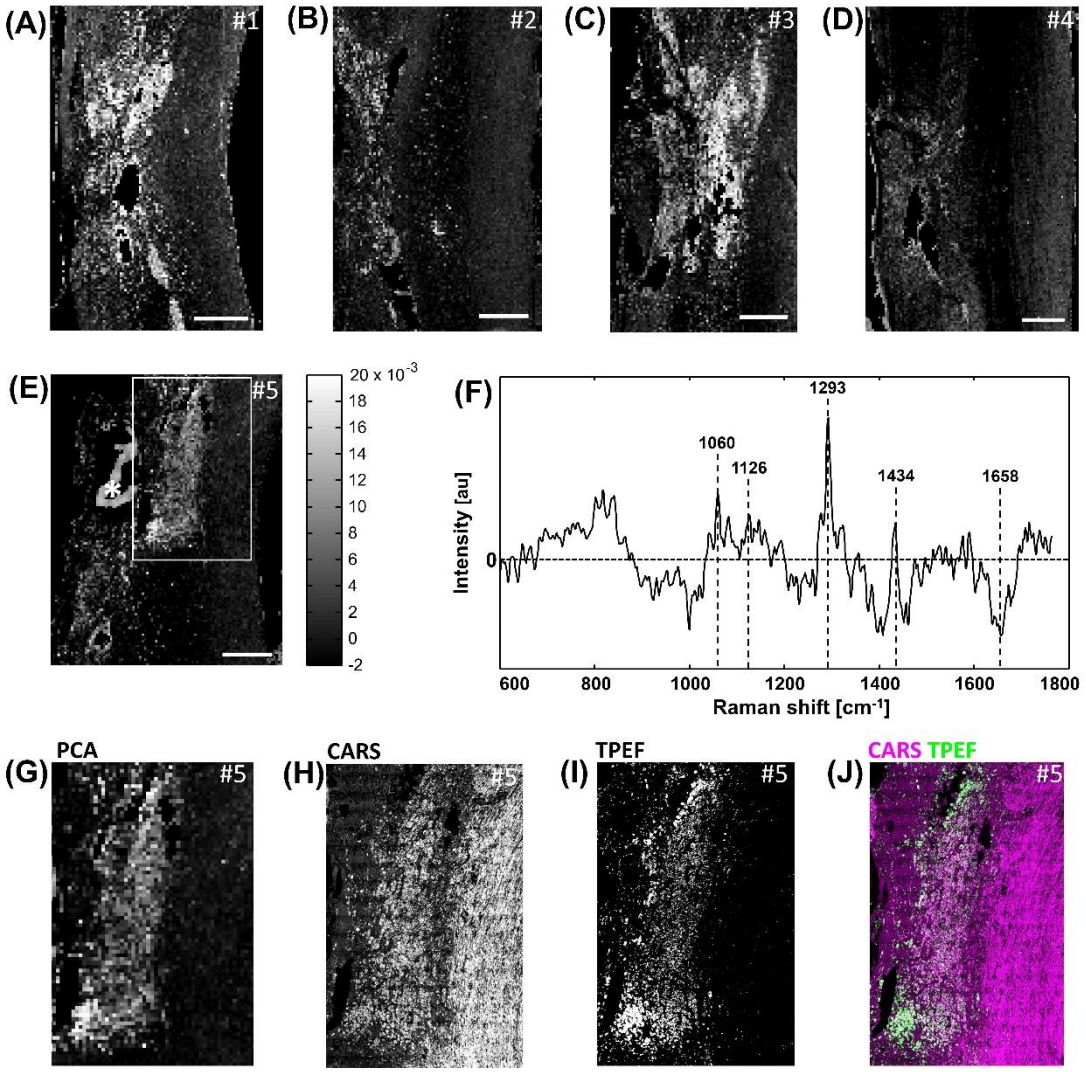

Figure 52. PCA: (A–E) maps of score values for samples #1 - #5 and (F) loading vector for the fifth component. (G): Zoom-in of the box in the score map of sample #5 shown in E; (H–J): CARS, TPEF, and merged images of sample #5, respectively, of the same region shown in G. Scale bar: 0.5 mm. * in E indicates the alginate hydrogel implant.

One recent study reported that the acute activation of microglial cells leads to increase of cellular total saturated fatty acids. Particularly, the content of palmitic acid (C16:0) and stearic acid (C18:0) is being elevated [265]. However, the presence of myristic acid (C14:0) is strongly suggested from the spectral pattern of the loading vector discussed above. The band positions of the loading vector are matching with high precision the positions of the bands

reported in Ref. [261]: the most intense Raman spectral bands of myristic acid are at 1062, 1125, 1294 and 1433 cm^{-1}, while the corresponding spectral bands of both palmitic and stearic acids are all shifted 5 to 12 cm^{-1} towards higher wavenumbers. The changes of myristic acid content upon activation of microglia was not reported [265]. However, from the results of this thesis, the increased content of myristic acid seems to be clearly related with the increased amount of inflammatory cells in comparison with other tissue regions.

Still, it remains unclear, whether the saturated fatty acids are produced during the myelin, which is laden in lipid droplets, degradation. In fact, whereas the upregulation of saturated fatty acids in activated microglia was addressed in Ref. [265], their subcellular localization and possible relation with lipid droplets have not been studied up to now. Moreover, no references, which would report the accumulation of saturated fatty acids inside the lipid droplets of immune cells could be disclosed. The only exception are the cases, where the immune cells are cultured in saturated lipids-enriched media. It is known that the lipids of CNS possess a very high content of polyunsaturated fatty acids, particularly arachidonic acid (C20:4) and docosahexaenoic acid (C22:6) [266]. Actually, the spectral signature of unsaturated fatty acids [i.e. oleic acid (C18:1)] was found, when the necrotic regions with presence of foam cells and macrophages in brain tissue modified by glioblastoma were investigated by Raman spectroscopy [88]. *In vitro* Raman microspectroscopic experiments of macrophages indicated that esterified unsaturated lipids is the main constituent of the lipid droplets [267,268]. By application of resonance Raman spectroscopy it was found that the unsaturated lipid moieties are highly abundant in lipid droplets in leucocytes. These lipid droplets also act as reservoir for arachidonic acid, which is involved in activation pathway of immune cells [269]. To sum up, the available references do not provide sufficient information for clear relation of the overexpression of saturated fatty

acids within the lesioned spinal cord tissue with the storage of myelin degradation products inside the lipid droplets in foam cells.

The direct identification of lipid droplets from other cellular components is not possible from the Raman data acquired in this study due to too low lateral resolution of the used Raman microspectrometer. However, the precise comparison of Raman score maps of the fifth principal component with CARS and TPEF images provides further insights. Detailed inspection of the spatial distribution of signals in the inflammatory regions reveals that the particular Raman score maps mimic the distribution of TPEF signal rather than distribution of lipid droplets localized by CARS signal [compare Figs. 52 (G) with 52 (H) and 52 (I)].

It was hypothesized that palmitic and stearic acids may be involved in the pathway, which modulates the expression of inflammatory cytokines, activation [265]. Also, it is known that myristic acid plays an important role in the cell lipid metabolism, as it regulates the production of polyunsaturated fatty acids (e.g. of docosahexaenoic acid) [270]. Furthermore, recent findings suggest the specific regulatory role of myristic acid by its capability to modify activities of enzymes or functions of proteins through their N-terminal myristoylation. In particular, myristic acid regulates mammalian desaturases, which are enzymes involved in the metabolism of lipids, activity [271]. These facts suggest that the small content of saturated fatty acids in foam cell dense regions of injured spinal cord are not just products of myelin degradation stored in lipid droplets, but are rather more likely to play an active role in the metabolism of lipids in activated microglia/macrophages.

3.3.4 Conclusions

1. FTIR and Raman microspectroscopic imaging enable to address different biochemical aspects of central nervous system tissue alterations induced by spinal cord injury.
2. FTIR and Raman chemical images of 28 injured rat spinal cords allowed to perform quantitative assessment of tissue demyelination and scarring in order to assess the therapeutic effects of non-functionalized soft alginate hydrogel implants. These implants (i) may help to preserve the overall tissue architecture and morphology, (ii) may limit the ongoing demyelination of CNS tissue and (iii) may reduce scarring at the chronic stage of SCI.
3. Both FTIR and Raman microspectroscopic imaging are superior for monitoring non-functionalized soft alginate hydrogel implants in SCI: particular implants have a long-term chemical stability up to six-months after the implantation in nervous tissue of rat spinal cord.
4. No massive axonal growth across the lesion could be proved in animals treated by using alginate hydrogel. Nevertheless, isolated axons inside the lesion were found by CARS imaging in several experimental samples supporting that the non-functionalized soft alginate hydrogel implants are permissive to axon growth in animal model.
5. Alterations of lipids, which are triggered by spinal cord injury-induced inflammation, was for the first time addressed by spectroscopic studies. It was shown that: (i) unspecific mapping of CH_2 (and sterol ring) Raman band intensity to address the lipid distribution does not enable to discern between preserved white matter and inflammatory regions; (ii) mapping of carbonyl Raman band intensity to address distribution of esterified lipids is an appropriate approach to localize inflammatory regions with lipid laden microglia/macrophages; (iii) inflammatory

regions of SCI are rich of saturated fatty acids, which are likely taking part in the lipid metabolism of activated microglia/macrophages.

REFERENCES

[1] W. Du, Y. Wang, Q. Luo, and B. F. Liu, “Optical molecular imaging for systems biology: From molecule to organism,” *Anal. Bioanal. Chem.* **386**, 444–457 (2006).

[2] N. Farahani and C. Monteith, “The coming paradigm shift: A transition from manual to automated microscopy,” *J. Pathol. Inform.* **7**, 35 (2016).

[3] C. Preza, D. L. Snyder, and J.-A. Conchello, “Theoretical development and experimental evaluation of imaging models for differential-interference-contrast microscopy,” *J. Opt. Soc. Am. A* **16**, 2185 (1999).

[4] L. L. de Matos, D. C. Trufelli, M. G. L. de Matos, and M. A. da S. Pinhal, “Immunohistochemistry as an important tool in biomarkers detection and clinical practice,” *Biomark. Insights* **2010** (2010).

[5] R. M. Levenson, A. Fornari, and M. Loda, “Multispectral imaging and pathology: seeing and doing more,” *Expert Opin. Med. Diagn.* **2**, 1067–1081 (2008).

[6] M. J. Baker, J. Trevisan, P. Bassan, R. Bhargava, H. J. Butler, K. M. Dorling, P. R. Fielden, S. W. Fogarty, N. J. Fullwood, et al., “Using Fourier transform IR spectroscopy to analyze biological materials,” *Nat. Protoc.* **9**, 1771–1791 (2014).

[7] S. Y. Lin, M. J. Li, and W. T. Cheng, “FT-IR and Raman vibrational microspectroscopies used for spectral biodiagnosis of human tissues,” *Spectroscopy* **21** (2007).

[8] M. Hermes, R. B. Morrish, L. Huot, L. Meng, S. Junaid, J. Tomko, G. R. Lloyd, W. T. Masselink, P. Tidemand-Lichtenberg, et al., “Mid-IR hyperspectral imaging for label-free histopathology and cytology,” *J. Opt.* **20** (2018).

[9] B. H. Hokr and V. V. Yakovlev, “Raman signal enhancement via elastic light scattering,” *Opt. Express* **21**, 11757 (2013).

[10] A. Volkmer, “Vibrational imaging and microspectroscopies based on coherent anti-stokes raman scattering microscopy,” *J. Phys. D. Appl. Phys.* **38** (2005).

[11] J. P. Pezacki, J. A. Blake, D. C. Danielson, D. C. Kennedy, R. K. Lyn, and R. Singaravelu, “Chemical contrast for imaging living systems: Molecular

vibrations drive CARS microscopy," *Nat. Chem. Biol.* **7** (2011).

[12] A. S. Marco Andreana, "Optical Microscopy: From Biophotonics to Geophotonics," *Opn*, 42–49 (2014).

[13] T. T. Le, S. Yue, and J.-X. Cheng, "Shedding new light on lipid biology with coherent anti-Stokes Raman scattering microscopy," *J. Lipid Res.* **51**, 3091–3102 (2010).

[14] I. Riemann, R. Le Harzic, K. Mpoukouvalas, A. Heimann, O. Kempski, and P. Charalampaki, "Sub-cellular tumor identification and markerless differentiation in the rat brain in vivo by multiphoton microscopy," *Lasers Surg. Med.* **44**, 719–725 (2012).

[15] S. Cha, "Update on brain tumor imaging," *Curr. Neurol. Neurosci. Rep.* **5** (2005).

[16] C. L. Evans, X. Xu, S. Kesari, X. S. Xie, S. T. C. Wong, and G. S. Young, "Chemically-selective imaging of brain structures with CARS microscopy," *Opt. Express* **15**, 12076 (2007).

[17] T. Meyer, N. Bergner, C. Bielecki, C. Krafft, D. Akimov, B. F. M. Romeike, R. Reichart, R. Kalff, B. Dietzek, et al., "Nonlinear microscopy, infrared, and Raman microspectroscopy for brain tumor analysis," *J. Biomed. Opt.* **16**, 021113 (2011).

[18] F. Sheerin, "Spinal cord injury: anatomy and physiology of the spinal cord.," *Emerg. Nurse* **12** (2004).

[19] S. Klussmann and A. Martin-Villalba, "Molecular targets in spinal cord injury.," *J. Mol. Med. (Berl).* **83**, 657–671 (2005).

[20] E. J. Bradbury and S. B. McMahon, "Spinal cord repair strategies: why do they work?," *Nat Rev Neurosci* **7**, 644–653 (2006).

[21] P. Freund, A. Curt, K. Friston, and A. Thompson, "Tracking changes following spinal cord injury: insights from neuroimaging," *Neurosci.* **19**, 116–128 (2013).

[22] Y. Shi, D. Zhang, T. B. Huff, X. Wang, R. Shi, X.-M. Xu, and J.-X. Cheng, "Longitudinal in vivo coherent anti-Stokes Raman scattering imaging of demyelination and remyelination in injured spinal cord," *J. Biomed. Opt.* **16**, 106012 (2011).

[23] R. Galli, O. Uckermann, M. J. Winterhalder, K. H. Sitoci-Ficici, K. D. Geiger, E. Koch, G. Schackert, A. Zumbusch, G. Steiner, et al., "Vibrational

spectroscopic imaging and multiphoton microscopy of spinal cord injury," *Anal. Chem.* **84**, 8707–8714 (2012).

[24] B. H. Stuart, *Infrared Spectroscopy: Fundamentals and Applications* (Wiley, 2005).

[25] W. David, *Molecular Symmetry* (John Wiley & Sons, Chichester, United Kingdom, 2009).

[26] B. C. Smith, *Fundamentals of Fourier Transform Infrared Spectroscopy, Second Editionitle*, Second (CRC Press, Boca Raton, USA, 2011).

[27] J. M. Thompson, *Infrared Spectroscopy* (CRC Press, Singapore, 2018).

[28] P. R. Griffiths and J. A. De Haseth, *Fourier Transform Infrared Spectrometry* (John Wiley & Sons, Hoboken, USA, 2007).

[29] S. M. LeVine and D. L. Wetzel, "Chemical analysis of multiple sclerosis lesions by FT-IR microspectroscopy.," *Free Radic. Biol. Med.* **25**, 33–41 (1998).

[30] R. Bhargava, "Infrared spectroscopic imaging: The next generation," *Appl. Spectrosc.* **66** (2012).

[31] J. E. Katon, "Infrared microspectroscopy. A review of fundamentals and applications," *Micron* **27** (1996).

[32] A. A. Ismail, F. R. van de Voort, and J. Sedman, "Fourier transform infrared spectroscopy: Principles and applications," *Tech. Instrum. Anal. Chem.* **18**, 93–139 (1997).

[33] W. M. Doyle, "Principles and applications of Fourier transform infrared (FTIR) process analysis," *Process Control Qual.* **2**, 11–41 (1992).

[34] L. M. Miller and P. Dumas, "Chemical imaging of biological tissue with synchrotron infrared light," *Biochim. Biophys. Acta - Biomembr.* **1758** (2006).

[35] Z. Movasaghi, S. Rehman, and D. I. ur Rehman, "Fourier Transform Infrared (FTIR) Spectroscopy of Biological Tissues," *Appl. Spectrosc. Rev.* **43**, 134–179 (2008).

[36] S. Akkas, M. Severcan, O. Yilmaz, and F. Severcan, "Effects of lipoic acid supplementation on rat brain tissue: An FTIR spectroscopic and neural network study," *Food Chem.* **105**, 1281–1288 (2007).

[37] B. W. Barry, H. G. M. Edwards, and A. C. Williams, "Fourier transform

Raman and infrared vibrational study of human skin: Assignment of spectral bands," *J. Raman Spectrosc.* **23**, 641–645 (1992).

[38] A. Barth and C. Zscherp, "What vibrations tell about proteins," *Q. Rev. Biophys.* **35**, (2002).

[39] I. Dreissig, S. Machill, R. Salzer, and C. Krafft, "Quantification of brain lipids by FTIR spectroscopy and partial least squares regression," *Spectrochim. Acta - Part A Mol. Biomol. Spectrosc.* **71**, 2069–2075 (2009).

[40] C. Krafft, S. B. Sobottka, G. Schackert, and R. Salzer, "Analysis of human brain tissue, brain tumors and tumor cells by infrared spectroscopic mapping," *Analyst* **129**, 921 (2004).

[41] G. Steiner, A. Shaw, L. P. I. Choo-Smith, M. H. Abuid, G. Schackert, S. Sobottka, W. Steller, R. Salzer, and H. H. Mantsch, "Distinguishing and Grading Human Gliomas by IR Spectroscopy," *Biopolym. - Biospectroscopy Sect.* **72**, 464–471 (2003).

[42] C. Beleites, G. Steiner, M. G. Sowa, R. Baumgartner, S. Sobottka, G. Schackert, and R. Salzer, "Classification of human gliomas by infrared imaging spectroscopy and chemometric image processing," *Vib. Spectrosc.* **38**, 143–149 (2005).

[43] N. Amharref, A. Beljebbar, S. Dukic, L. Venteo, L. Schneider, M. Pluot, R. Vistelle, and M. Manfait, "Brain tissue characterisation by infrared imaging in a rat glioma model.," *d* **1758**, 892–899 (2006).

[44] K. R. Bambery, E. Schültke, B. R. Wood, S. T. R. MacDonald, K. Ataelmannan, R. W. Griebel, B. H. J. Juurlink, and D. McNaughton, "A Fourier transform infrared microspectroscopic imaging investigation into an animal model exhibiting glioblastoma multiforme," *Biochim. Biophys. Acta - Biomembr.* **1758**, 900–907 (2006).

[45] C. Krafft, L. Shapoval, S. B. Sobottka, K. D. Geiger, G. Schackert, and R. Salzer, "Identification of primary tumors of brain metastases by SIMCA classification of IR spectroscopic images," *Biochim. Biophys. Acta - Biomembr.* **1758**, 883–891 (2006).

[46] K. Ali, Y. Lu, C. Christensen, T. May, C. Hyett, R. Griebel, D. Fourney, K. Meguro, L. Resch, et al., "Fourier transform infrared spectromicroscopy and hierarchical cluster analysis of human meningiomas.," *Int. J. Mol. Med.* **21**, 297–301 (2008).

[47] A. Beljebbar, N. Amharref, A. Lévèques, S. Dukic, L. Venteo, L. Schneider, M. Pluot, and M. Manfait, "Modeling and quantifying biochemical

changes in C6 tumor gliomas by fourier transform infrared imaging," *Anal. Chem.* **80**, 8406–8415 (2008).

[48] S. B. Sobottka, K. D. Geiger, R. Salzer, G. Schackert, and C. Krafft, "Suitability of infrared spectroscopic imaging as an intraoperative tool in cerebral glioma surgery," *Anal. Bioanal. Chem.* **393**, 187–195 (2009).

[49] K. Wehbe, R. Pineau, S. Eimer, A. Vital, H. Loiseau, and G. Déléris, "Differentiation between normal and tumor vasculature of animal and human glioma by FTIR imaging," *Analyst* **135**, 3052 (2010).

[50] L. P. Choo, M. Jackson, W. C. Halliday, and H. H. Mantsch, "Infrared spectroscopic characterisation of multiple sclerosis plaques in the human central nervous system.," *Biochim. Biophys. Acta* **1182**, 333–337 (1993).

[51] P. Heraud, S. Caine, N. Campanale, T. Karnezis, D. McNaughton, B. R. Wood, M. J. Tobin, and C. C. A. Bernard, "Early detection of the chemical changes occurring during the induction and prevention of autoimmune-mediated demyelination detected by FT-IR imaging," *Neuroimage* **49**, 1180–1189 (2010).

[52] J. Ruiz-Sanz, J. Ruiz-Cabello, P. L. Mateo, and M. Cortijo, "The thermal transition in crude myelin proteolipid has a lipid rather than protein origin," *Eur. Biophys. J.* **21**, 71–76 (1992).

[53] W. K. Surewicz, M. A. Moscarello, and H. H. Mantsch, "Fourier transform infrared spectroscopic investigation of the interaction between myelin basic protein and dimyristoylphosphatidylglycerol bilayers," *Biochemistry* **26**, 3881–3886 (1987).

[54] L. G. Rodriguez, S. J. Lockett, and G. R. Holtom, "Coherent anti-stokes Raman scattering microscopy: a biological review.," *Cytometry. A* **69**, 779–791 (2006).

[55] V. Šablinskas and J. Čeponkus, *Modernioji molekulių virpesinė spektrometrija* (Vilnius, Lietuva, 2014).

[56] J. R. Ferraro and K. Nakamoto, *Introductory Raman Spectroscopy* (Academic Press, San Diego, USA, 2012).

[57] C. Krafft, B. Dietzek, M. Schmitt, and J. Popp, "Raman and coherent anti-Stokes Raman scattering microspectroscopy for biomedical applications.," *J. Biomed. Opt.* **17**, 040801 (2012).

[58] F. Siebert and P. Hildebrandt, *Vibrational Spectroscopy in Life Science* (Wiley-VCH Verlag, Weinheim, Germany, 2007).

[59] K. J. I. Ember, M. A. Hoeve, S. L. McAughtrie, M. S. Bergholt, B. J. Dwyer, M. M. Stevens, K. Faulds, S. J. Forbes, and C. J. Campbell, “Raman spectroscopy and regenerative medicine: a review,” *npj Regen. Med.* **2**, 12 (2017).

[60] C. Krafft, B. Dietzek, and J. Popp, “Raman and CARS microspectroscopy of cells and tissues,” *Analyst* **134**, 1046 (2009).

[61] C. Gendrin, Y. Roggo, and C. Collet, “Pharmaceutical applications of vibrational chemical imaging and chemometrics: A review,” *J. Pharm. Biomed. Anal.* **48** (2008).

[62] N. Gierlinger and M. Schwanninger, “The potential of Raman microscopy and Raman imaging in plant research,” *Spectroscopy* **21** (2007).

[63] Y. Y. Huang, C. M. Beal, W. W. Cai, R. S. Ruoff, and E. M. Terentjev, “Micro-Raman spectroscopy of algae: Composition analysis and fluorescence background behavior,” *Biotechnol. Bioeng.* **105**, 889–898 (2010).

[64] P. Colomban, “Raman analyses and" smart" imaging of nanophases and nanosized materials,” *Spectrosc. Eur.* **15**, 8–16 (2003).

[65] A. Jorio, “Raman Spectroscopy in Graphene-Based Systems: Prototypes for Nanoscience and Nanometrology,” *ISRN Nanotechnol.* **2012**, 1–16 (2012).

[66] G. Gouadec and P. Colomban, “Raman Spectroscopy of nanomaterials: How spectra relate to disorder, particle size and mechanical properties,” *Prog. Cryst. Growth Charact. Mater.* **53** (2007).

[67] Y.-Z. Feng and D.-W. Sun, “Application of Hyperspectral Imaging in Food Safety Inspection and Control: A Review,” *Crit. Rev. Food Sci. Nutr.* **52**, 1039–1058 (2012).

[68] S. Lohumi, S. Lee, H. Lee, and B. K. Cho, “A review of vibrational spectroscopic techniques for the detection of food authenticity and adulteration,” *Trends Food Sci. Technol.* **46** (2015).

[69] H. Ahn, H. Song, D.-M. Shin, K. Kim, and J.-R. Choi, “Emerging optical spectroscopy techniques for biomedical applications—A brief review of recent progress,” *Appl. Spectrosc. Rev.* **53** (2018).

[70] C. Krafft and J. Popp, “The many facets of Raman spectroscopy for biomedical analysis,” *Anal. Bioanal. Chem.* **407** (2015).

[71] A. Downes and A. Elfick, “Raman spectroscopy and related techniques in

biomedicine," *Sensors* **10** (2010).

[72] D. Naumann, "FT-infrared and FT-Raman spectroscopy in biomedical research," *Appl. Spectrosc. Rev.* **36** (2001).

[73] M. Li, J. Xu, M. Romero-Gonzalez, S. A. Banwart, and W. E. Huang, "Single cell Raman spectroscopy for cell sorting and imaging," *Curr. Opin. Biotechnol.* **23** (2012).

[74] R. J. Swain and M. M. Stevens, "Raman microspectroscopy for non-invasive biochemical analysis of single cells.," *Biochem. Soc. Trans.* **35**, 544–549 (2007).

[75] T. Huser and J. Chan, "Raman spectroscopy for physiological investigations of tissues and cells," *Adv. Drug Deliv. Rev.* **89** (2015).

[76] A. C. S. Talari, Z. Movasaghi, S. Rehman, and I. U. Rehman, "Raman spectroscopy of biological tissues," *Appl. Spectrosc. Rev.* **50** (2015).

[77] D. I. Ellis and R. Goodacre, "Metabolic fingerprinting in disease diagnosis: biomedical applications of infrared and Raman spectroscopy," *Analyst* **131**, 875 (2006).

[78] Q. Tu and C. Chang, "Diagnostic applications of Raman spectroscopy," *Nanomedicine Nanotechnology, Biol. Med.* **8** (2012).

[79] C. Krafft, L. Neudert, T. Simat, and R. Salzer, "Near infrared Raman spectra of human brain lipids," *Spectrochim. Acta - Part A Mol. Biomol. Spectrosc.* **61**, 1529–1535 (2005).

[80] Z. Movasaghi, S. Rehman, and I. U. Rehman, "Raman spectroscopy of biological tissues," *Appl. Spectrosc. Rev.* **42** (2007).

[81] B. Prescott, W. Steinmetz, and G. J. Thomas, "Characterization of DNA structures by laser Raman spectroscopy," *Biopolymers* **23**, 235–256 (1984).

[82] H. Abramczyk and A. Imiela, "The biochemical, nanomechanical and chemometric signatures of brain cancer," *Spectrochim. Acta - Part A Mol. Biomol. Spectrosc.* **188**, 8–19 (2018).

[83] K. Tashibu, "[Analysis of water content in rat brain using Raman spectroscopy]," *No To Shinkei* **42**, 999–1004 (1990).

[84] A. Mizuno, H. Kitajima, K. Kawauchi, S. Muraishi, and Y. Ozaki, "Near-infrared Fourier transform Raman spectroscopic study of human brain

tissues and tumours," *J. Raman Spectrosc.* **25**, 25–29 (1994).

[85] S. Koljenović, L. P. in. Choo-Smith, T. C. B. Schut, J. M. Kros, H. J. Van den Berge, and G. J. Puppels, "Discriminating vital tumor from necrotic tissue in human glioblastoma tissue samples by Raman spectroscopy," *Lab. Investig.* **82**, 1265–1277 (2002).

[86] S. N. Kalkanis, R. E. Kast, M. L. Rosenblum, T. Mikkelsen, S. M. Yurgelevic, K. M. Nelson, A. Raghunathan, L. M. Poisson, and G. W. Auner, "Raman spectroscopy to distinguish grey matter, necrosis, and glioblastoma multiforme in frozen tissue sections," *J. Neurooncol.* **116**, 477–485 (2014).

[87] R. E. Kast, G. W. Auner, M. L. Rosenblum, T. Mikkelsen, S. M. Yurgelevic, A. Raghunathan, L. M. Poisson, and S. N. Kalkanis, "Raman molecular imaging of brain frozen tissue sections," *J. Neurooncol.* **120**, 55–62 (2014).

[88] N. Amharref, A. Beljebbar, S. Dukic, L. Venteo, L. Schneider, M. Pluot, and M. Manfait, "Discriminating healthy from tumor and necrosis tissue in rat brain tissue samples by Raman spectral imaging.," *Biochim. Biophys. Acta* **1768**, 2605–2615 (2007).

[89] C. Krafft, S. B. Sobottka, G. Schackert, and R. Salzer, "Near infrared Raman spectroscopic mapping of native brain tissue and intracranial tumors," *Analyst* **130**, 1070 (2005).

[90] C. Krafft, B. Belay, N. Bergner, B. F. M. Romeike, R. Reichart, R. Kalff, and J. Popp, "Advances in optical biopsy – correlation of malignancy and cell density of primary brain tumors using Raman microspectroscopic imaging," *Analyst* **137**, 5533 (2012).

[91] R. O. P. Draga, M. C. M. Grimbergen, P. L. M. Vijverberg, C. F. P. Van Swol, T. G. N. Jonges, J. A. Kummer, and J. L. H. Ruud Bosch, "In vivo bladder cancer diagnosis by high-volume Raman spectroscopy," *Anal. Chem.* **82**, 5993–5999 (2010).

[92] A. S. Haka, Z. Volynskaya, J. A. Gardecki, J. Nazemi, J. Lyons, D. Hicks, M. Fitzmaurice, R. R. Dasari, J. P. Crowe, et al., "In vivo margin assessment during partial mastectomy breast surgery using Raman spectroscopy," *Cancer Res.* **66**, 3317–3322 (2006).

[93] A. Mahadevan-Jansen, M. F. Mitchell, N. Ramanujam, U. Utzinger, and R. Richards-Kortum, "Development of a Fiber Optic Probe to Measure NIR Raman Spectra of Cervical Tissue in Vivo," *Photochem. Photobiol.* **68**,

427–431 (1998).

[94] A. Beljebbar, S. Dukic, N. Amharref, and M. Manfait, “Ex vivo and in vivo diagnosis of C6 glioblastoma development by Raman spectroscopy coupled to a microprobe,” *Anal. Bioanal. Chem.* **398**, 477–487 (2010).

[95] M. Kirsch, G. Schackert, R. Salzer, and C. Krafft, “Raman spectroscopic imaging for in vivo detection of cerebral brain metastases,” *Anal. Bioanal. Chem.* **398**, 1707–1713 (2010).

[96] M. Jermyn, K. Mok, J. Mercier, J. Desroches, J. Pichette, K. Saint-Arnaud, L. Bernstein, M. C. Guiot, K. Petrecca, et al., “Intraoperative brain cancer detection with Raman spectroscopy in humans,” *Sci. Transl. Med.* **7** (2015).

[97] J. Desroches, M. Jermyn, K. Mok, C. Lemieux-Leduc, J. Mercier, K. St-Arnaud, K. Urmey, M.-C. Guiot, E. Marple, et al., “Characterization of a Raman spectroscopy probe system for intraoperative brain tissue classification,” *Biomed. Opt. Express* **6**, 2380 (2015).

[98] J. Desroches, M. Jermyn, M. Pinto, F. Picot, M. A. Tremblay, S. Obaid, E. Marple, K. Urmey, D. Trudel, et al., “A new method using Raman spectroscopy for in vivo targeted brain cancer tissue biopsy,” *Sci. Rep.* **8** (2018).

[99] H. Chen, W. Xu, and N. Broderick, “Raman spectroscopy for minimally invasive spinal nerve detection,” in *M2VIP 2016 - Proc. 23rd Int. Conf. Mechatronics Mach. Vis. Pract.* (2017).

[100] T. A. Anderson, J. W. Kang, T. Gubin, R. R. Dasari, and P. T. C. So, “Raman Spectroscopy Differentiates Each Tissue from the Skin to the Spinal Cord,” *Anesthesiology* **125**, 793–804 (2016).

[101] T. Saxena, B. Deng, D. Stelzner, J. Hasenwinkel, and J. Chaiken, “Raman spectroscopic investigation of spinal cord injury in a rat model,” *J. Biomed. Opt.* **16**, 027003 (2011).

[102] F. El-Diasty, “Coherent anti-Stokes Raman scattering: Spectroscopy and microscopy,” *Vib. Spectrosc.* **55**, 1–37 (2011).

[103] C. L. Evans, E. O. Potma, M. Puoris’haag, D. Côté, C. P. Lin, and X. S. Xie, “Chemical imaging of tissue in vivo with video-rate coherent anti-Stokes Raman scattering microscopy.,” *Proc. Natl. Acad. Sci. U. S. A.* **102**, 16807–16812 (2005).

[104] C. L. Evans and X. S. Xie, “Coherent anti-Stokes Raman scattering

microscopy: chemical imaging for biology and medicine," *Annu. Rev. Anal. Chem.* **1**, 883–909 (2008).

[105] A. Zumbusch, G. R. Holtom, and X. S. Xie, "Three-dimensional vibrational imaging by coherent anti-stokes raman scattering," *Phys. Rev. Lett.* **82**, 4142–4145 (1999).

[106] J. Cheng, A. Volkmer, L. D. Book, and X. S. Xie, "An Epi-Detected Coherent Anti-Stokes Raman Scattering (E-CARS) Microscope with High Spectral Resolution and High Sensitivity," *J. Phys. Chem. B* **105**, 1277–1280 (2001).

[107] J.-X. Cheng, Y. K. Jia, G. Zheng, and X. S. Xie, "Laser-Scanning Coherent Anti-Stokes Raman Scattering Microscopy and Applications to Cell Biology," *Biophys. J.* **83**, 502–509 (2002).

[108] R. Galli, V. Sablinskas, D. Dasevicius, A. Laurinavicius, F. Jankevicius, E. Koch, and G. Steiner, "Non-linear optical microscopy of kidney tumours," *J. Biophotonics* **7** (2014).

[109] I. Toytman, K. Cohn, T. Smith, D. Simanovskii, and D. Palanker, "Wide-field coherent anti-Stokes Raman scattering microscopy with non-phase-matching illumination.," *Opt. Lett.* **32**, 1941–1943 (2007).

[110] R. S. Lim, J. L. Suhalim, S. Miyazaki-Anzai, M. Miyazaki, M. Levi, E. O. Potma, and B. J. Tromberg, "Identification of cholesterol crystals in plaques of atherosclerotic mice using hyperspectral CARS imaging," *J. Lipid Res.* **52**, 2177–2186 (2011).

[111] C. Matthäus, S. Dochow, G. Bergner, A. Lattermann, B. F. M. Romeike, E. T. Marple, C. Krafft, B. Dietzek, B. R. Brehm, et al., "In vivo characterization of atherosclerotic plaque depositions by Raman-probe spectroscopy and in vitro coherent anti-stokes Raman scattering microscopic imaging on a rabbit model," *Anal. Chem.* **84**, 7845–7851 (2012).

[112] M. Pucetaite, S. Tamosaityte, R. Galli, V. Sablinskas, and G. Steiner, "Microstructure of urinary stones as studied by means of multimodal nonlinear optical imaging," *J. Raman Spectrosc.* **48**, 22–29 (2017).

[113] X. Nan, J.-X. Cheng, and X. S. Xie, "Vibrational imaging of lipid droplets in live fibroblast cells with coherent anti-Stokes Raman scattering microscopy," *J. Lipid Res.* **44**, 2202–2208 (2003).

[114] H. Wang, Y. Fu, P. Zickmund, R. Shi, and J. X. Cheng, "Coherent anti-stokes Raman scattering imaging of axonal myelin in live spinal tissues," *Biophys. J.* **89**, 581–591 (2005).

[115] T. B. Huff and J.-X. Cheng, “In vivo coherent anti-Stokes Raman scattering imaging of sciatic nerve tissue.,” *J. Microsc.* **225**, 175–182 (2007).

[116] E. Bélanger, S. Bégin, S. Laffray, Y. De Koninck, R. Vallée, and D. Côté, “Quantitative myelin imaging with coherent anti-Stokes Raman scattering microscopy: alleviating the excitation polarization dependence with circularly polarized laser beams.,” *Opt. Express* **17**, 18419–18432 (2009).

[117] F. Z. Bioud, P. Gasecka, P. Ferrand, H. Rigneault, J. Duboisset, and S. Brasselet, “Structure of molecular packing probed by polarization-resolved nonlinear four-wave mixing and coherent anti-Stokes Raman-scattering microscopy,” *Phys. Rev. A - At. Mol. Opt. Phys.* **89** (2014).

[118] Y. Fu, H. Wang, T. B. Huff, R. Shi, and J. X. Cheng, “Coherent anti-Stokes Raman scattering imaging of myelin degradation reveals a calcium-dependent pathway in lyso-PtdCho-induced demyelination,” *J. Neurosci. Res.* **85**, 2870–2881 (2007).

[119] H. Ouyang, W. Sun, Y. Fu, J. Li, J.-X. Cheng, E. Nauman, and R. Shi, “Compression Induces Acute Demyelination and Potassium Channel Exposure in Spinal Cord,” *J. Neurotrauma* **27**, 1109–1120 (2010).

[120] Y. Shi, S. Kim, T. B. Huff, R. B. Borgens, K. Park, R. Shi, and J. X. Cheng, “Effective repair of traumatically injured spinal cord by nanoscale block copolymer micelles,” *Nat. Nanotechnol.* **5**, 80–87 (2010).

[121] G. de Vito, I. Tonazzini, M. Cecchini, and V. Piazza, “RP-CARS: label-free optical readout of the myelin intrinsic healthiness,” *Opt. Express* **22**, 13733 (2014).

[122] V. M. Betz, K. H. Sitoci-Ficici, O. Uckermann, E. Leipnitz, A. Iltzsche, C. Thirion, M. Salomon, H. Zwipp, G. Schackert, et al., “Gene-activated fat grafts for the repair of spinal cord injury: a pilot study,” *Acta Neurochir. (Wien).* **158**, 367–378 (2016).

[123] C. Cleff, A. Gasecka, P. Ferrand, H. Rigneault, S. Brasselet, and J. Duboisset, “Direct imaging of molecular symmetry by coherent anti-stokes Raman scattering,” *Nat. Commun.* **7** (2016).

[124] K. Bae, W. Zheng, and Z. Huang, “Quantitative assessment of spinal cord injury using circularly polarized coherent anti-Stokes Raman scattering microscopy,” *Appl. Phys. Lett.* **111** (2017).

[125] Y. Fu, T. J. Frederick, T. B. Huff, G. E. Goings, S. D. Miller, and J.-X. Cheng, “Paranodal myelin retraction in relapsing experimental autoimmune

encephalomyelitis visualized by coherent anti-Stokes Raman scattering microscopy," *J. Biomed. Opt.* **16**, 106006 (2011).

[126] J. Imitola, D. Co^té, S. Rasmussen, X. S. Xie, Y. Liu, T. Chitnis, R. L. Sidman, C. P. Lin, and S. J. Khoury, "Multimodal coherent anti-Stokes Raman scattering microscopy reveals microglia-associated myelin and axonal dysfunction in multiple sclerosis-like lesions in mice," *J. Biomed. Opt.* **16**, 021109 (2011).

[127] P. Gasecka, A. Jaouen, F. Z. Bioud, H. B. de Aguiar, J. Duboisset, P. Ferrand, H. Rigneault, N. K. Balla, F. Debarbieux, et al., "Lipid Order Degradation in Autoimmune Demyelination Probed by Polarized Coherent Raman Microscopy," *Biophys. J.* **113**, 1520–1530 (2017).

[128] T. B. Huff, Y. Shi, W. Sun, W. Wu, R. Shi, and J. X. Cheng, "Real-time CARS imaging reveals a calpain-dependent pathway for paranodal myelin retraction during high-frequency stimulation," *PLoS One* **6** (2011).

[129] R. Turcotte, D. J. Rutledge, E. Bélanger, D. Dill, W. B. Macklin, and D. C. Côté, "Intravital assessment of myelin molecular order with polarimetric multiphoton microscopy," *Sci. Rep.* **6** (2016).

[130] Y. Fu, T. B. Huff, H.-W. Wang, J.-X. Cheng, and H. Wang, "Ex vivo and in vivo imaging of myelin fibers in mouse brain by coherent anti-Stokes Raman scattering microscopy," *Opt. Express* **16**, 19396 (2008).

[131] C. Pohling, T. Buckup, A. Pagenstecher, and M. Motzkus, "Chemoselective imaging of mouse brain tissue via multiplex CARS microscopy," *Biomed. Opt. Express* **2**, 2110 (2011).

[132] T. Meyer, N. Bergner, A. Medyukhina, B. Dietzek, C. Krafft, B. F. M. Romeike, R. Reichart, R. Kalff, and J. Popp, "Interpreting CARS images of tissue within the C-H-stretching region," *J. Biophotonics* **5** (2012).

[133] R. Galli, O. Uckermann, A. Temme, E. Leipnitz, M. Meinhardt, E. Koch, G. Schackert, G. Steiner, and M. Kirsch, "Assessing the efficacy of coherent anti-Stokes Raman scattering microscopy for the detection of infiltrating glioblastoma in fresh brain samples," *J. Biophotonics* **10**, 404–414 (2017).

[134] T. T. Le, T. B. Huff, and J.-X. Cheng, "Coherent anti-Stokes Raman scattering imaging of lipids in cancer metastasis," *BMC Cancer* **9**, 42 (2009).

[135] R. Mitra, O. Chao, Y. Urasaki, O. B. Goodman, and T. T. Le, "Detection of Lipid-Rich Prostate Circulating Tumour Cells with Coherent Anti-Stokes Raman Scattering Microscopy," *BMC Cancer* **12** (2012).

[136] Y. Yang, F. Li, L. Gao, Z. Wang, M. J. Thrall, S. S. Shen, K. K. Wong, and S. T. C. Wong, “Differential diagnosis of breast cancer using quantitative, label-free and molecular vibrational imaging.,” *Biomed. Opt. Express* **2**, 2160–2174 (2011).

[137] L. Gao, F. Li, M. J. Thrall, Y. Yang, J. Xing, A. A. Hammoudi, H. Zhao, Y. Massoud, P. T. Cagle, et al., “On-the-spot lung cancer differential diagnosis by label-free, molecular vibrational imaging and knowledge-based classification,” *J. Biomed. Opt.* **16**, 096004 (2011).

[138] L. Gao, Z. Wang, F. Li, A. A. Hammoudi, M. J. Thrall, P. T. Cagle, and S. T. C. Wong, “Differential Diagnosis of Lung Carcinoma With Coherent Anti-Stokes Raman Scattering Imaging,” *Arch. Pathol. Lab. Med.* **136**, 1502–1510 (2012).

[139] P. J. Campagnola and L. M. Loew, “Second-harmonic imaging microscopy for visualizing biomolecular arrays in cells, tissues and organisms,” *Nat. Biotechnol.* **21** (2003).

[140] F. Helmchen and W. Denk, “Deep tissue two-photon microscopy,” *Nat. Methods* **2** (2005).

[141] A. Ustione and D. W. Piston, “A simple introduction to multiphoton microscopy,” *J. Microsc.* **243**, 221–226 (2011).

[142] J.-X. Cheng, A. Volkmer, and X. S. Xie, “Theoretical and experimental characterization of coherent anti-Stokes Raman scattering microscopy,” *J. Opt. Soc. Am. B* **19**, 1363 (2002).

[143] R. Cicchi, N. Vogler, D. Kapsokalyvas, B. Dietzek, J. Popp, and F. S. Pavone, “From molecular structure to tissue architecture: Collagen organization probed by SHG microscopy,” *J. Biophotonics* **6**, 129–142 (2013).

[144] B. Pearson and T. Weinacht, “Nonlinear optics: Three-in-one microscopy,” *Nat. Photonics* **6** (2012).

[145] R. Cicchi and F. S. Pavone, “Multimodal nonlinear microscopy: A powerful label-free method for supporting standard diagnostics on biological tissues,” *J. Innov. Opt. Health Sci.* **7**, 1–16 (2014).

[146] M. Oheim, D. J. Michael, M. Geisbauer, D. Madsen, and R. H. Chow, “Principles of two-photon excitation fluorescence microscopy and other nonlinear imaging approaches,” *Adv. Drug Deliv. Rev.* **58** (2006).

[147] A. Diaspro, G. Chirico, and M. Collini, “Two-photon fluorescence excitation and related techniques in biological microscopy,” *Q. Rev.*

Biophys. **38** (2005).

[148] P. Campagnola, “Second harmonic generation imaging microscopy: Applications to diseases diagnostics,” *Anal. Chem.* **83**, 3224–3231 (2011).

[149] X. Chen, O. Nadiarynkh, S. Plotnikov, and P. J. Campagnola, “Second harmonic generation microscopy for quantitative analysis of collagen fibrillar structure,” *Nat Protoc* **7**, 654–669 (2012).

[150] K. Tilbury and P. J. Campagnola, “Applications of second-harmonic generation imaging microscopy in ovarian and breast cancer,” *Perspect. Medicin. Chem.* **7**, 21–32 (2015).

[151] I. I. Patel, C. Steuwe, S. Reichelt, and S. Mahajan, “Coherent anti-Stokes Raman scattering for label-free biomedical imaging,” *J. Opt.* **15**, 094006 (2013).

[152] H. Wills, R. Kast, C. Stewart, R. Rabah, A. Pandya, J. Poulik, G. Auner, and M. D. Klein, “Raman spectroscopy detects and distinguishes neuroblastoma and related tissues in fresh and (banked) frozen specimens,” *J. Pediatr. Surg.* **44**, 386–391 (2009).

[153] H. Wills, R. Kast, C. Stewart, B. Sullivan, R. Rabah, J. Poulik, A. Pandya, G. Auner, and M. D. Klein, “Diagnosis of Wilms’ tumor using near-infrared Raman spectroscopy,” *J. Pediatr. Surg.* **44**, 1152–1158 (2009).

[154] S. K. Suvarna, C. Layton, and J. D. Bancroft, *Bancroft’s Theory and Practice of Histological Techniques*, 7th ed. (Elsevier Health Sciences, 2013).

[155] C. Karlsson and M. G. Karlsson, “Effects of long-term storage on the detection of proteins, DNA, and mRNA in tissue microarray slides.,” *J. Histochem. Cytochem.* **59**, 1113–1121 (2011).

[156] M. A. Seidu, A. R. Adams, R. K. Gyasi, Y. Tettey, D. O. Nkansah, and E. K. Wiredu, “Immunoreactivity of some epitopes in longtime inappropriately stored paraffinembedded tissues,” *J. Histotechnol.* **36**, 59–64 (2013).

[157] J. A. Ramos-Vara and M. A. Miller, “When Tissue Antigens and Antibodies Get Along: Revisiting the Technical Aspects of Immunohistochemistry-The Red, Brown, and Blue Technique,” *Vet. Pathol.* **51** (2014).

[158] R. Galli, O. Uckermann, E. Koch, G. Schackert, M. Kirsch, and G. Steiner, “Effects of tissue fixation on coherent anti-Stokes Raman scattering images of brain,” *J. Biomed. Opt.* **19**, 071402 (2013).

[159] E. Ó Faoláin, M. B. Hunter, J. M. Byrne, P. Kelehan, M. McNamara, H. J.

Byrne, and F. M. Lyng, “A study examining the effects of tissue processing on human tissue sections using vibrational spectroscopy,” *Vib. Spectrosc.* **38**, (2005).

[160] S. Devpura, J. S. Thakur, J. M. Poulik, R. Rabah, V. M. Naik, and R. Naik, “Raman spectroscopic investigation of frozen and deparaffinized tissue sections of pediatric tumors: Neuroblastoma and ganglioneuroma,” *J. Raman Spectrosc.* **44**, 370–376 (2013).

[161] Z. Huang, A. McWilliams, S. Lam, J. English, D. McLean, H. Lui, and H. Zeng, “Effect of formalin fixation on the near-infrared Raman spectroscopy of normal and cancerous human bronchial tissues,” *Int. J. Oncol.* (2003).

[162] E. Ó. Faoláin, M. B. Hunter, J. M. Byrne, P. Kelehan, H. A. Lambkin, H. J. Byrne, and F. M. Lyng, “Raman spectroscopic evaluation of efficacy of current paraffin wax section dewaxing agents,” *J. Histochem. Cytochem.* **53**, 121–129 (2005).

[163] J. Depciuch, E. Kaznowska, K. Szmuc, I. Zawlik, M. Cholewa, P. Heraud, and J. Cebulski, “Comparing paraffined and deparaffinized breast cancer tissue samples and an analysis of Raman spectroscopy and infrared methods,” *Infrared Phys. Technol.* **76**, 217–226 (2016).

[164] J. W. Wilson, S. Degan, W. S. Warren, and M. C. Fischer, “Optical clearing of archive-compatible paraffin embedded tissue for multiphoton microscopy,” *Biomed. Opt. Express* **3**, 2752 (2012).

[165] M. Zheng and W. Du, “Phase behavior, conformations, thermodynamic properties, and molecular motion of multicomponent paraffin waxes: A Raman spectroscopy study,” *Vib. Spectrosc.* **40**, 219–224 (2006).

[166] R. Lindenmaier, N. K. Scharko, R. G. Tonkyn, K. T. Nguyen, S. D. Williams, and T. J. Johnson, “Improved assignments of the vibrational fundamental modes of ortho-, meta-, and para-xylene using gas- and liquid-phase infrared and Raman spectra combined with ab initio calculations: Quantitative gas-phase infrared spectra for detection,” *J. Mol. Struct.* **1149**, 332–351 (2017).

[167] P. Meksiarun, M. Ishigaki, V. A. C. Huck-Pezzei, C. W. Huck, K. Wongravee, H. Sato, and Y. Ozaki, “Comparison of multivariate analysis methods for extracting the paraffin component from the paraffin-embedded cancer tissue spectra for Raman imaging,” *Sci. Rep.* **7** (2017).

[168] D.B. Nadini, “Cancer Cell Nucleus: An Insight,” *J. Mol. Biomark. Diagn.* **8**,

1–8 (2017).

[169] R. Galli, M. Kirsch, E. Koch, G. Schackert, G. Steiner, M. Kirsch and O. Uckermann, “Optical molecular imaging of corpora amylacea in human brain tissue,” *Biomed Tech* (2018).

[170] M. L. Bondy, M. E. Scheurer, B. Malmer, J. S. Barnholtz-Sloan, F. G. Davis, D. Il’yasova, C. Kruchko, B. J. McCarthy, P. Rajaraman, et al., “Brain tumor epidemiology: Consensus from the Brain Tumor Epidemiology Consortium,” *Cancer* **113** (2008).

[171] E. C. Holland, “Glioblastoma multiforme: The terminator,” *Proc. Natl. Acad. Sci.* **97**, 6242–6244 (2000).

[172] D. Ricard, A. Idbaih, F. Ducray, M. Lahutte, K. Hoang-Xuan, and J. Y. Delattre, “Primary brain tumours in adults,” *Lancet* **379**, (2012).

[173] H. L. Somerset and B. K. Kleinschmidt-DeMasters, “Approach to the intraoperative consultation for neurosurgical specimens,” *Adv. Anat. Pathol.* **18** (2011).

[174] M. Kirsch, J. Strasser, R. Allende, L. Bello, J. Zhang, and P. M. Black, “Angiostatin suppresses malignant glioma growth in vivo,” *Cancer Res* **58**, 4654–4659 (1998).

[175] M. Kirsch, P. Weigel, T. Pinzer, R. S. Carroll, P. M. L. Black, H. K. Schackert, and G. Schackert, “Therapy of hematogenous melanoma brain metastases with endostatin,” *Clin. Cancer Res.* **11**, 1259–1267 (2005).

[176] J. Schindelin, I. Arganda-Carreras, E. Frise, V. Kaynig, M. Longair, T. Pietzsch, S. Preibisch, C. Rueden, S. Saalfeld, et al., “Fiji: An open-source platform for biological-image analysis,” *Nat. Methods* **9** (2012).

[177] J. Yates, D. K. Thompson, C. P. Boesel, C. Albrightson, and R. W. Hart, “Lipid composition of human neural tumors.,” *J. Lipid Res.* **20**, 428–436 (1979).

[178] C. Beleites, K. Geiger, M. Kirsch, S. B. Sobottka, G. Schackert, and R. Salzer, “Raman spectroscopic grading of astrocytoma tissues: Using soft reference information,” *Anal. Bioanal. Chem.* **400**, 2801–2816 (2011).

[179] C. Krafft, S. B. Sobottka, K. D. Geiger, G. Schackert, and R. Salzer, “Classification of malignant gliomas by infrared spectroscopic imaging and linear discriminant analysis,” *Anal. Bioanal. Chem.* **387**, (2007).

[180] N. Bergner, T. Bocklitz, B. F. M. Romeike, R. Reichart, R. Kalff, C. Krafft,

and J. Popp, “Identification of primary tumors of brain metastases by Raman imaging and support vector machines,” *Chemom. Intell. Lab. Syst.* **117**, 224–232 (2012).

[181] S. Koljenović, T. C. Bakker Schut, R. Wolthuis, B. de Jong, L. Santos, P. J. Caspers, J. M. Kros, and G. J. Puppels, “Tissue characterization using high wave number Raman spectroscopy,” *J. Biomed. Opt.* **10**, 031116 (2005).

[182] D. Martin, M. Robbins, A. Spector, B. Wen, and D. Hussey, “The fatty acid composition of human gliomas differs from that found in nonmalignant brain tissue,” *Lipids* **31**, 1283–1288 (1996).

[183] T. Meyer, M. Chemnitz, M. Baumgartl, T. Gottschall, T. Pascher, C. Matthäus, B. F. M. Romeike, B. R. Brehm, J. Limpert, et al., “Expanding multimodal microscopy by high spectral resolution coherent anti-stokes Raman scattering imaging for clinical disease diagnostics,” *Anal. Chem.* **85**, 6703–6715 (2013).

[184] F. Galeffi and D. A. Turner, “Exploiting Metabolic Differences in Glioma Therapy,” *Curr. Drug Discov. Technol.* **9**, 280–293 (2012).

[185] C. Profyris, S. S. Cheema, D. W. Zang, M. F. Azari, K. Boyle, and S. Petratos, “Degenerative and regenerative mechanisms governing spinal cord injury,” *Neurobiol. Dis.* **15** (2004).

[186] N. Klapka and H. W. Müller, “Collagen matrix in spinal cord injury.,” *J. Neurotrauma* **23**, 422–435 (2006).

[187] M. C. Shearer and J. W. Fawcett, “The astrocyte/meningeal cell interface - A barrier to successful nerve regeneration?,” *Cell Tissue Res.* **305** (2001).

[188] K.-A. Nave and H. B. Werner, “Myelination of the Nervous System: Mechanisms and Functions,” *Annu. Rev. Cell Dev. Biol.* **30**, 503–533 (2014).

[189] L. A. Boven, M. Van Meurs, M. Van Zwam, A. Wierenga-Wolf, R. Q. Hintzen, R. G. Boot, J. M. Aerts, S. Amor, E. E. Nieuwenhuis, et al., “Myelin-laden macrophages are anti-inflammatory, consistent with foam cells in multiple sclerosis,” *Brain* **129**, 517–526 (2006).

[190] H. Li, M. L. Cuzner, and J. Newcombe, “Microglia-derived macrophages in early multiple sclerosis plaques,” *Neuropathol. Appl. Neurobiol.* **22**, 207–215 (1996).

[191] Y. Ohsaki, M. Suzuki, and T. Fujimoto, “Open questions in lipid droplet biology,” *Chem. Biol.* **21** (2014).

[192] M. Salehipour, E. Javadi, J. Z. Reza, M. Doosti, S. Rezaei, M. Paknejad, N. Nejadi, and M. Heidari, “Polyunsaturated Fatty Acids and Modulation of Cholesterol Homeostasis in THP-1 Macrophage-Derived Foam Cells,” *Int. J. Mol. Sci.* **11**, 4660–4672 (2010).

[193] M. Nhong, T. Wei, L. Boring, I. F. Charo, R. M. Ransohoff, and L. B. Jakeman, “Monocyte recruitment and myelin removal are delayed following spinal cord injury in mice with CCR2 chemokine receptor deletion,” *J. Neurosci. Res.* **68**, 691–702 (2002).

[194] N. Vallières, J. L. Berard, S. David, and S. Lacroix, “Systemic injections of lipopolysaccharide accelerates myelin phagocytosis during wallerian degeneration in the injured mouse spinal cord,” *Glia* **53**, 103–113 (2006).

[195] B. X. W. Wong, R. A. Kyle, K. D. Croft, C. M. Quinn, W. Jessup, and B. B. Yeap, “Modulation of macrophage fatty acid content and composition by exposure to dyslipidemic serum in vitro,” *Lipids* **46**, 371–380 (2011).

[196] K. R. Feingold, J. K. Shigenaga, M. R. Kazemi, C. M. McDonald, S. M. Patzek, A. S. Cross, A. Moser, and C. Grunfeld, “Mechanisms of triglyceride accumulation in activated macrophages,” *J. Leukoc. Biol.* **92**, 829–839 (2012).

[197] I. Tabas, “Cholesterol and phospholipid metabolism in macrophages,” *Biochim. Biophys. Acta - Mol. Cell Biol. Lipids* **1529** (2000).

[198] A. Khatchadourian, S. D. Bourque, V. R. Richard, V. I. Titorenko, and D. Maysinger, “Dynamics and regulation of lipid droplet formation in lipopolysaccharide (LPS)-stimulated microglia,” *Biochim. Biophys. Acta - Mol. Cell Biol. Lipids* **1821**, 607–617 (2012).

[199] M. T. Fitch, C. Doller, C. K. Combs, G. E. Landreth, and J. Silver, “Cellular and molecular mechanisms of glial scarring and progressive cavitation: in vivo and in vitro analysis of inflammation-induced secondary injury after CNS trauma.,” *J. Neurosci.* **19**, 8182–8198 (1999).

[200] S. David and J. Aguayo, “Axonal elongation into peripheral nervous system ‘bridges’ after central nervous system injury in adult rats.,” *Science* **214**, 931–933 (1981).

[201] B. S. Bregman, M. McAtee, H. N. Dai, and P. L. Kuhn, “Neurotrophic factors increase axonal growth after spinal cord injury and transplantation in the adult rat.,” *Exp. Neurol.* **148**, 475–494 (1997).

[202] P. D. Storer, D. Dolbeare, and J. D. Houle, “Treatment of Chronically Injured Spinal Cord With Neurotrophic Factors Stimulates II-Tubulin and

GAP-43 Expression in Rubrospinal Tract Neurons," *J. Neurosci. Res.* **74**, 502–511 (2003).

[203] V. S. Boyce and L. M. Mendell, "Neurotrophic factors in spinal cord injury," *Handb Exp Pharmacol* **220**, 443–460 (2014).

[204] E. J. Bradbury, L. D. F. Moon, R. J. Popat, V. R. King, G. S. Bennett, P. N. Patel, J. W. Fawcett, and S. B. McMahon, "Chondroitinase ABC promotes functional recovery after spinal cord injury," *Nature* **416**, 636–640 (2002).

[205] S. Martiñón and A. Ibarra, "Pharmacological neuroprotective therapy for acute spinal cord injury: state of the art.," *Mini Rev. Med. Chem.* **8**, 222–230 (2008).

[206] S. Thuret, L. D. F. Moon, and F. H. Gage, "Therapeutic interventions after spinal cord injury," *Nat. Rev. Neurosci.* **7**, 628–643 (2006).

[207] R. C. Assunção-Silva, E. D. Gomes, N. Sousa, N. A. Silva, and A. J. Salgado, "Hydrogels and Cell Based Therapies in Spinal Cord Injury Regeneration," *Stem Cells Int.* (2015).

[208] N. N. Madigan, S. McMahon, T. O'Brien, M. J. Yaszemski, and A. J. Windebank, "Current tissue engineering and novel therapeutic approaches to axonal regeneration following spinal cord injury using polymer scaffolds," *Respir. Physiol. Neurobiol.* **169**, 183–199 (2009).

[209] G. Perale, F. Rossi, E. Sundstrom, S. Bacchiega, M. Masi, G. Forloni, and P. Veglianese, "Hydrogels in spinal cord injury repair strategies," *ACS Chem. Neurosci.* **2** (2011).

[210] M. M. Pakulska, B. G. Ballios, and M. S. Shoichet, "Injectable hydrogels for central nervous system therapy," *Biomed. Mater.* **7** (2012).

[211] K. S. Straley, C. W. P. Foo, and S. C. Heilshorn, "Biomaterial Design Strategies for the Treatment of Spinal Cord Injuries," *J. Neurotrauma* **27**, 1–19 (2010).

[212] K. Y. Lee and D. J. Mooney, "Alginate: Properties and biomedical applications," *Prog. Polym. Sci.* **37**, 106–126 (2012).

[213] M. George and T. E. Abraham, "Polyionic hydrocolloids for the intestinal delivery of protein drugs: Alginate and chitosan - a review," *J. Control. Release* **114** (2006).

[214] K. Kataoka, Y. Suzuki, M. Kitada, K. Ohnishi, K. Suzuki, M. Tanihara, C. Ide, K. Endo, and Y. Nishimura, "Alginate, a bioresorbable material derived

from brown seaweed, enhances elongation of amputated axons of spinal cord in infant rats," *J. Biomed. Mater. Res.* **54**, 373–384 (2001).

[215] K. Kataoka, Y. Suzuki, M. Kitada, T. Hashimoto, H. Chou, H. Bai, M. Ohta, S. Wu, K. Suzuki, et al., "Alginate enhances elongation of early regenerating axons in spinal cord of young rats.," *Tissue Eng.* **10**, 493–504 (2004).

[216] C. A. McKay, R. D. Pomrenke, J. S. McLane, N. J. Schaub, E. K. Desimone, L. A. Ligon, and R. J. Gilbert, "An injectable, calcium responsive composite hydrogel for the treatment of acute spinal cord injury," *ACS Appl. Mater. Interfaces* **6**, 1424–1438 (2014).

[217] P. Prang, R. Müller, A. Eljaouhari, K. Heckmann, W. Kunz, T. Weber, C. Faber, M. Vroemen, U. Bogdahn, et al., "The promotion of oriented axonal regrowth in the injured spinal cord by alginate-based anisotropic capillary hydrogels," *Biomaterials* **27**, 3560–3569 (2006).

[218] E. Ansorena, P. De Berdt, B. Ucakar, T. Simón-Yarza, D. Jacobs, O. Schakman, A. Jankovski, R. Deumens, M. J. Blanco-Prieto, et al., "Injectable alginate hydrogel loaded with GDNF promotes functional recovery in a hemisection model of spinal cord injury," *Int. J. Pharm.* **455**, 148–158 (2013).

[219] N. O. Dhoot, C. A. Tobias, I. Fischer, and M. A. Wheatley, "Peptide-modified alginate surfaces as a growth permissive substrate for neurite outgrowth," *J. Biomed. Mater. Res. - Part A* **71**, 191–200 (2004).

[220] H. Daemi and M. Barikani, "Synthesis and characterization of calcium alginate nanoparticles, sodium homopolymannuronate salt and its calcium nanoparticles," *Sci. Iran.* **19**, 2023–2028 (2012).

[221] C. A. Tobias, S. S. W. Han, J. S. Shumsky, D. Kim, M. Tumolo, N. O. Dhoot, M. A. Wheatley, I. Fischer, A. Tessler, et al., "Alginate encapsulated BDNF-producing fibroblast grafts permit recovery of function after spinal cord injury in the absence of immune suppression.," *J. Neurotrauma* **22**, 138–156 (2005).

[222] L. N. Novikov, L. N. Novikova, A. Mosahebi, M. Wiberg, G. Terenghi, and J. O. Kellerth, "A novel biodegradable implant for neuronal rescue and regeneration after spinal cord injury," *Biomaterials* **23**, 3369–3376 (2002).

[223] L. N. Novikova, L. N. Novikov, and J. O. Kellerth, "Biopolymers and biodegradable smart implants for tissue regeneration after spinal cord

injury," in *Curr. Opin. Neurol.* **16** (2003).

[224] G. Perale, F. Bianco, C. Giordano, M. Matteoli, M. Masi, and a Cigada, "Engineering injured spinal cord with bone marrow-derived stem cells and hydrogel-based matrices: a glance at the state of the art.," *J. Appl. Biomater. Biomech.* **6**, 1–8 (2008).

[225] M. Matyash, F. Despang, R. Mandal, D. Fiore, M. Gelinsky, and C. Ikonomidou, "Novel Soft Alginate Hydrogel Strongly Supports Neurite Growth and Protects Neurons Against Oxidative Stress," *Tissue Eng. Part A* **18**, 55–66 (2012).

[226] M. Matyash, F. Despang, C. Ikonomidou, and M. Gelinsky, "Swelling and Mechanical Properties of Alginate Hydrogels with Respect to Promotion of Neural Growth," *Tissue Eng. Part C Methods* **20**, 401–411 (2014).

[227] Y. D. Teng, E. B. Lavik, X. Qu, K. I. Park, J. Ourednik, D. Zurakowski, R. Langer, and E. Y. Snyder, "Functional recovery following traumatic spinal cord injury mediated by a unique polymer scaffold seeded with neural stem cells.," *Proc. Natl. Acad. Sci. U. S. A.* **99**, 3024–3029 (2002).

[228] M. Geissbuehler and T. Lasser, "How to display data by color schemes compatible with red-green color perception deficiencies," *Opt. Express* **21**, 9862 (2013).

[229] A. B. Brizuela, L. C. Bichara, E. Romano, A. Yurquina, S. Locatelli, and S. A. Brandán, "A complete characterization of the vibrational spectra of sucrose," *Carbohydr. Res.* **361**, 212–218 (2012).

[230] E. D. Muse, H. Jurevics, A. D. Toews, G. K. Matsushima, and P. Morell, "Parameters related to lipid metabolism as markers of myelination in mouse brain," *J. Neurochem.* **76**, 77–86 (2001).

[231] K. Z. Liu, R. A. Shaw, A. Man, T. C. Dembinski, and H. H. Mantsh, "Reagent-free, simultaneous determination of serum cholesterol in HDL and LDL by infrared spectroscopy," *Clin. Chem.* **48**, 499–506 (2002).

[232] T. Hagg and M. Oudega, "Degenerative and Spontaneous Regenerative Processes after Spinal Cord Injury," *J. Neurotrauma* **23**, 263–280 (2006).

[233] S. D. Christie, B. Comeau, T. Myers, D. Sadi, M. Purdy, and I. Mendez, "Duration of lipid peroxidation after acute spinal cord injury in rats and the effect of methylprednisolone," *Neurosurg. Focus* **25**, E5 (2008).

[234] C. A. Oyinbo, "Secondary injury mechanisms in traumatic spinal cord injury: A nugget of this multiply cascade," *Acta Neurobiol. Exp. (Wars).* **71**

(2011).

[235] V. L. Arvanian, L. Schnell, L. Lou, R. Golshani, A. Hunanyan, A. Ghosh, D. D. Pearse, J. K. Robinson, M. E. Schwab, et al., “Chronic spinal hemisection in rats induces a progressive decline in transmission in uninjured fibers to motoneurons,” *Exp. Neurol.* **216**, 471–480 (2009).

[236] A. S. Hunanyan, V. Alessi, S. Patel, D. D. Pearse, G. Matthews, and V. L. Arvanian, “Alterations of action potentials and the localization of Nav1.6 sodium channels in spared axons after hemisection injury of the spinal cord in adult rats,” *J. Neurophysiol.* **105**, 1033–1044 (2011).

[237] G.-H. Choi and and J.-K. K. , Duk-Youn Kim , Ho-Sang Son , Hong-Tae Kim, “Alginate Gel Decreases Chondroitin Sulfate Proteoglycan Immunoreactivity Following Spinal Cord Injury: Preliminary Study,” *Tissue Eng. Regen. Med.* **3**, 472–477 (2006).

[238] R. Cheheltani, J. M. Rosano, B. Wang, A. K. Sabri, N. Pleshko, and M. F. Kiani, “Fourier transform infrared spectroscopic imaging of cardiac tissue to detect collagen deposition after myocardial infarction,” *J. Biomed. Opt.* **17**, 056014 (2012).

[239] K. Belbachir, R. Noreen, G. Gouspillou, and C. Petibois, “Collagen types analysis and differentiation by FTIR spectroscopy,” *Anal. Bioanal. Chem.* **395**, 829–837 (2009).

[240] V. Estrada, N. Brazda, C. Schmitz, S. Heller, H. Blazyca, R. Martini, and H. W. Müller, “Long-lasting significant functional improvement in chronic severe spinal cord injury following scar resection and polyethylene glycol implantation,” *Neurobiol. Dis.* **67**, 165–179 (2014).

[241] B. Sarker, R. Singh, R. Silva, J. A. Roether, J. Kaschta, R. Detsch, D. W. Schubert, I. Cicha, and A. R. Boccaccini, “Evaluation of fibroblasts adhesion and proliferation on alginate-gelatin crosslinked hydrogel,” *PLoS One* **9** (2014).

[242] A. R. Fajardo, M. B. Silva, L. C. Lopes, J. F. Piai, A. F. Rubira, and E. C. Muniz, “Hydrogel based on an alginate–Ca2+/chondroitin sulfate matrix as a potential colon-specific drug delivery system,” *RSC Adv.* **2**, 11095 (2012).

[243] H. J. Kong, D. Kaigler, K. Kim, and D. J. Mooney, “Controlling rigidity and degradation of alginate hydrogels via molecular weight distribution,” *Biomacromolecules* **5**, 1720–1727 (2004).

[244] M. S. Shoichet, R. H. Li, M. L. White, and S. R. Winn, “Stability of hydrogels used in cell encapsulation: An in vitro comparison of alginate and

agarose," *Biotechnol. Bioeng.* **50**, 374–381 (1996).

[245] M. Chanimov, S. Berman, V. Gofman, Y. Weissgarten, Z. Averbukh, M. L. Cohen, A. Vitin, and M. Bahar, "Total cell associated electrolyte homeostasis in rat spinal cord cells following apparently irreversible injury.," *Med. Sci. Monit.* **12**, BR63-7 (2006).

[246] G. M. Smith and S. M. Onifer, "Construction of pathways to promote axon growth within the adult central nervous system," in *Brain Res. Bull.* **84** (2011).

[247] C. J. Ek, M. D. Habgood, R. Dennis, K. M. Dziegielewska, C. Mallard, B. Wheaton, and N. R. Saunders, "Pathological Changes in the White Matter after Spinal Contusion Injury in the Rat," *PLoS One* **7** (2012).

[248] R. J. Dumont, D. O. Okonkwo, S. Verma, R. J. Hurlbert, P. T. Boulos, D. B. Ellegala, and a S. Dumont, "Acute spinal cord injury, part I: pathophysiologic mechanisms," *Clin. Neuropharmacol.* **24**, 254–264 (2001).

[249] T. Schmid, A. Messmer, B. S. Yeo, W. Zhang, and R. Zenobi, "Towards chemical analysis of nanostructures in biofilms II: Tip-enhanced Raman spectroscopy of alginates," *Anal. Bioanal. Chem.* **391**, 1907–1916 (2008).

[250] S. Ichioka, K. Harii, M. Nakahara, and Y. Sato, "An experimental comparison of hydrocolloid and alginate dressings, and the effect of calcium ions on the behaviour of alginate gel," *Scand. J. Plast. Reconstr. Surg. Hand Surg.* **32**, 311–316 (1998).

[251] M. C. Potcoava, G. L. Futia, J. Aughenbaugh, I. R. Schlaepfer, and E. A. Gibson, "Raman and coherent anti-Stokes Raman scattering microscopy studies of changes in lipid content and composition in hormone-treated breast and prostate cancer cells," *J. Biomed. Opt.* **19**, 111605 (2014).

[252] O. Uckermann, R. Galli, R. Beiermeister, K. H. Sitoci-Ficici, R. Later, E. Leipnitz, A. Neuwirth, T. Chavakis, E. Koch, et al., "Endogenous two-photon excited fluorescence provides label-free visualization of the inflammatory response in the rodent spinal cord," *Biomed Res. Int.* **2015** (2015).

[253] R. C. Armstrong, A. J. Mierzwa, C. M. Marion, and G. M. Sullivan, "White matter involvement after TBI: Clues to axon and myelin repair capacity," *Exp. Neurol.* **275** (2016).

[254] M. E. Vargas and B. A. Barres, "Why Is Wallerian Degeneration in the CNS So Slow?," *Annu. Rev. Neurosci.* **30**, 153–179 (2007).

[255] M. S. Brown, Y. K. Ho, and J. L. Goldstein, “The cholesteryl ester cycle in macrophage foam cells. Continual hydrolysis and re-esterification of cytoplasmic cholesteryl esters,” *J. Biol. Chem.* **255**, 9344–9352 (1980).

[256] E. B. Hanlon, R. Manoharan, T. W. Koo, K. E. Shafer, J. T. Motz, M. Fitzmaurice, J. R. Kramer, I. Itzkan, R. R. Dasari, et al., “Prospects for in vivo Raman spectroscopy,” *Phys. Med. Biol.* **45** (2000).

[257] M. Sekiya, J.-I. Osuga, M. Igarashi, H. Okazaki, and S. Ishibashi, “The role of neutral cholesterol ester hydrolysis in macrophage foam cells.,” *J. Atheroscler. Thromb.* **18**, 359–364 (2011).

[258] J. F. Goodrum, J. E. Weaver, N. D. Goines, and T. W. Bouldin, “Fatty Acids from Degenerating Myelin Lipids Are Conserved and Reutilized for Myelin Synthesis During Regeneration in Peripheral Nerve,” *J. Neurochem.* **65**, 1752–1759 (1995).

[259] J. F. Goodrum, T. Earnhardt, N. Goines, and T. W. Bouldin, “Fate of myelin lipids during degeneration and regeneration of peripheral nerve: an autoradiographic study.,” *J. Neurosci.* **14**, 357–367 (1994).

[260] J. R. Beattie, S. E. J. Bell, and B. W. Moss, “A critical evaluation of Raman spectroscopy for the analysis of lipids: Fatty acid methyl esters,” *Lipids* **39**, 407–419 (2004).

[261] K. Czamara, K. Majzner, M. Z. Pacia, K. Kochan, A. Kaczor, and M. Baranska, “Raman spectroscopy of lipids: A review,” *J. Raman Spectrosc.* **46** (2015).

[262] R. M. Adibhatla and J. F. Hatcher, “Lipid Oxidation and Peroxidation in CNS Health and Disease: From Molecular Mechanisms to Therapeutic Opportunities,” *Antioxid. Redox Signal.* **12**, 125–169 (2010).

[263] A. Negre-Salvayre, C. Coatrieux, C. Ingueneau, and R. Salvayre, “Advanced lipid peroxidation end products in oxidative damage to proteins. Potential role in diseases and therapeutic prospects for the inhibitors,” *Br. J. Pharmacol.* **153** (2008).

[264] J. De Gelder, K. De Gussem, P. Vandenabeele, and L. Moens, “Reference database of Raman spectra of biological molecules,” *J. Raman Spectrosc.* **38**, 1133–1147 (2007).

[265] E. B. Button, A. S. Mitchell, M. M. Domingos, J. H. J. Chung, R. M. Bradley, A. Hashemi, P. M. Marvyn, A. C. Patterson, K. D. Stark, et al., “Microglial cell activation increases saturated and decreases monounsaturated fatty acid content, but both lipid species are proinflammatory,” *Lipids* **49**, 305–

316 (2014).

[266] I. Carrié, M. Clément, D. de Javel, H. Francès, and J. M. Bourre, “Specific phospholipid fatty acid composition of brain regions in mice. Effects of n-3 polyunsaturated fatty acid deficiency and phospholipid supplementation.,” *J. Lipid Res.* **41** (2000).

[267] C. Matthäus, C. Krafft, B. Dietzek, B. R. Brehm, S. Lorkowski, and J. Popp, “Noninvasive imaging of intracellular lipid metabolism in macrophages by Raman microscopy in combination with stable isotopic labeling,” *Anal. Chem.* **84**, 8549–8556 (2012).

[268] C. Stiebing, C. Matthäus, C. Krafft, A.-A. Keller, K. Weber, S. Lorkowski, and J. Popp, “Complexity of fatty acid distribution inside human macrophages on single cell level using Raman micro-spectroscopy,” *Anal. Bioanal. Chem.* **406**, 7037–7046 (2014).

[269] H.-J. van Manen, Y. M. Kraan, D. Roos, and C. Otto, “Single-cell Raman and fluorescence microscopy reveal the association of lipid bodies with phagosomes in leukocytes.,” *Proc. Natl. Acad. Sci. USA* **102**, 10159–10164 (2005).

[270] V. Rioux and P. Legrand, “Saturated fatty acids: Simple molecular structures with complex cellular functions,” *Curr. Opin. Clin. Nutr. Metab. Care* **10** (2007).

[271] V. Rioux, F. Pédrono, and P. Legrand, “Regulation of mammalian desaturases by myristic acid: N-terminal myristoylation and other modulations,” *Biochim. Biophys. Acta - Mol. Cell Biol. Lipids* **1811** (2011).

ACKNOWLEDGEMENTS

I would like to sincerely thank all the many people, who directly or indirectly were supporting my research and me during the years of my PhD studies. These people made a great impact to my scientific achievements and personal development in solution-oriented thinking, which I believe, will help me a lot in my future, whatever it may bring.

Firstly, especially lots of nice words I want to give to my supervisor, Prof. Valdas Šablinskas. He was the one, showing me from the very beginning, how the scientist should be. Often strict and demanding, but at the same time incredibly supportive and understanding, Prof. Šablinskas steadily guided me through all the years of my scientific activities. I would like to express my gratitude to all the people belonging to department of General Physics and Spectroscopy of Faculty of Physics in Vilnius University, who were the first to open me the doors for scientific career as I was still a bachelor student. Dr. Justinas Čeponkus was always ready to give a good piece of advice, while Dr. Milda Pučetaitė, being one year further as I, was always a good example and inspiration to show, what a young scientist can reach, when she consistent follows her goals.

Secondly, I would like to express my gratitude to all the people from Clinical Sensoring and Monitoring at TU Dresden and Neurosurgery from Carl Gustav Carus University Hospital in Dredsen, who were not even kindly allowing to perform my research in Dresden, but also always actively took part in helping me to bring my research to successful results. Without them, this thesis would not be present.

Prof. Steiner was always ready to discuss and plan my research. His reasonable criticism was often a nice and needed push to bring my work to higher level of quality. Prof. Steiner was also extremely helpful and supportive as I was seeking to arrange my stay in Dresden on a long term. Prof. Kirsch was always a great example and prove for me that interdisciplinary science is possible and, in fact, so exciting and productive, when the scientists are thinking beyond their primary scientific field. Collaboration with him, as a medical doctor, was not only very productive, but also enabled to understand and work towards fulfilling the real needs of clinicians.

The two persons, namely Dr. Roberta Galli and Dr. Ortrud Uckermann, deserve special thanks from me. They were so much of help in various situations during my research, especially, when I was struggling with some problems. I learned a lot from their combined expertise: from Dr. Galli in the field of physics, whereas from Dr. Uckermann in the field of biology. Due to supportive and friendly atmosphere, working with them was always a pleasure.

Last, but not least, I would like to express my thankfulness to all the people, who somehow contributed to this research, but were not mentioned personally. Also, I am very much thankful for my family and friends in Vilnius and in Dresden, who were always believing in me, sometimes more than I by myself. I am particularly thankful for Klaus, who was so often interested in my work and who was always motivating me. Finally, many thanks go to Jürgen – for showing me how important it is to be patient and not to give up until you will reach your goals.